Electron Microscopy of Crystalline Phases and Solid Solution Behaviour in Model Leaf Waxes and Molecular Crystals

Emily Kate Wynne

Submitted in accordance with the requirements for the degree of
Doctor of Philosophy

The University of Leeds
School of Chemical and Process Engineering

May 2025

The candidate confirms that the work submitted is her own, except where work which has formed part of jointly-authored publications has been included. The contribution of the candidate and the other authors to this work has been explicitly indicated below. The candidate confirms that appropriate credit has been given within the thesis where reference has been made to the work of others.

Chapter 4 and 5 are based on work from a jointly authored publication:

Wynne, E., Connell, S.D., Shinebaum, R., Blade, H., George, N., Brown, A. and Collins, S.M. 2024. Grain and Domain Microstructure in Long Chain N-Alkane and N-Alkanol Wax Crystals. *Crystal Growth and Design*. **15**, p.22.

E.W. prepared the samples and collected bright field TEM and SAED data. **E.W.** and S.M.C. collected the SED data, and built the *Pbcm* and *A2$_1$am* $C_{31}H_{64}$ unit cells, and the *C2*/*c*, *P2$_1$*/*c* and *P2*/*c* $C_{30}H_{61}OH$ unit cells. **E.W.** carried out the electron diffraction simulations and processed the electron microscopy data. S.D.C. collected and processed the AFM data. **E.W.,** R.S., H.B., N.G., A.B., and S.M.C. designed the project. The manuscript was written through contributions of **all authors**.

Chapter 6 contains elements published the following journal:

Pham, S.T., Koniuch, N., **Wynne, E.**, Brown, A. and Collins, S.M. 2025. Microscopic crystallographic analysis of dislocations in molecular crystals. *Nature Materials 2025*., pp.1–6.

S.T.P. prepared the *p*-terphenyl and anthracene crystals. N.K. prepared the theophylline crystals. **E.W.** prepared the wax crystals. S.T.P., N.K., **E.W.** and S.M.C. acquired the electron diffraction data. S.T.P. and N.K. indexed the diffraction data. S.T.P. carried out the displacement measurements and dislocation analyses. S.M.C. created the geometric model and conceived the project. A.B. and S.M.C. supervised the execution of the project. **All authors** contributed to the writing and revision of the paper.

Acknowledgements

I would firstly like to express my thanks to both of my supervisors Dr Sean Collins and Professor Andy Brown, who have always gone above and beyond with help, invaluable guidance, encouragement, and support throughout my PhD. Their high attention to detail and knowledge has ensured I have constantly strived to improve my own skills throughout my PhD, and I believe I have greatly improved as such. I appreciate both of their endless patience with me over the last 4 years, and belief in me even when my own belief was lacking. Their expertise and thoughtful feedback, have been instrumental to this project. I would also like to thank my industrial supervisors Dr Neil George, Dr Adam Keates, Dr Helen Blade, and Dr Rachael Shinebaum for their help, insightful conversations and knowledge from an industrial perspective which steered me throughout this research. This project would not have been possible without all of their input.

I would like to thank everyone from LEMAS who I have worked with. In particular I would like to thank Dr Zabeada Aslam for her help and technical support, Dr Natalia Koniuch for her support and help with CrystalMaker, and Dr Sang Pham for his invaluable discussion on dislocation analysis. I would also like to thank all the PhD students and post-docs in office 4.20 for keeping me sane whilst writing this thesis; in particular, Jess, Rob, Martha, Ben and Becca. Thank you to those involved with the Molecules to Product CDT (Professor Elaine Martin, Angela Morrison, Charlie Jefferson, Professor John Blacker, Dr David Harbottle, Dr Nicole Hondow, and Professor Steve Marsden) for the opportunity to be part of the CDT and allowing me to be involved as cohort 2 student representative. Thanks to my team on my UKRI Policy Internship for being so welcoming from my first day, and encouraging me with my career.

I would like to thank Dr Tom Brown and Dr Fanny Nascimento Costa for their help with XRD data collection, and believing me every time I emailed saying I just needed one more piece of data. I would like to thank Dr Simon Connell for AFM data collection and insightful analysis. I would also like to thank Dr Adrian Cunliffe for TGA, DSC, and ATR-IR data collection. I would like to thank Dr Chris Pask and Dr Alex Heyam for XRD and NMR training respectively, and Rob Simpson for optical microscope training. I am grateful to the ePSIC team from Diamond Light Source, especially to Dr Mohsen Danaie, Dr Tom Slater and Dr Chris Allen for their help and support in data collection.

I would like to thank Anna Morrell for being the funniest person I know, providing me endless emotional support (sorry) and someone I can tell anything to without any judgement, Maisie Holbrow-Wilshaw for always meeting me for a coffee and inspiring

me to become physically fitter through her own achievements, Megan Bradbury for always going for a pint with me and two years of living together, and Dan Williams for always having a gossip with me. To all the other friends I have made living in Leeds but have not named, but you know who you are. I am glad I did this PhD to allow me to meet all of you, as my life is much better for it.

Finally, a thanks to my family. To my sister, Rachel Wynne, who is my best friend and has been there for me every step of the way and who is the first person I share all my achievements with, and my parents, Jackie and Tommy Wynne, who have always believed in me, and always been the first to read my work. This PhD would not have been possible without your support.

Abstract

Molecular organic crystals are widely used for applications in the pharmaceutical and agrochemical sectors. These crystals are often formed as part of a mixture of molecular components, forming co-crystals and solid solutions which impacts properties such as solubility and dissolution rates. Solid form molecular mixtures may give rise to chemical as well as structural heterogeneity across length scales. Understanding the nanoscale structure of these materials is therefore important to understand the resulting properties, physical or mechanical, in the development of new products for application as pharmaceuticals and agrochemicals. Many techniques traditionally used to characterise the structure of these systems are limited when it comes to the analysis of heterogeneity at the nanoscale. Scanning transmission electron microscopy (STEM) and specifically scanning electron diffraction (SED) is an emerging technique that offers high spatially resolved structural information at low electron doses, whilst associated spectroscopic methods can offer information on chemical heterogeneity. In this thesis SED and spectroscopic STEM-based techniques are used to study two organic solid solution systems; a replica leaf wax system of an *n*-alkane (*n*-hentriacontane, $C_{31}H_{64}$), and an *n*-alkanol (1-triacontanol, $C_{30}H_{61}OH$), and a barbituric acid (BA) and thiobarbituric acid (TBA) solid solution system for pharmaceutical applications.

This work first reveals the microscopic structure and heterogeneity of the replica leaf wax models based on the dominant wax types in the *Schefflera elegantissima* plant, namely $C_{31}H_{64}$ and $C_{30}H_{61}OH$ and their binary mixtures. SED reveals grain microstructure in $C_{31}H_{64}$ crystals and nanoscale domains of chain-ordered lamellae within these grains. Moreover, nematic phases and dynamical disorder coexist with the domains of ordered lamellae. $C_{30}H_{61}OH$ exhibits more disordered chain packing with no grain structure or lamellar domains. Binary mixtures from 0–50% $C_{30}H_{61}OH$ exhibit a loss of grain structure with increasing alcohol content accompanied by increasingly nematic rather than lamellar chain packing, suggesting a partial but limited solid solution behaviour. Together, these results unveil the previously unseen microstructural features that may govern flexibility and permeability of leaf cuticles.

Analysis then turns to studying the impact of exposing these waxes to an external molecule, tris(2-ethylhexyl)phosphate (TEHP) commonly used as an adjuvant to promote uptake of crop protection molecules after topical application of a spray to a leaf. A combination of bulk techniques (X-ray diffraction (XRD), differential scanning calorimetry (DSC)) and electron microscopy techniques at different wax to TEHP concentrations suggest possible etching and dissolution mechanisms that disrupt the crystalline paraffin wax structures, with a greater effect seen in the interaction with the

n-alkanol chains than the *n*-alkane chains. Wax crystal plane facet analysis by SED confirms the increased loss of material at crystal plane faces with a higher proportion of alcohol groups presenting at an exposed surface. In the paraffin wax solid solution system, spectroscopic techniques fail to differentiate the two wax components.

Finally, SED with elemental spectroscopy, energy dispersive X-ray spectroscopy, (EDS) is used to characterise the BA / TBA molecular alloying system prepared from ethanol solvents, where the two component molecules are similar except where a sulphur atom has replaced an oxygen atom in the TBA. X-ray diffraction (XRD) and differential scanning calorimetry (DSC) suggest the components form a solid solution over the range of 20 – 70 % TBA content albeit with some hydrate formation too. EDS is used to quantify increasing TBA content up to ~60 % TBA, above which additional sulphur (TBA) content cannot be differentiated due to the increasing Bremsstrahlung background contribution it makes to the EDS.

The SED implementation of 4D-STEM has been shown to reveal microstructural features within a molecular solid solution that are not accessible by bulk techniques (such as changes in grain orientation, order and disorder at the nanoscale and dislocations). SED also has the potential to explore the importance of functional groups in solid solution formation, interaction with external molecules, and how impurities may affect solid solution form and stability (for example hydrate formation). Together this work opens up new prospects for the wider study of molecular crystal, solid solution systems.

Table of Contents

List of Figures

List of Tables

Abbreviations

(hkl)	Miller indices of a crystal plane
[UVW]	Indices of beam direction
4D-STEM	4-dimensional scanning transmission electron microscopy
ADF	Annular dark field
AE	Alcohol ethoxylate
AFM	Atomic force microscopy
AI	Active ingredient
API	Active pharmaceutical ingredient
ATR-IR	Attenuated total reflection infrared spectroscopy
B	Burgers vector
BA	Barbituric acid
BF	Bright field
BSE	Back scattered electrons
CCDC	Cambridge Crystallographic Data Centre
C_F	Critical fluence
CIF	Crystallographic information file
COF	Covalent organic framework
Cryo-TEM	Cryogenic transmission electron microscopy
CTEM	Conventional transmission electron microscopy
D	Cumulative fluence or dose
DF	Dark field
DQE	Detective quantum efficiency
DSC	Differential scanning calorimetry
DTG	Derivative thermogravimetry
E_0	Beam energy
EDS/EDX	Energy dispersive X-ray spectroscopy
EELS	Electron energy loss spectroscopy
EM	Electron microscopy
E_s	Energy required to displace an atom at the surface of a sample
FEG	Field emission gun
FT-IR	Fourier transform infrared spectroscopy
FWHM	Full width at half maximum
$\mathbf{g}_{hkl}$	Notation that refers to the scattering vectors i.e. the positions marked by spots in a diffraction pattern
HAADF	High angle annular dark field
iDPC	Integrated differential phase contrast
IQR	Interquartile range

IW	Intracuticular wax
MOF	Metal organic framework
NMR	Nuclear magnetic resonance
PE	Polyethylene
ppm	Parts per million
pXRD	Powder X-ray diffraction
SADP	Selected area diffraction pattern
SAED	Selected area electron diffraction
SCXRD	Single crystal X-ray diffraction
SE	Secondary electrons
SE	Standard error
SED	Scanning electron diffraction
SEM	Scanning electron microscopy
SNR	Signal-to-noise ratio
STEM	Scanning transmission electron microscopy
STM	Scanning tunnelling microscopy
TBA	Thiobarbituric acid
TEHP	Tris(2-ethylhexyl)phosphate
TEM	Transmission Electron Microscopy
TGA	Thermogravimetric analysis
UV	Ultraviolet
vADF	Virtual annular dark field
VDF	Virtual dark field
VLCA	Very long chain aliphatics
WAXS	Wide-angle X-ray scattering
XRD	X-ray diffraction

Chapter 1
Introduction

Molecular organic crystals are widely used for applications in the pharmaceutical and agrochemical sectors. These crystals are often formed as part of a mixture of molecular components, forming co-crystals and solid solutions which impacts properties such as solubility and dissolution rates. In this process, crystallisation of a molecule of interest, for example an active pharmaceutical ingredient (API), may occur with excipient molecules (which may be solid under ambient conditions). Solid form molecular mixtures may give rise to chemical as well as structural heterogeneity across length scales. The possible changes in crystal form (polymorphs, solid solutions and co-crystals), microstructure (grains and defects) and stability that may occur must be considered since these will affect properties upon application. Nanoscale structure may also impact how external molecules interact with these systems, impacting properties such as diffusion rate.

Organic molecular solid solution systems are crystalline structures that form between two or more organic molecular crystals (Hill et al., 2023). Whilst similar to co-crystals, solid solutions have different structures which may change the properties of the system, so understanding nanoscale structure is vitally important. Solid solutions are proposed to form between molecular crystals which are isostructural and where the non-overlap volume between the components is minimised (Kitaigorodsky, 1984). The formation of solid solutions between pharmaceutical compounds can influence the properties of the molecular crystals, including dissolution rate and therefore bioavailability (Steed, 2013). Solid solutions may also form when there are small traces of impurities present (Kras et al., 2021). It is important for drug design to understand how the presence of impurities may drive crystallisation of the drug to a different polymorph form as a result of solid solution formation with these impurities. Solid solutions are typically characterised by techniques such as X-ray diffraction (XRD) and differential scanning calorimetry (DSC) (Lusi, 2018a), (Hill et al., 2023). There is also a question of solubility ranges across solid solution systems and the stability of these systems, with solid solution systems forming with trace amounts of a “guest” component, to the “guest” compound becoming the dominant fraction (Hill et al., 2023), (Shemchuk et al., 2016). There may be property changes with composition variation across these solid solution ranges, so understanding the nanoscale structure and stability of these systems is important to consider. However, for determining nanoscale heterogeneity within solid solution structures, these techniques, such as DSC and XRD, are limited.

Structure-property relationships are well studied and understood in metals and ceramics. For example, nanoscale structural changes at interfaces of metals and alloys can be analysed by electron microscopy (EM) techniques. This is achieved through a combination of multiple image and diffraction pattern analyses to determine grains, orientation relationships and boundary and defect structures (Forwood and Clarebrough, 2021). Structure-property relationships in solid-form molecular systems are less well established as organic materials are more prone to damage under the electron beam, so limiting the spatial resolution and number of analyses that can be acquired from a given region (Egerton, 2019). Organic molecular crystals have been studied by EM techniques since the 1960s to reveal crystal structures and some microstructural information. For example transmission electron microscopy (TEM) and selected area electron diffraction (SAED) have been used to study pharmaceutical compounds to reveal morphology, polymorph identification, mapping of crystal habit to crystal structure and basic crystal defect identification (Eddleston et al., 2010). This work has however been spatially limited such that mixing and interfaces between phases are not well described and the full characteristics of defects, such as slip systems for dislocations, are yet to be determined (Olson et al., 2018). More recent work has used conical dark field TEM techniques for the study of pharmaceutical compounds, identifying low levels of crystallinity in amorphous solid dispersions (S'Ari et al., 2021). These studies have highlighted the potential for scanning EM techniques to be used to study organic molecular systems, and in this thesis focus is placed on determining nanoscale structure in organic solid solution systems.

Advancements in EM detector technology have meant the development of low-dose EM techniques which can achieve a high signal to noise and therefore a high spatial resolution at these low electron doses. The development of 4D-scanning transmission electron microscopy (4D-STEM) techniques, where a 2D diffraction pattern is acquired at each scanned 2D image pixel across a field of view, has led to the analysis of nanoscale structural changes in organic materials (Ophus, 2019). This technique has recently been applied to polymer systems, structurally and chemically similar to paraffin waxes. Analysis has unveiled domain microstructures which affect physical and mechanical properties, as well as determining how external molecules may move across the materials (Chen et al., 2024). The opportunity is now here to use these techniques for the characterisation of organic molecular solid solution systems.

This project utilises low-dose, STEM techniques to study the nanoscale structure of two solid solution systems. The first solid solution system, a paraffin wax system, is studied as a simplified replica leaf wax system (Basson and Reynhardt, 1992). The intracuticular wax (IW) layer on a leaf contains long chain hydrocarbons and has been shown to constitute the principal barrier restricting herbicide movement into a plant

(Riederer and Müller, 2007), (Schonherr and Riederer, 1989). Specifically, the solid solution formation and microstructure of the wax components affects how molecules move across the IW layer i.e. the diffusivity properties of the structure is thought to be governed by a brick and mortar structure between crystalline and amorphous regions in the IW (Jetter and Riederer, 2016). An *n*-alkane, *n*-hentriacontane ($C_{31}H_{64}$), and an *n*-alkanol, 1-triacontanol, ($C_{30}H_{61}OH$), are studied, chosen as a model system for the IW layer in a simpler *Schefflera elegantissima* plant. Interactions of an external molecule, tris(2-ethylhexyl)phosphate (TEHP), with these individual components and binary mixtures are studied to understand how adjuvants, a compound added to a crop protection product to improve uptake of active ingredients, may interact with the IW layer based off this simple replica leaf wax model. The interaction between *n*-alkanes and *n*-alkanols with this external adjuvant are investigated, examining the effect increasing *n*-alkanol content may have on interactions between TEHP and wax as a model system for IW layer interactions.

Nanoscale structural heterogeneity can also be studied using EM spectroscopic techniques in combination with 4D-STEM techniques. A second solid solution system between two organic molecular crystals, barbituric acid (BA) and thiobarbituric acid (TBA) is also investigated. This solid solution system is studied as the presence of sulphur in TBA and not BA can be used as a chemical marker for spectroscopic characterisation. Compounds of this system have been used as anxiolytics and sedatives, have shown promise as antifungals, antibacterials, and anticancer agents (López-Muñoz et al., 2005), (Kidwai et al., 2005). The two compounds in this system exhibit polymorphism that affects solid solubility limits, co-crystal formation and subsequent properties such as solubility and melting points (Shemchuk et al., 2016). Uncertainty remains over solvent induced polymorph formation and what range co-crystals form vs a solid solution, and the stability of these solid solutions over time. 4D-STEM with elemental spectroscopy (EDS) presents the opportunity to further characterise this molecular alloying system. There is opportunity to explore possible phase separation where there is an unstable solid solution using these methods. STEM-EDS could identify domains of pure phases of one of the components, or if one component segregated to the surface of the particles in an unstable solid solution system.

The literature review in Chapter 2 first reviews current knowledge on the formation and characterisation of organic molecular solid solutions, and the potential to use emerging 4D-STEM techniques for the analysis of these systems where EM techniques have suffered from electron beam damage mechanisms previously. The project objectives are then outlined at the end of this chapter, aiming to use 4D-STEM and elemental spectroscopy techniques to examine nanoscale heterogeneity in these two solid

solution systems due to the impact this nanoscale structure may have on the materials properties. Chapter 3 then details the materials and methods used in this thesis. The results Chapters 4 – 7 then demonstrate analysis on the two solid solution systems identified (detailed at the end of the literature review). The paraffin wax solid solution system is first considered, using 4D-STEM to examine microstructure of these systems, the solubility limit of this solid solution system and then how external molecules interact with the system. A combination of 4D-STEM and elemental spectroscopy is then used to examine solid solution solubility and stability in the BA: TBA system. Conclusions and future work highlighted as a result of findings in this thesis are then found in Chapter 8.

Chapter 2
Literature Review

2.1 Structure Property Relationships

Understanding the nanoscale structure, or microstructure, of materials is important for understanding the properties of the material. Small changes in structure can have big effects on mechanical, thermal and electrical properties as is well established for metals and ceramics. This is important for the design of molecular products too such as in conjugated polymers where structural studies and molecular level modelling have been utilised to study the relationship between the structure and charge transport properties, for use in photovoltaics (Winokur and Chunwachirasiri, 2003), or for metallic glass materials where the atomic scale structure has been shown to determine mechanical properties such as stiffness, plasticity, and fragility (Cheng and Ma, 2011).

Structure-property relationships are important to consider across many molecular products, such as in the pharmaceutical and agrochemical sectors. In the preparation of pharmaceuticals, materials (active ingredients and excipients) go through many formulation steps. At any of these steps structure may change, potentially affecting the properties of the API in particular. Pharmaceuticals are formulated to control performance but may structurally change with, for example, shelf life storage. This is important for the effect this has on the solubility and so bioavailability of the API. Structure study is important to understand the life cycle of these types of formulations, for example there has been significant focus on amorphous solid dispersions and their stability (Ricarte et al., 2019).

In the agrochemical sector, the design and efficacy of crop protection products is the focus. An aspect of this requires understanding of the structure of plant leaves and specifically the microstructure of wax layers on and within the cuticle of leaves that control movement of molecules from the surface to within a leaf (Jetter and Riederer, 2016).

Organic materials with mixtures of different components, such as the waxes within a leaf or on the coating of a pharmaceutical tablet, have the possibility of phase separation, either on formation or during treatment/storage. Again, this will lead to different microstructures, and potentially preferential interaction with or between these separate phases. Thus the structures of these phases, the length scales over which they separate and how these phases and / or layers interact with one another, are of utmost importance for understanding properties of these materials. Examples of these materials include, but are not limited to, polymer nanoparticles, where layer

interactions affects the release kinetics of APIs in drug delivery polymeric nanoparticles (Koniuch et al., 2023), in biomaterials, where controlled layered structures can be utilised to enhance biocompatibility and additional active roles such as drug release (Ariga et al., 2008), and in the use of surfactants to control the crystallisation of droplets in oil-water formulations in the food industry (Liu et al., 2021).

Structure-property relationships in organic materials are studied utilising many different characterisation techniques. Atomic force microscopy (AFM) is a powerful technique that can characterise the surfaces of materials and their mechanical, electrical and magnetic material properties on the nanoscale (Stan and King, 2020). X-ray diffraction (XRD) is used to characterise the crystal structure of nanoscale materials (Holder and Schaak, 2019). Scanning electron microscopy (SEM) and transmission electron microscopy (TEM) are used to examine morphology such as formation of nanowires, rods, particles in polymer materials (Liu et al., 2010) (Yao and Zhao, 2014), or used for electron diffraction to study structure (Kolb et al., 2010), or where the structure directly affects properties in materials used for electrical transport, (Altoe et al., 2012), or in organic semiconductors (Eskelsen et al., 2013). Electron microscopy based structure studies of organic materials at molecular resolution have in theory been possible for many years but were difficult to undertake due to electron beam damage of the organics, however recent electron detector advancements have allowed the study of organic materials at sub-nanometre resolution with low dose conditions (Ophus, 2019). Specifically, the speed and sensitivity of detectors has improved such that they can collect measurable signals at low electron dose and exposure time.

This thesis uses primarily electron microscopy techniques to unveil the microstructure of solid solution materials that previously have not been seen. The following literature review first outlines the solid solution systems this work investigates, then discusses common characterisation methods used previously for structural understanding of these solid solution systems, the issues limiting these methods, and the importance of understanding the nanoscale structures of these systems.

2.2 Solid Solution Formation in Molecular Organic Systems

2.2.1 Solid Solution Formation

Organic molecular crystalline systems can contain more than one molecule or component. These molecular crystals can be ordered and stoichiometric, a co-crystal, or in the form of a solid solution. Solid solutions contain a major component, the host, and a minor component, the guest. In a solid solution, the guest molecules are distributed in the crystal lattice of the host in sites usually occupied by the host

molecule. Solid solutions can form across a wide range of concentrations, from small impurity trace amounts (Teerakapibal et al., 2020) through to the concentration is so high that a switch occurs and the guest becomes the dominant component (Shemchuk et al., 2016). Solid solution formation has been noted to have been overlooked in molecular systems previously (Hill et al., 2023), (Lusi, 2018a), but with advances in structural characterisation of disordered structures, there has been an uptake in the study of these systems. Studying molecular solid solutions isa important because incorporation of a guest into the crystal lattice of the host can alter the relative stabilities of different systems, for example by increasing the number of strong hydrogen bonds in the system (Cappuccino et al., 2023). This has implications for the solubility of these compounds, which is especially significant as many of these molecular compounds are used in drug compounds (Lusi, 2018c), (Cherukuvada and Nangia, 2013), (Spoletti et al., 2023). Solid solutions are similar to co-crystals (defined in the next sentence) but do not have ordering of molecular components i.e. have distinctly different structures to co-crystals, a visual representation of the differences is seen in Figure 2.1. Co-crystals are composed of two or more distinct molecular compounds in a fixed, stoichiometric ratio such that they form a uniform crystal lattice (Qiao et al., 2011), whereas in solid solutions the guest compound is randomly distributed across the host compound's molecular sites (Cherukuvada and Nangia, 2013). Co-crystals are particularly well studied in the pharmaceutical industry since they can influence the solid-state properties of a material such as the solubility and bioavailability (Steed, 2013).

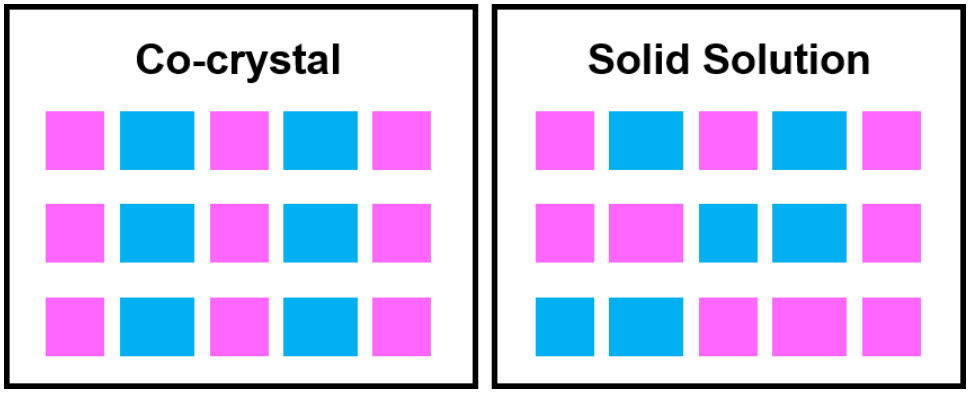

Figure 2.1: Visual representation of a co-crystal structure vs a solid solution. The different coloured rectangles represent different molecules in the compound.

In a solid solution, the two (or more) compounds are also structurally similar. Kitaigorodskii (1984) proposes that in organic molecular systems there are two conditions to achieve a stable solid solution. The first condition is a symmetric rule, where the pure components must be isostructural. The second condition is volumetric, where the non-overlap volume between two molecular components must be minimised

e.g. they must be of similar volumetric size in a given direction (Kitaigorodsky, 1984). However, certain molecular organic systems have been formed that break these rules because the pure compounds exhibit significantly different molecular structures, suggesting these rules may be too rigid (Cruz-Cabeza et al., 2018), (Schur et al., 2015).

Solid solutions can exist across a range of compositions; from very small molar fractions of guest molecules (essentially undetectable fractions) to equimolar fractions of the host and guest, to the guest actually becoming the dominant fraction. In some solid solution systems, there is a maximum value of the fraction of a guest that can be incorporated into the lattice of the solid solution, forming only a partial solid solution. In other systems, all compositions from 0% guest to 100% guest are possible, forming a continuous solid solution (Hill et al., 2023). It is the thermodynamic stability of the overall system which determines if partial or continuous solid solutions can form (Lusi, 2018b).

Paraffin waxes are a large class of materials that exhibit rich solid solution behaviour; they are soft, colourless solids derived (in the first instance) from petroleum, coal, or oil shale and consist of a mixture of hydrocarbon molecules containing between 20 and 40 carbon atoms. Chains of similar length form solid solutions, or when the chains are of dissimilar length, the co-packing is compensated by longitudinal molecular disorder in the longitudinal packing of the molecular chains or individual lamellae (with lamellae defined as distinct layers of chains). Solid solutions can be formed from binary and multicomponent systems (Dorset, 1990), (Dorset and Annis, 1996), (Douglas L. Dorset, 1997b). Atomic occupancies at the end of chains have a ~ Gaussian fall off, with a maximum atomic occupancy at chain centres (Dorset, 1995a). This means that chains of dissimilar length can form solid solutions, whilst satisfying the apparent volume requirements of the solid solution formation. The solid solution behaviour of paraffin wax materials are discussed further in a later section of this literature review.

2.2.2 Solid Solutions and Polymorphism

Many molecular compounds will crystallise in different polymorphs, where the same atoms will arrange themselves in different physical space leading to different crystal symmetry. Understanding these different polymorphs in relation to solid solution formation is important, but perhaps more importantly because of the effect of the resulting microstructures on the crystals properties, such as dissolution rates and bioavailability, understanding is vitally important in drug production, the most famous being the case of Ritonavir (Bauer et al., 2001). Initially, during development only one crystal form of Ritonavir was identified. However, later a lower free energy, more stable

polymorph was discovered, which was less soluble with lower bioavailability, which led to temporary removal of this drug from the market. It was also discovered that even a small amount of this second form could drive conversion of the first form to the second form, highlighting the importance of understanding all possible polymorphs for drug production and control.

The thermodynamic stability of different polymorphs can change depending on the presence of other molecules capable of forming a solid solution system with the host component. Solid solution formation is selective for different polymorphs, so can affect the thermodynamic stability of other polymorphs i.e., less stable polymorphs may be more likely to appear in the presence of impurities or guest molecules (Paolello et al., 2024).

The following examples focus on solid solution and co-crystal systems. A number of substituted benzamides have been developed as commercial drugs, however benzamide form III is a typically difficult to grow polymorph of benzamide and has been shown to grow as a result of crystallisation with a close relative structure, nicotinamide (Kras et al., 2021). These nicotinamide impurities are incorporated in lattice positions within the benzamide crystal structure forming a solid solution. Impurities can have a significant impact on the crystal phase outcome, especially when the impurity has a close molecular similarity with the desired compound. Understanding how even trace amount of impurities can influence polymorph form of a drug is vitally important for the pharmaceutical industry. Crystal morphologies can also be controlled by crystallisation in the presence of impurities as evidenced by Wang et al. who used a structurally similar impurity to salicylic acid to engineer hollow crystals, by dissolving the impure core (Wang et al., 2021). The structure this formed impacted the physical properties of salicylic acid such as solubility and melting properties. Hollow structures like these are of interest to the pharmaceutical industry as they have an increased surface area and enhance dissolution rate. The implications of solid solution formations in the presence of appropriate impurities is therefore important for crystal engineering. Impurities can make up a low concentration of the total content of a solid solution product making detection with bulk techniques challenging. This provides an opportunity for spatially resolved techniques such as microscopy. For example, electron microscopy has been utilised to identify low levels of crystallinity in amorphous solid dispersions, and how these crystalline phases changed to a different polymorph with ageing (S'Ari et al., 2021). An amorphous solid dispersion is a system where a poorly soluble drug is dispersed in a solid amorphous carrier to improve solubility and bioavailability. Whilst this system differs from a solid solution or co-crystal system, the study highlights how crystalline phases can be distinguished by EM techniques.

2.2.3 Solid Solutions and Hydrates

Solvent choice can direct polymorphism when crystallising organic materials, but the presence of water in these solvents may also direct formation of hydrate molecules. A hydrate forms when water molecules are incorporated into the crystal lattice (Qu et al., 2006). Solubility and dissolution rate of a given compound are also different at different hydration states (Zhu et al., 1996). Consideration of hydrated forms must therefore be accounted for during formation of solid solution and co-crystal systems when using solvents that are not anhydrous.

2.2.4 Solid Solution Characterisation

Solid solutions can be characterised by a range of techniques, ranging from bulk methods, such as powder and single crystal X-ray Diffraction (XRD), to thermal techniques, such as differential scanning calorimetry (DSC), to microscopic (optical, scanning probe and electron) and spectroscopic techniques (such as UV-vis, FT-IR and Raman spectroscopies).

X-ray diffraction (XRD) can be used to understand the host crystal structure and subsequent guest incorporation. Powder X-ray diffraction (pXRD) is a common technique used to determine a sample's crystalline structure. The method works by firing X-rays at a polycrystalline material and measuring the diffracted intensity as a function of the outgoing wave direction. The angle between the incoming and outgoing X-ray beam is defined as 2θ. This is defined by Bragg's law (Bragg et al., 1913). Crystalline materials have a repeating lattice of atomic order, and when X-rays interact with this structure (primarily due scattering by the electrons of the atoms, not the nuclei), they undergo constructive interference if the path differences of the scattered rays satisfy Bragg's law. Bragg diffraction occurs when electrons or X-rays, with a wavelength comparable to atomic spacings, are scatted by the atoms of a crystalline material and undergo constructive interference. Interference is constructive when the path difference between two adjacent, scattered rays or waves is a multiple of one whole wavelength (leading to a phase difference of n times 2π). The effect of the constructive interference is intensified when the reflections occur in successive crystallographic planes (hkl) of a crystalline lattice. This leads to Bragg's law:

$$2dsin\theta = n\lambda \tag{2.1}$$

where d is the inter-planar spacing, θ is the angle between the incident ray and the relevant crystal plane, n is a positive integer and λ is the wavelength of the incident wave. The diffracted X-rays are detected, and the angles at which diffraction occurs provide information about the arrangement of atoms and the spacing between atomic planes. Intensities of the peaks also give information on the structure factor of the

crystal, which gives information on atomic locations and whether their collective interference will produce a peak for each of the crystal planes or where there are systematic absences in the diffraction pattern. Intensity of the peaks is also affected by symmetry. If the crystal is of high symmetry, there will be more than one plane with the same equivalence in the system, so there will be a multiplicity factor for these planes in crystalline powders. For example, in a cubic system, the (100), (010), (001), $(\bar{1}00)$, $(0\bar{1}0)$ and $(00\bar{1})$ will be equivalent, so the multiplicity factor for the {100} family of planes is six. Pattern fitting software also takes into consideration temperature factors, as the greater the temperature the higher the atomic vibrations so the atoms are no longer in the perfect position.

This technique is useful when structural models are known, so it can be determined if there is a single phase or a mixture (Lusi, 2018b). However, when there is a mixture of phases with similar crystalline structures and therefore similar d-spacings between crystal planes, the XRD pattern output may have overlapping 2θ peaks, so it may be hard to assign phases where there are no defining phase peaks. pXRD has been reported to only detect levels of disorder in the form of crystal defects or amorphous phases down to around ~10% in a highly crystalline sample (Saleki-Gerhardt et al., 1994), so there is opportunity to employ other techniques for disorder detection at a smaller scale.

Where single crystals can be grown, single crystal XRD (SCXRD) can be used for crystal structure determination of the solid solution (Lusi et al., 2015). This is different to pXRD as SCXRD gives information on atom types and positions within an averaged unit cell, as well as information on the space group symmetry and unit cell. SCXRD can be used for unknown compounds, where pXRD is more typically used when a compound is known/assumed and the experimental pattern can be compared to a simulated pattern or patterns. This is also in part because growing a single crystal of good enough size and quality for an SCXRD measurement is not always possible.

Thermal techniques such as differential scanning calorimetry (DSC) can be used to provide evidence of solid solution formation. DSC measures the difference in the amount of heat needed to increase the temperature of a sample and reference material as a function of temperature. When a sample undergoes a physical transformation such as a phase transition, the direction of heat flow in or out (signifying an exothermic or an endothermic process) is required to maintain the sample at the same temperature as the reference. This technique does not give direct information on the structure but can provide information on the solid solution compound relative to the separate components. A solid solution should have a characteristic single melting event as the two components form one structure (Hill et al., 2023). A lower melting

point suggests the solid solution has a lower stability than the separate components, but this does not always occur on solid solution formation; in some cases, a higher melting point occurs when a solid solution is formed. DSC can also offer information on phase separation, where separate melting point transitions would be seen if the solid solution was not stable.

As the formation of solid solutions can give the molecules different physical properties to the individual components, solid solutions can be characterised by measuring properties such as dissolution and seeing how these change on solid solution formation (Nong et al., 2024). This is due to the possible formation of different bonding networks that may arise in solid solutions. The composition of solid solutions can also be confirmed using spectroscopies such as FT-IR, NMR and Raman which offer information on the chemical environments within the molecules (Hill et al., 2023).

EM techniques have been applied to study solid solution in systems such as paraffin wax solid solutions (Fryer et al., 1997), (Dorset, 1995b). EM is used for the characterisation of metal alloy systems, which are atomic substitutional or interstitial solid solutions as well as analysing microstructural features such as grain boundaries (interfaces between neighbouring grains) and for defect study such as faults and dislocations (Forwood and Clarebrough, 2021). However, EM techniques are not common techniques used to characterise organic solid solution systems due to issues such as electron beam damage limiting the useful signal to noise that can be obtained. However, advancements in detector technology mean EM techniques can now be used at appropriately low doses, so there is opportunity to unveil the microstructure of these systems. These techniques are discussed in more detail later in this literature review. First, the methodology and limitations of EM techniques will be discussed.

2.3 Electron Microscopy

2.3.1 Transmission Electron Microscopy

Transmission electron microscopy (TEM) is a tool that allows us to probe a local area of a sample, being able to capture images of molecules on the nanometre scale or of individual heavy atoms distributions (Meyer et al., 2008), (Williams and Carter, 2009). To achieve this, a thin specimen is irradiated with a parallel electron beam of uniform current density. The electrons are scattered by the sample, and an image or a diffraction pattern can be formed.

Complex organic materials are very sensitive to electron beam damage, and the damage process has been studied extensively in the literature, particularly by Egerton et al. (Egerton, 2013). Damage mechanisms are discussed in further detail in a later

section but are introduced here to highlight the interactions of the electron beam in TEM microscopy. Elastic or inelastic scattering give rise to different types of damage mechanisms within a sample (Egerton, 2012). Elastic scattering occurs when there is no loss of energy in the incident primary electron, and represents electrostatic deflection of incoming electrons by the Coulomb field of each atomic nucleus. Momentum is conserved in the system but the balance of each particles' momentum (that of electrons in the beam vs the atom) is changed in the interaction. This momentum can be transferred to the nucleus causing knock-on damage, i.e. displacement of a nucleus that itself then undergoes energy loss processes in the surrounding material.

Coherent elastic scattering gives rise to electron diffraction patterns but can result in atomic displacement of atoms in a crystalline material, electrostatic charging or electron beam sputtering. Back scattered electrons (BSE) also arise as a result of elastic scattering. Inelastic scattering represents Coulomb interaction of primary electrons with the sample which leads to the loss of energy to the incident primary electron. Characteristic X-rays are produced when an inner shell (e.g. K shell) electron is ejected from the atom by a high-energy electron. This hole is filled by an electron in an outer shell. This leads to the emission of X-rays of specific or characteristic energy which can be used for elemental analysis techniques. Bremsstrahlung X-rays have a continuous spread of energy and are generated when the primary-beam electrons lose energy due to inelastic scattering in the sample. Some of the lost energy is converted to X-rays which have a range of energies, from ~0 up to the beam energy E_o. Bremsstrahlung X-rays do not offer any possibility of elemental analysis. Secondary electrons (SE) are ejected from the conduction or valence bands of the atoms in the specimen. Usually SEs are not associated with any specific atom so do not hold any specific elemental information. SEs are used for imaging in scanning electron microscopy (SEM) more than in a TEM. The incident electron beam can generate phonons in any specimen. Phonons are collective oscillations of atoms in a solid that arise when the atomic lattice is struck by a beam of electrons and can cause lattice vibration, which causes the specimen to heat up and this can cause damage to the specimen.

Inelastic scattering can also lead to sample heating and radiolysis effects, which changes the structure of a material or removes material. Damage is assumed to be proportional to the energy deposited by the electron beam per unit volume of the specimen. Radiolysis is the predominant damage mechanism for organic materials in TEM as organic materials are non-conducting with a high number of weak secondary bonds and light elements that are easily displaced. Organics being non-conducting means the material cannot easily dissipate the electrons created by inelastic

scattering, enhancing damage by radiolysis. (Egerton, 2019), (Egerton, 2012), (Egerton et al., 2004).

Resolution is linked to signal, so trying to achieve a good resolution limits our ability to simply increase the diameter of the incident beam as a means of reducing damage. (Egerton, 2013). The obtainable spatial resolution of a specimen is limited by the electron fluence:

$$D = It/d^2 \tag{2.2}$$

that the specimen can withstand before the signal is degraded, where *I* is the current irradiating a specimen, *t* is time and *d* is the diameter of the beam. If N electrons are recorded from each resolution element (of area δ^2) the associated signal to noise ratio is:

$$SNR = (DQE)^{\frac{1}{2}} CN^{\frac{1}{2}} \tag{2.3}$$

where DQE is the detective quantum efficiency of the recording device (square of the actual SNR for the detector divided by the square of the ideal SNR for the detector), C is the signal/ background ratio (|ΔN|/N) such that CN is the signal (|ΔN|). Figure 2.2, taken from Egerton et al., shows a visual representation of these terms as a function of recorded signal versus the distance across the specimen.

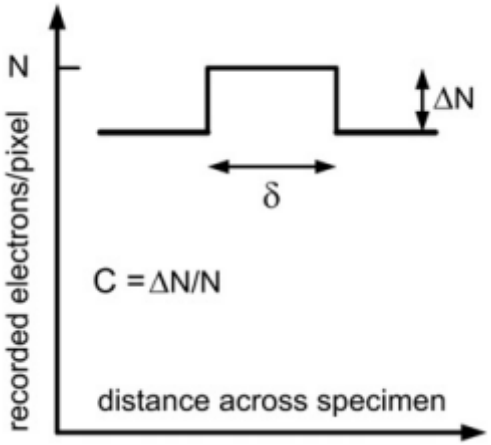

Figure 2.2: Recorded signal as a function of distance across the specimen, showing a change, Δ*N*, in the number, *N*, of recorded electrons per resolution element (size *δ*), the contrast ratio being defined here as *C*=|Δ*N*|/*N*. Figure taken from (Egerton, 2013).

As the radiation damage is determined by the number of electrons incident on the specimen and not the detector, it is lower by a factor F, so N becomes

$$N = F(\frac{D}{e})\delta^2 \tag{2.4}$$

where D is the electron fluence received by the specimen, e is the electric charge constant and F is the efficiency of the signal collection system. The dose limited resolution therefore becomes

$$\delta = N^{\frac{1}{2}}\left(\frac{FD}{e}\right)^{\frac{1}{2}} = (SNR)(DQE)^{-\frac{1}{2}}C^{-1}(FD/e)^{-\frac{1}{2}} \quad (2.5)$$

where δ is the diameter of the information (signal area) obtained from the specimen. A SNR of 5 gives a 98% probability of detecting an unknown signal in the presence of noise (Natusch et al., 1999). Egerton proposes that for a typical thin specimen under typical conditions for 100 keV irradiation of organic materials δ is ~5 nm which is a resolution typically obtainable in TEM (Egerton, 2013). This value will depend on the critical fluence of the specimen i.e. the characteristic (or critical) fluence of electrons that will reduce the signal by a factor 1/*e* ≈ 0.37 (Egerton, 2019), (Glaeser, 1971). F is dependent on imaging mode, in bright field it will have a value below 1, and for dark field imaging the value depends on elastic scattering cross sections, specimen thickness and geometry of the detector. DQE is dependent on the detector, C is dependent on the contrast, and D is the electron fluence.

There are different ways of obtaining an image from TEM. Bright field (BF) images are the most common obtained by TEM, where the areas that have scattered the electrons (and therefore where the sample lies) appear darker on the image. Most scattered electrons are contained within ± 5° of the direct beam (Williams and Carter, 2009). The areas with no sample transmit all the incident electrons and appear brighter. An objective aperture can select the transmitted electron beam so the scattered electrons beyond the collecting aperture are blocked, which forms the dark areas – this enhances the image contrast, especially if the sample is crystalline.

By instead configuring the electron optics such that only a subset of electrons scattered to angles outside the direct beam (such as those scattered to a specific Bragg angle) pass through the objective aperture, the electrons form a dark field (DF) image at the detector plane. This means the sample region that is scattering into the aperture appears bright. DF images can be formed either by tilting the incident beam or displacing the objective aperture to select the scattered electrons. In the latter case, these off-axis electrons suffer aberrations and astigmatism reducing the resolution of the DF image. By tilting the electron beam at an angle equal and opposite to the scattering angle, the scattered electrons now travel down the optic axis which gives a better focused image (Williams and Carter, 2009). Lighter elements are typically harder to image as they scatter the electron beam more weakly and exhibit less contrast. This quantity is known as the atomic scattering factor, which expresses how

the scattering strength of an individual atom varies with scattering angle and with the type of radiation used (Peng, 1999).

The theoretical, maximum resolution of an electron microscope is hard to achieve due to the aberrations inherent in the objective lens used. Aberration correctors greatly improved the resolution that was able to be achieved (Hetherington, 2004). In a standard electron microscope, spherical aberration in the objective lens is a factor that limits resolution when using a large objective aperture in TEM or a large convergence angle in STEM. Rays passing through a curved lens with spherical aberration at higher angles are bought to focus at a different point to lower angle rays as exhibited in Figure 2.3.

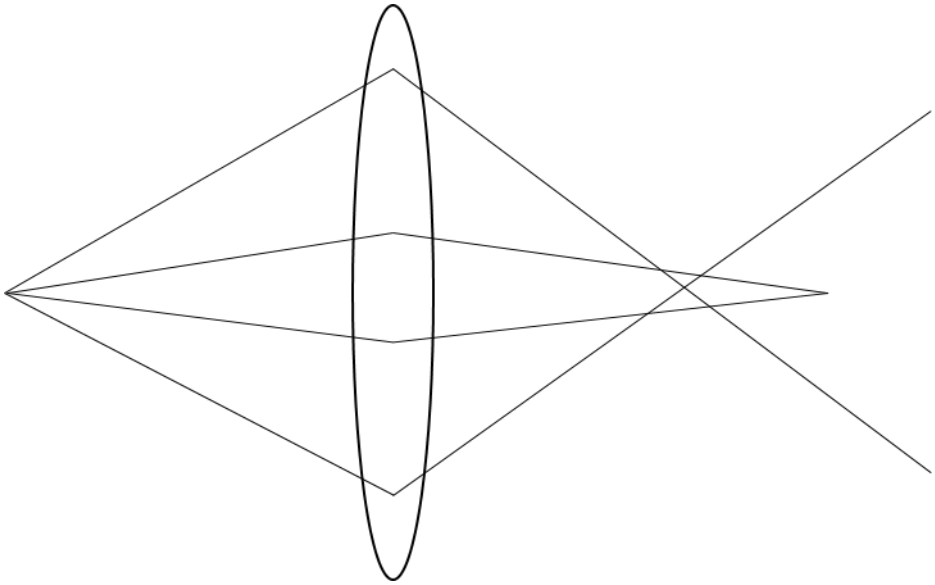

Figure 2.3: A schematic representation of spherical aberration within an electron microscope lens. Electrons scattered to higher angles are focused to a different point than electrons scattered to lower angles.

These higher angle rays carry information about the smaller spacings in the object. Aberration correctors work by bringing all the rays into focus at the same point. Multipole electromagnetic lenses are used that create a magnetic field with specific symmetries which correct for aberrations in the electron beam. Aberration corrected TEM or STEM is not utilised in this thesis, this work will be focussed on low-dose diffraction and diffraction contrast imaging at ~3 nm resolution. A review article by Smith considers aberration corrected TEM in more detail (Smith, 2008).

2.3.2 SAED

Selected area (electron) diffraction (SAD/ SAED) is an experimental technique that can be performed inside a transmission electron microscope, and is used to acquire near parallel beam electron diffraction from micrometre to ~ 100 nm sized features in

a TEM sample. It is achieved by introducing a selecting aperture into a plane conjugate with the specimen i.e. one of the image planes of the objective lens in the column. An intermediate lens then projects the back focal plane of the selected area onto the viewing area of the microscope. When the electron beam passes through the sample, the electrons are diffracted and the atomic planes act as a diffraction grating. The angle the electrons are diffracted depend on the crystal structure of the sample and the wavelength of the electron. This is defined by Bragg's law as outlined in the earlier XRD section. The difference between SAED and XRD is that electrons have a much smaller wavelength than X-rays and the sample is very thin in the direction of the electron beam. These factors have an effect on the Ewald sphere reconstruction.

Ewald's sphere is a geometrical formulation of expression of Bragg's law that defines a sphere where the initial and final scattering vectors are of equal magnitude and the radius is equal to the reciprocal of the wavelength of the incident wave (Ewald, 1969). An Ewald sphere illustrates which lattice planes, represented by points in the reciprocal lattice, will result in a diffracted signal for a given wavelength of the electron beam. The reciprocal lattice dots that are touched by the arc of the sphere are the ones that satisfy the Bragg equation and show up in the diffraction pattern. An Ewald sphere can be seen in Figure 2.4, where the radius is set to $1/\lambda$ where λ is the experimental wavelength, and $1/\lambda$ represents the length of the incident wavevector. $1/\lambda$ is large for electrons compared to the lattice spacing. The sphere in Figure 2.4 has a small radius of curvature to illustrate the concept, however for an incident energy beam of 200 or 300 keV used in TEM, the Ewald sphere can be approximated as a flat plane as the radius is much larger than the distance between reciprocal points, so more reciprocal lattice points will satisfy the Bragg condition.

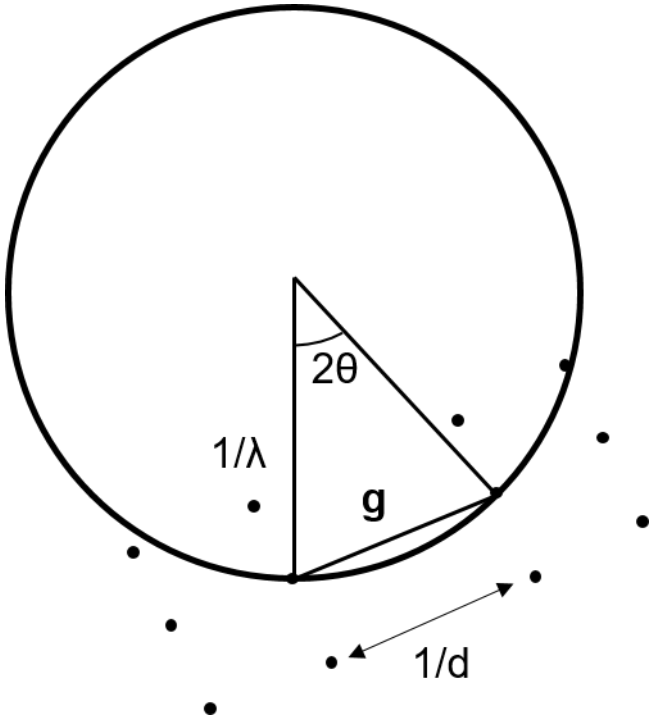

Figure 2.4: Ewald sphere. The reciprocal lattice spacing is determined by 1/d where d = lattice spacing and the radius of the sphere by 1/λ.

Scattering can also be seen for spots that do not perfectly satisfy Bragg's condition (Williams and Carter, 2009). For a perfect crystal, the repeating atoms are described by an infinite wavefunction of a fixed wavelength (perfect periodicity with infinite extent of the lattice). When the crystal is finite (limited in size by disruptions in the crystal lattice), this wavefunction cannot be used and a distribution of waves are used to describe the position of the atoms. When taking the Fourier Transform of this finite wavefunction, a distribution is seen instead of finite points. Where crystals are thin in one direction but extended in another, the reciprocal lattice becomes rod shaped (relrods) because of this distribution. Specimens have to be thin enough for electron transparency, so it is likely a sample is thin along the beam direction. Some crystals may be 'thin' in all directions, giving 'rel-blobs', and some are thin in two directions, giving 'rel-sheets' e.g. nanocrystals and thin domains or faults. When the Ewald sphere crosses a relrod, we will see a diffraction spot even if it does not satisfy the Bragg condition entirely. This will not be far from the Bragg condition if the Ewald sphere is flat. When the specimen is thin along the electron beam direction, we see planes that are nearly parallel to the incident beam. A diffraction pattern output is therefore obtained by measuring the intensity of scattered waves as a function of the scattering angle. When Bragg's law is satisfied, a Bragg peak of strong intensity is found. The output of a SAD experiment is a set of diffraction spots, a selected area diffraction pattern (SADP), each of which corresponds to a satisfied diffraction condition of the sample's crystal structure. Where multiple crystals lie in a field of view,

the output is a polycrystalline diffraction pattern where each ring corresponds to a certain d-spacing. Materials that contain no long range order, amorphous materials, can produce an electron diffraction pattern composed of diffuse concentric rings instead of spots (Figure 2.5).

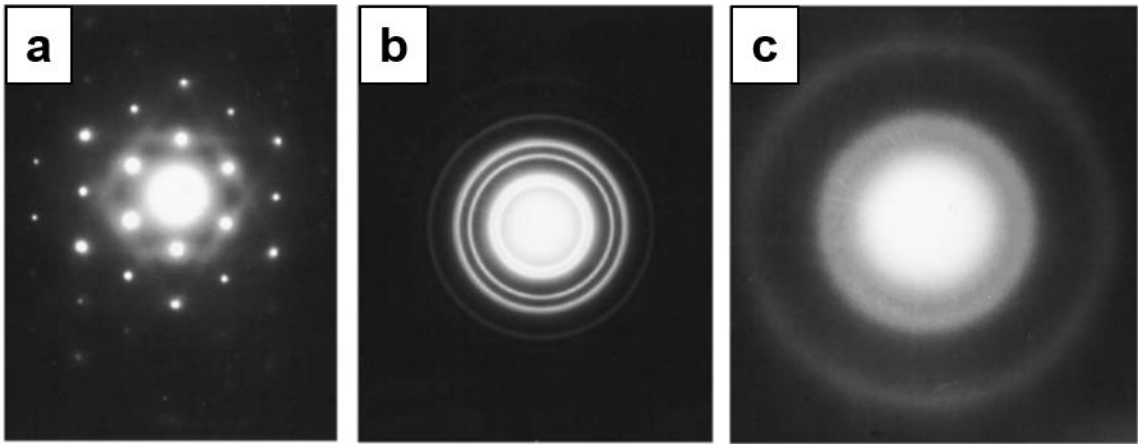

Figure 2.5: (a) Single crystal SAED pattern, (b) polycrystalline SAED pattern, (c) amorphous SAED pattern. Image taken from (Williams and Carter, 2009).

TEM and SAED techniques have been used to study molecular crystals and pharmaceutical compounds since the 1960s. Applications have included the investigation of defect structure of mesophases in a pharmaceutical substance, fenoprofen, by TEM imaging, where these defects impact the mechanical properties (Rades and Müller-Goymann, 1997), and the imaging of Taxol crystals, anti-cancer drug, that form in aqueous solution, important to understand for the crystalline behaviour of this drug in vivo (Liu et al., 2008). Significant understanding has been developed but much of this work has been spatial resolution limited and very recent progress on that will be discussed in the STEM section below. An additional aspect that the spatial resolution SAED brings to TEM analysis is sensitivity over the more bulk analytical techniques such as XRD. For example Eddleston et al. used SAED to characterise a range of pharmaceutical compounds, including theophylline, paracetamol and aspirin, and also pharmaceutical salts and co-crystals (Eddleston et al., 2010). They were able to identify different polymorphs of theophylline by SAED and this was a key finding as pXRD analysis of the same sample found the compound to be monophasic. They were also able to identify the presence of defects and dislocations in theophylline and to show that these are sites at which fracturing might occur when the crystals are stressed. This enabled them to link structural information to the solid state behaviour of the pharmaceutical compounds. SAED was also used to characterise crystallinity in solid dispersions (Ricarte et al., 2015). SAED in this study achieved improved crystal detection sensitivity over wide-angle X-ray scattering (WAXS), with WAXS failing to detect crystals in certain cases (and the SAED

technique having resolution down to the nanoscale of ~ 100 nm). SAED has also been used and combined with synchrotron powder data to characterise the unit cell parameters of two polymorph forms of roxifiban, a compound used to inhibit platelet aggregation (Li et al., 1999).

TEM is also used for the characterisation of pharmaceutical nanoparticles, evaluating morphology and particle size, providing complementary tools to bulk particle sizing methods such as dynamic light scattering (Klang et al., 2013). However, these nanoparticles are routinely stained to add contrast for imaging, which does not capture these particles in their native state and may oxidise coatings and change layer thicknesses (Pan et al., 2009). It is important to consider TEM sample preparation when using these methods for structural characterisation.

Advancements in TEM techniques for increased spatial resolution, and spectroscopic techniques also used to study molecular crystals, are discussed further in this section.

2.3.3 STEM

Scanning transmission electron microscopy (STEM) is a type of TEM where the electron beam is focused to a fine spot instead of being a parallel beam. This beam is then scanned over the sample. The differences between the TEM and STEM setup are visualised in Figure 2.6.

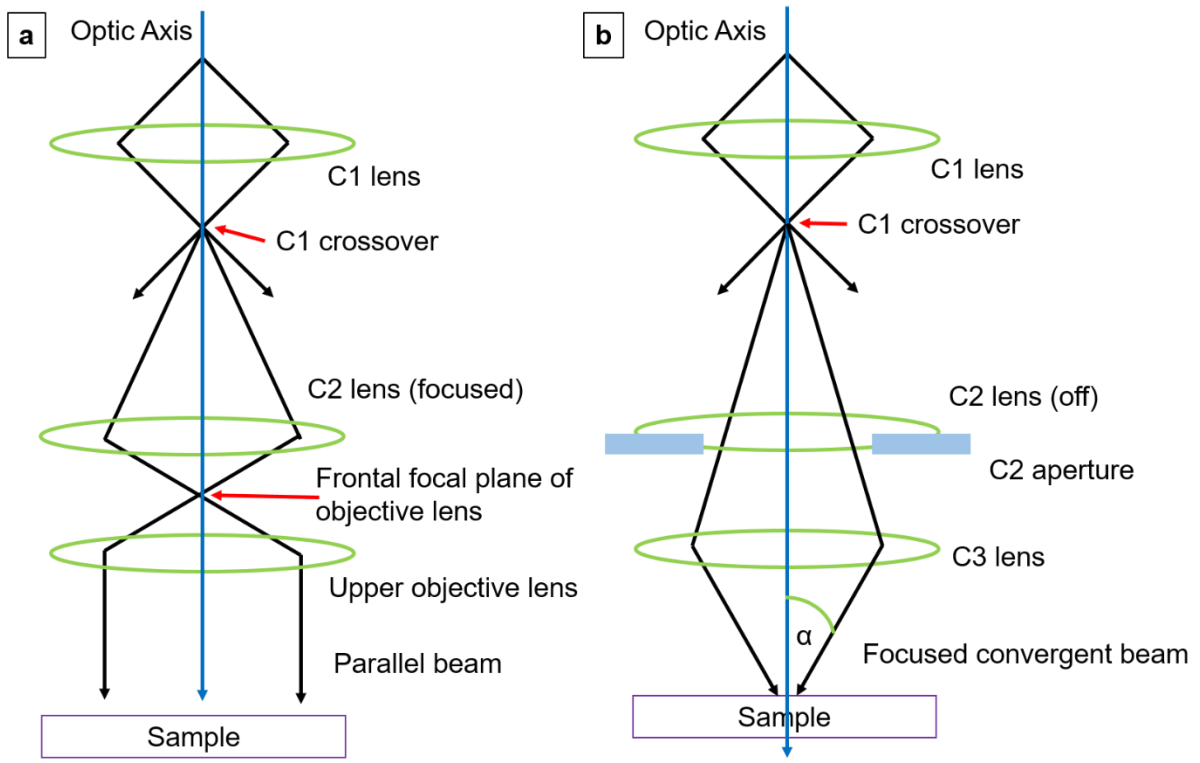

Figure 2.6: (a) TEM setup forming a parallel beam, (b) STEM setup forming a converged beam. Visual representation adapted from Williams and Carter (Williams and Carter, 2009).

Annular and BF detectors are frequently used for imaging and the collection angle of the detector can be changed by varying the camera length. STEM detectors allow for the simultaneous imaging of bright and dark field signals. STEM is also compatible with techniques such as electron energy loss spectroscopy (EELS) and energy dispersive X-ray spectroscopy (EDS). EELS and EDS are two elemental analysis techniques which give us information on which atoms are present in the system. Although it is possible to use these techniques in TEM, it does not offer the spatially resolved EELS and EDS analysis that is possible in STEM.

The addition of aberration correctors to STEM microscopes allows sub-Å resolution to be achieved. High brightness electron guns (e.g. field emission guns (FEGs)) can also achieve high resolution by producing an electron beam that is smaller in diameter, improving the SNR ratio.

Annular dark field (ADF) STEM imaging uses an annular detector to collect low angle ADF and the Bragg scattered electrons of the sample. This method can be used to generate diffraction contrast and image defects in crystalline samples. High angle annular dark field (HAADF) is a technique which produces an ADF image formed by electrons which have been inelastically scattered incoherently, from the nucleus of the atom, at high angles, higher than 50 mrad at 200 keV (Williams and Carter, 2009).

HAADF does not capture Bragg scattering. This technique is relatively insensitive to diffraction scattering and highly sensitive to the atomic number of the atoms (Z), hence why it is also known by Z-contrast imaging. Contrast is approximately proportional to Z^2 (Pennycook and Jesson, 1991), (Jesson and Pennycook, 1995). i.e. the higher the atomic number the stronger the scattering so heavier elements show up brighter for a sample of constant thickness. This however means lighter elements such as C, O, N and H are harder to image using this technique. For these reasons, HAADF imaging has seen particular success in the imaging of inorganic compounds such as metals, semiconductors and functional oxides (Nellist and Pennycook, 1996).

2.3.4 Energy Dispersive X-Ray Spectroscopy (EDX/ EDS)

EDS is an analytical technique that allows the analysis of the elemental composition of a compound. EDS can be carried out in a single selected area, obtaining a single spectrum, or elemental maps can be produced through a STEM-EDS setup. The electrons in the electron beam interact with a sample and as a result of this interaction, X-rays of characteristic energy are released. These X-rays are produced as an electron in one of the inner shells of atoms in the sample is removed, and this ionisation leaves the material in a higher energy state. The system energy is then lowered by electron transitions from an outer shell to the gap in the inner shell and an X-ray photon is emitted. The energy of this emitted X-ray is equal to the difference between the energies of the two atomic shells involved in the transition. For example, if an electron is lost from the K shell, an electron from the L shell will fill the gap, so the energy of the X-ray will be $E = E_K – E_L$. These X-rays are detected by an EDS detector, with the output being a spectrum of the intensity of this signal (counts) versus energy (eV). The energies of the characteristic X-rays identify the elements, and the relative intensities of these peaks allows the quantification of the concentration of the elements.

EDS-STEM has been used to map interfaces and grain boundaries in inorganic materials such as metallic alloys (Spurgeon et al., 2017), and for nanoparticle chemical and structural characterisation (Hodoroaba, 2019), (Esparza et al., 2013). STEM-EDS has also been used for characterisation of beam sensitive materials such as metal organic frameworks (MOFs) where it could confirm the presence of nanoscale metal oxide coatings on the surface of MOF particles (Denny et al., 2018). It has also been used to confirm elemental composition across interfaces in hybrid lead halide perovskites and hybrid glass phases (Li et al., 2023). However, these studies look at identifying heavier metal elements in an organic matrix, which are absent in purely organic materials. Lighter elements are harder to detect by EDS as less characteristic X-rays are generated in these elements because of the lower number of orbiting

electrons. This leads to a reduced signal to noise for these lighter elements, so signal is harder to obtain without further noise reduction algorithms (Kim et al., 2020).

Mapping of the same features in organic materials by EDS-STEM is more limited due to inherent beam damage of these materials. This technique is also not commonly used for the characterisation of organic solid solution systems, so the application of STEM-EDS for quantitative analysis of increasing concentration of guest molecules into a solid solution system is something that can be explored.

2.3.5 Electron Energy Loss Spectroscopy (EELS)

EELS is another elemental analytical technique that can be performed in the STEM setup (Egerton, 2011), (Colliex, 2022). In this method, the energy of the electron beam after interaction with the material is measured by an electron spectrometer. The primary electron beam will undergo inelastic scattering as a result of the interaction with the specimen, and this energy loss can be attributed to different events such as phonon and plasmon excitations, inter- and intra- band transitions or inner shell ionisations. The amount of energy needed to remove an inner-shell electron from any atom will have a particular value, so the output of measured energy loss can be used to determine the elemental composition of a sample.

EELS has been used to determine local composition and structure of a layered, polymeric nanoparticle system used for drug delivery (Koniuch et al., 2023). This study used cryo-TEM conditions, and low dose to minimise electron beam damage to the organic materials. The data were collected without staining the polymeric nanoparticles, as is commonly done for polymeric nanoparticles for EM studies, so the material was captured closer to its native state and the structure/thickness of the layers identified in order to provide parameters for the modelling of the release kinetics of the drug.

EELS techniques have also been applied for the study of other beam sensitive organic materials such as organic photovoltaics to obtain spatially resolved data of the thin films and at interfaces between the layers in the materials (Alexander et al., 2016), (Zhao et al., 2022). The structure of these materials, and these interactions between layers, have an effect on opto-electronic properties, so understanding the atomic structure is important.

An advantage of using EELS is that this technique can offer information on the type of bonding in a material, being able to differentiate between sp^2 and sp^3 carbon bonding for example (Papworth et al., 2000), so it can be a highly structurally sensitive technique. EELS has been used to identify polymers due to the complex covalent bonding of carbon atoms in different polymers and copolymers which give a unique

spectra or chemical fingerprint at the carbon K-edge (Colby et al., 2023), (Pal et al., 2021). As with EDS however, dose applied to the sample through this technique must be managed to minimise damage to the sample. However, EELS can produce a stronger signal than EDS because inelastic scattering events (which EELS detects) have higher cross sections than X-ray emission events, and because EELS spectrometers can collect electrons over a larger angular range than EDS detectors collect X-rays (MacArthur et al., 2016). In EELS, the inelastically scattered electrons are highly forward scattered, whereas in EDS X-rays are emitted in all directions, so detectors in the latter receive a lower signal. Dose management is therefore more of an issue in EDS than EELS.

Nanoscale quantification of the concentration of APIs in amorphous polymer matrices has also been shown to be possible through EELS at a sub 100 nm resolution (Ricarte et al., 2016). They used an indicative peak in the EELS spectrum of one component, a π–π* transition peak, to determine the concentration of that component in the polymer solid dispersion. They measured concentration changes over areas down to 50 x 50 nm. However, this study noted that electron beam damage may have introduced an error in the calculated concentration values due to changes in the shape of the measured spectra, so there is still scope to improve measurements by reducing beam damage factors.

2.4 Electron Beam Damage in TEM

2.4.1 Damage mechanisms

Detail on damage mechanisms has been derived in extensive work by Egerton on radiation damage in the TEM and has indicated ways to minimise these effects (Egerton, 2012), (Egerton et al., 2004), (Egerton, 2019), (Egerton, 2013).

Damage can be due to elastic (electron-nucleus) scattering or inelastic (electron-electron) scattering.

2.4.1.1 Atomic displacement

Elastic scattering involves no change in energy of the transmitted beam but momentum is transferred to the atomic nucleus. Conservation of energy dictates that the electron which is deflected through an angle in the field of a single atomic nucleus must transfer an amount of energy given by

$$E = E_{max} sin^2(\frac{\theta}{2}) \tag{2.6}$$

and

$$E_{max} = E_0 \frac{\left(1.02 + \frac{E_0}{10^6}\right)}{4.65.7A} \quad (2.7)$$

where *A* is atomic mass number, *θ* is angle in the field of a single atomic nucleus, *E* is amount of energy transferred and E_0 is incident energy electron (both energies in eV).

If *E* exceeds a displacement energy E_d of a specimen material, high angle elastic scattering can displace atomic nuclei to interstitial positions disrupting the crystalline structure. This is also known as knock-on displacement of atoms within a specimen. Knock-on damage is the main mechanism of beam damage in oxides (Jiang, 2015) and has been studied in graphene (Meyer et al., 2012). For TEM, atomic displacements are not expected at 100 keV unless the specimen contains hydrogen atoms. Most ejected hydrogen atoms have low kinetic energy, however, and produce little secondary damage. Therefore, to minimise this damage mechanism, accelerating voltages below the threshold energy of the material must be used (this threshold for C in a pristine graphite/graphene structure is considered to be 80 keV). At finite temperature there may be extra energy that can combine with the energy from the electron beam to favour displacement below the knock-on threshold. As displacement energies are also material dependent, there may not be a single “safe” energy.

2.4.1.2 Electron beam sputtering

If high angle elastic scattering occurs at an atom which lies at the surface of a specimen, the energy E_s required for displacement is much lower, as the atoms do not move to an interstitial space but are free to leave the specimen into the vacuum of the microscope. As with atomic displacement, significant sputtering only occurs for an incident energy that exceeds some threshold value. Sputtering mainly involves atoms with a low atomic number. The best way of avoiding electron sputtering is to limit the radiation dose, even with a low incident energy (Egerton, 2019).

2.4.1.3 Electron beam heating

Inelastic scattering involves collision between incoming electrons and atomic electrons, so energy can be transferred in the process, with most of this energy ultimately ending up as heat within the specimen. The local temperature is then higher than the temperature of the surroundings. Beam heating is a problem in TEM at high incident currents. Materials with low thermal conductivities, such as polymers, are more susceptible to melting or thermal degradation even at low current densities (Egerton et al., 2004). Lower temperature conditions minimises damage from heating effects in organic systems (Talmon, 1982).

2.4.1.4 Electrostatic charging

The net charge added to a film is dependent on both the backscattering coefficient and the yield for secondary electrons which are emitted with kinetic energy. When the incident electrons have a high energy, most secondary electrons are generated well below the surface of the specimen and do not escape into the vacuum, creating a negative surface potential to develop in the specimen. At low incident energy, the beam penetrates a few nm and most of the secondary electrons produced escape. This causes a positive surface potential to develop in the beam. TEM samples are thin specimens, and charging may produce a mechanical force that the specimen is unable to withstand. This is a problem with thin polymer samples in particular. Coating samples with a conducting film such as carbon can reduce charging effects (Egerton, 2014).

2.4.1.5 Radiolysis of organic materials

Organic materials, such as covalent organic framework (COFs) and metal organic frameworks (MOFs), and materials such as zeolites are the most prone to radiation damage from the electron beam (Mayoral et al., 2015) (Chen et al., 2020). Radiolysis is also the most prominent damage mechanism in beam damage of biological samples (Baker and Rubinstein, 2010). The electron beam causes excitation within a molecule that does not return to its original electronic state when de-excited again. Chemical bonds are broken and the molecule changes in shape, this leads to the loss of crystallinity. The loss of crystallinity can be recorded by the fading of diffraction patterns. The change in electronic configuration can be followed by loss of the fine structure in the electron energy-loss spectrum. Bond breaking leads to lower molecular weight fragments, which can then be lost from the material, so mass loss is seen from the material (Grubb, 1974). Mass loss has been observed in polymers, where the carbon backbone bonds are broken. It is possible for these fragments to cross-link, but when motion is restricted chains are less likely to recombine and the material is lost.

2.4.2 Critical fluence

Critical electron fluence (C_F) is a measurement that can be taken on a sample to quantify the materials sensitivity to the electron beam. Critical fluence is calculated by measuring the intensity of a feature, such as an electron diffraction spot, and determining the electron fluence at which the maximum intensity drops to e^{-1} during exposure to the electron beam (S'ari et al., 2019). Phenomenologically, this decay is assumed to be of an exponential form. By taking the natural logarithm of the maximum intensity of the feature you are measuring in each successive measurement, the exponential relationship is linearised and can be fit to the following Equation 2.12:

$$I = I_0 \exp(-\tau D) \quad (2.8)$$

for intensity *I* and cumulative fluence or dose *D* and decay rate τ at $I/I_0 = 1/e$ where I_0 is the original signal intensity. The critical fluence is then the positive reciprocal of the gradient (see Materials and Methods for further explanation on how this is derived).

Most commonly, higher order Bragg reflections are the first to fade as these correspond to smaller lattice spacings. Bond breakage first affects short range order. Organic pharmaceuticals are particularly sensitive to the electron beam, with a recent study of 20 active pharmaceutical ingredients (APIs) finding that under 200 keV irradiation, the majority of the compounds had a C_F less than 5 $e^-/Å^2$ (S'Ari et al., 2018). In comparison, inorganic materials such as zeolites have a much greater critical fluence of 100 – 600 $e^-/Å^2$ and transition metal oxides greater still at values larger than 10^7 $e^-/Å^2$, making these compounds much easier to image under the high intensity electron beam (Jones et al., 1975). Measuring of the critical fluence value for organic materials is vital for the planning of EM measurements, to determine the dose budget available for this material to obtain the information needed. Critical fluence can be difficult to determine where samples reorient on the grid to a more stable position when exposed to the electron beam. This can lead to an initial rise of intensity or a non-exponential decay (S'Ari et al., 2018). In these cases, the initial rise in intensity can be excluded from the fitting, with the gradient of the decrease in intensity still taken as the critical fluence.

2.4.3 Beam Damage Control

Minimising beam damage in TEM studies is vital for the study of organic materials. Dose can be reduced by limiting exposure time, or lowering the electron current density rate, but this means outputs suffer from low signal to noise (Jiang and Spence, 2012). Cryo-TEM aims to reduce beam damage to a sample, or increase the dose budget for a material, by reducing the temperature of the sample to liquid nitrogen temperatures. These low temperatures reduce the rates of some of the reactions involved in electron beam induced mechanisms such as radiolysis, so damage is decreased. Reducing to these temperatures has been shown to improve the critical fluence of paraffin wax films by a factor of three to four (Egerton, 2013). However, when the critical fluence values are so low for these materials to begin with, reported to be 5 – 10 $e^-/Å^2$ (Choe et al., 2020), even with this increase the critical fluence values are still low. To obtain microstructural information from these organic systems, there must be a trade-off between resolution, dose budget, and noise. Specialised techniques can now be used which find a balance between low dose conditions and nanometre scale resolution.

2.5 4D-STEM

4D-STEM is an umbrella term covering many different techniques. The term 4D STEM refers to recording 2D diffraction patterns of a focused electron probe over a 2D grid of probe positions, resulting in 4D datasets (Ophus, 2019). In the literature, these techniques can be found under many different names such as scanning electron diffraction or nanodiffraction, with applications including integrated differential phase contrast (iDPC) and ptychography. Scanning electron diffraction (SED) is a 4D-STEM technique, where a two-dimensional diffraction pattern is acquired at each probe position in an image as an electron probe is scanned (and dwelled) across the sample, which, with the appropriate shaped probe, gives a diffraction pattern output consisting of well separated spots rather than discs. The highly parallel probe (~ 1 mrad convergence angle) utilised in this technique enables crystallographic analysis of separated Bragg disks but limits the electron probe size to around a nanometre. Ist is possible to record diffraction spots to 1 $Å^{-1}$ which corresponds to structural (diffraction) information at the 1 Å scale and microstructural (image) information at the 1 nm scale. A representation of the technique is visualised in Figure 2.7.

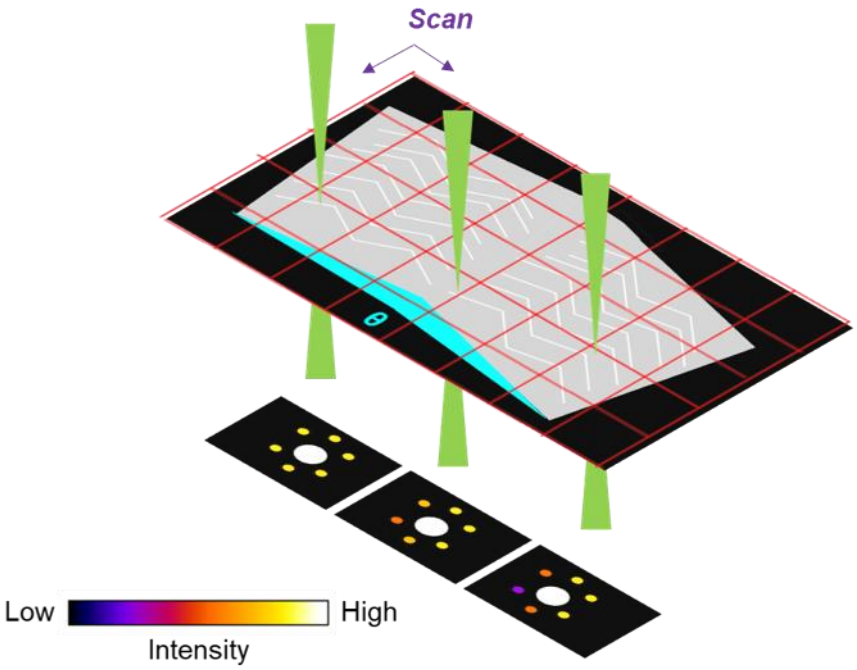

Figure 2.7: Representation of the 4D-STEM SED technique. The green cones visualise the movement of the probe over the sample.

Low electron currents can be used for this technique (1 pA), meaning low doses can be applied to the materials whilst maintaining a high signal to noise ratio (particularly with fast direct electron detectors), thus minimising damage to organic materials. This SED technique has been used to map defects in metal organic frameworks (Duncan

N Johnstone et al., 2020), to determine polymorphs and dislocations in crystalline pharmaceutical materials (Johnstone and Midgley, 2017) and resolving the local crystalline nanostructure in organic molecular crystals (Panova et al., 2019).

SED diffraction patterns, like those in SAED, may be analysed for information on the space group, crystal structure, and strain within the crystal. SED data can be analysed to provide structural insight in both real and reciprocal space. 4D-STEM has been used in the study of several polymer chain systems. The technique was applied for the imaging and study of domains in oriented and non-oriented polyethylene crystals, highly beam sensitive materials with similar chain packing similar to long chain paraffin waxes (Kanomi et al., 2021). Kanomi et al. were able to identify lamellae orientations (ordering of the molecular chains) in non-oriented samples were random where lamellae orientation in oriented samples was aligned in one direction. They noted that understanding the hierarchical structures of these ordered domains within polymers is important to understand higher-level structures such as the formation of spherulites, row structures, and shish kebab structures. These structures impact the mechanical and gas-barrier properties of the material.

It has further been used in the study of crystalline domains and their orientation in a block co-polymer (Chen et al., 2024). From 4D-STEM data, a new model for the structure of a block co-polymer of polystyrene and poly(ethylene oxide) was proposed with three levels of order at different length scales, the smallest length scale being the unit cell and the formation of individual crystalline domains. These crystalline domains in the poly(ethylene oxide) rich regions were 10 – 30 nm in size, and information on these domains could not be obtained using traditional TEM methods. In this structure, the polystyrene rich domains provide mechanical stiffness, and the poly(ethylene oxide) rich domains controls ion transport across the compound, so understanding this domain microstructure is important for determining physical properties of the electrolyte. This study highlights the importance of application of the SED technique to resolve spatial information in organic materials, offering structural information not accessible by other methods.

Scanning electron diffraction has been used to reveal the substructures inside ordered membrane domains in bio-membrane materials (Kinoshita et al., 2020), specifically phospholipid chains. They studied how these chains packed together, and by viewing diffraction patterns from selected areas, they were able to identify multiple subdomains with different crystallographic axis within a single ordered domain. This domain structure is of interest in these bio-membrane materials as these ordered domains regulate important biological functions, as it is widely believed that some membrane proteins are briefly entrapped in ordered domains.

SED was used to determine the nanostructure of a beam sensitive pharmaceutical co-crystal between paracetamol and theophylline (Johnstone et al., 2019), unveiling a twisted structure which may have a significant effect on physical, chemical and mechanical properties. 4D-STEM has also more recently been used to first report the crystal structure of Form I of a xanthine molecule (Helen W. Leung et al., 2025) and then SED was used to identify different polymorphic forms of a xanthine molecule, which may be present within single sub-micron particles (Helen W Leung et al., 2025). This latter study also identified planar disorder within crystalline domains. Xanthine is used in the synthesis of uric acid so is of interest in a pharmacological context, is a precursor for theophylline, and is also found in biogenic crystals. Biogenic crystals are produced by animals for functions such as in reflective structures to improve eyesight in low-light environments and are usually made from guanine. Unveiling the microstructure of xanthine has allowed comparison to the structure of guanine, to determine why some biogenic crystals are formed from xanthine. It is clear the microstructure or polymorphic form of xanthine may affect many properties such as optical properties, and mechanical and physicochemical properties, so understanding this microstructure is important. These studies have highlighted the importance of using 4D-STEM for study of molecular crystal microstructure, where different polymorphic forms can have different properties. These nanoscale structural features are important for understanding of the physical properties of these pharmaceutical materials. The opportunity to use SED for the study of nanoscale structure in solid solution systems is apparent.

There are some things to consider for 4D-STEM application. For a convergent probe, very finely spaced spots may not be separated (Williams and Carter, 2009). This is important to consider if using 4D-STEM to study systems where small d-spacing changes may occur with compositional change. For example, in solid solution formation the unit cell parameters may change as a result of guest incorporation, to ensure that these changes in d-spacings can be tracked an appropriate probe convergence should be selected. Sample preparation may also be an important consideration to observe microstructural features. In certain orientations of the sample to the electron beam, only a small fraction of the lattice may be observed, which may not offer the high spatially resolved information that the user is trying to obtain.

One of the simplest but significant processing procedures to extract information on the individual scattering vectors and therefore specific lattice planes is to use virtual annular dark field (vADF) images in low-dose 4D-STEM. Forming vADF images involves producing images which integrate over specific regions of diffraction space in every recorded diffraction pattern behind every image pixel. Virtual dark field (VDF) images are formed from virtual objective apertures (of any defined shape) which select

only certain (hkl) reflections. The dark field image is generated by summing the signal that falls within the defined area of reciprocal space from each diffraction pattern behind every image pixel. This is similar to using an objective aperture experimentally. This means that STEM-diffraction mapping can be used to image different phases within a material, by using these virtual apertures that allow the selection of multiple beams from the same dataset with high precision. Whereas conventional dark field requires deliberate placement of an objective aperture or tilting of the scattered beam into the objective aperture during the experimental acquisition, VDF can be done after a single-pass scan of a materials to get multiple VDF images from a single exposure i.e. is ideal for beam sensitive materials. In these images it is the isolation of the Bragg diffraction contributions that can improve the contrast of certain features, such as bend contours and breaks in contrast, which can highlight particular domains or defects such as dislocations.

Our work has shown how by forming virtual dark field images from (hkl) reflections from an SED dataset, it is possible to see how bend contours displace when passing across a dislocation line. This misalignment can be plotted as a function of the azimuthal angle relative to the horizontal axis of the diffraction pattern, and fitting to a geometric model gives the slip or Burgers vector direction of the dislocation (Pham et al., 2025). Dislocations and defects have an effect on the growth of crystals (Zhong et al., 2018), and the properties of the materials (Haneef et al., 2020), so understanding the type (screw, edge or mixed) and the slip system (slip direction and plane) of these features is important for control. Using the 4D-STEM approach enables information to be captured on a ‘one-shot’ basis, so this dislocation analysis can take place on beam sensitive samples whereas the previous multi-tilt analysis was confined to beam stable samples.

It is clear that varied microstructural information at the nanometre scale can be extracted from 4D-STEM techniques using a combination of direct image (real space) and diffraction (reciprocal space) information. This is especially in organic systems where this information was not possible to achieve before through other analytical or conventional microscopic tools. In particular, it could be useful to extract information on microscopic heterogeneity at the nanometre scale in molecular crystals, characterisation that has been lacking from solid solutions in molecular crystals currently.

2.6 Paraffin Waxes

Solid solutions formed between different long chain waxes have been studied by EM techniques but have not been so strongly linked to local microstructure, as discussed

further in this section. Waxes encompass a rich variety of technologically as well as biologically important solids. Some of the simplest waxes, paraffin waxes are used in many products from polishes, lubricants, and waterproof coatings to electrical insulators (Douglas L Dorset, 1997), (Freund and Mózes, 1982). Among diverse biological wax materials, the intracuticular wax (IW) layer on plant leaves plays a particularly important role in restricting water loss to protect the plant from dehydration and in other molecular diffusion to and from the leaf surface, (Schönherr, 1976). The IW layer is a feature of significant interest in crop plants and in terms of fundamental biological processes. IW layers contain a mixture of long chain hydrocarbons, so it is likely solid solutions form between these long chain hydrocarbons within this layer. Despite waxes comprising in large part simple linear chain hydrocarbon structures, which arrange in side-by-side chain packing in crystalline forms, they support a great deal of structural variety due to diverse ordering and disordering possibilities. They are structurally similar to polyethylene, the structure of which has been studied in EM and will be discussed further below. There is a question of whether waxes in the IW layers pack in a crystalline form, and what this crystalline structure is across the layer (Riederer and Müller, 2007). Determining the degree of (dis)ordered structure of these organic materials at the fundamental length scale of a few chain repeats (nanometer-scale) is crucial for underpinning understanding of how water and agrochemical active ingredients interact with plant crops (Riederer and Müller, 2007) but also across a number of sectors for understanding properties such as trans film diffusion, density, congealing point, and hardness (Roux, 1969).

In this thesis, investigation first focuses on a reduced set of long chain hydrocarbons found in leaf waxes to investigate microstructure and solid solution formation in compositionally similar materials. Different plants and varieties have very different compositions, but we focus on the *Schefflera elegantissima* plant, a simple plant with an IW layer consisting mainly of long chain alkanes and alcohols. Studying this simple system may lead to the discovery of features that can be linked to plant performance across many different species. The plant cuticle is the outermost layer of the leaf, with many different functions including defence against parasites, protection against ultraviolet (UV) radiation and water repellence as well as transpiration control (Riederer, 2007). The mechanisms of this transpiration barrier in the cuticle are largely unknown, although it is believed that the IW layer is the main barrier to transpiration rather than the epicuticular layer (Jetter and Riederer, 2016).

In leaves, although the composition of the wax layer varies between different plant species, the IW layer's structure is thought to have a 'brick and mortar' type arrangement consisting of highly crystalline packing of chains in aligned 'lamellar' blocks or 'bricks' surrounded by amorphous regions, (Riederer and Schreiber, 1995),

though the precise size and relative ordering of these lamellae has not been established. The layer consists of a diverse mix of aliphatic compounds. Two main components have been confirmed; linear very long chain aliphatics (VLCAs) and cyclic triterpenoids. The four most common classes of the long chain aliphatic wax components are alkanes, alcohols, fatty acids and aldehydes. Chain length of these molecules can vary from C_{16} to C_{35} (Zeisler-Diehl et al., 2018). This arrangement of disorder at chain ends and in the gaps between lamellae is thought to provide high diffusivity pathways through the wax layer. A visualisation of this proposed 'brick and mortar' type structure that forms the IW layer is seen in Figure 2.8, showing these chain ends terminating in disordered and potentially amorphous wax zones.

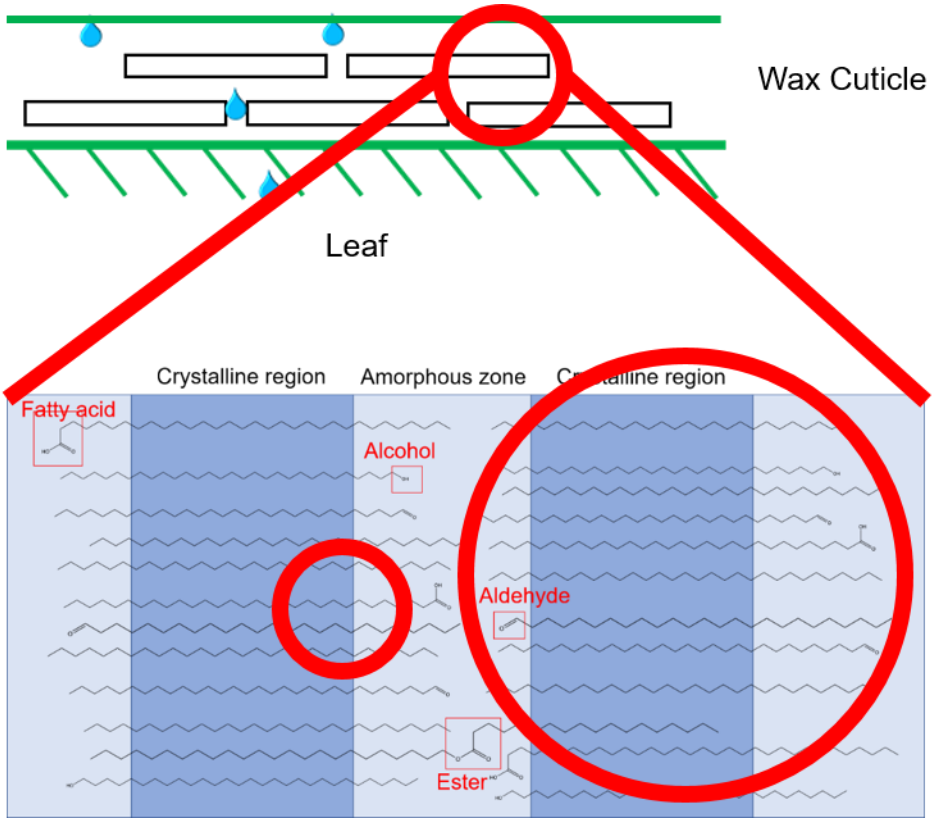

Figure 2.8: Representation of the proposed 'brick and mortar' model that forms the IW layer of a leaf.

Schönherr showed that extraction of cuticular waxes increases transpiration across *Citrus aurantium L*. leaves, pear (*Pyrus communis L*.) leaves and onion *(Allium cepa L*.) bulb scales by several orders of magnitude (Schönherr, 1976), however it has also been shown there is no correlation between water permeability and cuticle thickness (Riederer and Schreiber, 2001). The extraction involves removing the cuticular membrane from the leaves by placing small disks in a mixture of pectinase and cellulase and then placing these membranes in methanol and chloroform to extract the cuticular waxes from the selected cuticles. It has therefore been proposed that the

IW VLCAs may play a key role in the transpiration mechanisms. Understanding the structure of this layer to a greater degree may hold the answer to this question. This also has implications for the movement of other molecules across this barrier, such as small organic molecules called adjuvants which are added to crop protection products to aid the movement of active ingredients into a leaf following topical application such as spraying. Understanding the structure of the IW layer is therefore of importance for the design of these crop protection products.

Examination of waxes at the nanoscale is imperative to evaluate this hypothesis. IW layer structures can be very complex and therefore hard to study so to simplify, replica wax leaf systems can be prepared from pure long chain hydrocarbons. This approach enables exploration of inherent self-assembly and crystallisation processes in the underlying wax constituents. The likeness of paraffin waxes to leaf wax systems was first proposed by Basson and Reynhardt (Basson and Reynhardt, 1992). Simplified, replica leaf waxes provide a first route to revealing the structural complexity native to these long chain hydrocarbons and their mixtures.

Paraffin waxes, i.e., long chain alkanes, can be thought of as packing similarly to polyethylene. In polyethylene, the molecular chains pack in an extended linear conformation, but without lamellar ordering as the polyethylene is assumed to exhibit effectively infinite chain extension. Polyethylene is most commonly described by an orthorhombic sub-cell but can also exhibit monoclinic or triclinic sub-cells. The orthorhombic polyethylene unit cell is shown in Figure 2.9 (Monnerie, 1999).

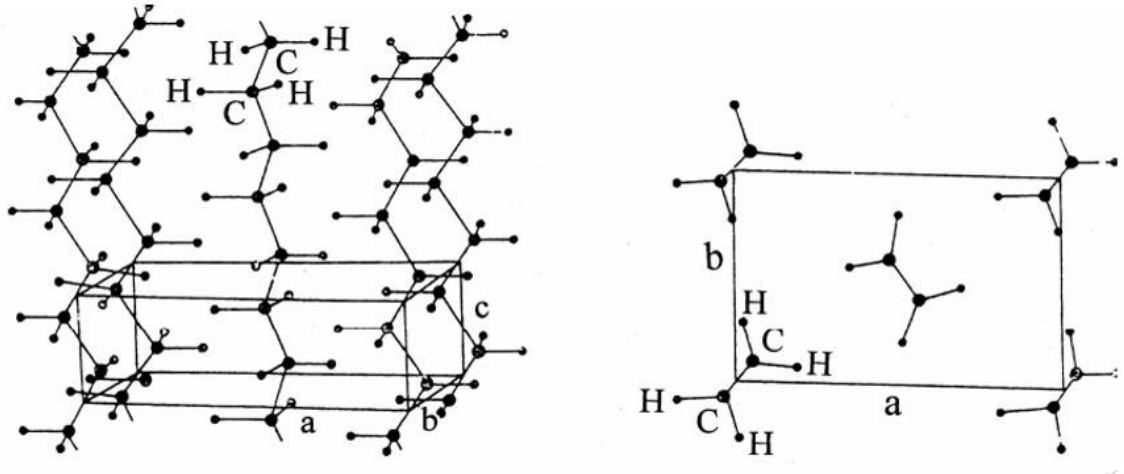

Figure 2.9: Polyethylene unit cell representation (side view on the left and plan view on the right), taken from (Monnerie, 1999).

Finite linear alkanes of *n* carbon atoms in high purity forms, with minimal chain length dispersion, organize into lamellar blocks with gaps in between aligned chain ends at

the boundaries of the block or lamella. These *n*-alkane chains pack with chains fully extended and end-to-end. Example unit cell representations can be seen in Figure 2.10, where the similarities to polyethylene in Figure 2.9 can be seen.

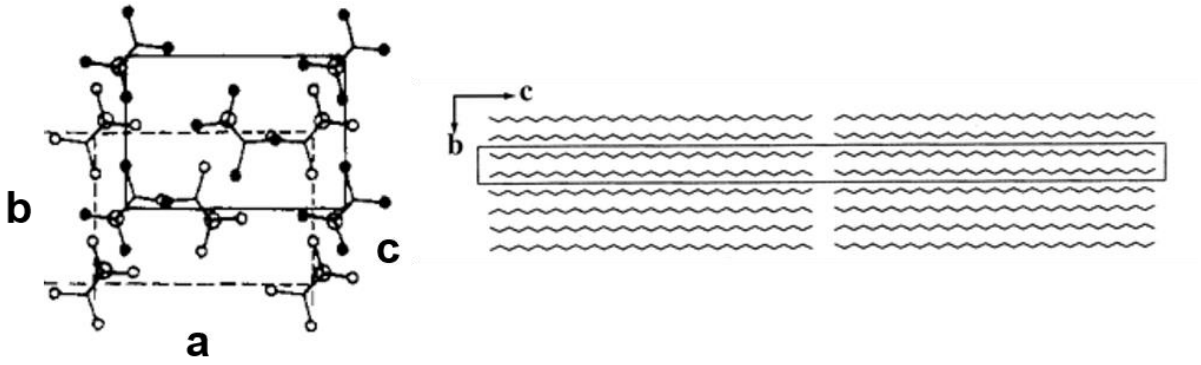

Figure 2.10: Odd-chain paraffin wax unit cell representations, plan view on the left taken from (Dorset, 1985a) and side view on the right from (Dorset, 2000a).

Molecules of equal length form well-defined lamellae where the length of the molecule determines the interlamellar spacing (Ensikat et al., 2006). Polydisperse *n*-alkane (paraffin) waxes readily form solid solutions, lowering the degree of ordering such that paraffins exhibit polymorphism based on chain length, purity and temperature (Fryer et al., 1997). Nevertheless, solid solutions of paraffins will still form single crystals when chain lengths are within four carbon units of each other.

Analytical techniques such as XRD and atomic force microscopy AFM have been used to characterize long chain waxes. SCXRD and pXRD have been used in early studies of wax structure, such as in structural studies of fatty acids (Malkin, 1952) and *n*-alkanes (Smith, 1953). For the *n*-alkanes, seminal predictions of crystal structures (Nyburg and Potworowski, 1973) have been verified through synchrotron powder diffraction (Craig et al., 1994). Powder XRD patterns from a typical bulk assembly of microcrystals can provide somewhat limited information about the lamellar stacking of the chain layers and the preferred sub-cell packing of the polyethylene repeat. It is known that high molecular weight polyethylene can fold to form thin single crystal lamellae with the molecular chains initially shown to be perpendicular to the flat faces of the crystals (Keller, 1957). It has since been observed that chain tilt relative to the lamella normal can affect the sharpness of chain folding (affecting the interlamellar distance) and whether chains form isolated or stacked lamellae, with isolated lamellae commonly exhibiting chain tilt angles close to a thermodynamically favored 34° and stacked lamellae exhibiting smaller tilt angles (Kanomi et al., 2023). AFM has revealed defects in paraffin crystals such as spiral growth formed by screw dislocations (Olson et al., 2018). XRD and AFM, however, do not afford insight into the spatial

arrangement of lamellar microstructure accessible using TEM techniques (Ensikat et al., 2006).

Dorset and colleagues have used SAED to extensively characterize and determine the structure of paraffin waxes at the length scale of a few micrometers (Douglas L. Dorset, 1997b), (Douglas L. Dorset, 1997a), (Dorset, 1990), (Dorset, 1986), (Dorset and Hauptman, 1976). Obtaining single crystal diffraction data by SAED accordingly has a much less stringent requirement on crystal size relative to X-ray approaches. However, TEM samples must be sufficiently thin to be electron transparent. Using established procedures for molecular crystal orientation control (Wittmann et al., 1983), (Wittmann and Lotz, 1990), Dorset and colleagues prepared electron transparent paraffin single crystals in two key orientations, with chains parallel and with chains perpendicular to the electron beam. These studies have revealed molecular packing symmetry as well as signatures of interlamellar disorder in a variety of single and multi-component waxes. Although many other orientations on surfaces are conceivable, these two selected orientations follow the symmetry of *n*-alkane and *n*-alkanol molecules in the solid state: the chains parallel to the electron beam offer a unique view of the side-by-side packing of these chains, and the chains perpendicular to the beam presents one of several orthogonal perspectives to examine the key end-to-end packing of chains. Together, these two orientations provide an important set for initial investigations of the wax microstructure in pure *n*-alkanes, *n*-alkanols, and significantly for IW layer research their binary mixtures.

Morphology can also be dependent upon the functional groups found in the carbon chains, with oxygen containing functional groups requiring extra space and hindering the formation of the orthorhombic structure (Ensikat et al., 2006). Although the study by Ensikat et al used SAED in addition to XRD to study these structures, they noted how the SAED data collected was of poorer quality. This was due to the background signal from the supporting film and because of electron beam damage. There is therefore a clear knowledge gap in structure determination of these wax systems that can be addressed by the more recently developed 4D-STEM, low dose electron diffraction techniques.

Fryer et al also used electron diffraction techniques with paraffins and their solid solutions (Fryer et al., 1997). They found that solid solutions of paraffins will form single crystals with well-defined lattices, as long as the chain lengths were within four carbon units of each other and irrespective if they were odd or even chain numbers as no crystal segregation occurred when analysing lattice fringe separation as a function of composition for the solid solutions. These measurements are based on the lattice

parameter in one dimension e.g. a single set of fringes from a crystal in a single orientation.

XRD analysis by Lüth et al (Lueth et al., 1974) proposed that the co-packing of dissimilar chain lengths was compensated by longitudinal molecular disorder in individual lamellae. Later ED work by Dorset supported this model. Crystal structures were determined by direct phase methods, originally described by Dorset and Hauptman (Dorset and Hauptman, 1976). The Miller indices of (01ℓ) diffraction patterns are related to the carbon chain length, n, in C_nH_{2n+2} of the average lamellae, where ℓ = 2n, 2n+2. For epitaxially orientated samples the space group is *Pna2₁* or *A2₁am*, for even or odd chain samples respectively (Dorset, 1995a). An earlier Dorset paper found that even chain paraffins crystallise as the orthorhombic polymorph, whereas the odd chain paraffins do not crystallise in their lowest energy form (Dorset, 1986). Overall, electron diffraction work by the Dorset group found that for binary solutions, the average structure resembled that of a pure paraffin but with a Gaussian distribution of atomic occupancies near the chain ends. These findings match well with electron diffraction studies of natural waxes, showing the binary solutions of paraffin waxes are a good model for the crystalline region of a leaf wax (Douglas L. Dorset, 1997b). The Dorset and EM work has highlighted the presence of 00ℓ spots around the central beam, corresponding to the end-to-end chain packing, and diffuse scattering as features in the diffraction patterns of these materials (Dorset, 1995a), (Dorset et al., 1984). However, this diffuse scatter was explained by a thermal model, but noted that further study should be done to distinguish thermal diffuse scattering from defect diffuse scattering. These studies also do not consider how these features change across crystals i.e. the microstructural impact. As outlined earlier in this literature review, VDF images can be formed from individual (hkl) spots, so it is possible that the location of highly ordered end-to-end chain packing may be tracked across crystals using 4D-STEM techniques and signal from the 00ℓ spots.

There is therefore opportunity to study the microstructure of these paraffin waxes at a scale that has not been accessible before to understand the chain packing of individual paraffin components, and the solid solution behaviour or phase separation between two components across polycrystalline assemblies of these materials. There is also the possibility that EM techniques can unveil the solubility limit across the solid solution system between a binary mixture of two waxes. This structural information can therefore be evaluated against the ‘brick and mortar’ model, by viewing the structure across a range of levels from crystal grain structure to individual lamellar microstructure.

A second investigation of this thesis then focuses on a molecular solid solution of structurally similar but compositionally different molecules to explore whether a combination of diffraction (4D-STEM) and elemental spectroscopy (EDS) can identify solubility limits. Alloying isomorphous crystals of barbituric acid (BA) and thiobarbituric acid (TBA) yields solid solutions of general formula BA_xTBA_{1-x} ($x < 0.8$) (Shemchuk et al., 2016). Barbituric acid (BA) is an organic compound that is the parent compound of many barbiturate drugs, a class of central nervous system depressant drugs. Thousands of related barbiturate compounds have been synthesised in the century or so since its first introduction, of which 50 are or have been used clinically (López-Muñoz et al., 2005). Thiobarbituric acid (TBA) is an isostructural organic compound, where one of three oxygen atoms that bind to the pyrimidine heterocyclic skeleton has been replaced by a sulphur atom. BA and TBA derivatives have been used in herbicides, fungicides, and as antiviral agents (Kidwai et al., 2005). These compounds are therefore of interest to both the pharmaceutical and agricultural sectors.

Using XRD and DSC, Shemchuk et al. found that in this system, BA and TBA form a solid solution with a solubility range from 20% TBA to 80% TBA in the overall composition (Shemchuk et al., 2016). They also suggest that after 3 months left at room temperature in ambient conditions that the solid solutions with a TBA content over 50% convert to a 50:50 co-crystal with excess TBA. Another phenomenon they explored was the shift of the (202) diffraction peak to lower 2θ values in the XRD spectra with increasing TBA content in the solid solution. Whilst DSC and XRD offer information on the bulk powders of the solid solution compositions, they do not offer insight to structural heterogeneity within the compounds. For compositions where the mixtures possibly form a 50:50 co-crystal with excess TBA, local analysis techniques such as EM may be able to highlight where these mixtures have formed. There is therefore opportunity to use SED to explore the (202) diffraction spot shift with increasing TBA, and EDS to explore the elemental composition in individual particles in this system. These techniques can assess the structural heterogeneity that may occur at the nanoscale within these solid solution compounds.

2.7 Outlook

This literature review has summarised the current understanding on solid solution formation in molecular compounds focusing on characterisation, and the difference between these and co-crystals. This distinction is important for the potential changes of properties these materials may exhibit based on differences in their crystalline packing, i.e. their structure-property relationship. This literature review has also summarised the current understanding of long chain hydrocarbon packing in leaf wax layers, and how simple replica systems can be formed from paraffin long chain waxes.

How these crystalline components pack together, and whether they form solid solution systems in these layers, is of importance for understanding how molecules may move across this barrier when leaving (transpiration) or entering (active ingredient delivery for crop protection) the leaf. However, there is a current lack of data on how these solid solutions vary across and between crystals in an assemblage of waxes and a lack of microstructural information on these structures. Likewise solid solution limits in the isostructural but compositional BA/ TBA system are not fully understood or linked to microstructure in an assemblage of crystals. Establishing the solubility limits for this system will be useful for understanding polymorph formation for pharmaceutical and agrochemical applications, and include the goal of assessing solid solution stability over time and hydration state.

This review has also explored the current common characterisation methods used to study these systems previously. The more ‘bulk’ techniques fail to unveil the microstructure of the materials, which may mean the potential implications for the properties of these materials are not fully understood. The issues with microstructural characterisation of these organic systems, focusing on electron beam damage problems when using electron microscopy techniques, have also been identified. It is apparent there is opportunity with 4D-STEM to unveil the microstructure of these organic systems, particularly in the solid solution systems that have suffered from a lack of consideration in the literature previously.

Dorset SAED work showed the clear advantages of using electron diffraction over XRD data, especially for structure determination of a binary wax system. 4D-STEM techniques have been used to characterise structurally similar polymer systems, so the opportunity to now use SED for domain microstructure analysis on these systems is now upon us. Wax materials also form solid solutions so there is opportunity to examine how these structures change upon addition of one wax to another. Solid solutions are not as commonly characterised by EM techniques, in particular in beam sensitive organic molecular solid solution systems. There is opportunity to understand the microstructure of the crystalline systems that form on solid solution formation and how certain polymorphs can drive solid solution formation. Understanding the microstructure of these systems is important for the understanding of their properties, and how external molecules may interact with the structures.

This thesis utilises low-dose electron microscopy techniques to probe the nanoscale structure of organic materials; a replica leaf wax binary mixture system, and a solid solution between two small organic molecules of similar structure but different composition that exhibit structural polymorphism.

2.8 Objectives and Thesis Outline

This thesis looks to characterise two solid solution systems and use microscopic techniques to obtain highly resolved structural data and information on the microstructure of these systems and how this might be used to assess solubility limits. There is unresolved microscopic heterogeneity in multi-component crystals and solid solution systems, from their initial preparation to changes in structure upon chemical (water and or other adjuvant molecules) with these systems, and stability of these systems over time (and temperature). Advancements in low-dose EM techniques mean there is opportunity to study this at a scale not accessible before and therefore link the microstructural development to the solubility limits.

The specific research objectives for this research and the results chapters in which they are addressed are presented below:

- To identify the crystal structure packing of a long chain alkane, $C_{31}H_{64}$, a long chain alcohol, $C_{30}H_{61}OH$ with TEM, SAED and AFM data. The results are reported in Chapter 4 reveal deviations from the expected, simple orthorhombic, end to end chain packing originally reported for PE and pure waxes and are published in Wynne et al. (Wynne et al., 2024).
- Having identified the crystal structure packing of the long chain alkane, $C_{31}H_{64}$, a long chain alcohol, $C_{30}H_{61}OH$ components, results reveal defined grain microstructure in $C_{31}H_{64}$ crystals and nanoscale domains of chain-ordered lamellae within these grains while the $C_{30}H_{61}OH$ exhibits more disordered chain packing with no grain structure or lamellar domains using SED, a 4D-STEM technique, to evaluate these nanoscale features not visible at a larger scale. The solid solution and phase separation behaviour of the binary mixtures are considered and because there is a loss of grain structure with increasing alcohol content are shown to separate at about 30% alcohol content. The results are reported in Chapter 5 and are published in Wynne et al. (Wynne et al., 2024).
- Once the microstructure and solubility limits of the wax components is understood, it must then be understood how exposure to external molecules affects these microstructures. The interaction between tris(2-ethylhexyl)phosphate (TEHP) and $C_{31}H_{64}$ and $C_{30}H_{61}OH$ and a binary mixture is studied using a range of microscopic techniques, optical microscopy, TEM, SAED, EDS and SED, and analytical techniques, NMR, FT-IR, DSC, using different wax: TEHP ratios to evaluate the interaction. The results reveal that the TEHP etches and disrupts the paraffin wax structures in apparently greater amounts for the long chain alcohols than the alkanes, these are reported in Chapter 6 and contain elements published in Pham et al. (Pham et al., 2025).

- Having studied heterogeneity across the wax solid solution system, analysis turns to a different solid solution system between two similar components but with greater chemical heterogeneity. To evaluate and characterise the formation of a solid solution system between two small organic molecules, barbituric acid and thiobarbituric acid, with a focus on assessing the feasibility of using energy-dispersive X-ray spectroscopy (EDS) and scanning electron diffraction (SED) to monitor microstructural and compositional variations across the reported solid solution range. The results confirm that a stable solid solution forms up to 50% TBA and concentrations above that readily breakdown to a co-crystal, and these are reported in Chapter 7.

Chapter 3
Materials and Methods

3.1 Materials

n-*hentriacontane*

Samples of n-hentriacontane ($C_{31}H_{64}$) were purchased from Sigma-Aldrich with >98% reported purity.

1-triacontanol

Samples of 1-triacontanol ($C_{30}H_{61}OH$) were purchased from Caymen Chemicals with >98% reported purity.

Binary mixtures of n-hentriacontane and 1-triacontanol

Binary mixtures were prepared using a molar fraction of the two components melted together above 90 °C and allowed to cool and crystallize to homogenize the samples prior to any subsequent melting.

All wax samples were prepared in two ways on continuous amorphous carbon supported on a copper mesh grids for TEM analysis following methods established in the literature (Wittmann and Lotz, 1990), (Fryer et al., 1997).

The first method of preparation was drop casting from solution. 1 mg of the long chain hydrocarbon was partially dissolved in 30 µL hexane to form a supersaturated solution. Hexane was purchased from Fisher Scientific with a reported purity of >95%. 2 µL of the supersaturated solution was dropped onto a continuous carbon film supported on a copper 300 mesh grid and the hexane left to evaporate naturally, leaving crystalline regions of the product on the grid, giving chains orientated in the “down-chain” orientation i.e. along the chains or the [001] direction.

The second method relies on mixing the paraffin in the solid state with a large excess of benzoic acid crystals, melting the mixture (at up to 100 °C) and crystallizing the paraffin on the benzoic acid crystals to template the growth of extended plate-like wax crystals with the long hydrocarbon chain in the plane of the plates. Benzoic acid was purchased from Insight Biotech with a >99.5% reported purity and used as received. Briefly the paraffin-benzoic acid mixture was enclosed between two glass slides. A flat aluminum bar with one end on a hotplate, (hotplate heated to 100 °C) provided the temperature gradient, and the glass ‘sandwich’ was slid slowly (~1 cm per second) up and down the bar causing the mixture to melt and then solidify. The mixture was determined to have melted when the mixture changed from a white solid powder mixture to a colorless liquid mixture between the two glass slides. Recrystallization

was identified by the formation of white crystals within a few seconds of cooling. Once cool, the two sheets were separated, and the two layers of the mixture obtained were floated on to a water surface. The benzoic acid dissolved in the water and the remaining wax specimens were picked up on plasma cleaned TEM grids. This procedure resulted in paraffin crystals supported on the carbon film of the TEM grid, giving chains lying flat on the TEM grid support film surface.

Tris(2-ethylhexyl) phosphate (TEHP)

TEHP was purchased from Sigma-Aldrich with reported 97% purity. TEHP was used without further purification.

Adjuvant Exposure

For electron microscopy (EM) experiments, EM grids prepared in the “down-chain” orientation were exposed to TEHP by partially dipping the grid into a droplet of TEHP. This was done to achieve exposure of the materials without total wash-off of the wax crystals. For all other measurements, $C_{31}H_{64}$ and $C_{30}H_{61}OH$ crystals were exposed to TEHP by pipetting droplets onto the wax material on glass slides and/ or thin carbon films for TEM.

Barbituric acid (BA)

Barbituric acid was purchased from Sigma-Aldrich with reported 99% purity and used without further purification.

Thiobarbituric acid (TBA)

2-thiobarbituric acid was purchased from Sigma-Aldrich with reported 98% purity and used without further purification.

Barbituric acid and thiobarbituric acid binary mixtures

Binary mixtures of BA and TBA were prepared using a molar fraction of the two components, with both components dissolved in 20 mL of boiling ethanol after which the solvent was left to evaporate at room temperature. Ethanol was purchased from VWR International with reported purity of ≥99.5%, and used as received.

BA, TBA, and BA: TBA solid solution samples were prepared for EM analysis by a dry powder transfer onto the grid. This procedure involved placing a continuous carbon film supported on a copper 300 mesh grid between two pieces of lens tissue paper and placing a small amount of powder on top of the grid. The pieces of paper were shaken, with the powder and grid within, to disperse the powder onto the EM grid.

For NMR analysis, DMSO-d6 was purchased from Eurisotop with 99.8% reported purity. $CDCl_3$ was purchased from VWR Chemicals with 99.8% reported purity.

3.2 Electron Microscopy

3.2.1 Transmission Electron Microscopy (TEM)

Transmission electron microscopy (TEM) is a tool that allows us to probe a local area of a sample, being able to capture images of molecules on the nanometre scale or of individual heavy atoms distributions (Meyer et al., 2008), (Williams and Carter, 2009). To achieve this, a thin specimen is irradiated with a parallel electron beam of uniform current density. The electrons are scattered by the sample and this radiation passes through an objective lens. This lens focuses the electrons forming the initial image of the specimen in its image plane, and generating a diffraction pattern in its back focal plane. A set of intermediate and projector lenses then magnify this initial image to give a final image of the specimen (Williams and Carter, 2009). Electron microscopes are capable of imaging at a higher spatial resolution than light microscopes due to the smaller de Broglie wavelength of accelerated electrons. Resolution of a microscope is defined by Abbe's equation (Equation 2.2) (Helmholtz and Fripp, 1876):

$$d = \frac{0.61\lambda}{n\,sin\alpha} \tag{3.1}$$

where d is the resolution (the distance between two points that are just resolved), λ is the wavelength of energy source, n is the refractive index of the medium and α is the aperture angle. The wavelength of an electron is approximately dependent upon the accelerating voltage (if ignoring relativistic effects):

$$\lambda = \frac{h}{\sqrt{2meV}} \tag{3.2}$$

where h is Planck's constant, m is the electron mass, e is the electronic charge and V is the accelerating voltage. Relativistic effects cannot be ignored above 100 keV because the velocity of the electrons becomes greater than half the speed of light, so Equation 2.3 can be modified to:

$$\lambda = \frac{h}{\sqrt{2meV(1 + \frac{eV}{2mc^2})}} \tag{3.3}$$

Using these constant values, the wavelength of the electron can be approximated to:

$$\lambda = \sqrt{(\frac{1.5}{V})}\,nm \tag{3.4}$$

At 300 keV, the electron wavelength is ~2 pm, giving a theoretical resolution of ~0.002 nm using Abbe's equation, but this has never been achieved experimentally. Muller et al. achieved the highest experimental resolution in a TEM of 0.02 nm (Chen et al.,

2021). Due to the reciprocal dependence of the wavelength on the accelerating voltage, the higher the accelerating voltage the higher resolution that can be achieved. However, higher accelerating voltages also cause more atomic displacement damage to the sample, so there has to be a trade-off between the two (Egerton, 2012).

Conventional TEM (CTEM) was used in Chapter 4 and Chapter 6 for the imaging of the wax materials and the wax materials after exposure to TEHP. CTEM was carried out using an FEI Titan^3 Themis operated at a 300 kV accelerating voltage at room temperature. The FEI Titan^3 Themis S/TEM microscope was equipped with a high-brightness 'X-FEG' electron gun, an S-TWIN objective lens, a Gatan OneView 4K CMOS digital camera and a continuously variable gun lens to control the beam current. 'Low-dose' TEM was achieved by spreading the monochromator lens to reduce the electron flux to less than 1 $e^{-}/Å^2$ s. Images were acquired with a 1 second exposure time and diffraction patterns were acquired with a 4 second exposure time.

3.2.2 Selected Area (Electron) Diffraction (SAED)

Selected area electron diffraction patterns were acquired for the wax materials in both prepared orientations in Chapter 4, and the 'down-chain' oriented wax materials exposed to TEHP in Chapter 6. SAED patterns were captured during the 'low-dose' TEM setup described above and at room temperature. A selected area aperture of 20 μm diameter was used for diffraction pattern collection giving a selecting aperture in the image plane of approximately 200 nm diameter.

3.2.3 Scanning Transmission Electron Microscopy

The imaging mode utilised for STEM analysis of the BA:TBA solid solution compounds in Chapter 7 was high-angle annular dark-field (HAADF) imaging. The Titan^3 Themis 300 STEM conditions used were 300 kV accelerating voltage, 20 μs dwell time, 5 pA beam current, and 10 mrad probe convergence semi-angle (α) and a camera length of 90 mm projecting on to the FEI HAADF detector.

3.2.4 Energy Dispersive X-Ray Spectroscopy (EDX/ EDS)

All EDS data was captured on the Titan^3 Themis 300 microscope which is equipped with an attached FEI 64 Super-X four-detector EDX system. Samples were not prepared any differently for EDS from the procedures for TEM grid preparation already outlined. EDS spectroscopy of TEHP exposed wax crystals in Chapter 6 was obtained as a single acquired spectrum in TEM mode. STEM-EDS mapping spectroscopy of the BA:TBA solid solution systems in Chapter 7 was carried out during STEM experiments with a pixel dwell time of 20 μs and using the Thermofisher Velox acquisition software. Pixel size varied with individual particle measurements, but

magnification was adjusted to maximise the particle coverage in the field of view and minimise carbon background contributions.

STEM-EDS data were used to analyse the ratio of sulphur in the BA: TBA mixtures. The ratio between the sulphur peak and the background was calculated by processing the data, acquired in Velox, in the Hyperspy software. This approach has been used in microanalysis for biological systems (Warley, 1997). The procedure carried out in Hyperspy was: An EDS spectrum for each measured particle was formed by summing the X-ray intensities measured from all pixels containing the particle. The sulphur:background ratio was calculated by integrating the signal under the *K*α sulphur peak, found at 2.3 keV over an energy window of 0.178 keV, and dividing it by the integrated signal of pure background from a same sized energy window immediately before the sulphur peak (Figure 7.19b, Chapter 7). EDS measurements were taken on individual particles only. Several repeat measurements were taken for each composition from different particles on the same grid.

Fitting of the curve to the average sulphur: background ratio values was carried out in the Origin graph plotting software using a new user defined function to fit.

3.2.5 Electron Energy Loss Spectroscopy (EELS)

EELS data were captured from the $C_{30}H_{61}OH$ wax material in the STEM setup. This was done at room temperature. STEM-EELS spectrum imaging was undertaken in the image-coupled mode using a 0.25 eV per channel dispersion on the spectrometer. Data were collected with a 50 pA probe, a spectrometer collection semi-angle of 8.7 mrad, dwell time of 1 µs, and pixel size of 3.3 x 3.3 nm. Dual EELS collection mode enabled core-loss energy calibration against the zero loss peak (ZLP) energy. The data presented in Chapter 5 were taken at room temperature.

3.2.6 Scanning Electron Diffraction (SED)

SED data were acquired using a JEOL ARM300CF fitted with an ultrahigh-resolution pole piece, a cold field emission gun, and aberration correctors in both the probe forming and image-forming optics (Diamond Light Source, UK). The instrument was operated at 300 kV. A nanobeam configuration was obtained by switching off the aberration corrector in the probe forming optics and using a 10 µm condenser aperture to obtain a convergence semi-angle <1 mrad and a diffraction-limited probe diameter of approximately 5 nm. The probe current was measured using a Faraday cup as 1 pA, and the exposure time was 600 µs or 1 ms per probe position. The estimated electron fluence for the 600 µs dwell time, assuming a disk-like probe, was ~ 5 $e^{-}/Å^{2}$. A diffraction pattern was acquired at every probe position using a Merlin-Medipix

hybrid counting-type direct electron detector (Quantum Detectors, UK). EM sample grids were prepared as already outlined for the $C_{31}H_{64}$ and $C_{30}H_{61}OH$ individual and binary mixture wax samples, and the BA and TBA samples.

3.2.7 SED Data Analysis

Data processing was carried out using the Pyxem (version 0.11.0) open-source Python library for multidimensional diffraction microscopy (Duncan N. Johnstone et al., 2020). Calibration data were recorded from standard MoO_3 and Au-cross-grating samples as reported previously. The rotation between the scan direction and the diffraction pattern was calibrated by identifying the angle between the characteristic long axis of MoO_3 crystals of known habit and the corresponding diffraction spots. An Au-cross-grating with a 500 nm period was used to calibrate the image pixel size. By recording an SED data set from polycrystalline Au, a diffraction pattern consisting of characteristic rings was acquired and fitted to a set of ellipses to determine residual elliptical distortions and to determine the diffraction camera calibration. For long chain hydrocarbon and BA and TBA samples, the direct beam was first aligned to pixel precision and then centred using a cross-correlation function in Pyxem to subpixel precision. An affine transformation matrix was used to remove the measured elliptical distortions and the pattern rotation relative to the scan direction.

Diffraction patterns, originally 515 × 515 pixels, were cropped to 514 × 514 pixels and then binned by a factor of 2 to produce diffraction patterns with dimensions 257 × 257 pixels. Low-angle annular dark field (ADF) images were formed by integrating the diffraction pattern at each probe position between an inner radius of 2.1 mrad and an outer radius of 7.5 mrad to produce an image dominated by diffraction contrast. Medium-angle ADF images, denoted ADF-1 images, were formed by integrating the diffraction pattern at each probe position between an inner radius of 2θ = 12.0 mrad and an outer radius of 2θ = 26.0 mrad, (beyond the scattering angles observed for the first order Bragg diffraction spots) to form an image dominated by mass–thickness contrast. A second set of medium-angle ADF images, denoted ADF-2 images, were formed by integrating the diffraction pattern at each probe position between an inner radius of 2θ = 16.2 mrad and an outer radius of 2θ = 26.0 mrad, similarly to form an image with greater contributions from mass–thickness contrast. Average electron diffraction patterns were obtained by taking the mean intensity from all diffraction patterns contributing to an image. Virtual dark field (VDF) images were produced in Pyxem by defining regions of interest in the diffraction pattern and integrating the signal from these regions. Simulated diffraction patterns were produced using the DiffSims package as part of Pyxem by defining a crystal orientation by its direction [UVW] along the electron beam trajectory. Diffraction patterns are presented as the

square root of recorded intensity (applied in ImageJ software) for improved visualization of high and low intensity features simultaneously. Poisson distribution statistics for signal-to-background evaluation were carried out using the Scipy Python package. Grain size measurement in Chapter 5 was carried out in ImageJ. SED diffraction patterns in Chapter 7, where the orientation of the sample on the grid was unknown, were indexed using the CrystBox software.

3.2.8 Facet Analysis

Facet angles were measured in ImageJ. These surfaces were analysed by drawing a straight line parallel to the inferred projected surface, pre-exposure, defined by aligning a line along the top of the remaining protruding features. The angle between this straight line and parallel to the edge of a pit was measured in ImageJ. The amount of alcohol groups at the surface of different crystallographic planes was measured in Vesta by cutting the crystal at the plane being studied. When assessing groups at the surface, it was ensured the cut through the crystal of the plane of interest was adjusted to ensure the position of the cut left all molecules intact, so only whole molecule projections were assessed. The orientation of the molecules in the unit cell was determined by indexation of the diffraction pattern. Next, the crystal planes aligned in real space with the observed surfaces were extracted with reference to the indexed diffraction pattern. Molecules were also counted as being at the surface if there was empty space between that molecule and the drawn surface, meaning TEHP interaction could be possible.

3.3 Powder X-Ray Diffraction (pXRD)

Powder X-ray diffraction patterns of the $C_{31}H_{64}$ and $C_{30}H_{61}OH$ individual and binary wax samples pre and post exposure to TEHP in Chapter 6 were recorded using a PANalytical Aeris Benchtop XRD using copper K_α radiation (Cu $K_\alpha \lambda$ = 1.541 Å). Samples were compacted into a sample plate and flattened, and scanned at a step size of 0.0217° 2θ, in the scan range of 10°–30° over 2 minutes.

For these samples, peaks were fit to a Gaussian function in the Origin graph plotting software, and the full width at half maximum values were calculated from this fitting.

Powder X-ray diffraction patterns of BA, TBA, and BA: TBA mixtures in Chapter 7 were recorded using a Bruker D2 diffractometer using copper K_α radiation (Cu $K_\alpha \lambda$ = 1.541 Å). A small amount of sample was placed on top of a flat sample plate and flattened, and scanned at a step size of 0.0217° 2θ, in the scan range of 5°–50° over 40 minutes.

Simulated XRD patterns were created using the CrystalMaker and CrystalDiffract software packages (http://crystalmaker.com). Where CIF files were available from the

Cambridge Structural Database (CCDC), these were used. Where there was no cif file deposited in this database, and no cif file could be found in the literature, unit cell structural models were built (as described below).

The CCDC references for the cif files used and the structures they describe are as follows: barbituric acid form I (CCDC reference: 857275), barbituric acid form II (CCDC reference: 250445), thiobarbituric acid form I (CCDC reference: 1270397), barbituric acid dihydrate (CCDC reference: 1106126), thiobarbituric acid hydrate (CCDC reference: 755268), $BA_{0.5}TBA_{0.5}$ (CCDC reference: 1498572), $BA_{0.7}TBA_{0.3}$ (CCDC reference: 149573).

In Chapter 7, experimental and simulated patterns were overlaid, and the unit cell parameters were changed in Crystal Diffract for a best fit of the simulated patterns to the experimental data. These unit cell parameters were updated in the cif files in Vesta, and these new cif files were used to index electron diffraction data in Chapter 7.

3.4 Unit Cell Structural Model Building and Simulated Diffraction Patterns

The *Pbcm* and *A2₁am* $C_{31}H_{64}$, and *C2/c, P2₁/c* and *P2/c* $C_{30}H_{61}OH$ unit cell models were built by extending the repeating pattern of carbon atomic coordinates in reported structures for shorter chain hydrocarbons. These space groups use Hermann-Mauguin notation (Burzlaff and Zimmermann, 2016). The first letter describes the arrangement of the unit cell, with *P* describing a primitive unit cell, and *A* and *C* describing a single face centred cell. The subsequent letters and numbers describe the symmetry elements in the unit cell. For example, *P2₁/c* can be broken down to a *2₁* screw axis along the *b*-axis, and a *c* glide plane perpendicular to the *c*-axis.

The *Pbcm* $C_{31}H_{64}$ structure was adapted from the structure for tricosane ($C_{23}H_{48}$) reported by Smith (Smith, 1953) by extending the carbon chain and maintaining C-C distances. The *A2₁am* $C_{31}H_{64}$ was in turn adapted from the carbon spacings in the *Pbcm* cell by shifting the atomic coordinates to the symmetric positions outlined for the alternative setting *Bb2₁m* by Lüth et al. (Lueth et al., 1974) followed by necessary axis adjustments. Lattice parameters were defined for the *Pbcm* and *A2₁am* unit cells using experimental data. The *C2/c* $C_{30}H_{61}OH$ structure was adapted from the structure for *n*-eicosanol ($C_{20}H_{41}OH$) reported by Michaud et al (Michaud et al., 2000). The *P2₁/c* $C_{30}H_{61}OH$ structure was adapted from the structure for 1-heptadecanol ($C_{17}H_{35}OH$) reported by Seto (Seto, 1962). The *P2/c* $C_{30}H_{61}OH$ structure was adapted from the Pbcm unit cell by reducing the space group symmetry and asymmetric substitution of the terminal C for O. The lattice parameters for the *P2₁/c* and *C2/c* unit cells were

calculated by extending the unit cells so that the previous C-C and O-O distances (in Å) were retained.

In order to carry out electron diffraction simulations to illustrate the effects of dynamical disorder, a simple model of unidirectional chain sliding for kinematical diffraction calculations was built. Toward this end, supercell structures of the $C_{31}H_{64}$ *$A2_1am$* were constructed to support fine-scale sampling of scattering vectors hkℓ in reciprocal space. First, the space group symmetry was reduced to *P1*. This unit cell was then extended along the b-axis by 10, 15, and 20 repeat unit cells using Vesta software. Chains were displaced along the c-axis by shifting the atomic coordinates of one molecule in the supercell by a set value smaller than the C-C bond distance (0.83 Å displacement along the c-axis, compared to 1.28 Å between adjacent carbon atoms along the c-axis). These structures represent the characteristic type of symmetry breaking in snapshots of molecular sliding motion. More complete simulations are possible with distributions of displacements and using dynamical scattering calculations (Eggeman et al., 2013). However, this simple model provides the necessary elements for reproducing the qualitative characteristics of the diffuse scattering arising from disorder in the form of unidirectional displacement.

For zone axis pattern simulations electron diffraction patterns were simulated using SingleCrystal, part of the CrystalMaker software. For patterns away from high symmetry zone axis orientations, electron diffraction patterns were simulated using the DiffSims package as part of Pyxem to incorporate effects of the Ewald sphere. Briefly, in Pyxem (version 0.11.0), diffraction is modelled by the intersection of the Ewald sphere (set by the beam energy) and a reciprocal lattice given by a unit cell (including the atom basis), where the finite extent of the reciprocal lattice sites are modelled by an allowed excitation error (accounting for the shape factor for thin, electron-transparent crystals). Intensities are modelled at each reciprocal lattice site by the kinematical intensity (square of the modulus of the structure factor) and modified according to the excitation error relative to the Ewald sphere for a given orientation of the sample relative to the electron beam. Crystal orientations in the simulations were defined by the unit cell direction [UVW] along the electron beam trajectory.

3.5 Critical Fluence Determination

Critical fluence values were assessed by recording a time-series of SAED patterns at constant electron flux (fixed beam current) to track the decay of Bragg spot intensity with cumulative electron fluence. SAED Bragg diffraction spot decay measurements were taken on the pure phase $C_{31}H_{64}$ and pure phase $C_{30}H_{61}OH$ samples and a binary

mixture of the two components with 50 % $C_{30}H_{61}OH$ in the “down-chain” orientation. Based on critical fluence values for paraffins with similar chain lengths reported in the literature, the electron beam flux was set up to support recording 20-30 data points containing observable diffraction intensities. All diffraction pattern series were acquired using the Titan^3 Themis 300 microscope. An electron beam flux of 0.03 $e^-/Å^2$ s at a fixed magnification was used giving a screen current of 0.076 nA. These values were calibrated using a Faraday cup. The cumulative electron fluence can be calculated by multiplying the time the sample has been exposed to the electron beam (in s) by the electron flux (*J*):

$$F(\mathrm{e}^-/\mathrm{Å}^2) = J \times (t_0 + t) \tag{3.5}$$

where *J* is the electron flux ($e^-/Å^2$ s), t_0 is the time representing the initial electron exposures including the time taken to record an initial image and an initial diffraction pattern (in s) and *t* is the subsequent acquisition time of the following time-series diffraction patterns (in s).

The critical fluence can be determined by assuming an exponential decay of diffraction intensity with accumulated fluence:

$$I = I_0 \exp(-\alpha F) \tag{3.6}$$

where *I* is the recorded intensity in a given time-series frame, I_0 is the initial intensity in the first frame, *F* is the cumulative fluence and α is the decay rate constant (s^{-1}). Taking the natural logarithm of the maximum intensity of the spots in each pattern linearizes the exponential relationship. The positive reciprocal of the gradient is then taken as the critical fluence.

3.6 Atomic Force Microscopy (AFM)

Atomic Force Microscopy (AFM) images were acquired using a Dimension FastScan-Bio (Bruker) on a Nanoscope V controller. Peak Force tapping in air was performed using ScanAsyst Fluid probes (Bruker) with a spring constant of approximately 0.60 N/m (probes were calibrated individually using the thermal noise method), a peak force amplitude of 150 nm, a setpoint of 1.2nN, a peak force tapping frequency of 1 kHz and scan rate of approximately 0.5-2 Hz, depending upon image size and resolution. Deflection sensitivity was calibrated on a sapphire sample prior to measuring the sample. Data were acquired in Quantitative Nanomechanical Mode, including the adhesion channel. Although tip radius was not calibrated (a nominal value of 5 nm was input) this does not affect any measurements presented. All data were processed and analyzed using Nanoscope Analysis 3.0. In order to preserve an accurate representation of the 3D terrace structure and subsequent line sections, the images

were initially levelled with a 0-order line fit (i.e., a DC offset) to eliminate z-drift between scan lines, and then flattened with a 1D plane-fit using a manually defined reference plane encompassing a single flat terrace region, made possible due to the inherent linearity of the FastScan scanner.

Samples were prepared for AFM analysis by drop casting the warm hexane solution onto mica sheets.

3.7 Differential Scanning Calorimetry (DSC)

Differential Scanning Calorimetry (DSC) is a thermal analysis technique used to study how a material absorbs or releases heat as its temperature is changed. In DSC, a sample and an inert reference are heated (or cooled) at the same controlled rate. The instrument measures the difference in heat flow between them. When the sample undergoes a physical or chemical change it absorbs or releases heat, producing a peak or shift in the DSC curve (Gill et al., 2010).

DSC measurements in Chapter 6 were performed with a Mettler Toledo DSC 1. 10 – 15 mg samples were placed in open aluminium pans, and the heating was carried out at 5 °C min^{-1} between 30 and 150 °C in an N_2 atmosphere.

DSC measurements in Chapter 7 were performed with a Mettler Toledo DSC 1. 10 – 15 mg samples were placed in open aluminium pans, and the heating was carried out at 10 °C min^{-1} between 60 and 300 °C in an N_2 atmosphere.

3.8 Thermogravimetric Analysis (TGA)

Thermogravimetric Analysis (TGA) is a technique used to measure changes in a material's mass as it is heated, cooled, or held at constant temperature under a controlled atmosphere. The sample is placed on a high-precision balance inside a furnace, and the weight of the sample is continuously recorded as temperature changes. Mass loss indicates processes such as decomposition or combustion (Zainal et al., 2021).

TGA measurements of the pure wax materials in Chapter 6 were performed with a Mettler Toledo TGA/DSC 3+. 10 – 15 mg samples were placed in open aluminium pans, and heating was carried out at 10 °C per minute between 30 and 500 °C in an N_2 atmosphere.

TGA measurements of pure TEHP and the TEHP exposed wax materials in Chapter 6 were performed with a Shimadzu TGA-50. 10 – 15 mg samples were placed in open aluminium pans and heating was carried out at 10 °C per minute between 30 and 500 °C in an N_2 atmosphere.

3.9 Nuclear Magnetic Resonance (NMR)

Nuclear magnetic resonance (NMR) spectroscopy is a non-destructive technique that provides information on the chemical structure and local environments of a compound by probing the magnetic properties of atomic nuclei in a very strong external magnetic field. Certain nuclei possess a nuclear spin and therefore a magnetic dipole moment. When placed in a strong magnetic field, these nuclei occupy discrete spin states. NMR detects transitions between these states, which occur at characteristic resonance frequencies for each type of nucleus. Some nuclei will have a nuclear spin of 0, and therefore not observable by NMR. Each observable nucleus absorbs energy at a frequency that depends on its local electronic environment. Variations in this frequency are described by the chemical shift (δ), which is measured relative to a standard reference compound such as tetramethylsilane (Veeman, 1997).

Nuclear magnetic resonance (NMR) spectra were recorded on a two-channel Bruker AV3HD NMR spectrometer operating at 9.4 T (400 MHz ^{1}H, ^{31}P) and equipped with a 5 mm BBO probe. Chemical shifts are reported in parts per million (ppm), referenced to the solvent. Prior to analysis, samples in Chapter 6 were dissolved in and referenced to $CDCl_3$, and samples in Chapter 7 were dissolved in and referenced to d6-DMSO.

3.10 Attenuated Total Reflectance-Infrared Spectroscopy (ATR-IR)

Attenuated Total Reflectance-Infrared Spectroscopy (ATR-IR) is a non-destructive technique where an infrared beam is directed into a crystal with a high refractive index (such as diamond used in this work). When the IR light reflects internally at the diamond and sample interface, it produces a wave that penetrates a few micrometres into the sample. Molecules within this penetration depth absorb specific IR wavelengths corresponding to their vibrational modes. The detector then measures the attenuated light, producing an IR spectrum characteristic of the sample's molecular structure and functional groups (Tiernan et al., 2020).

ATR-IR spectra were recorded on a Bruker Vertex 80v, fitted with a Bruker A225/Q Platinum ATR with a diamond crystal. The scan range was 4000-650cm^{-1}, 32 scans were taken per spectrum and the resolution was 4cm^{-1}. Powder and liquid samples were added to the stage directly.

3.11 Paraffin Wax Solubility in TEHP

The solubility of the two paraffin wax materials in TEHP was measured by using Crystalline, a crystallisation platform that uses a camera with up to 0.63 micrometres per pixel resolution to identify the presence of solids retained in a solution. Using this technique traces of 0.5 mg of solid wax in 8 mL of TEHP were still seen after ~30

minutes of agitation. 0.5 mg of material was then added to 20 mL of TEHP, where wax crystals could still be seen by eye.

3.12 Optical and Cross Polarised Microscopy

Optical microscopy uses the same fundamental principles as a TEM as both rely on the interaction of a source with a sample to form an image. However, optical microscopes use visible light as the illumination source and glass lenses to focus the beam, instead of electrons and electromagnetic lenses. As the wavelength of visible light is the limiting factor of resolution, maximum theoretical resolution is much higher in a TEM; 200 nm in an optical microscope using the wavelength of blue light in Abbe's equation, compared to maximum experimental resolution of ~0.02 nm in a TEM (discussed previously).

A polarising light lens (polariser) works by allowing only light oscillating in a specific direction to pass through. When this polarised light interacts with a sample, an anisotropic material can split it into two components, called the ordinary and extraordinary rays, traveling at different speeds in different directions. In contrast, an isotropic material has only one refractive index, so it does not alter the polarised light and both components continue at the same speed, remaining in phase. When this unchanged light encounters the analyser (the second polarising filter, oriented perpendicular to the first), it is blocked, and the material appears dark. Anisotropic materials such as crystalline polymers have several refractive indexes, so the two rays become out of phase with one another when interacting with the sample, and recombine to give a light signal (Wolman, 1975).

Particles that appear white against the background are optically anisotropic, and molecular crystalline materials are generally anisotropic. If the material was amorphous, or isotropic, then the particles would 'disappear' against the background (Dombrowski, 2013).

Samples for optical microscopy were prepared by measuring 4 mg of wax material onto a glass slide. When TEHP was added, a glass cover slip was added over the sample to aid spreading of the droplet, and to make the droplet thin enough to be able to image the wax crystals. Cross polarised light microscopy images were captured on an Olympus SZX10 Macro Stereo microscope with transmitted cross polarised light (SZX2-CPO) and an analyser lens was attached. Images were recorded with an Axiocam 305 camera, with a DF PLAPO 1X objective lens attached. Images were analysed in ImageJ. Particle size was measured using the Feret diameter (largest axis of the particle). Figure 1 shows an optical microscope image captured of $C_{31}H_{64}$ samples that have been exposed to TEHP. The measured Feret diameter is indicated

for individual particles. This approach was taken for measurement of all non-spherical particles.

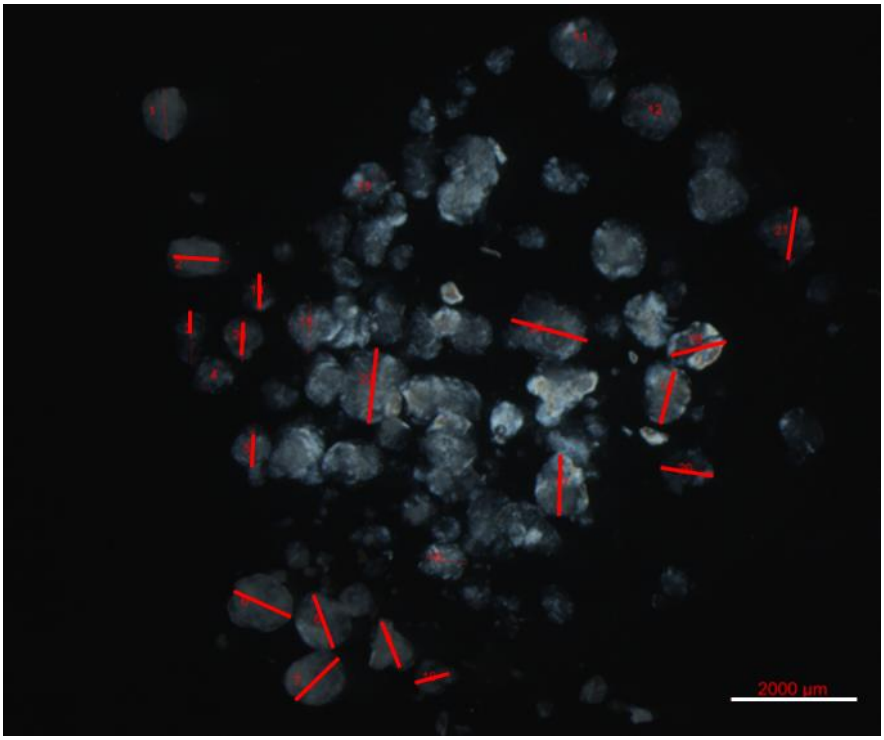

Figure 3.1: Optical microscope image captured of $C_{31}H_{64}$ samples that have been exposed to TEHP where individual particles are numbered and the Feret diameter indicated.

Chapter 4
Unit Cell Structure of Long Chain *N*-alkane and *N*-alcohol Hydrocarbons

4.1 Introduction

This chapter explores the crystalline structure of single-component $C_{31}H_{64}$ and $C_{30}H_{61}OH$ crystals, two common components found in the intracuticular wax layer of a leaf. In this chapter, conventional TEM, SAED, and AFM results are used to assess the crystal packing of these chains.

Currently, in the literature, there lies some ambiguity on which space groups long chain hydrocarbons, such as the ones studied in this chapter, pack in. Symmetry of long chain hydrocarbons is dependent on chain length, if the number of carbons in the chain is odd or even, and temperature (Lueth et al., 1974). For odd *n*-alkanes, shorter chains pack with monoclinic or triclinic symmetry, with chains with 11 or more carbons packing with orthorhombic symmetry. For even *n*-alkanes, chains pack with triclinic symmetry when $6 < n < 26$, and monoclinic symmetry when $n > 26$, where n = the number of carbons within a chain. Both odd and even *n*-alkanes exhibit a hexagonal phase just below the melting point (Atkinson and Richardson, 1969). In the hexagonal phase, molecules are packed in a hexagonal 2D lattice in the plane perpendicular to the *c*-axis, being rotationally disordered around their long chain axis. As the chains can rotate this phase is of higher symmetry than the orthorhombic, monoclinic or triclinic symmetry, which all have fixed rigid packing.

Even within these sub groups there lies some ambiguity, for example for odd *n*-alkanes with 11 or more carbons Smith reports a *Pbcm* symmetry (Smith, 1953), whilst Dorset reports an $A2_1am$ symmetry when prepared with a benzoic acid template (Dorset, 2002). Whilst these are both orthorhombic unit cells, there are distinct differences between the unit cells, which in turn affects the diffraction patterns observed. The critical fluence of these beam sensitive materials is determined from three different measurements to define the parameters for electron microscopy study and consider the mechanism of beam damage.

The wax crystals are prepared in two orientations, with chains perpendicular to the support film (parallel to the electron beam), denoted the ‘down-chain’ orientation, or with chains parallel to the support film (perpendicular to the electron beam), denoted the ’chains-flat’ orientation. Although many other orientations on surfaces are conceivable, these two selected orientations follow the symmetry of *n*-alkane and *n*-alkanol molecules in the solid state: the chains parallel to the electron beam offer a

unique view of the side-by-side packing of these chains, and the chains perpendicular to the beam presents one of several orthogonal perspectives to examine the key end-to-end packing of chains. Together, these two orientations provide an important set for initial investigations of the wax microstructure in pure *n*-alkanes, *n*-alkanols, and their binary mixtures in the next chapter.

The results in this chapter explore the specific space group and packing geometries of $C_{31}H_{64}$ and $C_{30}H_{61}OH$ crystals. Signatures of lamellar ordering are identified, signalling the key differences between $C_{31}H_{64}$ and $C_{30}H_{61}OH$ packing.

4.2 Symmetry of long chain alkanes

Pure, single-component even and odd *n*-alkanes exhibit distinct packing symmetries, with even *n*-alkanes favouring monoclinic unit cells and odd *n*-alkanes packing in orthorhombic symmetry (Nyburg and Potworowski, 1973). Even *n*-alkanes can pack more efficiently end-to-end with a higher packing density as the carbon at the start of the chain faces the opposite direction to the carbon group at the end of the chain, so the next neighbouring chain can pack closer. In the odd *n*-alkanes, the end groups face the same direction, so neighbouring chains cannot pack as closely as the even *n*-alkanes (Boese et al., 1999). With small amounts of impurities, however, even *n*-alkanes adopt orthorhombic packing which may explain the preponderance of orthorhombic forms with polyethylene-like domains in plant waxes (Ensikat et al., 2006). Odd *n*-alkanes with 11 or more carbons ($n \geq 11$) consistently adopt orthorhombic symmetry with distinct layers of chains, defined as lamellae. Reports of the space group odd *n*-alkanes pack with in the literature vary. Smith reported a structure solution for the $n = 23$ alkane (*n* carbon atoms) with *Pbcm* space group symmetry. In Smith's structure, the long chain end-to-end packing is along the *c*-axis such that mirror planes at $c/4$ and $3(c/4)$ coincide with the molecular mirror symmetry (Smith, 1953). Dorset, in contrast, has reported odd *n*-alkanes packing with $A2_1am$ symmetry when prepared with a benzoic acid epitaxial template to yield crystals with chains perpendicular to the electron beam in SAED (Dorset, 2002). In the $A2_1am$ unit cell, the long chains are likewise along the *c*-axis, but with the molecular mirror planes at $c/2$ and c. Figure 4.1 shows two unit cell structural models; a *Pbcm* and an $A2_1am$ $C_{31}H_{64}$ structure, built for this work by extending the repeating pattern of carbon atomic coordinates in reported structures for shorter chain hydrocarbons as there are no reported structures for $C_{31}H_{64}$ in the literature. The mirror planes for each respective structure as described above are indicated with red dotted lines.

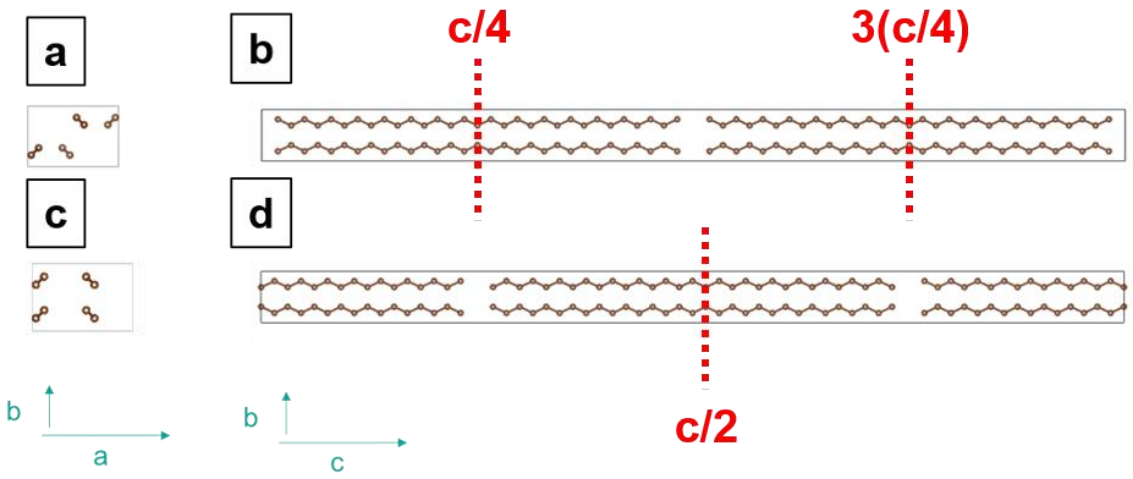

Figure 4.1: (a,c) Representation of carbon chain packing in $C_{31}H_{64}$ as seen by the electron beam in the 'down-chain' drop cast prepared orientation, the [001] direction for *Pbcm* (a) and *A2₁am* (c) symmetry. (b,d) Representation of carbon chain packing in $C_{31}H_{64}$ as seen by the electron beam in the 'chains-flat' epitaxially prepared orientation, the [010] direction for *Pbcm* symmetry (b) and the [100] direction for *A2₁am* symmetry (d). The *Pbcm* and *A2₁am* orthorhombic unit cells are defined by a = 7.44 Å, b = 4.93 Å, c = 82.59 Å.

The difference in chain packing is perhaps most noticeable in two visualizations, depicted in Figure 4.2. Firstly, when viewed along chains, i.e., along [001] and here denoted the 'down-chain' orientation, the offset between sequentially stacked chains differs. The green triangles added in Figure 4.2 highlight this chain offset difference, with the offset chain lying in the centre of this triangle in the *Pbcm* unit cell. Secondly, when viewed with the chains flat, i.e., perpendicular to [001] in these orthorhombic unit cells and here denoted the 'chains-flat' orientation, the sequential chains along the *c*-axis in the *A2₁am* structure are rotated by 180°.

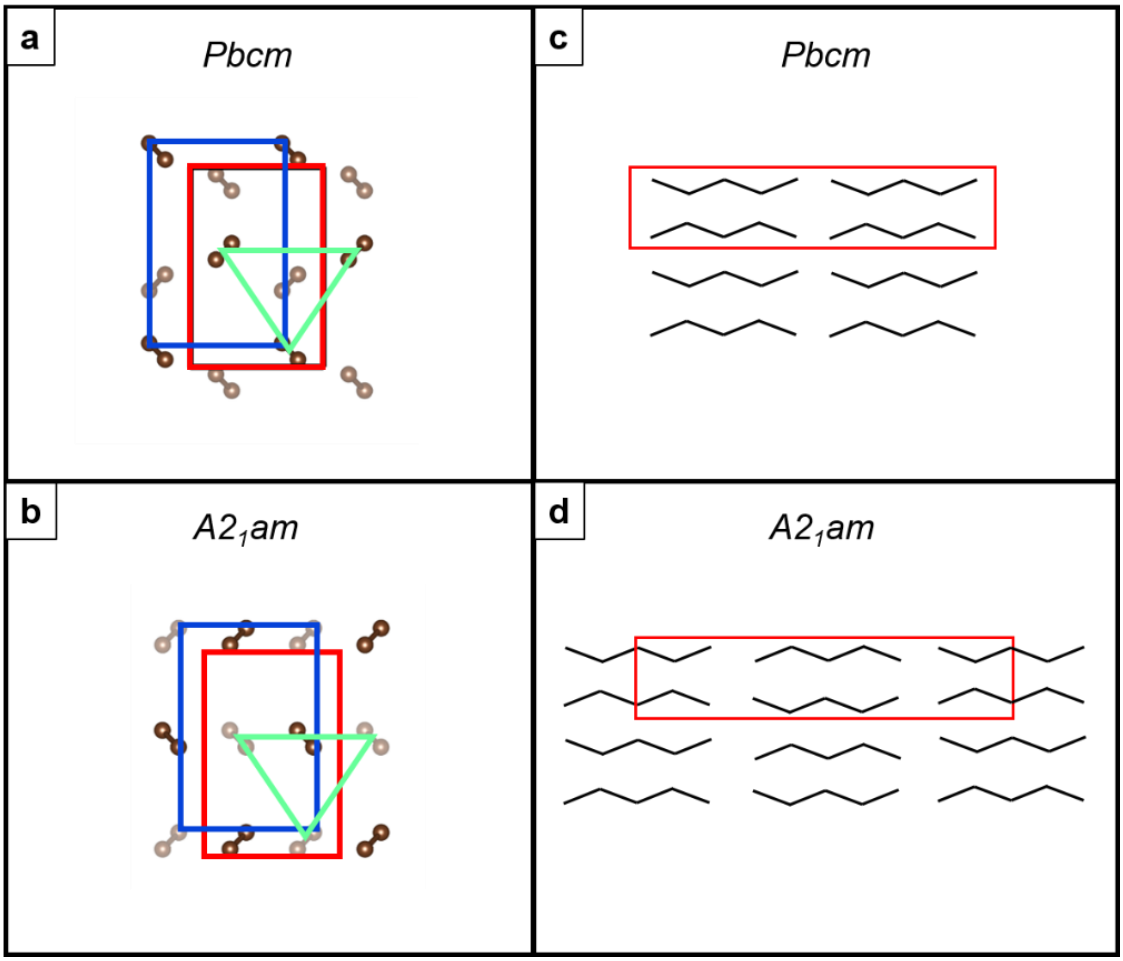

Figure 4.2: (a,b) Representation of carbon chain packing as seen by the electron beam in the 'down-chain' orientation, the [001] direction, for the alkane packed with (a) *Pbcm* symmetry and (b) *A2₁am* symmetry. (c,d) Representation of carbon chain packing as seen by the electron beam in the 'chains-flat' orientation for the alkane packed with (c) *Pbcm* symmetry ([010] direction) and (d) *A2₁am* symmetry ([100] direction). The red boxes indicate the unit cell for the indicated space group symmetry, and the blue boxes indicate the polyethylene type cell. The green triangles show the gap that forms between chains in neighbouring lamellar layers. Alternate chains are faded to represent the offset of chains in real space in neighbouring lamellar layers.

Irrespective of the precise unit cell for alkane lamellae, additional disordered states have been identified with chains slipping across lamellar regions giving rise to "nematic" phases (Dorset, 1999). Earlier XRD analysis by Lüth (Lueth et al., 1974) provides further evidence of this general characteristic, where longitudinal molecular disorder within individual lamellae was proposed to compensate co-packing of dissimilar chain lengths (Dorset, 2000b). These "nematic" phases draw parallels with the 'brick and mortar' model proposed for the structure of the IW layer comprised of both ordered and disordered regions.

Electron diffraction is highly sensitive to this chain ordering, particularly for crystals oriented with chains perpendicular to the electron beam, or equivalently with ‘chains-flat’ on the support film of a TEM grid. In this latter orientation, if the chains pack with nematic ordering, then the 0kℓ diffraction pattern strongly resembles that of polyethylene, with the $\{011\}_{PE}$ reflections consisting of a single, dominant spot (Figure 4.3a-b). Here, the subscript PE denotes the polyethylene sub-cell, and $\ell_{PE} = 1$ coincides with $\ell = n + 2$ for n carbons (Dorset, 1999), (Douglas L Dorset, 1997). When the chains pack with defined lamellae, then the diffraction pattern will contain additional reflections arising from the interlamellar spacing around the strong polyethylene type reflections (Figure 4.3c-e), with the $\{01\ell\}$ for $\ell = n$ particularly pronounced. However, the size and shape of regions with lamellar ordering and their position relative to nematic phases within wax crystals remain obscured by diffraction analysis without coordinated real-space imaging. This ordering concept is investigated further in Chapter 5.

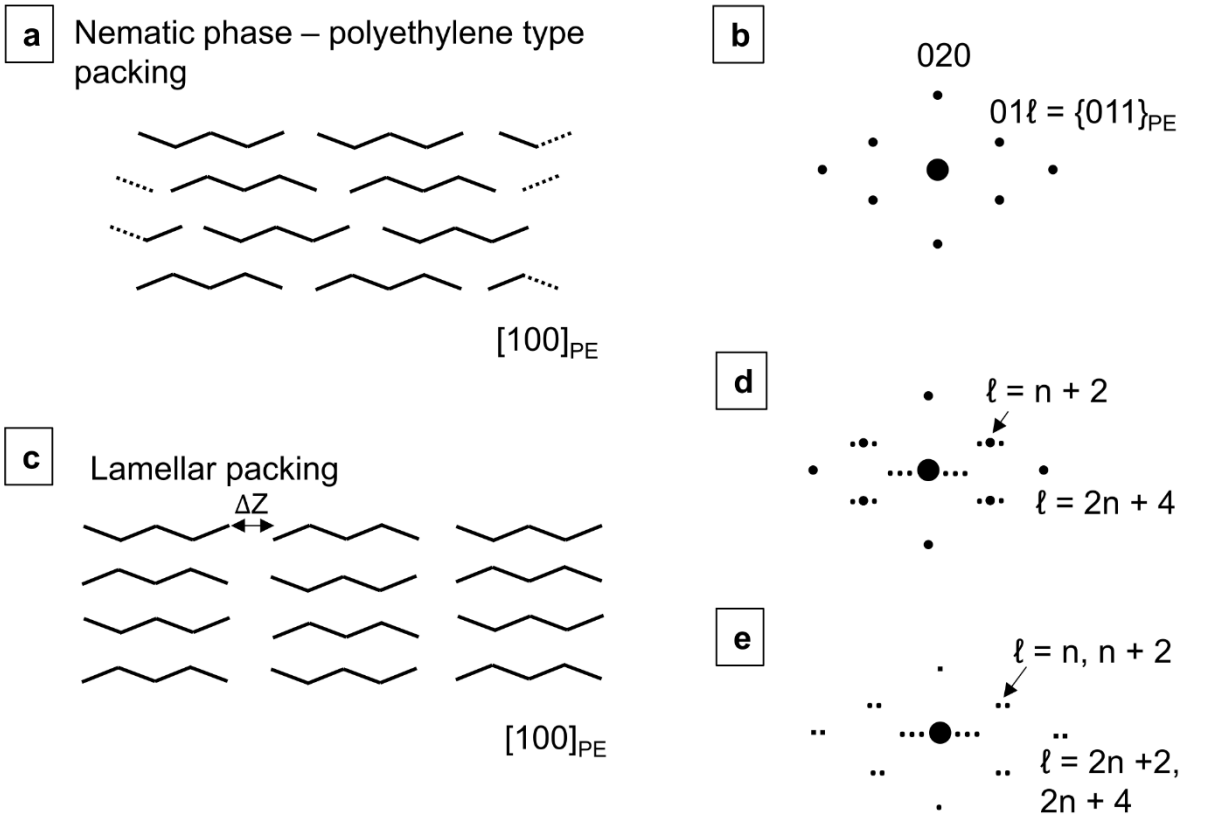

Figure 4.3: Representation of the *n*-alkane nematic phase shown with carbon chain packing in the 'chains-flat' orientation. (b) A schematic representation of the corresponding electron diffraction pattern exhibits a polyethylene-like arrangement of spots with no splitting of the 01ℓ peaks. (c) Representation of *n*-alkane packing with lamellar ordered shown with carbon chains packing in the 'chains-flat' orientation. (d), (e) Schematic representations of the electron diffraction patterns for two cases: (d) If the interlayer spacing is an integer multiple of the half zig-zag repeat in the carbon chain, with the distance between lamellae defined as $\Delta Z = 3(c_{PE}/2)$ for polyethylene sub-cell c-parameter c_{PE}, then the diffraction pattern will contain lamellar reflections with a strong single maxima. (e) If $\Delta Z \neq 3(c_{PE}/2)$, then the 01ℓ polyethylene reflections split into two reflections.(Dorset, 1999)

4.3 Symmetry of long chain alcohols

Long chain primary alcohols (*n*-alkanols) are known to pack differently to the *n*-alkanes. A key distinction arises from the asymmetry of the chain end containing the alcohol moiety. The alcohol groups form a hydrogen bonding network at one end of the chains, driving alcohol-alcohol interactions as a guiding organizational principle for *n*-alkanol crystallization. Typical packing motifs are described by either a monoclinic γ form (*C2/c* unit cell), a "staircase" packing with chain ends offset rather than aligned, (Cuevas-Diarte and Oonk, 2021), or by a monoclinic β form with the chain ends aligned in lamellae but with *gauche* conformations at the chain ends to accommodate a hydrogen bonding network between the terminal alcohol groups ($P2_1/c$ unit cell) (Seto,

1962). Dorset has proposed long chain alcohols may also pack in an orthorhombic β form, with similar structural characteristics to the *n*-alkanes (Dorset, 1979). A *P2/c* unit cell was built following the *Pbcm* structure of the *n*-alkanes to model these characteristics. These structural models, built from previous reports on shorter *n*-alkanols, can be viewed in Figure 4.4 and provide an overview of the key functional group interactions and resulting packing motifs possible in $C_{30}H_{61}OH$. In the 'down-chain' orientation (Figure 4.4a,c,e) all considered structures exhibit packing as in the polyethylene sub-cell (blue boxes), albeit with a variety of displacements similar to differences between the *Pbcm* and $A2_1am$ *n*-alkane unit cells. This approach of building the unit cell was taken instead of a more classical approach such as using single crystal XRD (SCXRD) to solve the structure. SCXRD determination would be difficult to do on these wax materials as SCXRD can only be used for large, high-quality single crystals without large disorder and defects (Li and Sun, 2017). Defects are commonly found in these materials (Pham et al., 2025), and disorder is found within these systems as discussed further below. Distinct lamellae, units of chain packing with distinct gaps between layers, are visible in the β form unit cells, (Figure 4.4d, 4.4f), whereas these are not seen in the γ form due to the offset of chains in the staircase packing (Figure 4.4b).

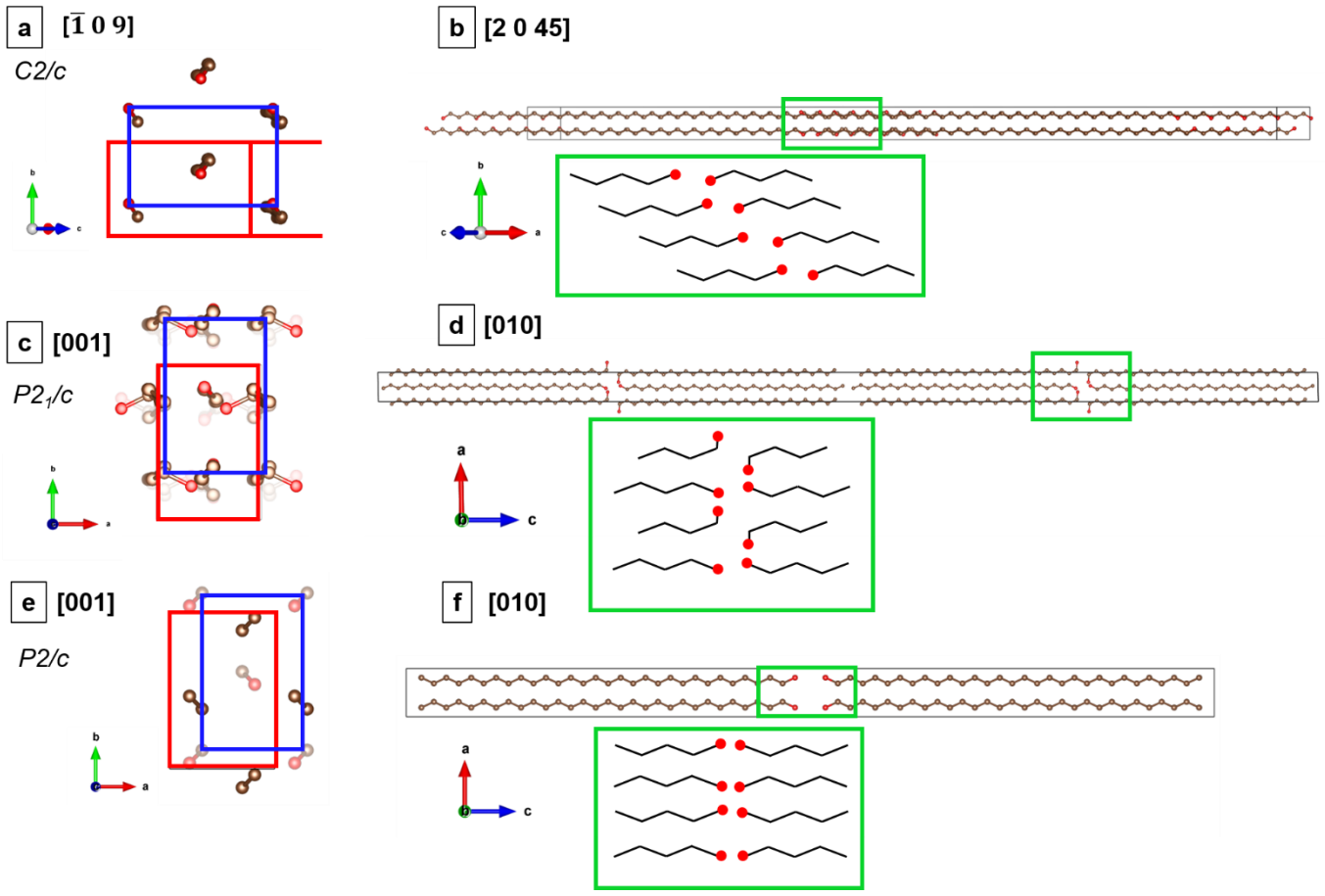

Figure 4.4: (a,c,e) Representation of carbon chain packing as seen by the electron beam in the 'down-chain' drop cast prepared orientation, the [$\bar{1}$ 0 9] for *C2/c* symmetry (a), and the [001] direction for *P2₁c* (c) and *P2/c* symmetry (e). (b,d,f) Representation of carbon chain packing as seen by the electron beam in the 'chains-flat' epitaxially prepared orientation, the [2 0 45] direction for *C2/c* symmetry (b), and the [010] direction for *P2₁c* (d) and *P2/c* symmetry (f). The green boxes contain simplified representations of the chains highlighting the packing at the chain ends, where the red circles represent the alcohol group. The *C2/c* monoclinic unit cell is defined by a = 132.91 Å, b = 4.93 Å, c = 9.00 Å, β = 93.01°. The *P2₁/c* monoclinic unit cell is defined by a = 5.03 Å, b = 7.40 Å, c = 160.77 Å, β = 91.18 °. The *P2/c* orthorhombic unit cell is defined by a = 4.96 Å, b = 7.42 Å, c = 82.59 Å. The red boxes indicate the unit cell in the chains down orientation, and the blue boxes indicate the polyethylene type cell.

4.4 Transmission Electron Microscopy

4.4.1 Critical fluence

The critical fluence of a material is a measurement to quantify the sensitivity of a sample to the electron beam. The critical fluence value is an important factor in the design of electron microscopy experiments for soft matter due to the material damage caused by the electron beam. To study the structure of these materials using electron microscopy techniques, the critical fluence of the material must first be determined to

consider their sensitivity to the electron beam, so a diffraction pattern with structural information can be obtained. Phenomenologically, beam damage has been observed to follow an exponential decay (Henderson and Glaeser, 1985). The wax materials are known to be very beam sensitive in comparison to inorganic materials such as copper phyhalocyanine (Egerton, 2019) and calcite (Hooley et al., 2017) due to the weaker bonds in organic materials making beam damage mechanisms such as radiolysis more likely. Critical fluence values for loss of crystallinity were therefore calculated to aid in setting up experiments at a known amount of damage and to acquire data in such a way that key diffraction information would not be lost. A critical fluence, C_F, is defined as the rate of exponential decay of a particular signal (in this case diffraction spot intensity), or the total number of electrons per unit area irradiating the sample when the intensity of a feature drops to e^{-1} (~ 37 %) of the initial maximum intensity. This decay can be defined by the following Equation 4.1:

$$I = I_0 \exp(-\tau D) \tag{4.1}$$

for intensity I and cumulative fluence or dose D and decay rate τ at $I/I_0 = 1/e$ where I_0 is the original, unirradiated signal intensity.

The intensity values are extracted from a diffraction pattern dose damage series, where the intensity of a Bragg spot is measured over a series of diffraction patterns to determine the decay and therefore the materials critical fluence i.e. the characteristic measure of damage or beam induced crystallographic disorder. When the natural log of the intensities is plotted against fluence, the critical fluence can be determined by taking the positive reciprocal of the gradient from the linear fit of the plot formed. The example seen in Figure 4.5a shows an example of where a first order Bragg spot for a $C_{31}H_{64}$ crystal has decayed in an exponential fashion (linearized). However, the spots do not always decay in a perfect decreasing linear fashion when normalised, with an initial increase in intensity in the first few recorded diffraction patterns sometimes observed (Figure 4.5b). S'Ari et al. have observed this phenomenon in other organic crystals, and attributed this initial increase to reorientation of the crystal on the grid to zone axis orientation, with the reorientation induced by the electron beam (S'Ari et al., 2018), and this has also been observed in organic polymers (Grubb, 1974).

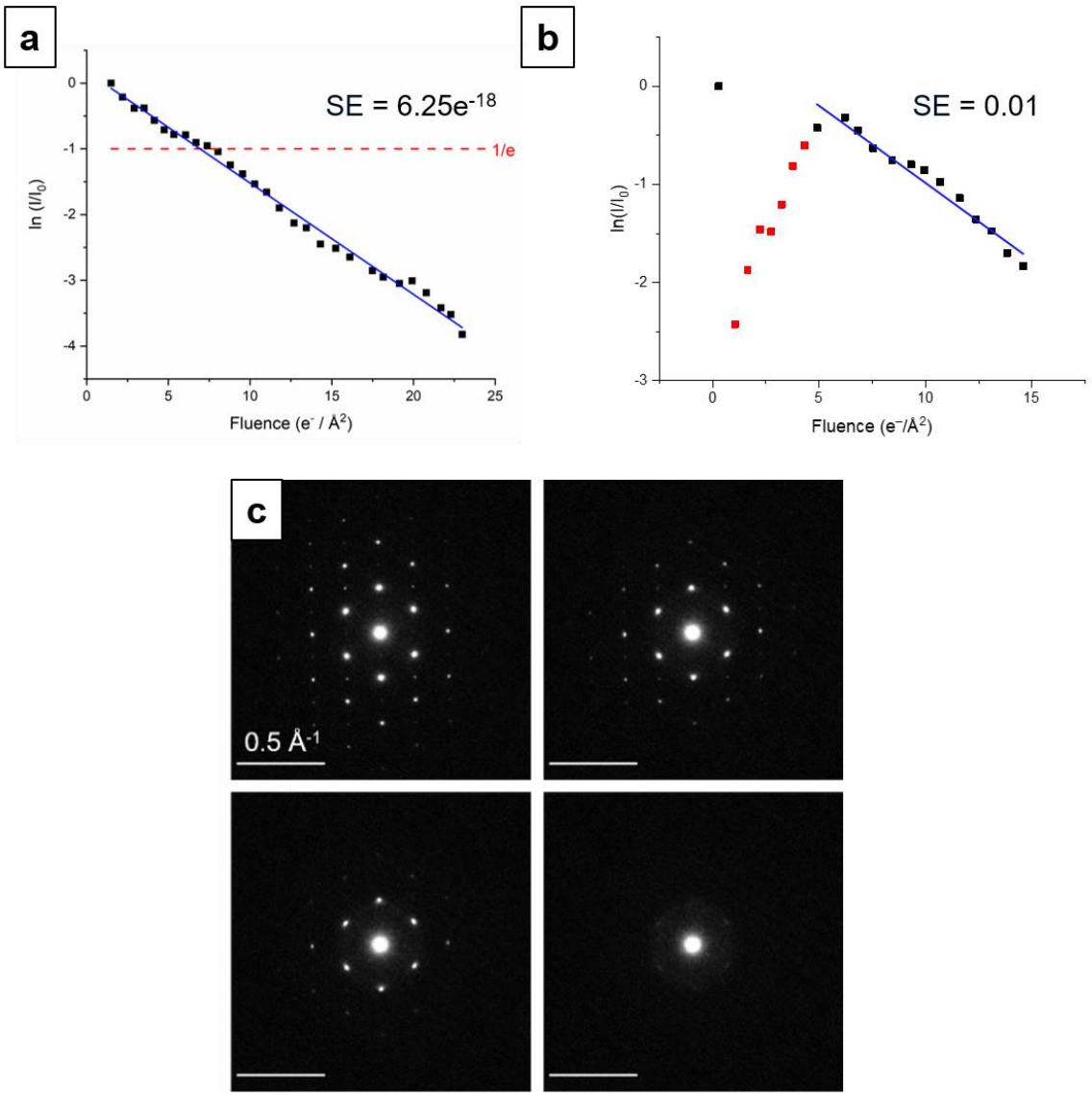

Figure 4.5: A plot of the natural log of the decay of the normalised intensity of a diffraction spot versus total accumulated fluence, with an as expected linear decay (a) and with an initial increase in intensity due to crystal reorientation (b) with standard errors in each individual measurement. The decay of Bragg spots as seen in captured diffraction patterns (c). C_F values (Table 4.1) calculated from gradient of linear fit (blue). This is fit to Equation 4.1.

Variables such as temperature and accelerating voltage (kV) affect critical fluence measurements. A higher accelerating voltage gives the electrons in the electron beam a higher energy, and if this energy is higher than the displacement energy of the atoms in the material, atoms can be directly displaced or knocked-on (Egerton, 2012). However, at lower accelerating voltages, radiolysis becomes a primary damage mechanism. This is due to the ionisation cross section for inelastic scattering having an inverse relationship with this accelerating voltage, so atoms are more likely to be displaced by radiolysis at lower accelerating voltages (Egerton, 2013). A lower temperature also reduces the effects of radiolysis, which can be explained by reduced

atomic mobility at lower temperature (Egerton, 1980). The method of determination of the critical fluence, whether viewed by decay of a diffraction spot, or an element peak in an EELS spectrum, also has an effect on the measured value (Li and Egerton, 2004). This difference arises from the fact that diffraction patterns measures destruction at long-range order and EELS peaks measure destruction at short-range order and these different properties of the material, such as the intramolecular bonds and molecular packing, have different characteristic damage rates. The value for critical fluence is therefore dependent on kV, temperature, specimen thickness and the method used to measure the critical fluence. Critical fluence measurement experiments can be designed to extract the information needed for dose budgeting and temperature optimisation for whichever measurement is needed from a sample.

Table 4.1: Critical dose or fluence of electrons (C_F) ($e^-/Å^2$) that produces significant damage to the structure of these synthetic waxes as monitored by SAED Bragg diffraction spot decay, SED Bragg diffraction spot decay and as monitored by integrated intensity regions of interest from high angle regions of the SED. Uncertainties are given as the standard error estimated from replicate measurements across several reflections within a diffraction pattern and across multiple crystals.

Sample	C_F SAED	C_F SED	C_F vADF
n-hentriacontane ($C_{31}H_{64}$)	5.5 (± 0.7)	15.1 (± 0.7)	250 (± 80)
1-triacontanol ($C_{30}H_{61}OH$)	6 (± 2)	10.9 (± 0.9)	230 (± 30)

Table 4.1 shows the determined values for the pure phase $C_{31}H_{64}$ and $C_{30}H_{61}OH$ and a 50:50 binary mixture of the two components as monitored by SAED Bragg diffraction spot decay, SED Bragg diffraction spot decay and as monitored by integrated intensity regions of interest from high angle regions of the SED. Whilst this chapter does not contain any SED data analysis (see Chapter 5), the SED critical fluence is reported here to be able to compare values obtained by the two techniques. C_F values determined from SAED measurements show the alkane and alcohol end member phases have values within the order of 10^1 $e^-/Å^2$. These calculated values match previous reported values of the critical fluence for paraffin waxes (Choe et al., 2020). Uncertainties estimated from replicate measurements are reported in Table 4.2 with standard errors generally below 1 $e^-/Å^2$ with the exception of {020} reflections in

$C_{30}H_{61}OH$. These appear at higher scattering angle than {110} and {200} reflections; reflections at higher scattering angles decay more rapidly and therefore contribute fewer data points for a fixed flux. These reflections were chosen as these reflections had the highest intensity in the initial diffraction patterns, so the decay could be tracked.

Table 4.2: Calculated standard deviation and standard error for each method and sample. Standard error is calculated by dividing standard deviation by $\sqrt{N}$. Measurements are taken from individual spots within the same diffraction pattern and across multiple crystals. The measurements are grouped by the d-spacings of the scattering vectors corresponding to the planes {hkl}. *N* is the number of measurements and *d* is the d-spacing of the set of lattice planes.

Method	**Sample**	***d*** **(Å)**	**{hkl}**	**Critical fluence average** **(e^-/ Å²)**	**Standard Deviation** **(e^-/ Å²)**	***N***	**Standard Error** **(e^-/ Å²)**
SAED	n-hentriacontane ($C_{31}H_{64}$)	4.3	{110}	7.1	3.2	28	0.6
		3.9	{200}	5.4	3.1	16	0.8
		2.2	{020}	5.5	1.6	10	0.5
		1.9	{400}	4.1	1.2	2	0.8
	1-triacontanol ($C_{30}H_{61}OH$)	4.3	{110}	8.3	1.8	16	0.5
		3.9	{200}	6.4	1.4	8	0.5
		2.2	{020}	4.5	4.9	2	3.5
SED	n-hentriacontane ($C_{31}H_{64}$)	4.3	{110}	14.5	1.8	4	0.9
		3.9	{200}	14.4	0.6	2	0.5
		2.2	{020}	16.4	1.0	2	0.7

	1-triacontanol ($C_{30}H_{61}OH$)	4.3	{110}	10.0	0.7	8	0.2
		3.9	{200}	11.0	1.5	4	0.7
		2.2	{020}	11.7	3.8	4	1.9
vADF	n-hentriacontane ($C_{31}H_{64}$)	-	-	247	110	2	80
	1-triacontanol ($C_{30}H_{61}OH$)	-	-	226	43	2	31

C_F values calculated from SED measurements were slightly higher than the values calculated by SAED. The area illuminated by the beam in SED (7 nm^2, 3 nm diameter) was calculated to be smaller than the pixel size (7.7 nm at 100 kx magnification and 3.8 nm at 200 kx). It is important to note the beam is not a perfectly uniform flat-disk, with the profile of an Airy disk and intensity sharply peaked in the centre with tails of rippling intensity (Bustillo et al., 2021). The dose per frame was calculated to be 5.3 $e^-/Å^2$ at 300 kV, with a semi-angle of 0.8 mrad, a probe current of 1 pA and a dwell time of 600 µs. As the area illuminated by the beam was calculated to be smaller than the pixel size, the whole sample is not being exposed to the same fluence so this result would be expected. If the probe was larger than the pixel size, this would be called ‘oversampling’ where the probe has sampled overlap, causing extra damage to the areas doubly exposed (Bustillo et al., 2021). This minor exposure difference may be causing the difference in critical fluence value seen. A recent paper by Egerton discusses the idea that there is a “dose-dependence point spread function”, where in STEM more electrons are concentrated in the middle of the probe, and therefore that area is damaged most, and some tail electron fluence, where less damage occurs (Egerton and Watanabe, 2022). The combination of these two effects may explain the difference in SAED and SED critical fluence values, but as they are still within the same order of magnitude (10^1) these subtleties do not have a significant effect for the design of experiments for these waxes as it is still essential care is taken to minimise exposure of the sample to the electron beam.

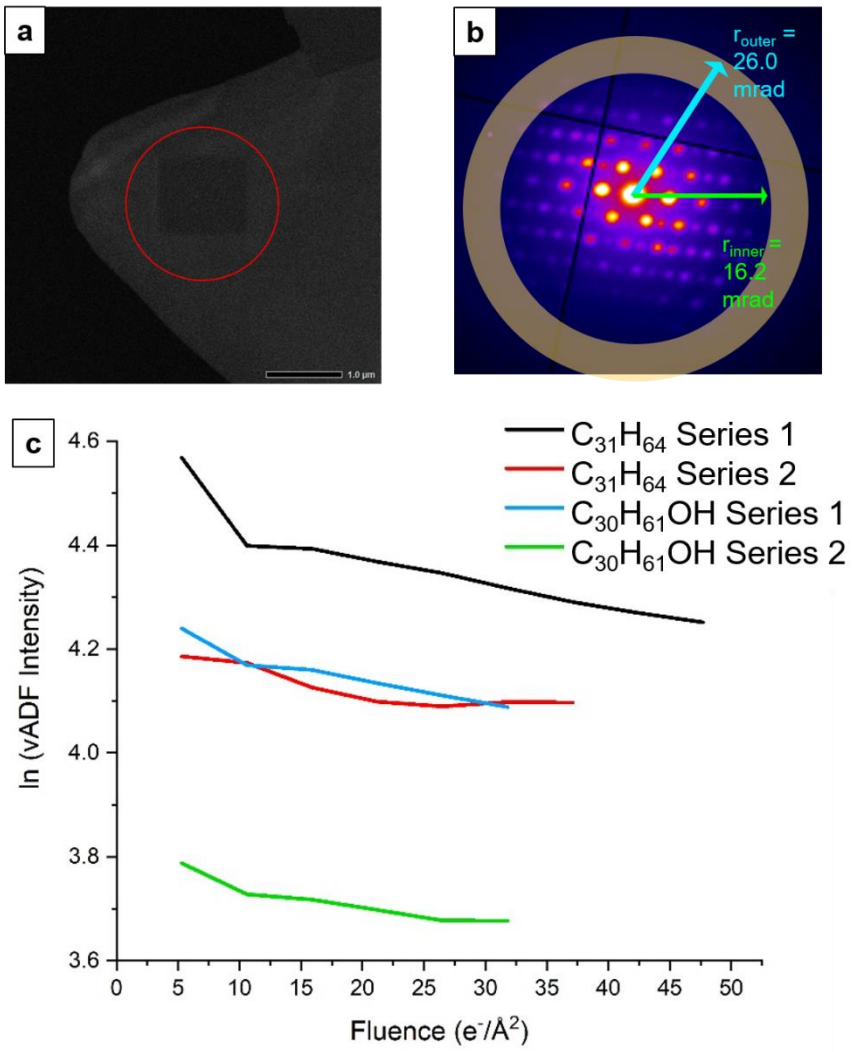

Figure 4.6: (a) Image showing darker rectangular areas (circled in red) where the beam had probed in earlier measurements. (b) Visualisation of the virtual aperture detector regions placed on the average diffraction pattern for these measurements. (c) Average intensity of a vADF image plotted against fluence.

Figure 4.6a shows a crystal after successive SED measurements were taken. This is an ADF-STEM image taken at a lower magnification than the SED measurements were taken, so the darker rectangle indicates the area the probe scanned in the subsequent SED measurements. The observation of dark regions, circled in red, left behind where the beam had scanned implied the sample had become thinner, due to mass loss, in these regions. Mass loss occurs within organic materials when the electron beam induces electron excitation within each molecule and the de-excitation may not return the molecule to its original electronic state, causing chemical bond breakage (Egerton and Rauf, 1999), (Egerton et al., 2004). If this bond breakage leads to the formation of volatile products, this results in mass loss. Mass loss is particularly potent in light atoms such as hydrogen and oxygen, for example voids formed from hydrogen gas formation within a vitrified sample (Koniuch et al., 2023). However, the

C-C bond has been found to be much more resistant to radiation than the C-H bond (Stenn and Bahr, 1970). The average intensity of a vADF was plotted against fluence, and the C_F vADF intensity values presented in Table 4.1 were determined. The angles of the inner and outer apertures were defined as 16.2 mrad and 26.0 mrad respectively for the vADF detector, as illustrated in Figure 4.6b. These angles span a range beyond the angles of strong Bragg scattering in these wax samples.

An exponential decay was also seen in these profiles (shown on a natural logarithm scale in Figure 4.6c), suggesting the beam damage mechanism has an element of mass loss. Isaacson (Isaacson, 1979) states that the dose required for mass loss and composition change in an organic material is usually greater than the dose which gives diffraction-pattern fading (loss of long-range order), as it requires greater reorganisation and therefore greater energy. For the waxes measured here, the vADF C_F values are far larger, an entire order of magnitude, than the values calculated through measurement of the Bragg reflection intensity which agrees with Isaacson. Mass loss most likely occurs from the surface of the material, so damage in the 'bulk' of the crystals is not seen, which could be why this mechanism of damage is much slower. It may take more energy to form volatile products from the breakage of the C-C bond, the main component of both chains, so mass loss is slower.

As the Bragg reflection decay is the fastest, we infer that loss of structural order is the rate determining damage step, and the damage to the sample caused by the electron beam can be concluded to be mainly due to disruption in crystal symmetry, and not complete volatilization of the material. The beam sensitivity of these materials has been previously managed by cooling to liquid helium temperatures (Zemlin et al., 1985) and cooling to cryogenic temperatures using liquid nitrogen as a coolant has been shown to reduce radiolytic mechanisms at these lower temperatures, and volatilization of damaged products is also reduced (Egerton, 1980). Further work could therefore include an SED dose damage study at these temperatures. If this mass loss was not seen at lower temperatures, it would suggest that the low temperature had stabilised the sample to this radiolytic beam damage mechanism, and therefore the mass loss is not a result of this primary mechanism.

4.5 Bright field imaging and selected area electron diffraction

After determining the critical fluence of the materials, experimental data were collected on the $C_{31}H_{64}$ and $C_{30}H_{61}OH$ crystals. Figure 4.7 presents conventional TEM analysis of single-component $C_{31}H_{64}$ and $C_{30}H_{61}OH$ crystals. The crystals were prepared following established procedures (Wittmann et al., 1983) to produce crystals either with chains perpendicular to the support film (parallel to the electron beam), denoted

the ‘down-chain’ orientation, or with chains parallel to the support film (perpendicular to the electron beam), denoted the ’chains-flat’ orientation. To prepare the samples in the ‘down-chain’ orientation, 1 mg of $C_{31}H_{64}$ / $C_{30}H_{61}OH$ was dissolved in 60 µL of warm hexane, and 2 µL of this supersaturated solution was drop cast onto an individual grid. The ‘chains-flat’ samples were prepared using a co-templating method, by melting the wax samples with benzoic acid in a glass slide “sandwich”. The benzoic acid was washed away with water, and the wax samples collected on the EM grids. The benzoic acid directed the chains to orient epitaxially. The direction of chain growth was validated through SAED pattern collection and observation. Measurements were taken under ‘low-dose’ conditions to minimize beam damage to the samples, due to similar long chain alkanes undergoing significant damage at low electron fluence (Choe et al., 2020). To achieve ‘low-dose’ conditions, the parallel beam illumination was spread to just enough to see the sample, at the lowest magnification in the SA range. Exposure to the electron beam was also minimised by beam blanking when not actively collecting data. Bright field (BF) TEM images in Figure 4.7 show contrast arising primarily from diffraction, with darker regions reflecting greater diffraction. Contrast also arises from mass-thickness contrast. Crystals formed in a ‘down-chain’ orientation exhibited well-defined facets with commonly observed facet angles of ~109° (angles outlined by red lines in Figure 4.7a-b). Additional dark and light ripples across the crystals were attributed to bend contours, specific regions of the crystal where bending on the support film modifies the diffraction condition. A darker region near the top edge of Figure 4.7b arises from where multiple crystals are lying on top of one another, and due to mass-thickness contrast the thicker region will appear darker. The corresponding SAED patterns showed a set of four equidistant spots within a consistent set of six strong lowest-angle reflections (Figure 4.7e-f), showing two perpendicular mirror planes marking out two principal symmetry axes between the $(110)_{PE}$ and $(200)_{PE}$ reflections in a hexagonal pattern. These first order reflections can be indexed with respect to the polyethylene cell as $(110)_{PE}$, with a d-spacing distance of ~4.3 Å, and $(200)_{PE}$, with a d-spacing distance of ~3.9 Å, where PE denotes the polyethylene cell. The patterns were therefore indexed to the $[001]_{PE}$ zone axis, i.e., with the electron beam direction parallel to $[001]_{PE}$. The corresponding crystal facets were indexed to $\{110\}_{PE}$ planes, suggesting a facet angle of approximately 113°, broadly consistent with the 109° angle measured from the bright field TEM image.

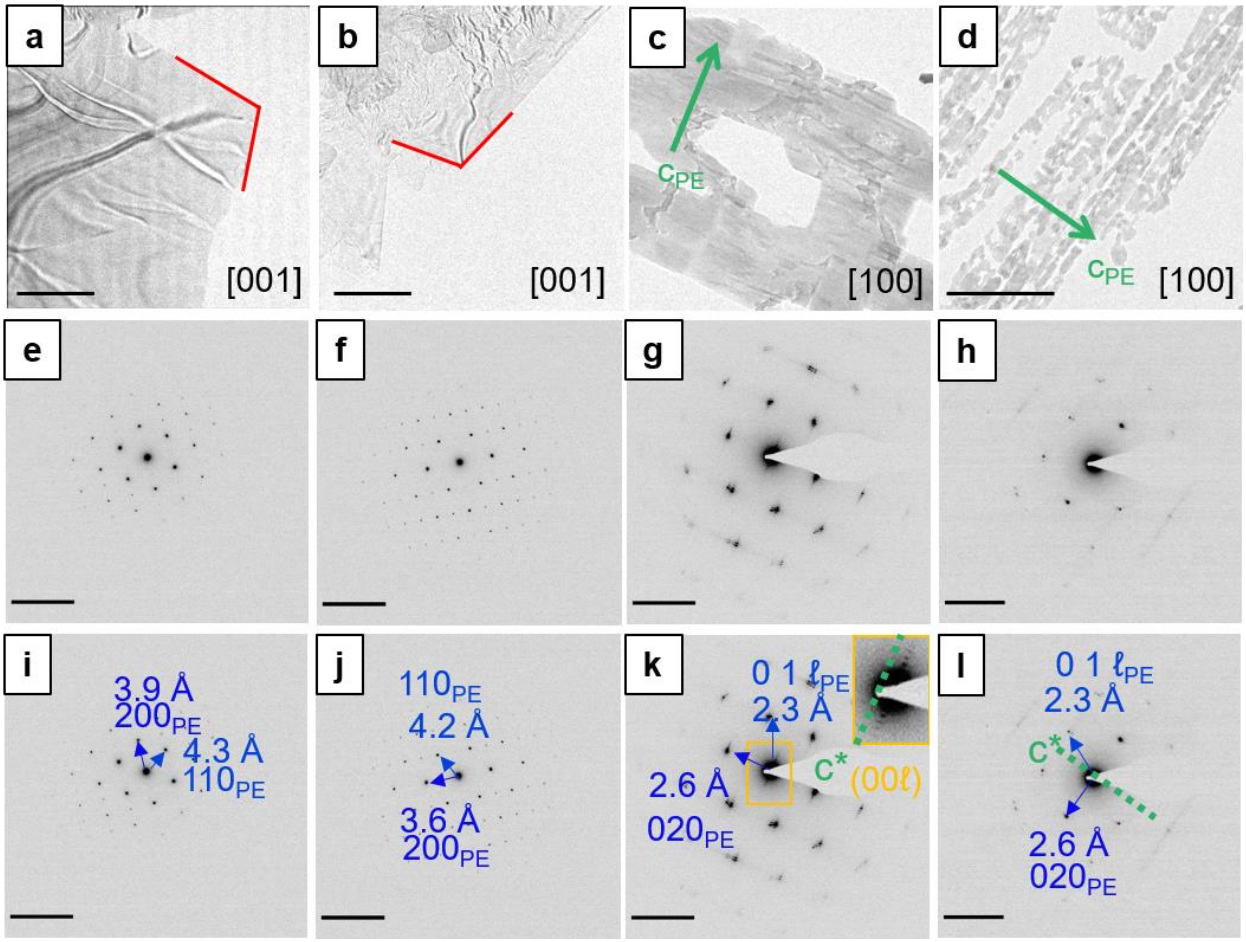

Figure 4.7: (a)-(d) Bright field (BF) TEM images and (e)-(h) SAED patterns for (a,e) $C_{31}H_{64}$ prepared to align the alkane chains parallel to the electron beam ('down-chain' orientation), (b,f) $C_{30}H_{61}OH$ prepared in the 'down-chain' orientation, (c,g) $C_{31}H_{64}$ prepared to align alkane chains perpendicular to the electron beam ('chains-flat' orientation), and (d,h) $C_{30}H_{61}OH$ prepared in the 'chains-flat' orientation. Red lines indicate the measured facet angles. Green arrows indicate the *c*-axis direction (alkane chain axis) following the polyethylene cell (c_{PE}). Arrows overlaid on the SAED patterns mark the indexation of the patterns to the PE cell in the $[001]_{PE}$ 'down-chain' orientation and the $[100]_{PE}$ 'chains-flat' orientation. The inset in (g) shows an expanded section of the SAED pattern marked by the yellow box in (g), with the c^*_{PE} reciprocal lattice direction of the *c*-axis marked by the green dashed line. The zone axes indicated in a-d indicate the zone axes in the corresponding diffraction patterns in the respective columns. BF image scale bars indicate 2 µm. SAED pattern scale bars indicate 0.5 Å^{-1}.

Crystals formed in a 'chains-flat' orientation were prepared via a co-melt templating method to direct the crystallization of the hydrocarbons epitaxially on excess benzoic acid. These crystals appear as thin films with a rectangular or block type shape (Figures 4.7c-d). SAED patterns from these crystals (Figure 4.7g-h) showed strong reflections at d-spacings of 2.6 Å, assigned to the $(020)_{PE}$ spacing, and 2.3 Å, assigned to $(011)_{PE}$ or equivalently (01ℓ) reflections with $\ell = n + 2$ for n atoms (C + O) in the

chain. These two strong reflections are indicative of orthorhombic packing in polyethylene (Dorset and Moss, 1983) and paraffin waxes (Ensikat et al., 2006).

The patterns were therefore indexed to the $[100]_{PE}$ electron beam direction. Figures 4.2 and 4.4 highlight the visibility of end-to-end alkyl chain packing in the considered space group symmetries for *n*-alkanes (*Pbcm* and *$A2_1am$)* and *n*-alkanols (*C2/c, $P2_1/c$, and P2/c*). The long axis of the chains (*c*-axis in the PE and all *n*-alkane unit cells) coincides with the short length of the approximately rectangular film blocks (green arrows, Figure 4.7c-d).

The SAED patterns were indexed to the specific unit cells for $C_{31}H_{64}$ and $C_{30}H_{61}OH$. As discussed, for $C_{31}H_{64}$, there remains some ambiguity in the preceding literature on whether the alkane chains adopt *Pbcm* or *$A2_1am$* space group symmetry. If the alkane chain packs with *$A2_1am$* symmetry, the (110) reflections should be symmetry forbidden when viewed along [001]. The appearance of these reflections in our data may suggest the ‘down-chain’ samples exhibit *Pbcm* space group symmetry rather than the *$A2_1am$* packing reported by Dorset. The (110) reflections are symmetry allowed in *Pbcm* whereas very similar spots can be seen in simulated SAED patterns for the *$A2_1am$* structure when viewing down the [011] axis (Figure 4.8c). This axis is only a small 3° tilt from the [001] axis. Notably, both orientations closely resemble SAED patterns reported by Dorset and colleagues.

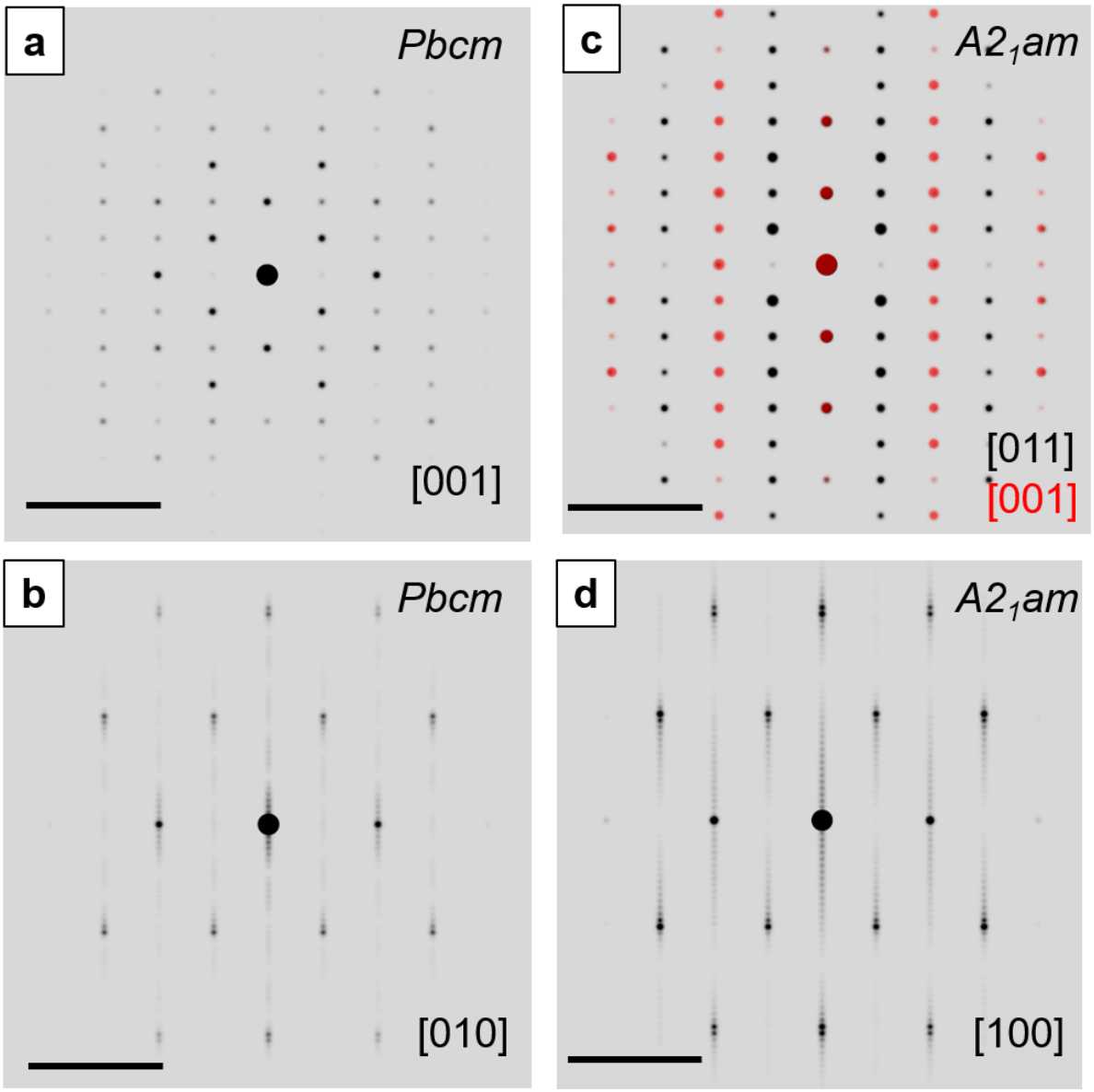

Figure 4.8: Simulated diffraction patterns for $C_{31}H_{64}$ with *Pbcm* symmetry (a,b), $C_{31}H_{64}$ with *A2₁am* symmetry (c,d). Diffraction patterns corresponding to the 'down-chain' orientated chains are found in (a,c) and diffraction patterns corresponding to the 'chains-flat' orientated chains are found in (b,d).

The patterns simulated from the *Pbcm* [001] direction and the *A2₁am* structure [011] direction are not readily distinguishable. The appearance of strong bend contours (Figure 4.7a-b) indicates there is some variation in the crystal orientation across the field of view, perhaps explaining this 3° tilt from zone axis and so contributions from *A2₁am* {111} reflections cannot be excluded. In either case, these crystals are in the 'down-chain' orientation.

A similar ambiguity in the literature surrounds long chain alcohol packing. A monoclinic γ-form unit cell for $C_{30}H_{61}OH$ (see also Figure 4.4) was constructed following the solved structure for γ-form n-eicosanol (Michaud et al., 2000)·(Ventolá et al., 2002).

The unit cell (Figure 4.4b) has lattice parameters a = 132.9 Å, b = 4.9 Å, c = 9.0 Å, and β = 93.0° and exhibits staggered chain ends or 'staircase' packing. The $C_{30}H_{61}OH$ SAED pattern can be indexed to the [$\bar{1}$ 0 9] direction in this crystal packing (Figure 4.9). However, if the chains were to pack with this staircase symmetry, a crystal sitting flat on a solid support (as used here in TEM and AFM) would not appear in the 'down-chain' orientation as the chains would be tilted relative to a planar support. The experimental observation of such a 'down-chain' orientation suggests the chains pack with more defined lamellar, end-to-end packing, as in the alkane. This arrangement would resemble the known monoclinic β-form ($P2_1/c$ space group symmetry), such as that reported by Seto for $C_{17}H_{35}OH$, (Seto, 1962), or an orthorhombic β-form, as suggested by Dorset (Dorset, 1979). Accordingly, $C_{30}H_{61}OH$ β-form unit cells were built (see also Figure 4.4). The $C_{30}H_{61}OH$ SAED pattern is indexed to the [001] direction in both of these structures (Figure 4.9). The intensities of the $(110)_{PE}$ type reflections in the $P2_1/c$ simulated SAED pattern have a lower intensity than the $(200)_{PE}$ reflections (Figure 4.9c), which matches the measured experimental intensities for these reflections in Figure 4.7f. The $P2_1/c$ unit cell, therefore, appears to offer the best unit cell description of the 'down-chain' $C_{30}H_{61}OH$ crystals.

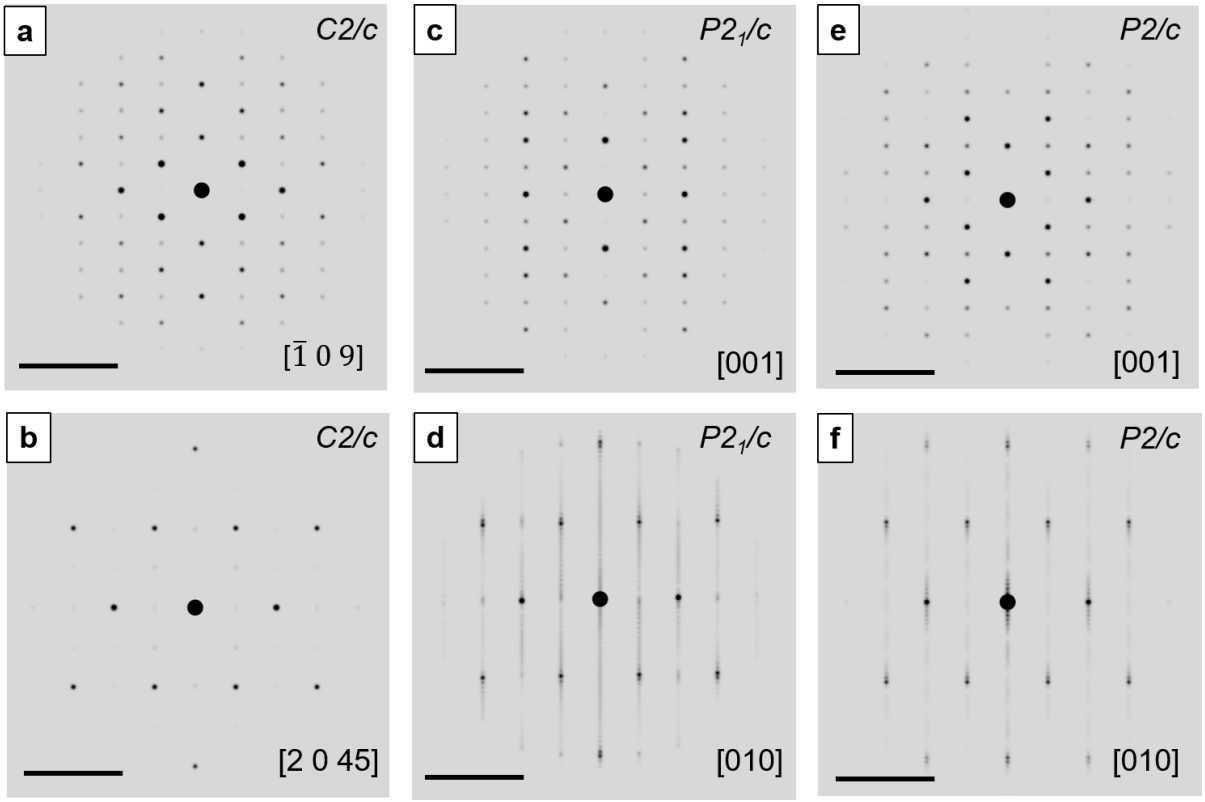

Figure 4.9: Simulated diffraction patterns for $C_{30}H_{61}OH$ with *C2/c* symmetry (a,b), *$P2_1c$* symmetry (c,d) and *P2/c* symmetry. Diffraction patterns corresponding to the 'down-chain' orientated chains are found in (a,c,e) and diffraction patterns corresponding to the 'chains-flat' orientated chains are found in (b,d,f).

Turning to the 'chains-flat' orientation, SAED patterns from $C_{31}H_{64}$ crystals were indexed to the *A2₁am* unit cell unambiguously. Figures 4.8b and 4.8d show simulated patterns using the *Pbcm* and *A2₁am* structures viewed along $[010]_{Pbcm}$ and $[100]_{A21am}$, respectively. At first glance, these patterns appear very similar in terms of symmetries and interplanar spacings (d-spacings). Inspection of simulated patterns overlaid on top of the experimental SAED patterns from $C_{31}H_{64}$ crystals, however, reveals marked differences (Figure 4.10).

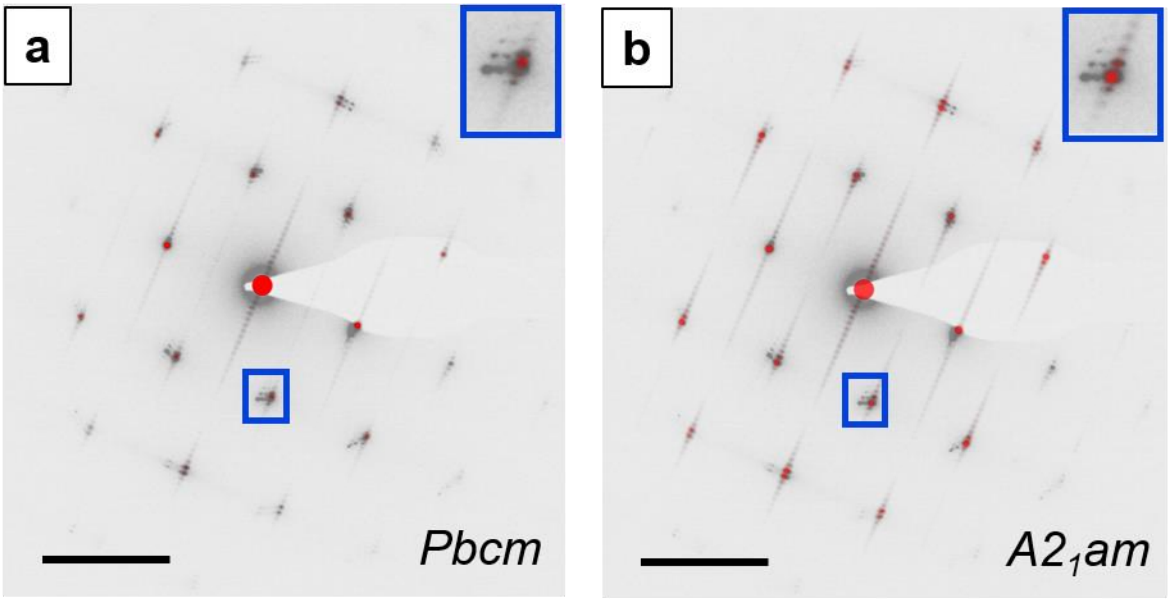

Figure 4.10: Simulated diffraction patterns (red) overlaid on experimental data for the 'chains-flat' orientated $C_{31}H_{64}$ chains. Insets show the magnified 01ℓ spots. The *Pbcm* simulated pattern is the [010] zone axis, and the *A2₁am* simulated pattern is on the [100] zone axis.

In the *Pbcm* pattern, the 01ℓ reflection appears as a single strong peak at ℓ = 32. In the *A2₁am* pattern, the 01ℓ reflection splits into two strong peaks at ℓ = 31 and ℓ = 33, in agreement with previous reports by Dorset and colleagues of strong reflections at ℓ = *n* and ℓ = *n* + 2 for *n* carbons in the alkyl chain (Dorset, 1995b). Whereas the simulated SAED pattern for the *A2₁am* unit cell matches the experimental pattern, the simulated SAED pattern for the *Pbcm* unit cell shows a spot midway between the two experimental intensity maxima (Figure 4.10). The crystals prepared in the 'chains-flat' orientation are therefore assigned to the *A2₁am* space group and the patterns were indexed to the $[100]_{A21am}$ zone axis (Figure 4.11g).

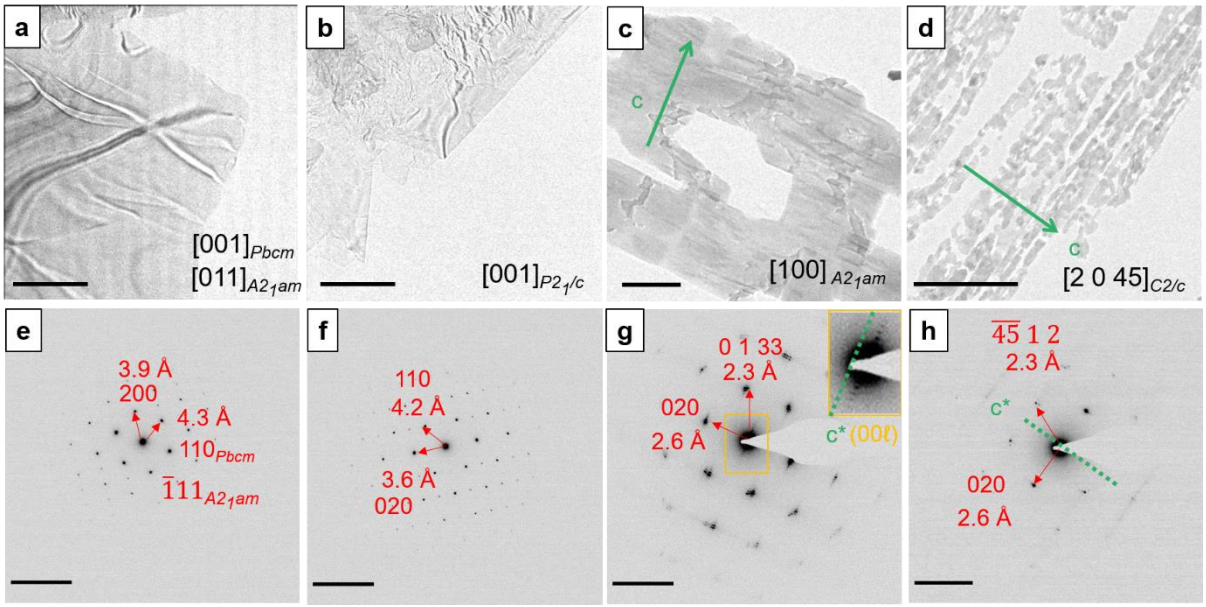

Figure 4.11: (a)-(d) Bright field (BF) TEM images and (e)-(h) indexed selected area electron diffraction (SAED) patterns for (a,e) $C_{31}H_{64}$ prepared to align the alkyl chains parallel to the electron beam ('down-chain' orientation), (b,f) $C_{30}H_{61}OH$ prepared in the 'down-chain' orientation, (c,g) $C_{31}H_{64}$ prepared to align alkyl chains perpendicular to the electron beam ('chains-flat' orientation), and (d,h) $C_{30}H_{61}OH$ prepared in the 'chains-flat' orientation. Green arrows indicate the *c*-axis direction (alkyl chain axis) following the polyethylene cell (c_{PE}). The inset in (g) shows an expanded section of the SAED pattern marked by the yellow box in (g), with the c^*_{PE} reciprocal lattice direction marked by the green dashed line. Arrows overlaid on the SAED patterns mark the indexation of the patterns to the labelled respective indexed orientation. BF image scale bars indicate 2 µm. SAED pattern scale bars indicate 0.5 $Å^{-1}$.

It is possible that benzoic acid templating induces a different molecular packing arrangement to the packing arising from solution crystallization. However, these results focus on the observation of lamellar ordering only visible in the 'chains-flat' orientation, and the changes induced by the incorporation of $C_{30}H_{61}OH$ in like-for-like samples.

Figure 4.11g shows 00ℓ spots around the central beam for $C_{31}H_{64}$ crystals, further confirming the 'chains-flat' crystals exhibit lamellar layers with well-ordered end-to-end packing. If well-ordered end-to-end packing was not seen, then these 00ℓ spots would be absent (Figure 4.3). Dorset and colleagues have noted the relative intensity of these spots as a marker of deviations from well-ordered lamellae in favour of nematic phases (Dorset, 1999). These spots are notably mostly absent in the SAED patterns of $C_{30}H_{61}OH$ in the 'chains-flat' orientation (Figure 4.11h).

Based on the $C_{30}H_{61}OH$ *C2/c* unit cell with 'staircase' packing, the 00ℓ are expected to be absent. This is because in this arrangement of chains, there are no defined lamellae when viewing the 'chains-flat' direction due to the overlapping of chains lying behind.

The experimental data shows good agreement with a simulated diffraction pattern from the $C_{30}H_{61}OH$ *C2/c* unit cell oriented along [2 0 45], confirming the chains lie flat on the support film in these samples. This orientation was found through rotating the simulated structure to the 'chains-flat' orientation. The 'staircase' offset in the chain ends explains the loss of 00ℓ packing, similarly to the smaller chain offsets in the nematic phases in *n*-alkanes. Weak 00ℓ spots were observed in a single example of a 'chains-flat' $C_{30}H_{61}OH$ crystal (Figure 4.12).

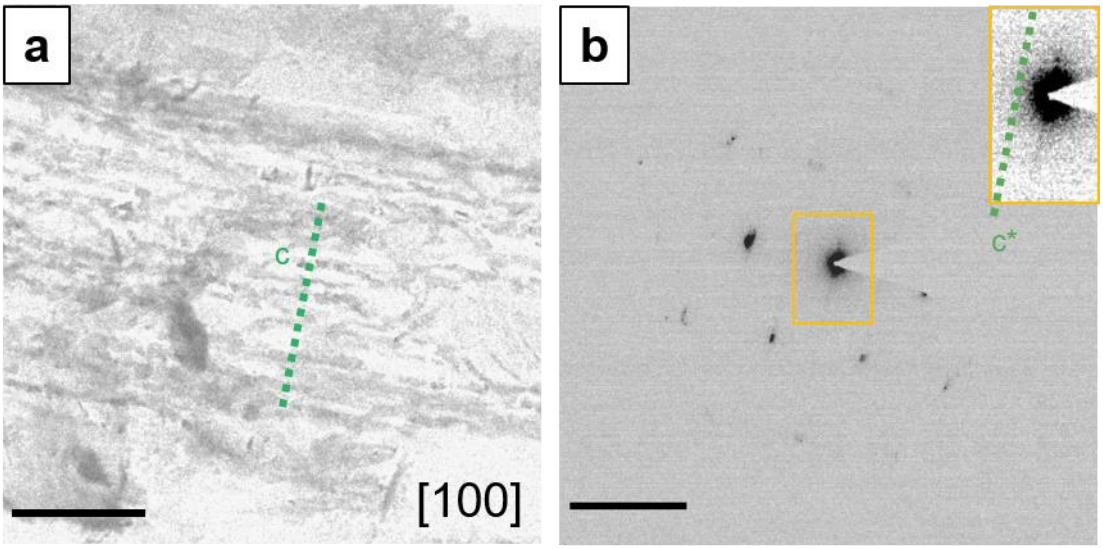

Figure 4.12: A BF image of $C_{30}H_{61}OH$ flat chain epitaxially prepared crystals and the corresponding SAED pattern showing an example of 00ℓ spots. The BF image scale bar indicates 2 μm and the diffraction pattern scale bar indicates 0.5 $Å^{-1}$.

The simulated patterns for 'chains-flat' for the *P2/c* and $P2_1/c$ unit cells both suggest the presence of 00ℓ spots as these unit cells have a higher degree of symmetry than seen in the *C2/c* unit cell due to the defined lamellae giving a higher number of repeated positions through the unit cell. As with the alkane, it may be the benzoic acid templating induces a different molecular packing arrangement to solution crystallization. Alternatively, the lack of 00ℓ spots in most alcohol SAED patterns may be due to disordered chain packing in the form of nematic phases derived from the *P2/c* and $P2_1/c$ unit cells (as opposed to ordered staircase packing). This is particularly true given that 00ℓ spots were not universally observed in 'chains-flat' $C_{31}H_{64}$ crystals either, despite all unit cell descriptions establishing lamellar packing as the preferred molecular packing arrangement in the *n*-alkanes.

Lines of diffuse scattering along 0*k*ℓ for $\ell = 2n + 2$ (perpendicular to row of 00ℓ spots) were observed in both the $C_{31}H_{64}$ and $C_{30}H_{61}OH$ SAED patterns (Figure 4.11). This diffuse scattering intensity is consistent with observations previously reported on other *n*-alkanes by Dorset (Dorset, 1985b). This diffuse scattering is absent in kinematical

diffraction simulations of unit cell models as it can be broadly attributed to disorder. This question is pursued further in Chapter 5.

A model was built to illustrate how chain displacement in this structure contributes to the diffuse scatter signal. Figure 4.13a shows a simple model where one chain has been displaced in a supercell structure consisting of 10 repeat unit cells. This structure was built by reducing the space group symmetry of the $A2_1am$ structure to *P1* and extending in the b direction. Figure 4.13c shows the resultant simulated diffraction pattern where a singular chain displacement has been applied for three supercell structures consisting of 10, 15 and 20 repeat unit cells. The applied chain displacement is small, with the entire chain shifting a distance less than the length of one C-C bond. In this simulation, the diffuse streaks can be seen perpendicular to the 00ℓ lines, and can be compared to the lack of diffuse streaks in the simulated diffraction pattern of the 'perfect' supercell in Figure 4.13b. In a more complicated system, with several chain displacements, there would be an increase of this diffuse scatter signal. This shows how this disordered structure model is valid, and that diffuse scatter being present is the result of chain displacement within the crystal structure.

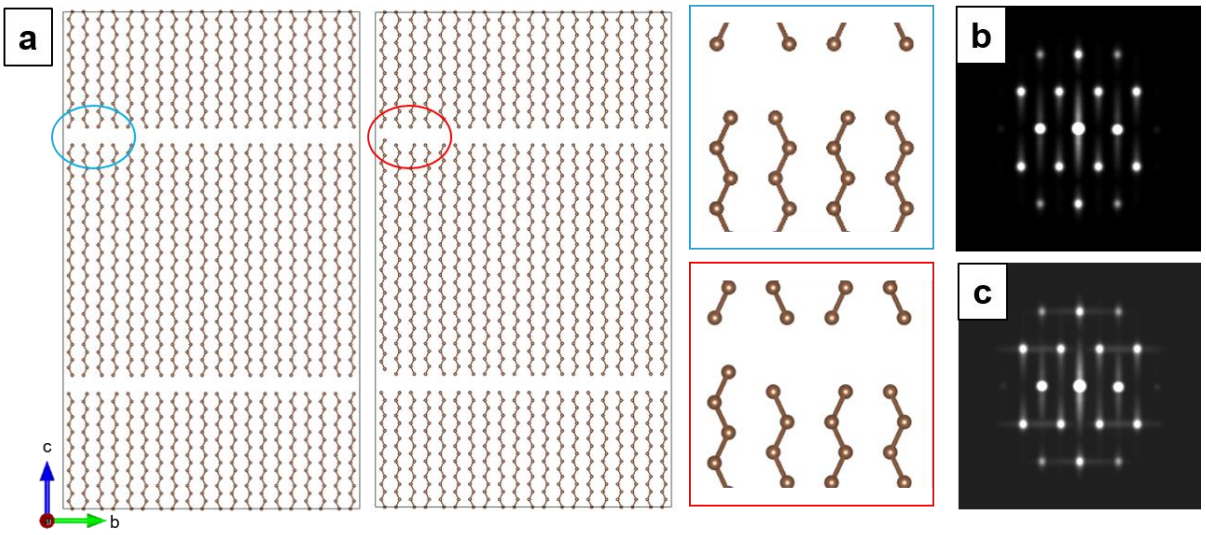

Figure 4.13: (a) A built supercell structure extended in the b direction with 10 repeat unit cells, with a 'perfect' supercell on the left, and a supercell with a displaced chain on the right. The blue and red circled regions have been enlarged to clearly show the displaced chain. (b) A simulated diffraction pattern of the 'perfect' supercell, where 00ℓ spots can be seen around the central beam. (c) Three simulated diffraction patterns overlaid, from supercell structures with 10, 15 and 20 repeat unit cells with one chain displaced. In this diffraction pattern, diffuse scatter (perpendicular to the 00ℓ spots) can be seen as a result of this chain displacement. These diffraction patterns were simulated in Pyxem.

As the d-spacings for the $C_{31}H_{64}$ and $C_{30}H_{61}OH$ chains are very similar, it was not possible with the resolution of the microscope to distinguish between the two chains

using electron microscopy techniques alone, meaning additional techniques must be utilised. This is particularly important when exploring the binary mixtures of the two chains in the next chapter.

4.6 Atomic force microscopy

To further probe the unit cell structural models for $C_{31}H_{64}$ and $C_{30}H_{61}OH$, atomic force microscopy (AFM) on each single-component crystal was carried out. AFM allows the measurement of surface forces such as adhesion by measuring the force between the tip attached to the cantilever and the said surface (Burnham et al., 1990). A fluid probe was used in tapping mode to obtain the data, with all data processed and analysed using Nanoscope Analysis 3.0. In this tapping mode, almost all lateral forces are eliminated, leading to less damage for soft matter materials (Wang et al., 2003). Figure 4.14 presents height and adhesion images obtained for $C_{31}H_{64}$ and $C_{30}H_{61}OH$ crystals. Terracing, defined by plateaus of equal height steps, can be seen in both samples. Adhesion mapping of $C_{31}H_{64}$ and $C_{30}H_{61}OH$ show pronounced differences between the alkane and the alcohol. $C_{31}H_{64}$ crystals exhibit a consistent, flat adhesion value across the detected terrace structures, with reduced adhesion at step edges due to the lower tip-sample contact area in regions of high curvature (Figure 4.14b). $C_{30}H_{61}OH$ crystals, however, show patches of two different adhesion values across many terrace structures (Figure 4.14e).

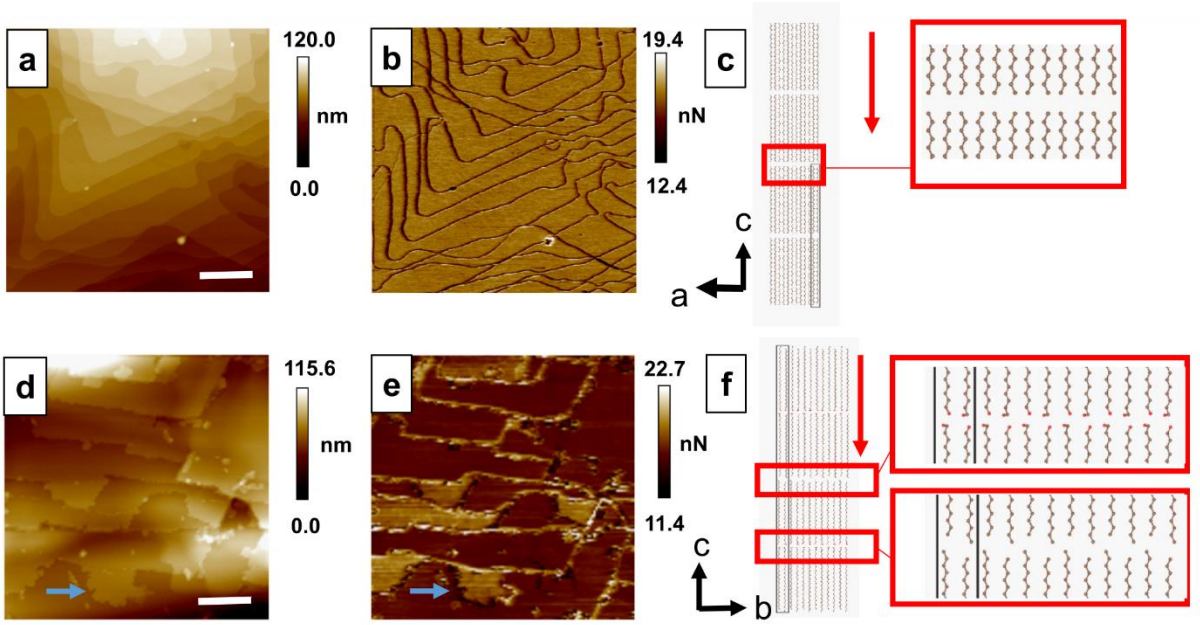

Figure 4.14: Height (a,d) and adhesion profiles (b,e) obtained through AFM for 'chains-down' $C_{31}H_{64}$ (a-c) and $C_{30}H_{61}OH$ (d-f) crystals. Blue arrows indicate a region in the $C_{30}H_{61}OH$ crystal where a height change corresponds to an adhesion change in their respective plots. 'Chains-down' unit cell representations of $C_{31}H_{64}$ (c) and $C_{30}H_{61}OH$ (f) chains with a red arrow to indicate the viewing direction of the AFM probe. Magnified sections show the differences in end-to-end chain packing in the alkane vs alcohol. Scale bars indicate 1 µm.

These AFM images of $C_{31}H_{64}$ crystals also confirmed that crystals formed in the 'down-chain' orientation exhibited well-defined facets with facet angles of ~109° and 65° (Figure 4.15), consistent with BF-TEM images.

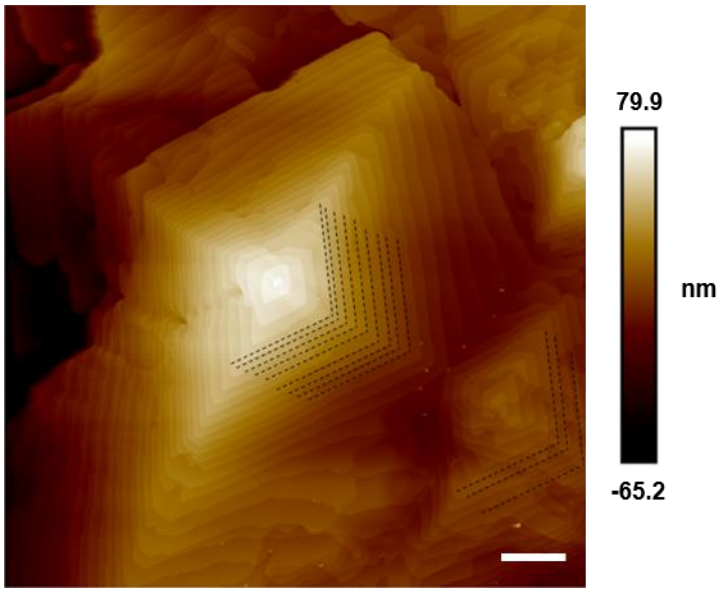

Figure 4.15: AFM height map of a $C_{31}H_{64}$ crystal. Scale bar indicates 4 µm. Dashed lines mark angle measurements of a series of terraces, with an estimated angle of 109°.

The regular terracing in the $C_{31}H_{64}$ sample, enabled the construction of a height histogram (Figure 4.16). Height information for every pixel was extracted from the image shown in Figure 4.14a, and plotted. The histogram was fitted with a multi-peak Gaussian fit and the difference between peaks, indicated by the red arrows, and therefore the height difference between all 18 peaks, was calculated to be 4.0 ± 0.1 nm. From the crystal structure, the half-cell distance is *c*/2 = 4.1 nm, including interlamellar space, and the carbon-to-carbon distance is $C_{31} – C_1$ = 3.8 nm, not including terminal protons. The AFM step height is therefore consistent with the molecular chain length extended in the expected linear conformation for $C_{31}H_{64}$.

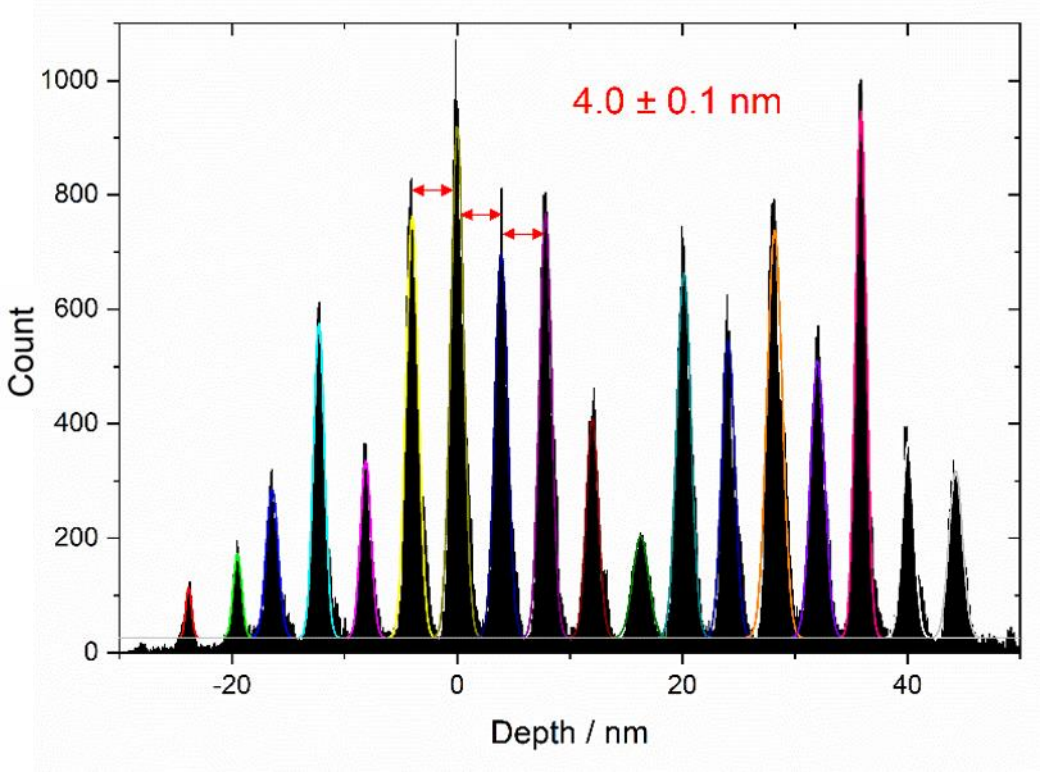

Figure 4.16: Histogram showing the height distribution across the $C_{31}H_{64}$ sample as measured by AFM.

Returning to the adhesion plots, the regions of higher and lower adhesion coincide with step changes in height values. Additional profiles showing the alignment of step height and adhesion changes are shown in Figure 4.17. The blue lines indicate the variation in adhesion across both samples; a consistent value across the alkane sample and alternating between two values in the alcohol.

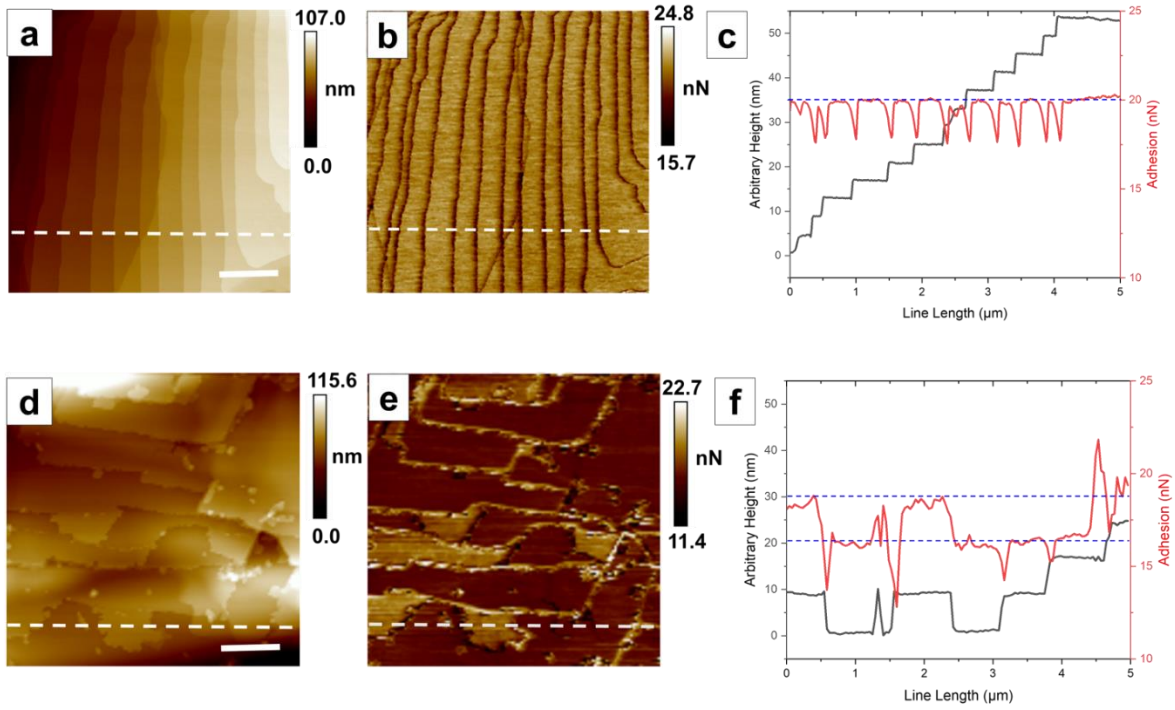

Figure 4.17: Height and adhesion profiles, with values along the indicated line plotted, obtained through AFM for $C_{31}H_{64}$ (a-c) and $C_{30}H_{61}OH$ (d-f) samples. Blue dotted lines indicate the variation in adhesion values across both samples. Scale bars indicate 2 μm.

Across this field of view, $C_{30}H_{61}OH$ crystals also show an average 8.3 nm step height, equal to two $C_{30}H_{61}OH$ molecular chains end-to-end in contrast to the single-molecule step heights observed in $C_{31}H_{64}$ crystals. The height of two chains stacked in the idealized β-form *P2₁/c* structure is 8.3 nm. Notably, the height of two chains in the *C2/c* structure is only 6.6 nm due to the tilt of the chains, again suggesting the chains do not pack with *C2/c* symmetry when crystallized from solution onto a flat surface.

Together, differences in adhesion corresponding to terraces and a preference for double-steps map to key features of the β-form $C_{30}H_{61}OH$ unit cells (*P2₁/c* and *P2/c*). The β-form unit cells exhibit a chemically distinct two-molecule repeat, where surfaces terminated by alcohol groups are expected to exhibit different adhesion properties to methyl-terminated surfaces. The strong hydrogen bonding between alcohol groups, with hydrogen bond donor-acceptor pairs represented particularly in the *P2₁/c* structure, explains these double-step height features. Given the thermodynamically favourable hydrogen bonding interactions, unpaired or dangling alcohol groups are likely to make a significant contribution to raising the surface free energy or promoting further molecular attachment (Van Oss et al., 1986). The Gibbs–Curie–Wulff theorem proposes that crystals will grow to minimise the number of high-energy surfaces (Curie, 1885), (Li et al., 2016). This increases growth velocities, in comparison to

methyl-terminated, van der Waals interacting surfaces. As such, double steps between methyl-terminated terraces appears the most likely step arrangement. These AFM observations, together with TEM and SAED analyses, provide experimental confirmation of end-to-end functional group interactions that distinguish $C_{30}H_{61}OH$ crystals from $C_{31}H_{64}$ crystals despite otherwise similar chain lengths and polyethylene-like side-by-side chain packing.

4.7 Summary

Long chain *n*-alkane ($C_{31}H_{64}$) and *n*-alkanol ($C_{30}H_{61}OH$) crystals relevant to the composition of IW layers in plant leaves were prepared in two orientations for the examination of crystals along and across the chain axis by electron and atomic force microscopy. Critical fluence measurements concluded that the primary damage mechanism to these materials is radiolysis as opposed to mass loss, and determined a critical fluence value similar to the expected value for paraffins, and similar values to other organic materials that have been studied using low-dose conditions previously.

The orientation and possible unit cell assignments were evaluated using SAED. It can be concluded that $C_{31}H_{64}$ chains pack with $A2_1am$ symmetry in the 'chains-flat' orientation as confirmed by the better match of the 01ℓ spots in the experimental and simulated data. This would mean the chains pack in systematic rows in this orientation, compared to the chain offset in neighbouring chains in the *Pbcm* packing, which may start to offer insight into how molecules can move through the intracuticular wax layer. In the 'down-chain' orientation, it is possible the chains pack with either symmetry. To match the experimental data there must be a degree of buckling in the $A2_1am$ symmetry causing the three degree tilt away from zone axis. However, as shown by the bend contours in the bright field images of both $C_{31}H_{64}$ and $C_{30}H_{61}OH$ there is a degree of buckling in all crystals, and a three degree tilt from the expected zone axis is not seen in any other experimental patterns. It is possible that the benzoic acid templating and drop casting from solution methods of crystallisation result in different crystal packing, so the chains may not necessarily pack with the same space group symmetry in the two different orientations studied in this work.

AFM height and adhesion mapping showed alternate packing of terminal alcohol groups in $C_{30}H_{61}OH$. It can be concluded that $C_{30}H_{61}OH$ chains pack with $P2_1/c$ in the 'down-chain' orientation due to the relative intensities of the (110) and (200) diffraction spots in the [001] diffraction pattern, and the fact the chains must lie on a flat substrate. In the 'chains-flat' orientation, although we mostly do not see 00ℓ spots as the simulated pattern suggests we should for $P2_1/c$ symmetry, we can attribute this to

disorder within the crystal packing. Alternatively as with $C_{31}H_{64}$, this could be the result of the chains packing with *C2/c* symmetry in this orientation due to the crystal growth dependent on preparation method. The *C2/c* unit cell also draws similarities with the $P2_1/c$ nematic phase, where chains have undergone a displacement along the c-axis. However, the difference being the chain displacements in the $P2_1/c$ nematic phase are small (less than one C-C bond length as shown by the diffuse scatter modelling), with the displacements in the *C2/c* packing being larger than this bond length.

This chapter has addressed the question of the space groups two long chain hydrocarbons, $C_{31}H_{64}$ and $C_{30}H_{61}OH$, pack at room temperature by using a combination electron diffraction and AFM techniques. From these results, differences between the packing in the $C_{31}H_{64}$ and $C_{30}H_{61}OH$ have been identified. However, the unit cell picture only offers an average representation of chain packing, so does not capture small differences in packing within a crystal network. As shown by nematic phases, chain disorder affects the spots observed in the average diffraction pattern. This overall picture may miss microstructural detail where there may be more ordered or disordered packing. The next chapter uses SED to look at the microstructure of the two components to determine whether the unit cell is effective at capturing the structure of these wax crystals at the nanoscale as separate components and as binary mixtures.

Chapter 5
Nanoscale Structure of Long Chain *N*-alkanes, *N*-alcohols and Binary Mixtures

5.1 Introduction

In the previous chapter SAED results were used to determine how $C_{31}H_{64}$ and $C_{30}H_{61}OH$ crystals pack at the micrometre scale. In this chapter we turn to a nanobeam diffraction technique, scanning electron diffraction, to determine how these materials pack at the nanoscale, a scale not easily accessible for organic materials by traditional bulk techniques (such as XRD and DSC) or SAED. Determining the degree of (dis)ordered structure of organic materials at the fundamental length scale of a few chain repeats (nanometre-scale) is crucial across a number of sectors for understanding properties such as trans film diffusion, density, congealing point, and hardness (Roux, 1969), as well as underpinning understanding of how water and agrochemical active ingredients interact with plant crops (Riederer and Müller, 2007). Due to the chance of beam damage, there is a limited amount of high resolution structural data on molecular paraffin crystals. Zemlin and Dorset used liquid helium to cool a paraffin sample and were able to achieve structural images at a 0.25 nm resolution, and identified edge dislocations within the crystal (Zemlin et al., 1985). However, cooling to liquid helium temperature is experimentally difficult, and helium has a global limited supply so using it as a coolant is expensive (He et al., 2024). This chapter looks to determine the microstructure of these materials at a nanometre spatial resolution at room temperature.

4D-STEM, or SED, has been used to explore the nanoscale structure of many beam-sensitive organic materials including MOFs (Zhang et al., 2022), perovskites (Doherty et al., 2020), and polymers (Calderón Ortiz et al., 2024). The application of 4D-STEM to a block co-polymer system unveiled three levels of order at different length scales and identified nanometre-scale domain size and orientation of crystalline sections of the material (Chen et al., 2024). Kanomi et al. also studied a polyethylene lamellae, and revealed the existence of tilted chains within lamellar crystals, so therefore different inner-chain orientations at a nanometre-scale resolution (Kanomi et al., 2023). 4D-STEM may therefore offer insight on the structure of $C_{31}H_{64}$ and $C_{30}H_{61}OH$ at a nanoscale level, as these materials are very similar to the materials investigated in these studies.

This chapter also explores binary mixtures of $C_{31}H_{64}$ and $C_{30}H_{61}OH$ to build towards a replica leaf wax model. Binary mixtures of alkane and alcohol mixtures have been

explored previously using bulk techniques such as DSC and XRD (Leyva-Gutierrez and Wang, 2021), (Fagerström et al., 2013) which suggest phase separation of the two chains at a 50:50 composition at room temperature, with a eutectic forming at higher temperatures (65 °C). Binary mixtures of two alkane chains have been extensively studied by both XRD (Lueth et al., 1974) and electron microscopy (Dorset, 1990) (Fryer et al., 1997). Initially it was proposed that chains form solid solutions if the two components are of a similar chain length, with the same symmetry (Kitaigorodskii, 1961), (Mnyukh, 1960). Later, models for solid solutions containing molecules of different length proposed the chains are arranged where one end of the shorter molecule may pack level with the end of the longer molecule, or both ends of the shorter molecule fall short of the longer chain ends (Asbach et al., 1979). However, solid solutions between chains of different lengths only form up to a limit, for example Fryer was not able to form a solid solution between chains with 44 carbons and 19 carbons (Fryer et al., 1997). Dorset used electron microscopy to also show solid solution formation between even and odd chain alkanes, expected to not form due to symmetry, is possible. This occurs when the odd-chain paraffin produces a higher energy form of packing which can more readily combine with the even-chain paraffin (Dorset, 1985b).

A binary mixture between two similar length alcohol chains has also been studied by Guo et al. with DSC and FT-IR (Guo et al., 2024). They discovered a complex system, where chains of similar length showed different phase transition pathways when heated, showing even closely related compounds can behave differently even within the same binary system and the ability of differing chains to act as individual molecules. It is apparent that binary mixtures of long-chain hydrocarbons exhibit significant complexity. This chapter shifts focus to a binary mixture of an alkane and an alcohol with similar chain lengths, utilising microscopic techniques to analyse the microstructural changes resulting from their formation.

This chapter first uses SED to evaluate the microstructure of $C_{31}H_{64}$ and $C_{30}H_{61}OH$ at a higher resolution than accessible with SAED. These results are compared to the space group assignments in the first chapter, with the unit cell picture of chain packing evaluated and deviations identified. Results then turn to the use of electron microscopy and AFM to look specifically at the microstructure of a binary mixture between $C_{31}H_{64}$ and $C_{30}H_{61}OH$. These binary mixtures span a range of compositions from 0 to 100% $C_{30}H_{61}OH$ content, and it is determined how this introduction of the long chain alcohol into the binary system introduces disorder.

5.2 Microstructure in Long Chain Alkanes

Figure 5.1 shows an SED dataset from $C_{31}H_{64}$ crystals prepared in the ‘chains-flat’ orientation to examine lamellar packing. Lamellar packing is defined as the packing of the chains into distinct layers with an interlamellar gap. To achieve low-dose SED conditions, a beam energy of 300 keV is used, plus a beam current of 1 pA, dwell time of 1 ms, and a beam convergence angle of <1 mrad at room temperature to minimize radiation damage from radiolysis. This 300 keV beam energy was used instead of a lower beam energy such as 80 keV as the inelastic cross section increases at lower beam energies, increasing damage via radiolysis which is not useful for the organic molecular crystals studied here, so lower beam energies were not explored. These conditions offer a trade-off between the reduction of beam damage (given lower rates of radiolytic damage are observed in organic materials at higher beam energies) (Ventolá et al., 2002) whilst still achieving moderate diffraction resolution to distinguish the Bragg reflections (diffraction disk radius $\alpha/\lambda \sim 0.05$ Å^{-1} for convergence semiangle α and de Broglie wavelength λ) whilst also retaining a manometre scale probe (Chapter 3.2.6). These conditions give a probe fluence of ~ 5 e^{-}/Å^2 for a single exposure. In this SED data Bragg spots out to scattering angles corresponding to d-spacings of 1.19 Å and 0.87 Å can be detected, in the “down-chain” and “chains-flat” orientations, respectively, confirming we retain high-resolution structural information under these conditions. As established, the diffraction patterns of the ‘chains-flat’ oriented crystals are characterised by the presence of 00ℓ spots around the central beam, the splitting of the 01ℓ Bragg spots into two Bragg spots, and the presence of diffuse scattering signal along 0$k\ell$ for $\ell = 2n + 2$.

Figure 5.1a shows a low-angle ADF-STEM image (formed using an inner angle of 2.1 mrad and outer angle of 7.5 mrad). Figure 5.1b presents the corresponding average diffraction pattern from the entire field of view. The presence of defined Bragg spots indicate a single crystal in the field of view, if there were several crystals a polycrystalline pattern would be seen with a set of concentric circles at different d-spacings. The diffraction pattern was indexed to the same PE unit cell (*Pbcm*) as in SAED (Chapter 4 Figure 4.14), which can also be indexed to the $A2_1am$ unit cell. The reciprocal space c^*-axis indicates the chains lie perpendicular to the long, linear features. The pattern also exhibits diffuse scattering along 0$k\ell$ for $\ell = 2n + 2$ as observed by SAED.

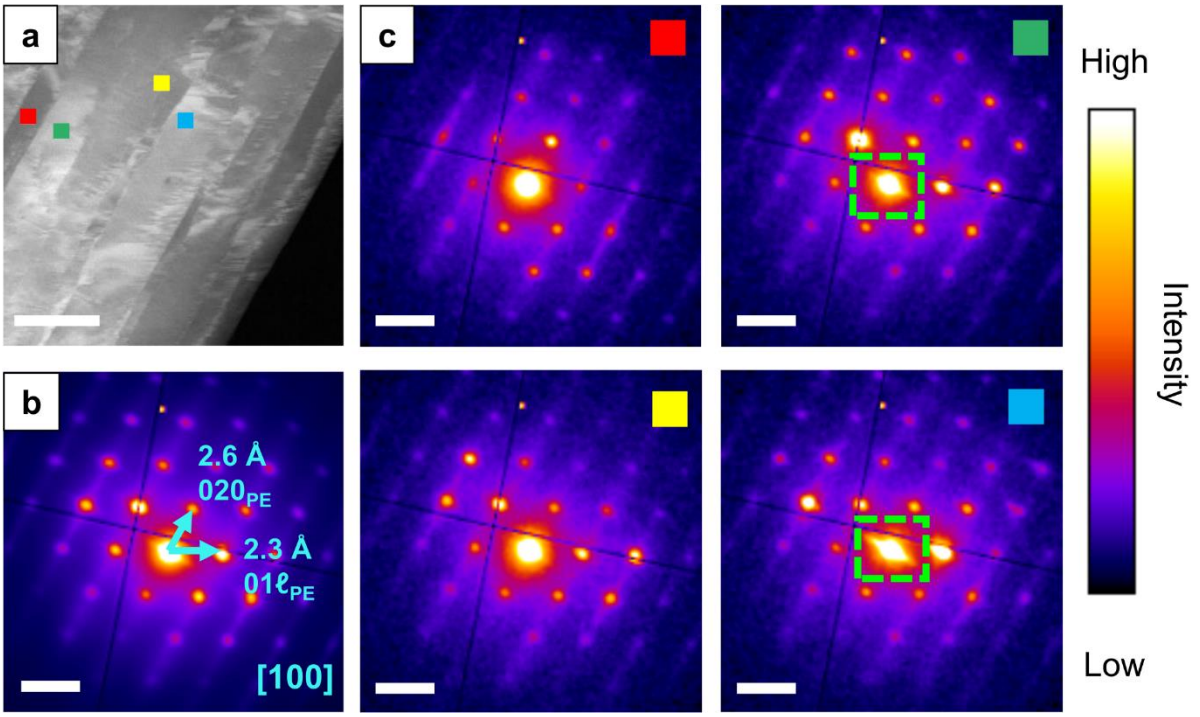

Figure 5.1: (a) ADF-STEM image of a $C_{31}H_{64}$ crystal. (b) The average diffraction pattern from the entire field of view. (c) Summed diffraction patterns from an area of 10 x 10 pixels shown by the boxes in the [100] orientated $C_{31}H_{64}$ crystal(s) (a). Dashed green rectangles indicate the presence of 00ℓ spots (elongated intensity around the zero order spot running diagonally top left to bottom right). The dark cross lines outline the quadrants formed due to the Medipix detector. Diffraction patterns are shown after rotation calibration and distortion correction. The bright field image scale bar indicates 500 nm. All diffraction pattern scale bars indicate 0.5 $Å^{-1}$.

The ADF-STEM image exhibits significant variation in intensity, consistent within elongated rectangular regions in the image, from here called grains. To understand the origin of this image contrast, spatially resolved diffraction patterns from across a set of these regions were extracted (Figure 5.1c). These smaller squares covered areas 80 x 80 nm. These patterns show the same set of Bragg spots as in the average pattern (Figure 5.1b) but exhibit variation in the intensities of spots across each pattern with respect to the average diffraction pattern, which can be attributed to slightly different tilts of each grain within the crystal (tilts relative to the electron beam). This is obvious in the red and green diffraction patterns, with the intensity of spots focused in the lower right area of the red diffraction pattern, and the intensity of spots focused in the upper right area of the green diffraction pattern. These observations are consistent with Laue circle like features, where the crystal is exhibiting small tilts away from the fully aligned zone so the Ewald sphere intersects with the reciprocal lattice at different positions causing a change in intensities observed. This is explored further in Section 5.2.2.

Figure 5.2 shows further examples of grains within the crystals and the extracted diffraction patterns in additional $C_{31}H_{64}$ crystals. Similar observations are seen; the presence of diffuse scatter, the varying presence of 00ℓ spots in individual diffraction patterns, and a variation in relative Bragg spot intensities from grain to grain.

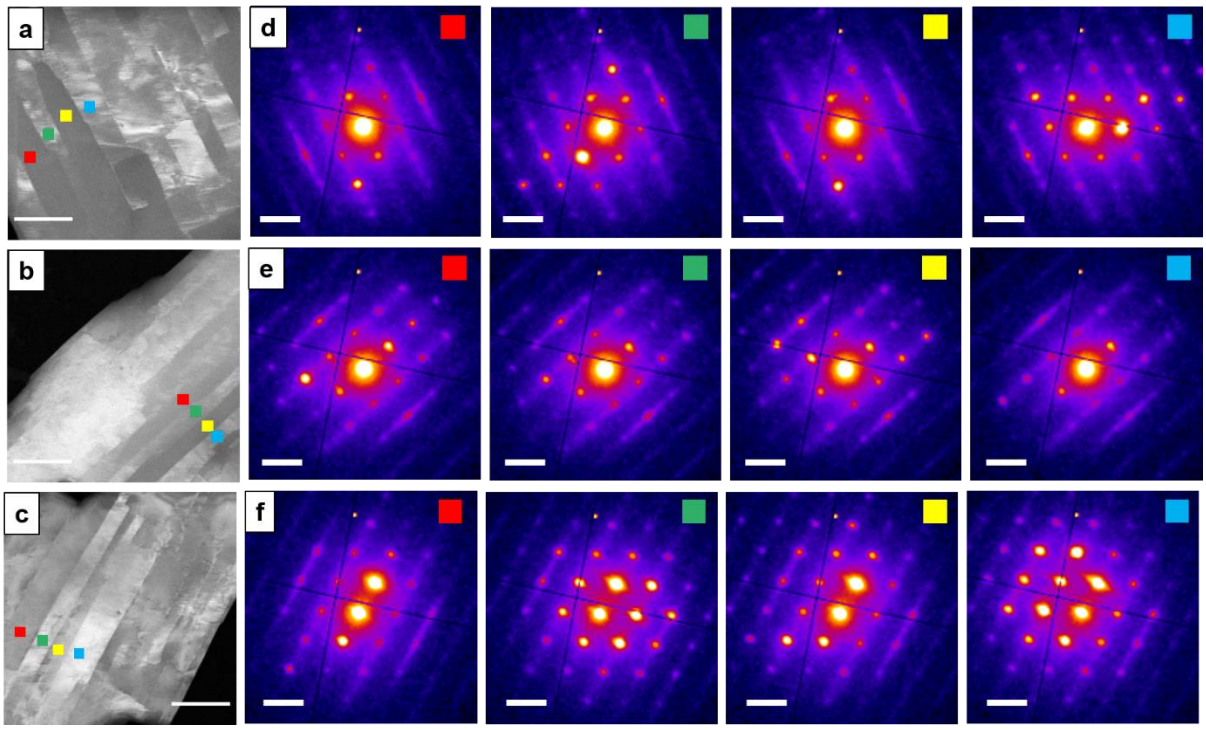

Figure 5.2: (a,d) (b,e) (c,f) Summed diffraction patterns (d-f) from an area of 10 x 10 pixels shown by the coloured boxes in the corresponding [100] orientated n-hentriacontane ($C_{31}H_{64}$) crystals (a-c). All bright field image scale bars indicate 500 nm. All diffraction pattern scale bars indicate 0.5 $Å^{-1}$.

5.2.1 vADF Contrast

Virtual ADF (vADF) images across a series of ADF collection angles (Figure 5.3) were constructed with the set of collection angles outlined in Figure 5.3. The vADF image obtained using the low-angle ADF collection range (Figure 5.3a) should display contrast based on diffraction intensity, capturing signal primarily from the high-intensity first-order Bragg reflections. The two medium-angle ADF images (Figures 5.3b and 5.3c) are generated from signals beyond this immediate Bragg scattering, making their contrast more likely to arise from mass-thickness variations rather than just diffraction effects. In this set of images, with increasing collection angle beyond the Bragg scattering in the zero order Laue zone the contrast between grains deteriorates, confirming the grain contrast primarily emerges from variation in diffraction intensities.

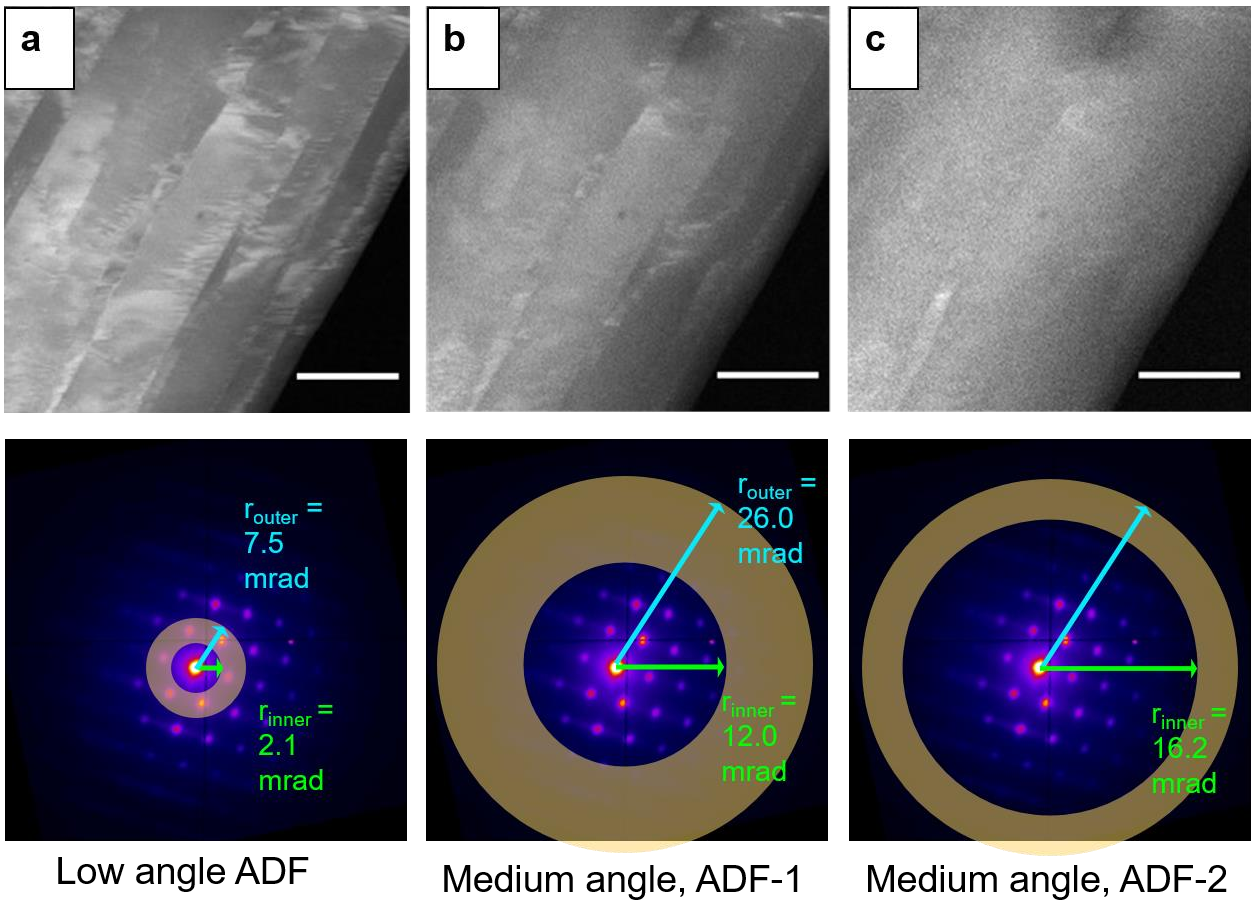

Figure 5.3: Images of a $C_{31}H_{64}$ epitaxially orientated crystal with increasing vADF angle, (a) low angle ADF (b) medium angle, ADF-1 (c) medium angle, ADF-2. All scale bars indicate 500 nm and the reciprocal lattice collection angles are shown in the corresponding diffraction patterns under each vADF image.

5.2.2 Tilt Observations

As it is established variations in contrast are dominated by diffraction and not mass-thickness, the observed Bragg spot intensity variations in Figure 5.1c can be understood as arising from small variations in the local orientation of the crystal within these grains. Through comparison with kinematical simulations of mis-tilted $C_{31}H_{64}$ crystals (Figure 5.4), the spatially isolated patterns (Figure 5.1c) were assigned to orientations <1° from the [100] zone axis. The misorientation analysis revealed two angular variations, one away from the [100] axis (defined as θ in Figure 5.4) and a further rotation about this axis (defined as Φ in Figure 5.4), though with no rotation of the pattern on the detector itself. The variation in the second rotation about [100] (Φ) follows a consistent counterclockwise rotation in the diffraction data when moving from left to right in the image (Figure 5.5), suggesting a degree of coherence likely emerging during crystal growth on or against adjacent grains within the larger wax crystal plate.

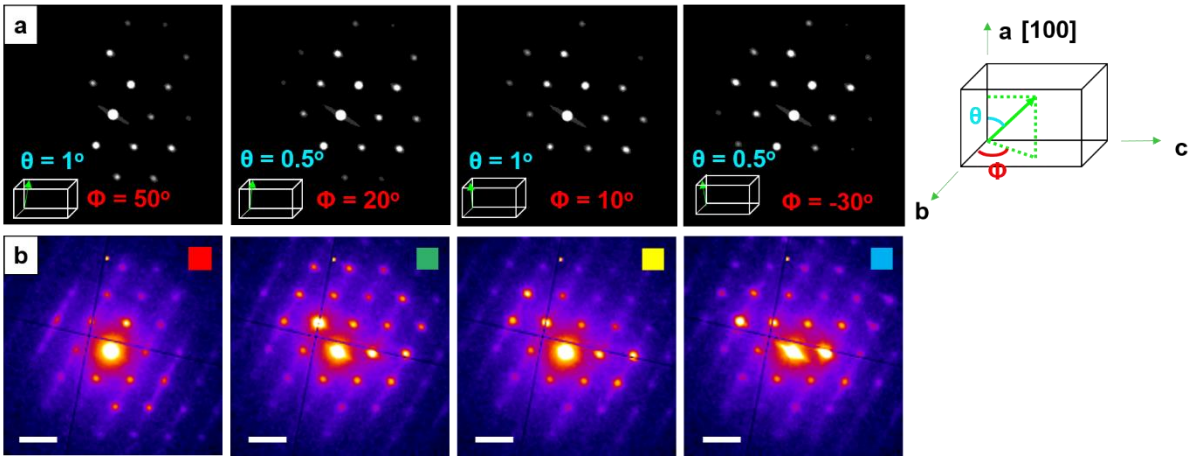

Figure 5.4: (a) Diffraction patterns simulated using Pyxem to apply a defined tilt to the diffraction pattern produced by the $C_{31}H_{64}$ crystals. These are compared to experimental diffraction patterns extracted from smaller areas within a $C_{31}H_{64}$ SED dataset seen in Figure 5.1. The schematic shows how θ and Φ are defined relative to the crystal zone axis. The green arrows show a schematic representation of a relative tilt between the electron beam and the unit cell.

5.2.3 00ℓ Bragg Signal and Diffuse Scatter Signal

Figure 5.1c also highlights the presence of 00ℓ spots observed in some, but not all, spatially resolved diffraction patterns (dashed green rectangles). These 00ℓ spots are a defining characteristic of well-ordered end-to-end chain packing in lamellar domains as illustrated in Chapter 4. Variation in the intensities of the 00ℓ spots can be ruled out due to orientation changes based on comparison with electron diffraction simulations as they are consistently seen in simulations with a small applied tilt (Figure 5.4). Instead, the experimental observation of 00ℓ spots in only some areas of the crystal plate indicates there are variations in the order or disorder of the lamellar packing across the grains in the field of view.

To isolate the spatial variation in 00ℓ spot intensity, a virtual dark field (VDF) image was constructed, formed from the 00ℓ spots by placing small virtual apertures around these features, effectively as a post-processing mask on the diffraction plane in the four-dimensional dataset (shown as white-grey ovals on the average diffraction pattern, Figure 5.5). The placement of the virtual apertures is shown in Figure 5.5b, and the corresponding 00ℓ VDF image is shown in Figure 5.5c. Narrow rectangular domains of bright intensity appear in the 00ℓ VDF (Figure 5.5c), providing a map of the location of ordered lamellae within the $C_{31}H_{64}$ grains. While in several cases the 00ℓ domains extend across the entire width of the grain they are part of, many of the domains are not the full width of the grains. There is also always a clear break in the intensity between 00ℓ domains at the grain boundaries. These observations point to local, highly ordered end-to-end packing being confined within a grain. The ordered

end-to-end packing may also extend only part way across the grain, indicating a transition to nematic phases within the width of single grains.

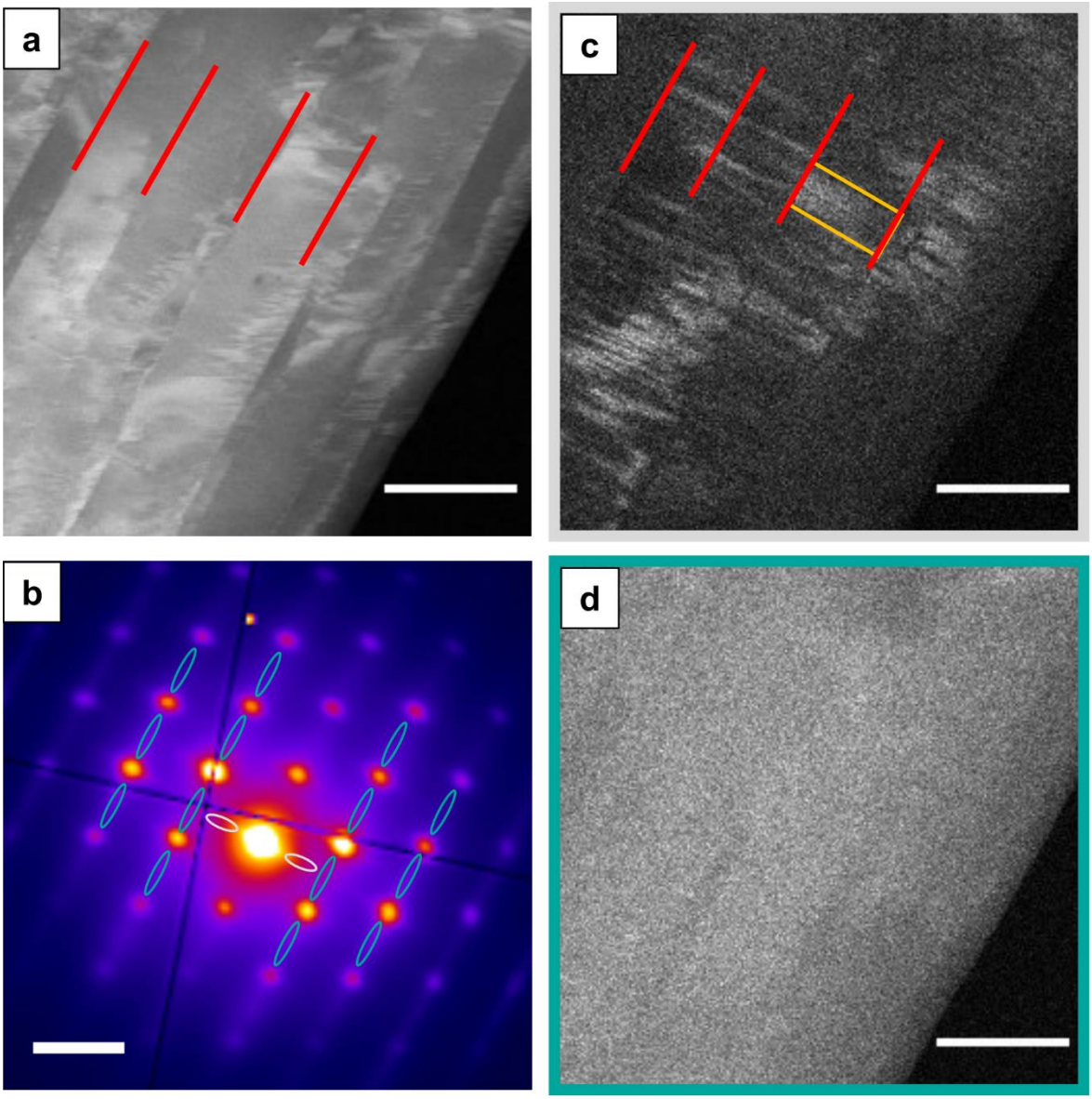

Figure 5.5: (a) Low angle ADF image of a $C_{31}H_{64}$ epitaxially orientated crystal with grain boundaries highlighted with red lines. (b) Average diffraction pattern of crystal in (a). (b) Average diffraction pattern. (c) VDF (00ℓ) image produced from signal area defined by the grey/white ovals in (b), with grain boundaries highlighted with red lines and a domain of lamellar ordering highlighted by orange lines. (d) VDF image produced from diffuse scattering signal in the diffraction pattern defined by the blue ovals in (b). All bright field image scale bars indicate 500 nm. The diffraction pattern scale bar indicates 0.5 $Å^{-1}$.

To further confirm the domain assignment of lamellar ordering of the 00ℓ VDF intensity, diffraction patterns only from bright regions in the 00ℓ VDF were extracted showing the presence of intense 00ℓ spots (Figure 5.6).

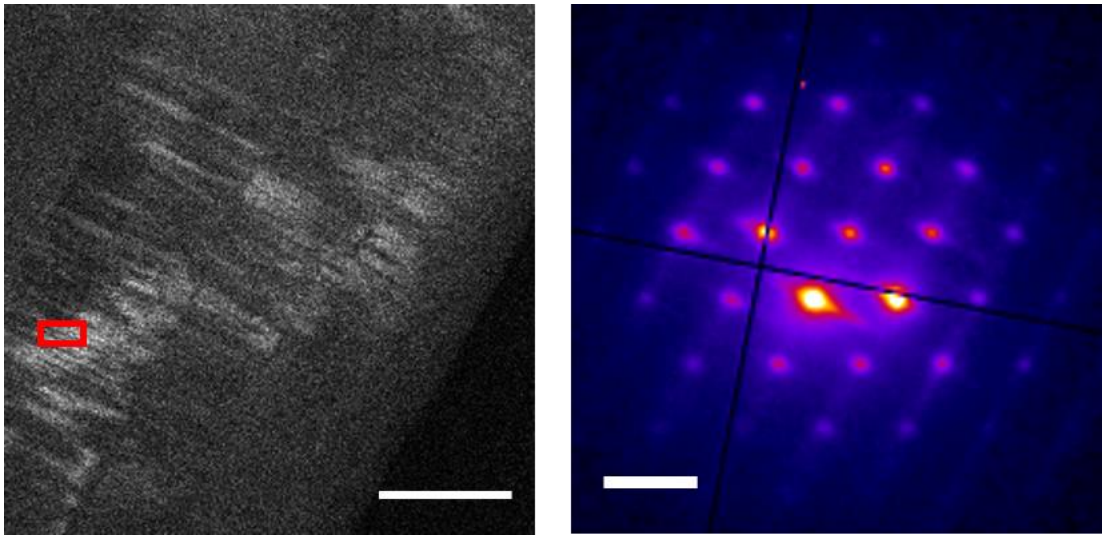

Figure 5.6: Diffraction patterns extracted from areas where the sharp, high intensity lines were seen in the VDF produced from the 00ℓ signal areas in Figure 5.5. The bright field image scale bar indicates 500 nm. The diffraction pattern scale bar indicates 0.5 Å^{-1}.

Ordered lamellae are expected to exhibit distinct diffraction intensities both at 00ℓ and the 01ℓ first order reflections for ℓ = *n*, *n* + 2 (Chapter 4, Figure 4.3), with the ℓ = *n* + 2 as the single, dominant feature when no lamellar order is retained (nematic phases). While the SED patterns do not completely resolve the 00ℓ or 01ℓ spots, the spots show defined elongation along 00ℓ and 01ℓ. These two features are correlated in spatially resolved diffraction patterns from bright areas across the field of view in Figure 5.6a (Figure 5.7), with increases in 00ℓ intensity corresponding to increased ellipticity at the 01ℓ first order reflections in the extracted diffraction patterns.

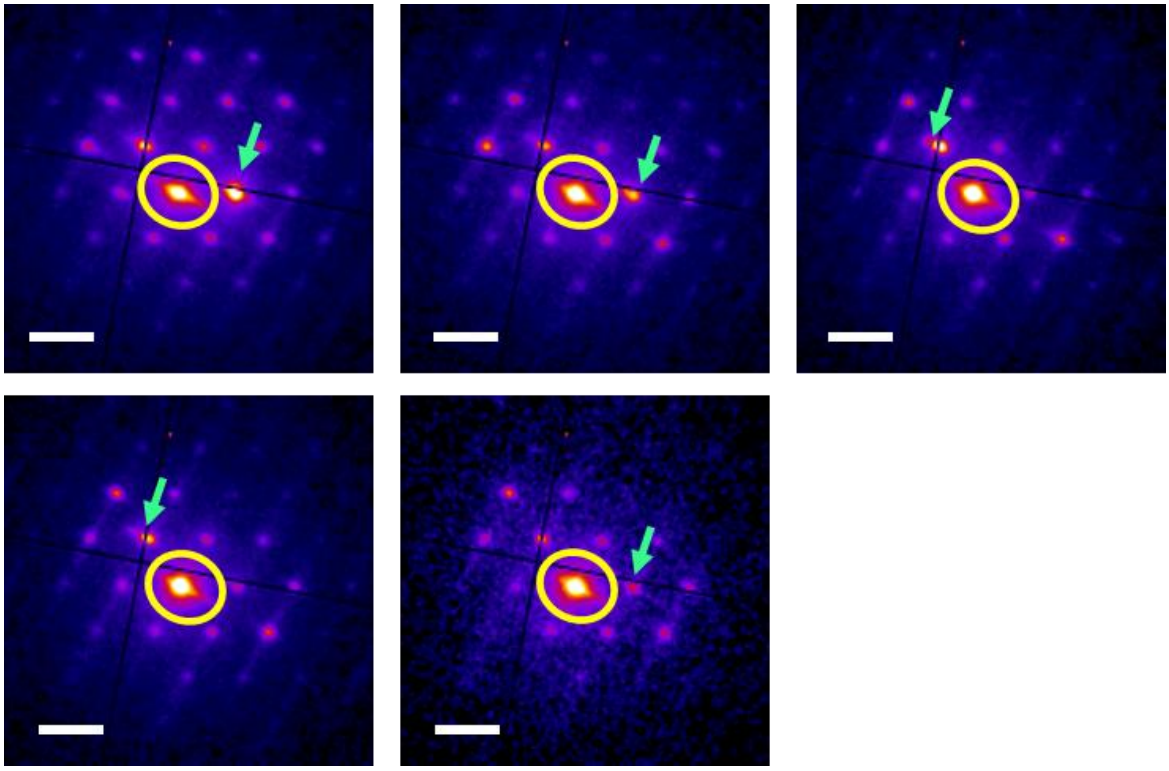

Figure 5.7: Diffraction pattern extracted from a region where the sharp, high intensity lines were seen in VDFs produced from 00ℓ signal areas, such as the red box in Figure 5.6. The 01ℓ peaks, pointed out by green arrows in each pattern, have an elliptical shape suggesting splitting of these peaks, also showing lamellar ordering is found within these regions. The 00ℓ spots in each individual pattern are circled in yellow.

The long axis of the domains of 00ℓ intensity lies perpendicular to the major surface facet and is therefore aligned with the row of 00ℓ spots and the *c**-axis. That is, the long axis of the domains in Figures 5.5c and 5.6a align with the molecular chain axis. The average length of these domains determined across six fields of view was 332 nm (sample standard deviation s = 112 nm). For c = 8.26 nm, these lines correspond to approximately 40 unit cells packing together, i.e., 80 molecules packing end to end (s ~14 unit cells). These standard deviations refer to the width of the distribution of lengths rather than an uncertainty in the precision of their measurement.

The SED data also enable a separate analysis to the 00ℓ intensity of the lines of diffuse intensity at 0kℓ at fixed ℓ. Figure 5.5d shows a VDF image formed from these regions of diffuse scattering, indicated by the blue ovals in Figure 5.5b. This VDF image shows even intensity across the entire field of view, indicating no correlation between the end-to-end chain ordering and the diffuse scattering intensity. This image is the result of background and diffuse scatter signal in the diffraction patterns. Further analysis presented in Figure 5.8 validates that this diffuse scatter and corresponding VDF image is in fact real signal and not just due to sample thickness effects. Line profiles

were drawn bisecting the diffuse scatter streaks to measure the intensity of the diffuse scatter signal versus the background signal on either side of the line, the blue lines in Figure 5.8a and 5.8b illustrate the positions of these lines in the average diffraction pattern and a single pixel diffraction pattern respectively. Figure 5.8c shows the resultant line profiles of the summed intensity (detector counts) over the diffuse scatter in the average diffraction pattern (black line) and a single pixel diffraction pattern (red line). The background signal for the average diffraction pattern is $N \sim 6.6 \times 10^6$ detector counts therefore the variance, $3\sqrt{N} = 7.7 \times 10^3$ detector counts. So, the background signal plus $3\sqrt{N}$ remains less than 7×10^6 while the peak intensity of the diffuse signal is 9.4×10^6 detector counts. Results above a background plus $3\sqrt{N}$ value are significant due to the 3σ statistical rule, where 99.7% of data will fall within 3 standard deviations from the mean, so anything above this value is beyond what would be expected from any background noise. The probability of a background intensity equal or greater than the diffuse peak value being observed for these values is indistinguishable from 0 at double precision floating point format. This was calculated using Scipy and the poisson.sf() survival function in Python. This uses a Poisson distribution to determine whether an electron count has a value higher than the background threshold. This is a single-tailed probability as it focuses on the chance of observing a value only higher than background.

In turn, the signal for the diffuse scattering peak compared to the background signal in the single pixel diffraction pattern can also be compared. The background signal for the single pixel diffraction pattern is ~ 112 detector counts and the variance, $3\sqrt{N} =$ 32 detector counts. So the background signal plus $3\sqrt{N} = 144$, the peak intensity of the diffuse signal is 207 detector counts so this signal is also significant. The probability of a background intensity equal or greater than the diffuse peak value being observed for these values is $3.5e^{-16}$. Figure 5.8e shows a VDF formed from background signal, corresponding to the aperture positions signalled by the ovals in Figure 5.8d. Figure 5.8f shows the image produced by subtracting this background signal from Figure 5.8d, which produces a VDF that can be taken as a ‘real’ positive signal and has an intensity variation that follows the specimen thickness. We can conclude that diffuse scatter is a significant signal that can be found everywhere in the crystal. In Figure 5.8f a dashed square marks an area used for inspection of the counts encoded in the grayscale image. The average of the background-subtracted counts in the yellow square is ~120. The image in Figure 5.5d has an average of ~ 260 counts, and the image Figure 5.8e has an average of ~ 140, indicating Figure 5.8f is statistically separable from the background.

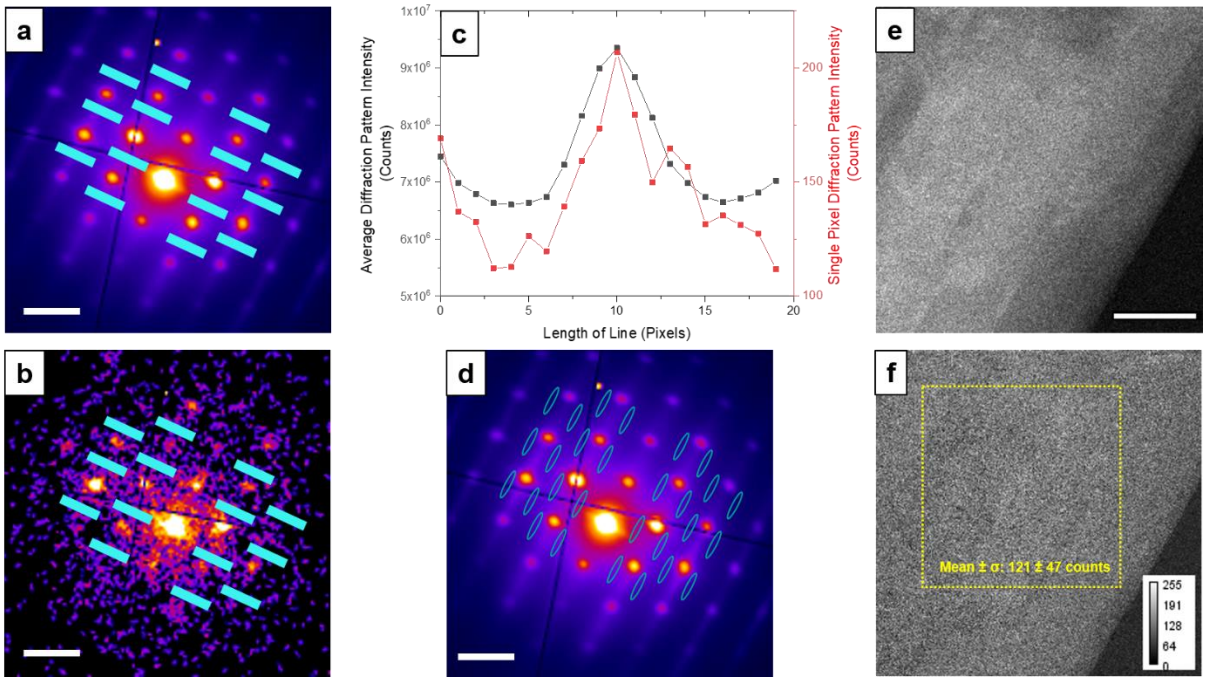

Figure 5.8: An analysis of the signal in the diffuse scattering signal encoded in the VDF image in Figure 7d. (a) Integrated diffraction pattern and (b) a single pixel diffraction pattern extracted from the dataset shown in Figure 7. The light blue lines mark the positions of a series of line profiles used to extracted and sum the diffuse scattering signal and local background, depicted in the form of intensity line profiles in (c). The integration over these line profiles mimics the selection of matched virtual apertures in Figure 5.7. In (c) the black trace shows the integrated line profile for the integrated pattern and the red trace shows the integrated line profile for the single-pixel pattern. (d) Ovals mark the positions of virtual apertures used to form a VDF estimating the background off the diffuse scattering streaks (taken as double the background counts for Figure 5.7d given twice the apertures). (f) A VDF image formed by subtracting the estimated background intensity from the VDF in Figure 5.7d (diffuse scattering signal counts).

Figure 5.9 presents further inspection of the diffuse scattering intensity across two different grains in Figure 5.1 through 4 line profiles measuring intensity along the diffuse scatter, intersecting Bragg reflections. Where intensity of the Bragg spots is higher for a light domain (green) than a dark domain (red), the intensity of diffuse scattering is consistent across both the dark and light grain. This is particularly pronounced in the blue and yellow line profiles where the 01ℓ Bragg spots have a much larger relative intensity in the light domain, but diffuse scatter signal is consistent along the two lines. These differences in the mapped VDF intensities identify distinct structural origins for the disorder contributing to the diffuse scattering intensity and the disorder contributing to the loss of 00ℓ spot intensity.

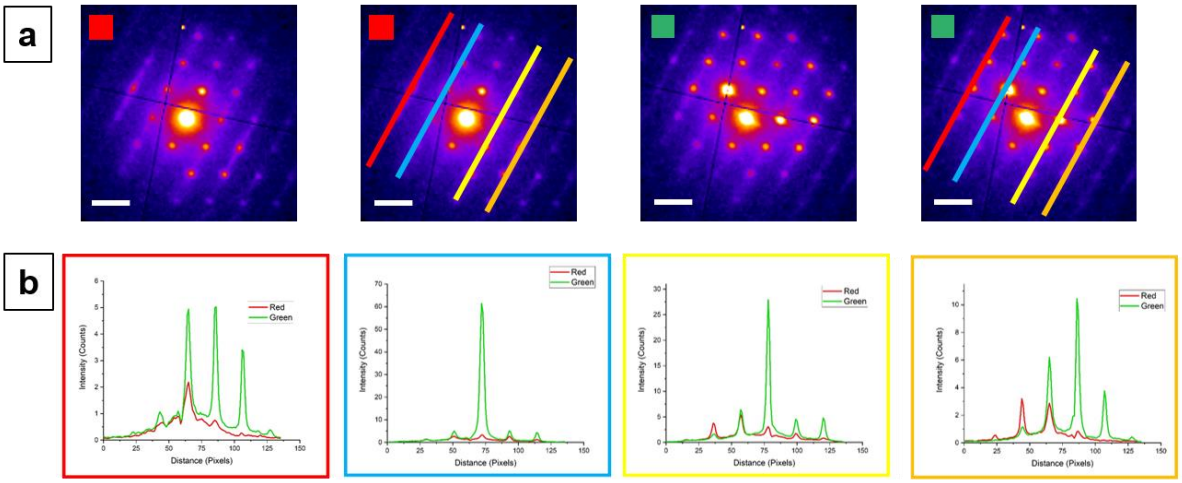

Figure 5.9: Line profiles across (hkl) reflections measuring intensity corresponding to the areas outlined by the red and green boxes in Figure 5.1. Diffraction pattern scale bars indicate 0.5 Å^{-1}.

5.2.4 Structural Model

Bringing all of these analyses together, Figure 5.10 presents a unified structural model for each of the observed diffraction signals. Beginning with the diffuse scattering, Figure 5.10a depicts displacements along the chain axis that give rise to diffuse scattering streaks in the diffraction pattern perpendicular to the chain axis. This schematic follows established models for dynamical disorder in molecular crystals exhibiting linear displacements, e.g., due to vibrational modes (Eggeman et al., 2013). The linear displacement of the molecule creates a range of interplanar angles (δ, ε, θ) and interplanar spacings (l, m, n) that contribute to a line of diffuse diffraction intensity reflecting the distribution of chain displacements.

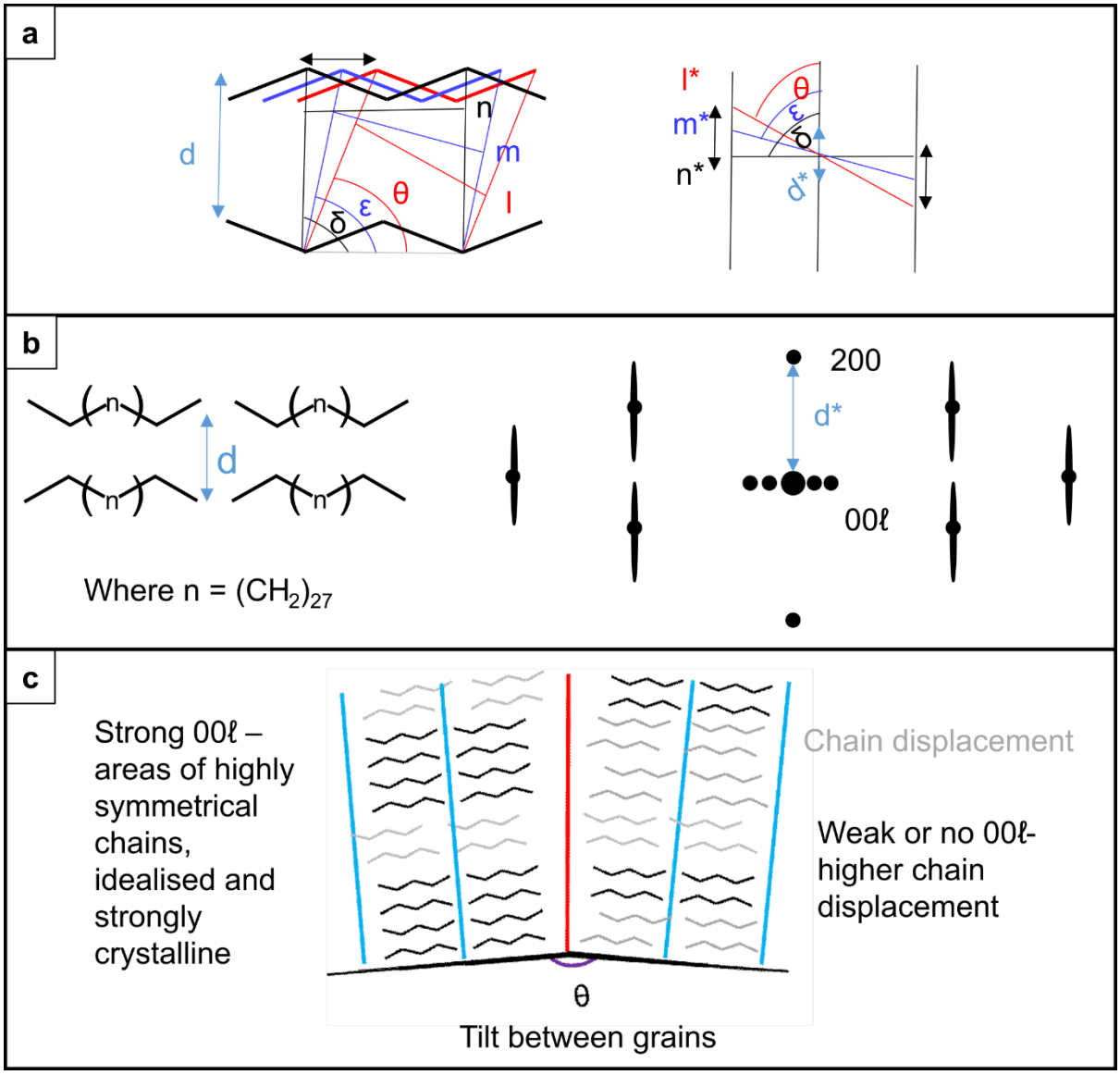

Figure 5.10: (a) Proposed model to explain how chain offset may contribute to diffuse scattering in the observed diffraction patterns, adapted from Eggeman (Eggeman et al., 2013). (b) Simplified representation of the unit cell of the $C_{31}H_{64}$ packing looking down the [100] direction and corresponding diffraction pattern formed from this chain orientation. (c) Proposed structural model to show how chain packing and offset contributes to the diffuse scattering and 00ℓ spots around the central beam and first order reflections are seen. Chain packing on the left and right of the red line correspond to the grains seen, and the tilt seen between them. The left grain corresponds to one with more domains of ordered packing and therefore higher intensity Bragg diffraction. The right grain corresponds to one of higher chain displacement and therefore lower intensity Bragg diffraction.

The presence of diffuse scatter streaks in this simplified model illustrates how chain displacement contributes to the diffuse scatter signal. A simplified representation of $C_{31}H_{64}$ chain orientations viewed along [100] and the corresponding diffraction pattern are shown in Figure 10b to illustrate how this model relates to the real space packing

of the chains and to the resulting diffraction pattern. While the SED data do not distinguish between static and dynamical disorder, the absence of correlation with the loss of 00ℓ intensity points to dynamical displacements. Previous work on waxes has likewise shown a decrease in diffuse scattering in SAED when cooled, (Dorset et al., 1984), suggesting that the displacements likely arise from dynamical disorder.

Figure 10c in turn combines the diffuse scattering model with the grain and domain structures recorded in SED (Figures 5.2 and 5.5). Across the largest length scales, $C_{31}H_{64}$ grains exhibit small relative mis-orientations of up to ~1°, forming a microstructure comprising elongated rectangular grains micrometers in length and <500 nm in width. Within these grains, there are well-ordered lamellar domains exhibiting strong 00ℓ diffraction forming anisotropic domains ~300 nm long and ~ 40 nm wide as well as regions where nematic ordering dominates. Within both well-ordered lamellar domains and disordered nematic phases there is additionally dynamical disorder along the chain axis. Beyond a simple ‘brick and mortar’ model, this description identifies regions of lamellar order co-existing with nematic phases rather than identifying fully amorphous interface regions.

5.3 Microstructure in Long Chain Alcohols

$C_{30}H_{61}OH$ crystals in the ‘chains-flat’ orientation were analysed in a similar way to understand the microstructure of both end-members when subsequently looking at binary mixtures of the two components. Figure 5.11 presents a low-angle ADF-STEM image, average diffraction pattern, and spatially resolved diffraction patterns extracted from areas of equivalent size and equidistant to those in Figure 5.6 for $C_{31}H_{64}$. Spatially isolated diffraction from similar length scales to the grain structure in $C_{31}H_{64}$ show no changes in the distribution of diffraction intensity, for example the relative intensities of the 01ℓ spots across the extracted areas are mostly consistent. This lack of intensity variation suggests no tilt within the crystals. Secondly, no 00ℓ diffraction spots or signatures of elliptical elongation of spots were observed in any $C_{30}H_{61}OH$ crystals. These observations are consistent with simulations of the γ-form *C2/c* unit cell containing staircase packing in the alcohol or, for the β-form unit cells (*$P2_1/c$* or *P2/c)*, nematic phases (Chapter 4). Figure 5.12 shows additional examples of similar $C_{30}H_{61}OH$ crystals showing no distinct grain structure and extracted diffraction patterns with no 00ℓ spots (around the central beam or first order reflections), or crystal tilt. The extra, white contrast in Figure 5.12a-b can likely be ascribed to increased thickness of the crystal in these areas.

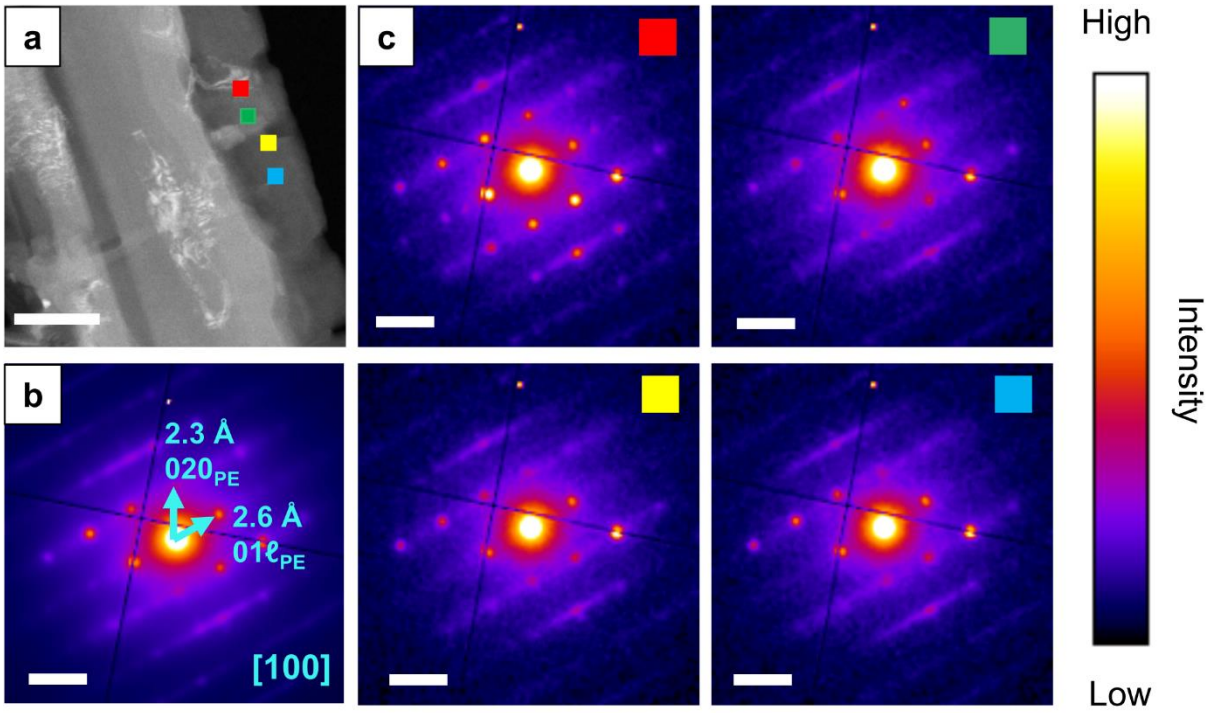

Figure 5.11: (a) ADF-STEM image of a $C_{30}H_{61}OH$ crystal. (b) The average diffraction pattern from the entire field of view. (c) Summed diffraction patterns from an area of 10 × 10 pixels shown by the boxes in the [100] orientated $C_{30}H_{61}OH$ crystal (a). The bright field image scale bar indicates 500 nm. All diffraction pattern scale bars indicate 0.5 $Å^{-1}$.

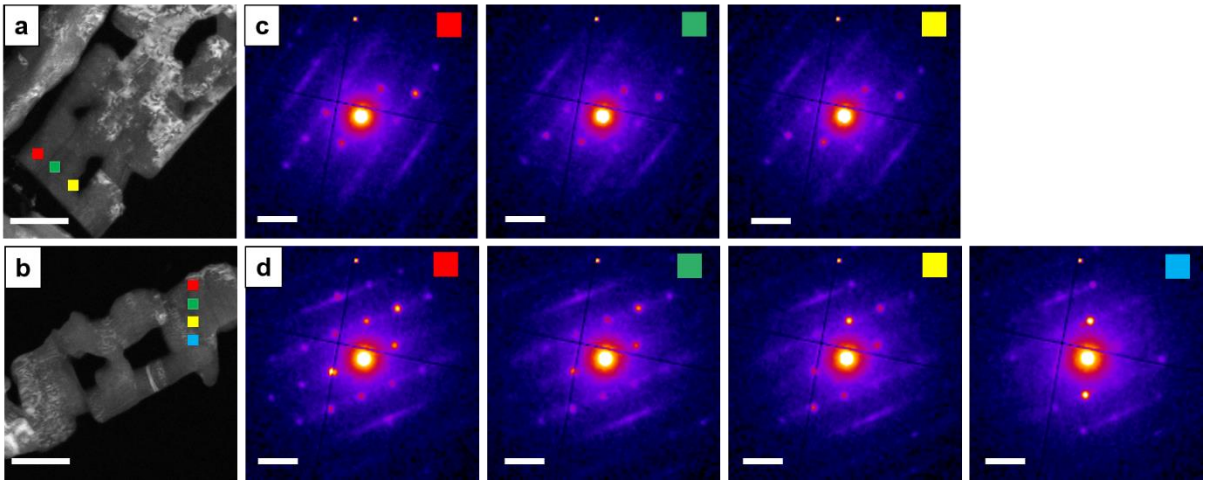

Figure 5.12: (a,c) (b,d) Summed diffraction patterns (c-d) from an area of 10 x 10 pixels shown by the outlined boxes in the corresponding [100] orientated 1-triacontanol ($C_{30}H_{61}OH$) crystals (a-b). All bright field image scale bars indicate 500 nm. All diffraction pattern scale bars indicate 0.5 $Å^{-1}$.

These $C_{30}H_{61}OH$ crystals were indexed as for SAED (Figure 4.7, Chapter 4) to the [100] PE zone axis, and can be indexed to the [2 0 45] zone axis for a modelled *C2/c* unit cell for $C_{30}H_{61}OH$.

5.3.1 vADF Contrast

Both the low-angle ADF-STEM image and the corresponding diffraction patterns show distinct differences to the features observed in $C_{31}H_{64}$ crystals (Figure 5.1, Figure 5.11). First, no grain structure is observed in the low-angle ADF-STEM image of $C_{30}H_{61}OH$. Overall, the crystal exhibits a blocky structure as seen in TEM (Chapter 4), but grain structure is not observed within these blocks in either TEM or SED. With increasing vADF collection angle, contrast remains (Figure 5.13), in a difference to the fading contrast seen in $C_{31}H_{64}$ (Figure 5.3). If this contrast was due to diffraction variation, the images produced by the apertures outside the Bragg scattering (Figure 5.13c) would not show contrast.

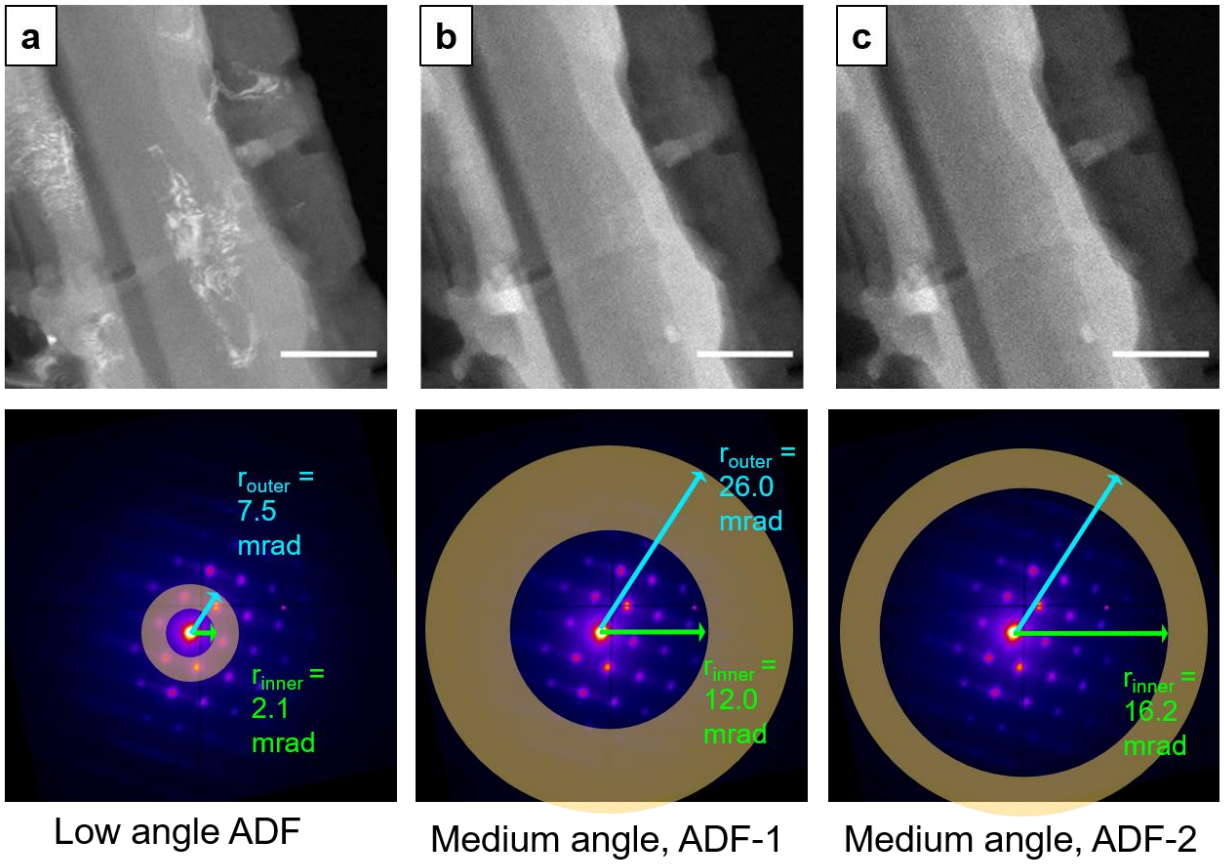

Figure 5.13: Images of a $C_{30}H_{61}OH$ epitaxially orientated crystal with increasing vADF angle, (a) low angle ADF (b) medium angle, ADF-1 (c) medium angle, ADF-2. All scale bars indicate 500 nm.

Where there are variations in contrast, extracted diffraction patterns from different areas of contrast show near identical diffraction patterns in terms of their relative intensities. For the $C_{31}H_{64}$ crystals, where there is difference in contrast in the images due to diffraction variation, the diffraction patterns from brighter areas correspond to diffraction patterns with higher Bragg spot intensity and vice versa. This lack of change

in intensity in the diffraction patterns extracted in Figure 5.14 indicate that areas with increased intensity in the ADF image arise from mass-thickness contrast (Figure 5.14).

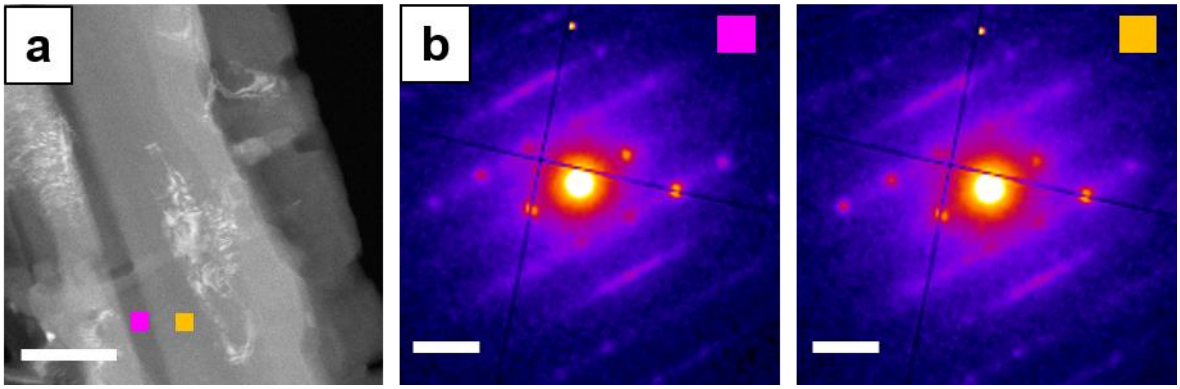

Figure 5.14: [100] orientated 1-triacontanol ($C_{30}H_{61}OH$) crystal(s). (b) Summed diffraction patterns from an area of 10 x 10 pixels shown by the outlined boxes in the [100] orientated 1-triacontanol ($C_{30}H_{61}OH$) crystal(s) (a). The bright field image scale bar indicates 500 nm. All diffraction pattern scale bars indicate 0.5 $Å^{-1}$.

5.3.2 Diffuse Scattering

The $C_{30}H_{61}OH$ crystals likewise exhibit diffuse scattering as for $C_{31}H_{64}$ indicating a similar dynamical chain displacement disorder mode in the alcohol and in the alkane. Figure 5.15 presents analyses of the diffuse scattering intensity across the yellow and blue areas in Figure 5.15. In between Bragg spots the intensity is also above zero, indicating the presence of a diffuse scatter signal. For each line, there is no significant difference in intensity for the two different regions across the Bragg scattering and diffuse scatter. Increases in intensity where the line intersects a Bragg spot is matched across both regions. These line profiles show consistent levels of Bragg and diffuse scattering intensities across two neighbouring fields of view. This is consistent with the lack of tilt in these crystals, as the intensity of Bragg spots does not change.

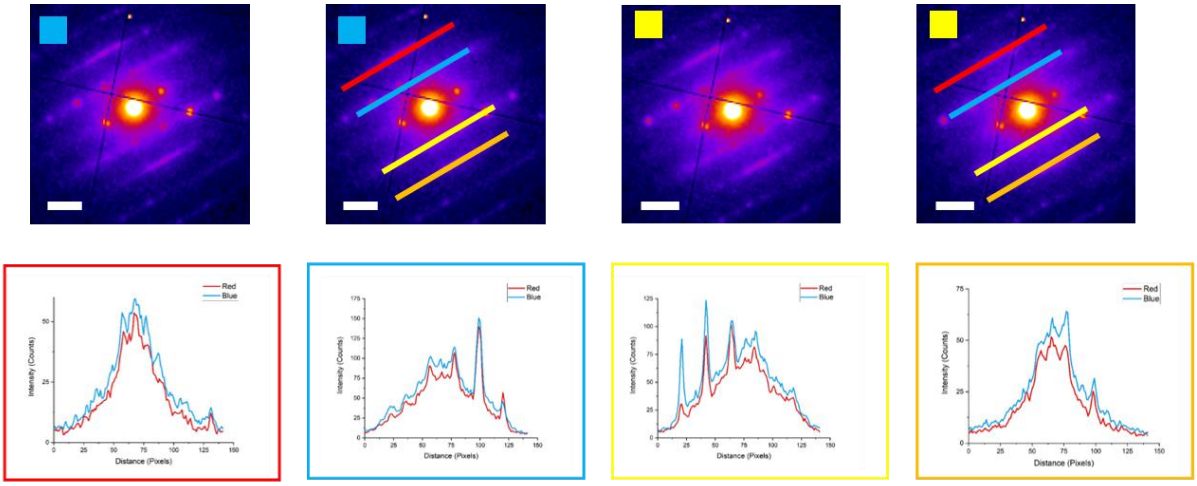

Figure 5.15: Line profiles across (hkl) reflections measuring intensity corresponding to the areas outlined by the pink and orange boxes in Figure 5.14. Diffraction pattern scale bars indicate 0.5 Å^{-1}.

5.3.3 00ℓ Spots

As 00ℓ spots were rarely seen in $C_{30}H_{61}OH$ crystals, VDF images using a virtual aperture for where 00ℓ spot positions should be were formed. No contrast attributable to 00ℓ diffraction was observed (Figure 5.16c). A diffraction pattern from the bright area in Figure 5.16d was extracted to observe if any 00ℓ spots could be seen in this smaller area, but as Figure 5.16f shows these spots are not present, although this pattern suffers from low signal to noise due to being summed over a low number of pixels. Figure 5.17 presents VDF images formed from the same 00ℓ spot area in the corresponding diffraction patterns for additional $C_{30}H_{61}OH$ crystals, but no sharp bright areas were seen in these images either. These suggest a lack of highly ordered domain packing within the $C_{30}H_{61}OH$ crystals.

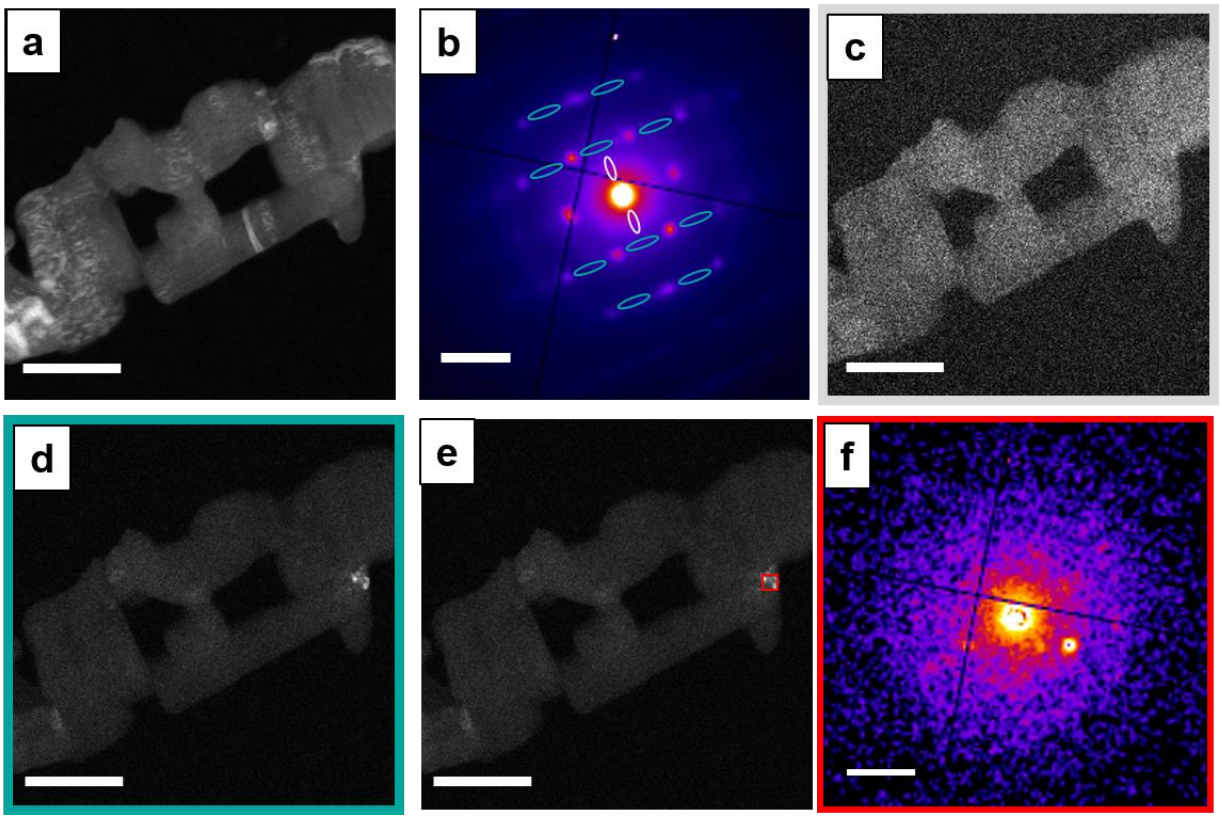

Figure 5.16: (a) Low angle ADF image of a $C_{30}H_{61}OH$ epitaxially orientated crystal. (b) Average diffraction pattern of crystal in (a). (c) Virtual dark field image produced from signal area defined by the grey ovals in the average diffraction pattern (b). (d) Virtual dark field image produced from diffuse scattering signal in the diffraction pattern defined by the blue ovals in the average diffraction pattern (b). (e) Repeat of (d) with red box outlining the area used to form (f), a summed diffraction pattern.

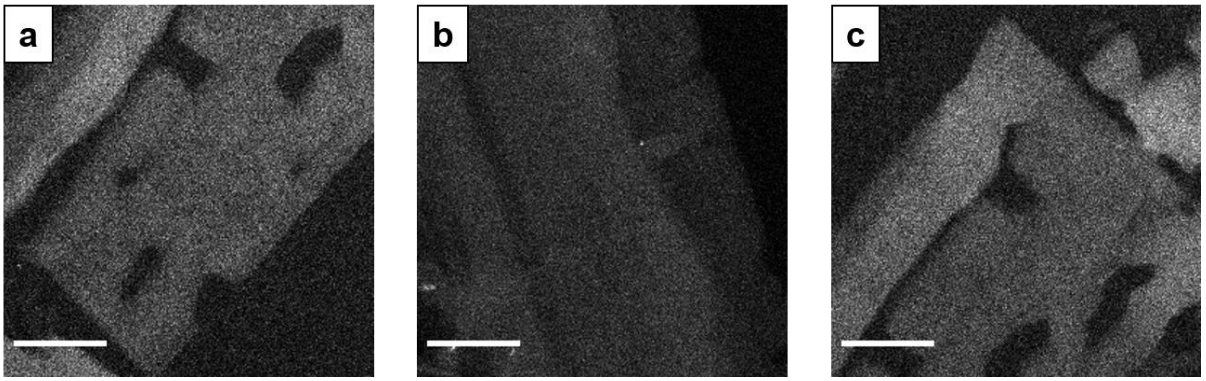

Figure 5.17: Virtual dark field images produced from signal area in the average diffraction pattern for each corresponding dataset along the c* direction next to the central beam (where a 00ℓ line signal should arise). All bright field image scale bars indicate 500 nm.

The staircase or nematic phase packing as well as the strong hydrogen bonding interactions between paired alcohol groups within $C_{30}H_{61}OH$ crystals (Figure 5.18) likely explains the observed differences in crystal formation in the 'chains-flat'

orientation between $C_{31}H_{64}$ and $C_{30}H_{61}OH$ (Cuevas-Diarte and Oonk, 2021). Figure 5.18 is a simplified schematic where the black lines represent the carbon chain backbone, and the red circles represent the –OH groups in the $C_{30}H_{61}OH$ chains. In the alkane, where a hydrogen bonding network is not present, when there is a tilt between domains the alkane chains can slip to fill the gap. In the alcohol, this tilt causes disruption of the strong hydrogen bonding network so isn't favoured. Changes in orientation across alcohol-terminated groups would therefore require distortion and loss of stabilising hydrogen bonding interactions. Grain formation is likely disfavoured by the less ordered stacking in the staircase or nematic phase structure.

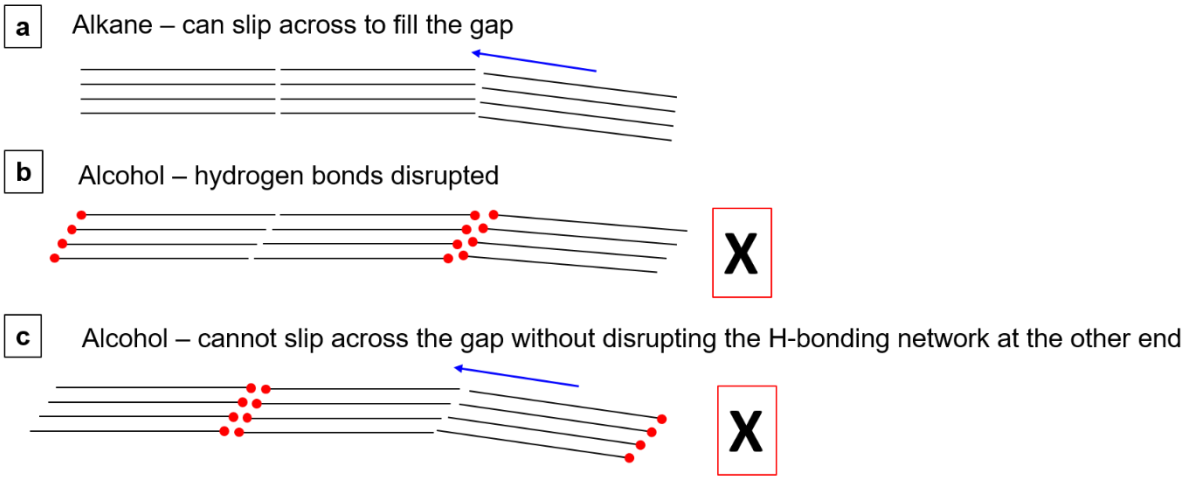

Figure 5.18: A simplified schematic to show a possible explanation why grain structure is lost in $C_{30}H_{61}OH$ vs $C_{31}H_{64}$. The black lines represent the carbon chains, with the red circle representing the alcohol group in $C_{30}H_{61}OH$. The $C_{31}H_{64}$ chains pack in straight lines end to end, whereas the $C_{30}H_{61}OH$ chains arrange with a "staircase" packing. With this staircase packing, there is a barrier to the chains tilting not seen in $C_{31}H_{64}$ (b and c). The X in the red box indicates these two schematics are unlikely to happen.

Together, the presence of grain microstructure and lamellar ordering in $C_{31}H_{64}$ crystals, and the lack of both of these features in $C_{30}H_{61}OH$, stand out as defining characteristics of each end-member ($C_{31}H_{64}$ and $C_{30}H_{61}OH$), setting up further examination of intermediate compositions in binary mixtures.

5.4 Binary Mixtures

5.4.1 Scanning Electron Diffraction

Comprehension of the microstructure in binary mixtures of the two components is important to understand how these two end-members may interact with each other and then how molecules may be able to move across this barrier in crops. Figure 5.19 extends the SED analysis to binary mixtures from 15 to 50% $C_{30}H_{61}OH$ within $C_{31}H_{64}$.

This range corresponds to the compositions of biological interest, with the total alcohol content estimated at 15-30% in the *Schefflera elegantissima* plant (Jetter and Riederer, 2016). Figure 5.19 shows low-angle ADF-STEM images and corresponding average diffraction patterns from the entire field of view for each endmember as well as for 15%, 30%, and 50% $C_{30}H_{61}OH$, all prepared in the 'chains-flat' orientation. The low-angle ADF-STEM images reveal defined grain microstructure across compositions from 0-30% $C_{30}H_{61}OH$, with only some grain structure visible at 50%. The grain structure, where visible, follows a consistent crystallographic orientation with the short axis of the grains aligned with the unit cell *c*-axis (Figure 5.19, dashed and solid blue lines in diffraction and ADF-STEM images, respectively). Overall, with increasing $C_{30}H_{61}OH$ content the definition of grain boundaries decreases, with shorter and more curved boundaries appearing at 30% and 50% $C_{30}H_{61}OH$. These observations may reflect increasing nematic phases (tending toward staircase-like packing) bridging across grains. VDF images were formed using a virtual aperture for 00ℓ spot positions for 15%, 30%, and 50% $C_{30}H_{61}OH$ in addition to the VDF images formed for the pure endmembers (Figure 5.19, third row). No contrast attributable to 00ℓ diffraction was observed in the 50% $C_{30}H_{61}OH$ VDF image. Some bright patches were seen in the 15% $C_{30}H_{61}OH$ VDF image, whereas some bright sharp lines of intensity, as seen in the pure $C_{31}H_{64}$ VDF image, were seen in the 30% $C_{30}H_{61}OH$ VDF image. These images were chosen as representative of further datasets of the sample.

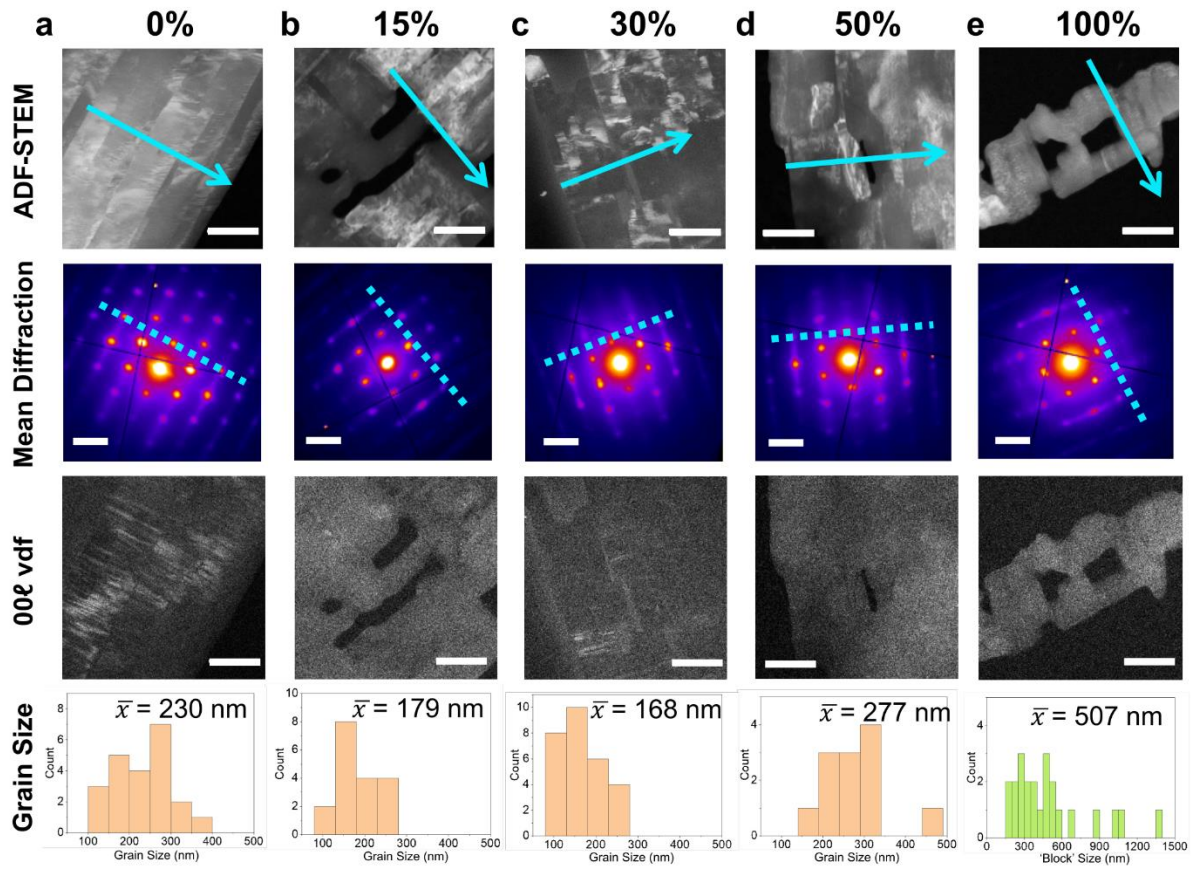

Figure 5.19: ADF images and corresponding average diffraction patterns of [100] orientated binary mixture crystals. Compositions range from pure phase $C_{31}H_{64}$ on the left, with increasing alcohol content, to pure phase $C_{30}H_{61}OH$ on the right. The percentage indicates the content of alcohol by molar fraction in the composition. Green arrows indicate the *c*-axis direction (alkyl chain axis) following the polyethylene cell (c_{PE}). Arrows overlaid on the SED patterns mark the indexation of the patterns to the PE cell in the $[001]_{PE}$ 'down-chain' orientation and the $[100]_{PE}$ 'chains-flat' orientation. Corresponding VDF images, produced from the signal area in the average diffraction pattern for each corresponding dataset along the c* direction next to the central beam (where a 00ℓ line signal should arise), are found in the third row. Histograms of measured grain sizes for each respective composition and the average grain size are included below. The histogram below the pure phase $C_{30}H_{61}OH$ ADF image and diffraction pattern indicates the measured 'block' sizes, believed to indicate the size of extended crystal growth in this system. All ADF scale bars indicate 500 nm, all diffraction pattern scale bars indicate 0.5 $Å^{-1}$.

Again, to further confirm the domain assignment of lamellar ordering of the 00ℓ VDF intensity, diffraction patterns only from bright regions in the 00ℓ VDF for both 15% and 30% $C_{30}H_{61}OH$ were extracted (Figure 5.20). The presence of 00ℓ spots in these diffraction patterns, not seen in the average diffraction pattern, confirms some lamellar order within the crystals up to 30%, which decreases with addition of alcohol after this point. This ordering is not to the same extent as we see in the pure $C_{31}H_{64}$, as indicated

by the lower relative intensity of the 00ℓ spots, demonstrating disruption to the lamellae on addition of alcohol to the binary mixture.

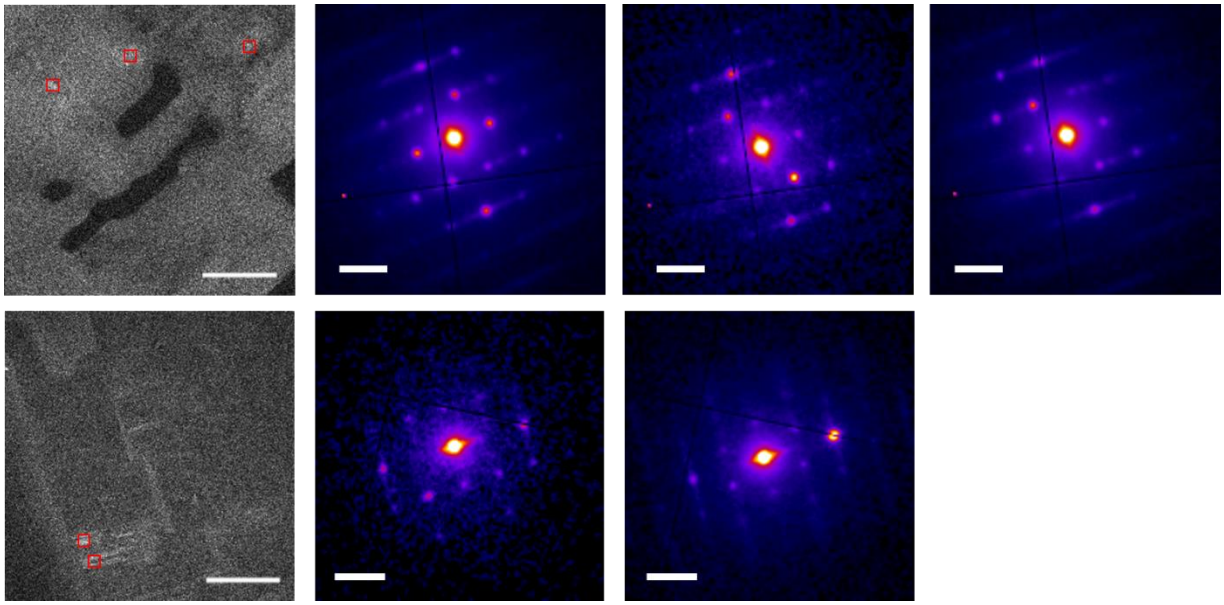

Figure 5.20: Summed diffraction pattern extracted from bright pixel areas, (red squares) in 15% $C_{30}H_{61}OH$ (top row) and 30% $C_{30}H_{61}OH$ (bottom row) 00ℓ vdf images (images repeated here from Figure 20).

Histograms of grain size, taken as the grain width, showed no consistent trend across this composition range (Figure 5.19, bottom row). The average grain size decreased from 0% to 15% to 30% $C_{30}H_{61}OH$, but falls broadly between 150-300 nm. Certainly the incorporation of moderate quantities (0-50%) of $C_{30}H_{61}OH$ does not alter the grain size substantially. Notably, the increase in average grain size at 50% $C_{30}H_{61}OH$ may arise from reduced precision in measurements due to the loss of defined boundaries. As no grains were visible in 100% $C_{30}H_{61}OH$, a 'block' size was measured instead to evaluate any similarity in these blocks and the grains observed in the other compositions. The average size of these blocks in 100% $C_{30}H_{61}OH$ was 507 nm, roughly double the size of the grains seen in the pure $C_{31}H_{64}$ and binary mixtures, and so any correspondence between these features and the tilted grains in 0-50% $C_{30}H_{61}OH$ was ruled out.

5.4.2 Atomic Force Microscopy

Recognizing the value of adhesion mapping by AFM for the observation of alcohol group termination in the 'down-chain' orientation (Chapter 4, Figure 4.14), further AFM data for the binary mixtures in the 'down-chain' orientation were acquired. Figure 5.21 presents height and adhesion mapping by AFM of 0%, 30%, 50%, and 100% $C_{30}H_{61}OH$ prepared by drop-casting on mica, as well as matched low-angle ADF-STEM images from SED prepared by drop-casting onto continuous carbon TEM grids.

For 0% and 30% $C_{30}H_{61}OH$, the images all show faceted crystals with terraces (height images) with consistent adhesion. The low-angle ADF-STEM images exhibit some bend contour contrast but otherwise show smoothly varying contrast within micron-sized regions. At 50%, both AFM and low-angle ADF-STEM highlight pronounced differences: the AFM height image shows a much more substantial variation in height at the sub-micrometre length scale. As with the pure alcohol, the adhesion values at 50% $C_{30}H_{61}OH$ are bimodal, seen more clearly in Figure 5.22.

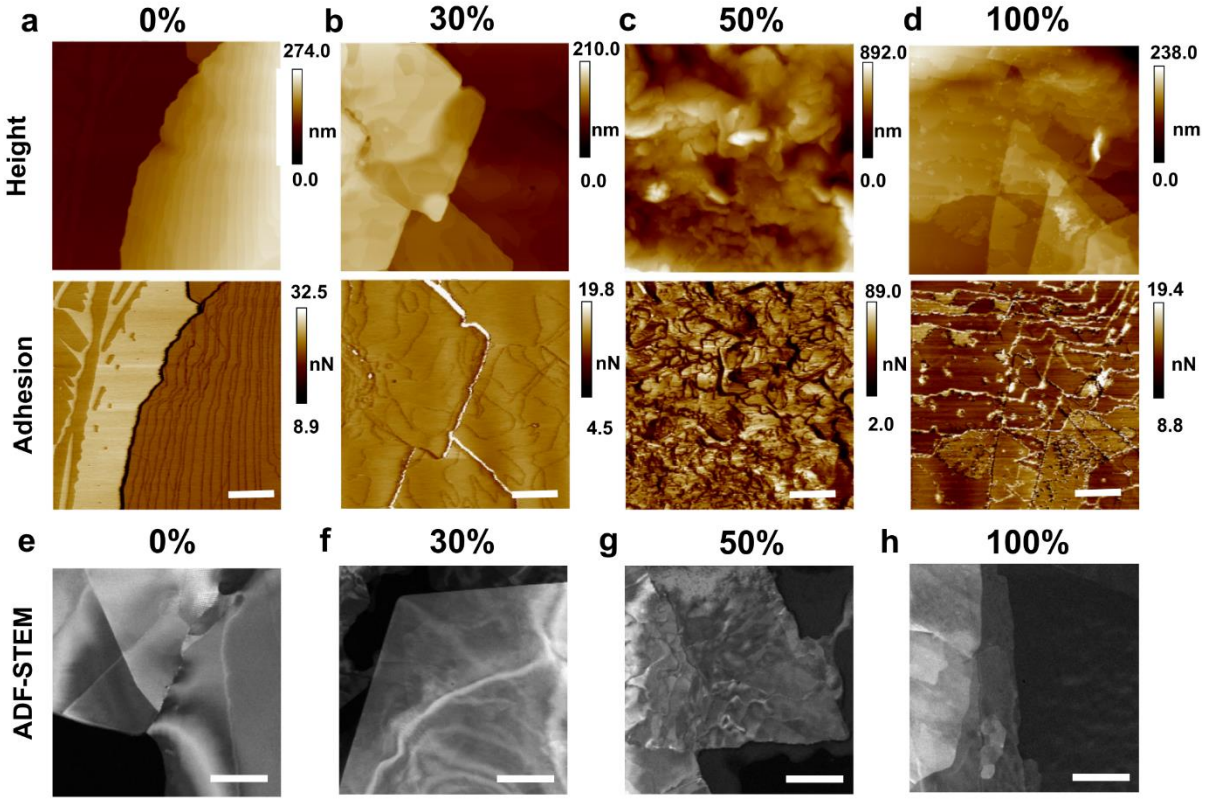

Figure 5.21: Height and adhesion profiles (a-d) obtained through AFM, and ADF STEM images (e-h) for pure phase alkane, alcohol and binary mixture samples. Compositions range from pure phase $C_{31}H_{64}$ (a, e), with increasing alcohol content, to pure phase $C_{30}H_{61}OH$ (d, h). The percentage indicates the content of alcohol by molar fraction in the composition. The two AFM panels in the 100 % alcohol composition column are reproduced from Figure 2. Scale bars for the AFM data indicate 2 µm. Scale bars for the STEM images indicate 500 nm.

The adhesion image likewise exhibits sub-micrometre variations, and contrast variations with irregular contours at similar length scales were also recorded in low-angle ADF-STEM. At 100% $C_{30}H_{61}OH$, the AFM height once again was comprised of terraces with the characteristic bimodal adhesion variation between steps. The low-angle ADF-STEM image for $C_{30}H_{61}OH$ also shows faceted crystals with micrometre-scale limited intensity variation within plates.

The lack of bimodal adhesion variation between steps at 30% $C_{30}H_{61}OH$ shows no observable systematic ordering of the terminal alcohol groups at this composition. At 50% $C_{30}H_{61}OH$, the adhesion data together with significant contrast variations in low-angle ADF-STEM may point to separation of phases in these drop-cast mixtures (Figure 5.22), possibly into two or more immiscible phases. Up to 30% $C_{30}H_{61}OH$, the data appears consistent with the formation of a single crystal, likely a solid solution within the $C_{31}H_{64}$ structure, as may be expected from the rich solid solution formation expected from alkanes of similar lengths (Fryer et al., 1997),'(Kitaigorodskii, 1961), (Dorset, 1987). SED of the 'chains-flat' samples point to a similar conclusion, with the loss of distinct grain structures arising above the 30% $C_{30}H_{61}OH$ (Figure 5.19). At higher $C_{30}H_{61}OH$ content, the competition between staircase packing in $C_{30}H_{61}OH$ and lamellar ordering in $C_{31}H_{64}$ likely introduces structural disruption of the wax microstructure. Due to the similarity in d-spacings, however, an unambiguous evaluation of changes in the crystal phases with compositions beyond changes in the systematic changes in disordered microstructure is not possible by these electron diffraction measurements. The limit in precision of the d-spacing measurements is dependent on the convergence angle of the electron beam with a reciprocal relationship between the two. Due to the similarity in chain length between the two molecules, the d-spacings of the two molecules are too similar to distinguish.

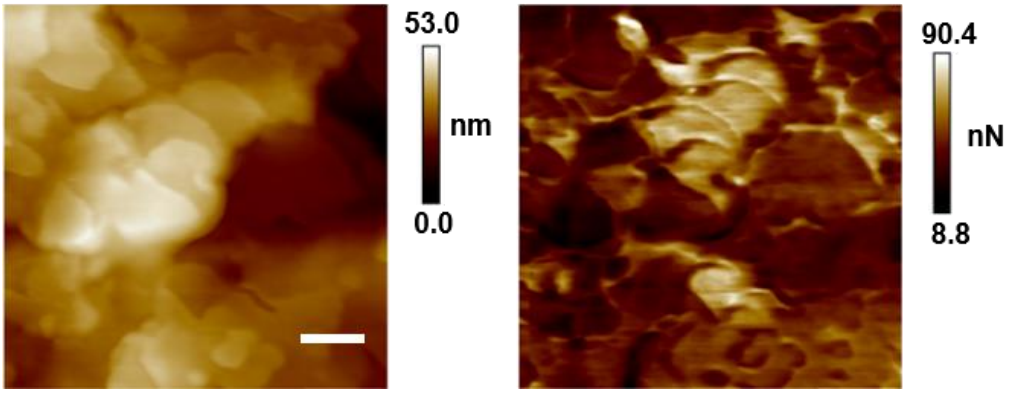

Figure 5.22: Height and adhesion profiles obtained through AFM for a binary mixture containing 50% $C_{30}H_{61}OH$. The scale bar indicates 250 nm. The higher magnification means bimodal adhesion variation is more clearly seen.

It is important to consider the way these samples are prepared for EM and if this has an effect on the crystallisation of the binary mixture, i.e. whether $C_{30}H_{61}OH$ is in fact incorporated in the $C_{31}H_{64}$ crystals or they crystallise in two separate structures. 'Chains-flat' oriented samples are prepared from the melt using benzoic acid as the template, with the two hydrocarbon end-members solidifying together, separate to the benzoic acid. As the binary mixture crystals are prepared this way it can be concluded that melting and re-solidifying together does in fact incorporate the $C_{30}H_{61}OH$ chains

within the crystals separate to the benzoic acid. There are microstructural changes observed as a result of additional $C_{30}H_{61}OH$ content, which reinforces the conclusion that $C_{30}H_{61}OH$ is incorporated within the crystal and causes these changes. For the 'down-chains' orientated samples, there is a risk that only $C_{31}H_{64}$ or $C_{30}H_{61}OH$ will be nucleated during evaporation of the solvent. However, as AFM has shown, there are variations in the crystals prepared across the composition range. This supports the fact that there are $C_{30}H_{61}OH$ content induced changes, so it can be concluded that for this orientation too the $C_{30}H_{61}OH$ chains are incorporated into the crystals.

5.4.3 Electron Energy Loss Spectroscopy

Electron energy loss spectroscopy (EELS) can be a powerful tool to provide elemental information from a sample at the nanometre scale. It was explored whether the O *K*-edge could be resolved in the EELS spectrum of a $C_{30}H_{61}OH$ sample, and if this could be mapped to provide an elemental indicator for where the $C_{30}H_{61}OH$ chains incorporate within a binary mixture. Figure 5.23 shows an example EELS spectrum from a bulk $C_{30}H_{61}OH$ sample prepared 'down-chains'. The oxygen *K*-edge onset is at ~532 eV in an EELS spectrum. In this figure, a small peak can be seen at this energy loss when the background is subtracted, which can be attributed to the O *K*-edge. However, compared to the C *K*-edge onset at ~285 eV, this O *K*-edge peak is barely visible and difficult to resolve as a real signal. This signal is small because for every oxygen atom in the sample, there will be 30 carbon atoms, and the carbon support EM grid will also increase the carbon edge signal in comparison to the oxygen signal. To try and increase the signal from the oxygen *K*-edge, EELS spectra were acquired under cryo conditions. Cryo conditions should increase the stability of the sample to the electron beam so a higher signal could be obtained. However, the presence of vitreous ice meant the O signal from the wax sample was swamped by the O signal from the ice.

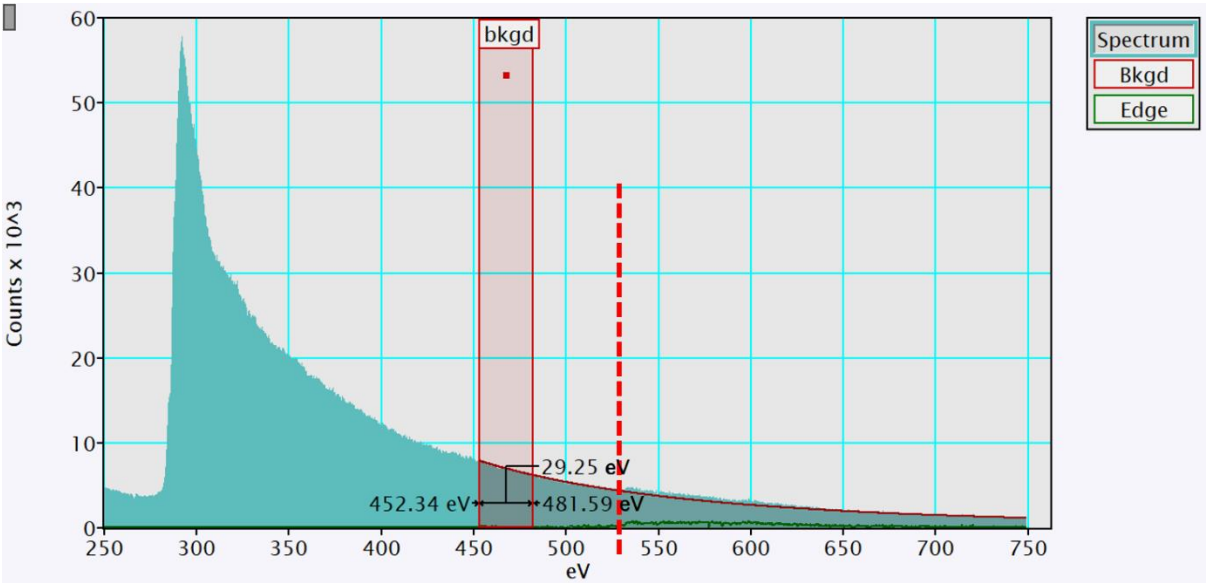

Figure 5.23: EELS spectrum of a $C_{30}H_{61}OH$ crystal. The background window is identified in red, and has been subtracted from the signal to form the green edge line.

5.5 Summary and Implications for Leaf Waxes

The central role of the IW layers on plant leaves in controlling functions such as restricting water loss and determining molecular diffusion rates to the leaf surface is well established and is important for both biological understanding and for developing agrochemical crop protection strategies (Riederer and Müller, 2007),(Kunz et al., 2022) Directly observing and quantifying the hypothesized, heterogeneous 'brick and mortar' structure of the IW layer is therefore crucial for understanding the mechanisms underpinning its functions. The nanoscale analyses of replicate leaf waxes presented in this work reveal the co-existence of highly ordered domains of lamellar packing within larger, anisotropic grains within each $C_{31}H_{64}$ crystal together with nematic phases of disordered chains surrounding the domains of lamellar packing. These observations refine the 'brick and mortar' with nanoscale crystallographic precision. Moreover, the systematic loss of lamellar domains with corresponding increase in nematic phase content, and reduction in grain microstructure with alcohol content while retaining dynamical disorder in the chain packing are all likely to increase diffusion rates through a wax crystal. This points to the balance of *n*-alkane and *n*-alkanol composition as a source of composition-determined microscopic diffusion pathways through the IW layer in plant leaves. Thus the microscopic heterogeneity of these waxes reported here provides structural outlines for mechanistic models of layer flexibility, permeability to molecules, such as those found in crop protection products, in leaf waxes, and how the IW layer stops dehydration in plants.

Low-dose SED revealed a hierarchical tilted grain microstructure in $C_{31}H_{64}$, containing ordered lamellar domains as well as nematic phases and dynamical disorder along the chain axis. The grain microstructure could be thought of as anisotropic as it extends in a long way in directions normal to the long axis of the chains but extends only tens of unit cells along the long axis of the chains. Grain microstructure was absent in $C_{30}H_{61}OH$ crystals and no lamellar ordering was observed. These observations suggest significant staggered or disordered alignment of chain ends as described in nematic phase packing, possible in β-form $C_{30}H_{61}OH$, or ordered staircase packing typical of γ-form $C_{30}H_{61}OH$. Experimental evidence of grain microstructure, mis-aligned chain ends and nematic phases co-existing with lamellar ordering, and dynamical disorder suggest the unit cell descriptions serve as guideposts only for the 'endmember' structural motifs in what is otherwise a complex, nanoscale landscape comprising a distribution of structures at the nanoscale.

Moreover, not only does this heterogeneity of ordered and disordered structures vary spatially, it also varies systematically with composition in binary mixtures of these *n*-alkanes and *n*-alkanols. At intermediate compositions, increasing alcohol content correlated with a loss of grain structure in 'chains-flat' crystals and changes toward smaller, granular structures in 'down-chain' crystals. These microscopic observations separate and assign features not otherwise distinguishable in measurements at lower spatial resolution. Disentangling lamellar ordering and diffuse scattering at the nanoscale opens new avenues for analysis of diverse wax crystals and to test order-disorder hypotheses only indirectly assessed previously.

The retention of microstructure reminiscent of the single-component $C_{31}H_{64}$ wax up to 30% $C_{30}H_{61}OH$ suggests likely solid solution behaviour in the composition range of plant IW layers. The presence of regions with nematic ordering mirror the 'mortar' description in the prevailing 'brick and mortar' structural hypothesis, i.e., the introduction of $C_{30}H_{61}OH$ may provide the disordering required for high-diffusion pathways. Compositions at or beyond 50% $C_{30}H_{61}OH$ appear to introduce more significant microstructural modifications. These findings establish an initial basis for examining more complex wax compositions. Intracuticular wax layers of other species contain additional functional groups such as ketones and esters (Buschhaus and Jetter, 2011). Additional interactions between these additional functional groups may further affect microstructure, and wax materials properties. In particular for plants, the structure of the IW layer is important to limit non-stomatal water loss against drought (Jetter and Riederer, 2016), so establishing a structure-property relationship could be used to engineer crops to improve cuticle performance (Jenks et al., 2007), (Buschhaus and Jetter, 2012). In the next chapter, the interaction of the endmembers

and a binary mixture with a molecular adjuvant is studied, exploring how these replica leaf wax systems may interact with components in crop protection products.

In this results chapter identifying the OH group in the $C_{30}H_{61}OH$ chains was found to be difficult using spectroscopic techniques. In the final results chapter, Chapter 7, a different solid solution forming system consisting of two small organic molecules is studied using miocroscopic techniques where it may be possible to see a Bragg spot/spacing shift as a result of solid solution formation, and the presence of a high concentration chemical tag allows the exploration of solid solution tracking through spectroscopic characterisation (such as EELS or EDS). Where this chapter also focused on solid solution formation in long chain molecules, the final chapter looks at a solid solution between two small molecular crystals which may have more applicability to the pharmaceutical industry.

Chapter 6

Evaluation of the Microscopic Mode of Action of an Adjuvant, TEHP, with Long Chain *N*-Alkane and *N*-Alkanol Materials

6.1 Introduction

In Chapters 4 and 5, a hierarchical microstructure of highly ordered domains within larger grains in *n*-hentriacontane crystals was established, where addition of 1-triacontanol (alcohol terminated) wax introduces disorder into the binary mixture system. This system is taken as a representative model for similar *n*-alkane and *n*-alkanol systems of similar chain lengths, and as a model of a synthetic intracuticular wax layer (IW). The IW layer on a leaf controls the movement of molecules in and out of the upper surface of a leaf. It is important to understand this structure for the design of crop protection products applied by spraying on this upper leaf surface. Crop protection products typically contain an active ingredient (AI), and other components which aid the ability of the formulation to reach the target region of the leaf. One of these components is called an adjuvant. This chapter will investigate the effect of exposing *n*-alkane, *n*-alkanol and binary mixtures of these waxes to an adjuvant compound, adjuvant tris(2-ethylhexyl)phosphate (TEHP), assessing bulk characteristics such as solubility, melt temperature and crystallinity and linking these to microstructure measured by TEM and SED. TEHP is a common adjuvant addition to crop protection products and has been shown to increase diffusion of AIs across leaf cuticles (Arand et al., 2018). There is therefore interest as to whether TEHP exposure alters the structure of these synthetic IWs, and what the mechanism of interaction is between this adjuvant and the IW model layer.

An adjuvant in an agrochemical formulation has been defined in many different ways (Hazen, 2000); a general definition can be given as “any compound that is added to a herbicide formulation to facilitate the mixing, application or effectiveness of the herbicide” (Tu and Randall, 2003). These chemically or biologically active compounds either increase the desired impact of the formulation or decrease the total amount of formulation needed to achieved a desired impact. Adjuvants are well known to enhance the uptake and improve the activity of foliar applied herbicides (Kirkwood, 1993).

Adjuvants can generally be classified into three categories; surfactants, oil-based adjuvants, or spray adjuvants. Surfactants and oil-based adjuvants can both improve the wetting and spreading ability of the spray droplets on the surface of the leaf (Schreiber et al., 1996), (Nairn and Forster, 2024). They both also interact with the

cuticle layer of the leaf (Hu et al., 2019). Spray adjuvants change the properties of the spray mix itself, such as pH adjustment and buffering or as solubility agents (Tu and Randall, 2003). However, there can be overlap between these definitions, for example surfactants can change physico-chemical properties of the spray mix, such as surface tension, so there are many possible mechanisms of action for how adjuvants are effective (Janku et al., 2012).

The leaf wax layers, particularly the intracuticular layer, constitute the principal barrier restricting herbicide movement into a plant (Schonherr and Riederer, 1989). Adjuvants modify the properties of the spray solution to improve the ability of the AI to target, penetrate or protect the target organism. Here we focus on adjuvants that are considered to improve uptake within a leaf. Adjuvants can be incorporated into a formulation or can be added separately into the spray tank alongside other agrochemical products (Cox and Zeiss, 2022). These formulations are usually sprayed onto crops, so the formulation and adjuvant are found in the liquid state. TEHP is found as a liquid at room temperature, but other adjuvants are found in the solid form so are dissolved or otherwise dispersed in a liquid formulation. Adjuvants can also enhance product performance by replacing high value or high toxicity AIs with lower value surfactants/ molecules. This leads to less chemical environmental pressures and improved food safety due to lower residue levels (Tu and Randall, 2003).

Understanding the as yet unknown mechanism of adjuvants is difficult as one adjuvant may impact several steps of the application procedure. These stages can be thought of as; (1) initial droplet formation, (2) droplet application, e.g. wetting and retention, and (3) interaction with the cuticular membrane (Stock and Briggs, 2000). Arand et al. investigated the function of different adjuvants on cuticular penetration of the AI pinoxaden and its efficacy to control weed growth by measuring different properties such as retention, spreading and diffusion and observing which mechanisms featured in the action of each adjuvant (Arand et al., 2018). Adjuvants were applied as aqueous solutions or emulsions in droplet form with an adjuvant concentration of 0.1 % (w/v). Tracking the amount of AI that had passed into a receiver droplet of water on the other side of the membrane by ultra-performance liquid chromatography-mass spectrometry served to measure the diffusion across a membrane. Compared to the ethoxylated ester adjuvants studied, the adjuvant TEHP did not increase retention and spreading of the AI but did increase the diffusion of the AI across isolated cuticular membranes. As TEHP greatly increased AI uptake, even though it did not greatly increase retention or spreading of the droplets, the authors identified movement across this cuticle as the significant barrier to AI uptake. However, no mechanism for this movement explaining how TEHP aided the diffusion relative to the ethoxylated esters was offered. The Arand et al study highlights the benefits of taking a multi-technique approach

measuring droplet contact angle, surface tension, and diffusivity across the membrane, evaluating different properties such as retention, spreading and cuticular diffusion, to determining the mechanism of action of these adjuvants.

Understanding the mechanism of action of particular adjuvants that facilitate the movement of molecules across the leaf wax barrier may offer insights needed for the improved design and development of crop protection products that act within a leaf. There are several potential mode of actions for how adjuvants may work, including acting as a plasticiser, dissolution of the wax materials, or potentially introducing disorder or amorphous phases in the IW layer. There is some similarity between these modes of action, for example dissolution of materials at the atomic scale may introduce disorder into a system. This also opens the question of concentration of the adjuvant compared to the wax and how this may affect the mode of action. For example, low concentrations of the adjuvant may dissolve within a wax, but large concentrations of the adjuvant may act instead as a solvate and dissolve the wax itself. These factors are important factors to consider when trying to determine the mode of action.

A plasticiser is a chemical which is added to a polymer to increase its flexibility. The plasticiser incorporates in between the polymer chains and makes the material more flexible. The long chain waxes studied in this thesis have similarities to polymers with extended carbon chain backbones, albeit more extended backbone chains in polymers. TEHP has been shown to act as a plasticiser with synthetic rubbers and polyvinyl chloride (PVC) (Marklund et al., 2005). Furthermore, TEHP has been suggested to act as a plasticiser specifically with long chain wax materials and plant cuticles (Bronzato et al., 2023), (Kunz, 2023), but this piece of work comments on the need for further study of the system to fully quantify the mechanism of action of TEHP as a plasticiser. A different class of adjuvant, alcohol ethoxylates (AE), have been ascribed to act as a plasticiser due to increase in AI diffusion when the AE is present (Burghardt et al., 1998). The quantitative measure of free volume in the amorphous wax fraction also increases in the presence of the AE.

Fagerström proposed that surfactants, $C_{10}EO_7$ and $C_8G_{1.6}$, interact with the crystalline parts of the IW layer, by incorporating within crevices, and irreversibly creating a more fluid, softer cuticle wax (Fagerström et al., 2014). The effect of $C_{10}EO_7$ was stronger than the effect of $C_8G_{1.6}$. TEHP is larger than both molecules but more similar to the larger molecule of $C_8G_{1.6}$ than $C_{10}EO_7$, so it may not interact with the same mechanism of action as it cannot incorporate in the crevices in the same way. Figure 6.1 shows the different molecules. Studies have looked at performing molecular dynamic simulations to understand the movement of volatile organic compounds across a model cuticle, concluding that diffusivity increased in completely amorphous waxes

(Ray et al., 2022). Such studies underscore the effect of crystalline ordering on cuticular permeability. This previous study, however, focused on the epicuticular wax layer. Chapters 4 – 5, in contrast, have focused on the IW layer. The previous chapters established the effect of *n*-alkanol wax content on the order or disorder in a binary wax system rich in *n*-alkane wax, so it stands to reason the *n*-alkanol content in an IW layer may affect the mechanism of adjuvant interaction or movement across this barrier.

AFM results from Walker showed regions of a live leaf surface that have globular wax features becoming smoother in areas exposed to TEHP deposits and then dried (Walker, 2017). The leaf system this was applied to, a Field Bean, has little to no reported extracuticular wax layer (Riederer, 2007), so suggests these globular wax structures are a result of the IW layer. TEHP in this case was applied as droplets at concentrations of 0.2% w/w in deionised water. This result suggests the TEHP may work by breaking down the globular structures and this may involve changing the morphology of the IW layer.

This chapter focuses on the interaction of TEHP with synthetic IWs, looking at the structural and crystallographic effect of addition of TEHP specifically to $C_{31}H_{64}$ and $C_{30}H_{61}OH$ crystals and binary mixtures. TEHP is a viscous, colourless to pale yellow liquid that is immiscible in water, but soluble in alcohol, acetone and ether. The structure of the TEHP molecule is shown in Figure 6.1.

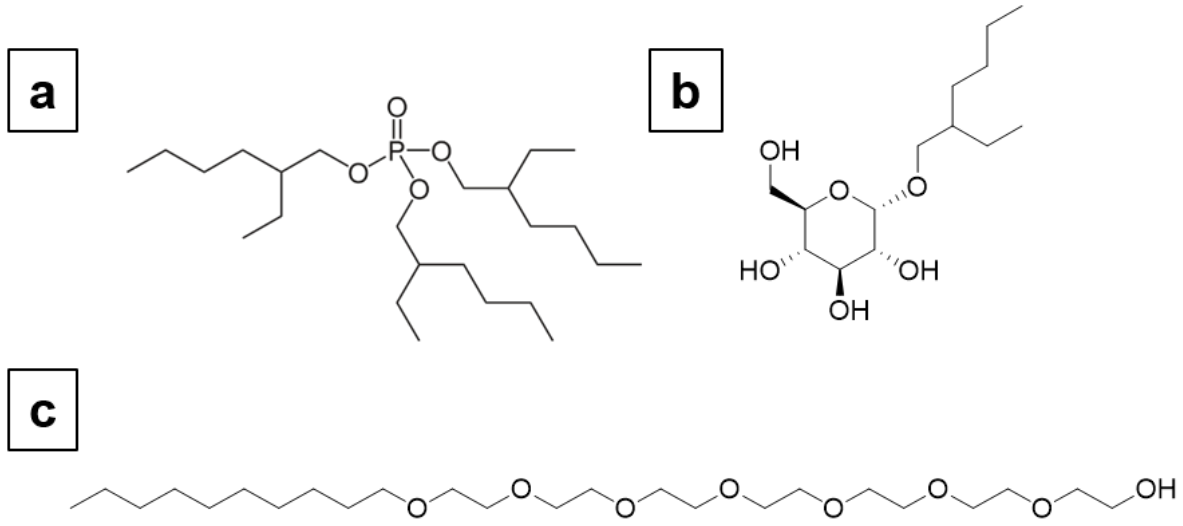

Figure 6.1: (a) Structure of the tris(2-ethylhexyl)phosphate (TEHP) molecule. (b) Structure of the $C_8G_{1.6}$ surfactant. (c) Structure of the $C_{10}EO_7$ surfactant.

This chapter uses a range of techniques to assess these changes from the bulk material, e.g. DSC, and XRD, to the nanoscale, e.g. TEM, SED, and EDS. These different techniques are used as a way to probe different properties in order to link the nanoscale structure of synthetic IWs exposed to TEHP to any observed changes in bulk properties, which may link to diffusion rates within the waxes. This chapter

assesses these techniques against the potential mechanisms of action of TEHP; dissolution of material or acting as a plasticiser.

6.2 Solubility

The solubility at room temperature of the two wax samples, $C_{31}H_{64}$ and $C_{30}H_{61}OH$ when immersed in TEHP, was initially tested. This solubility of both materials was tested at room temperature because the application of adjuvants to leaves would not occur at an elevated temperature. The purpose of determining the solubility was to probe whether dissolution of the material was a factor in the mechanism of action of TEHP exposure on waxes. Solubility is typically studied by isothermal and nonisothermal or polythermal methods (Mohan et al., 2002). Isothermal methods involve measuring the solubility at a constant controlled temperature with agitation. The first method requires adding the solute in excess and stirring for 4 – 24 hours, and the resulting solution is then analysed for the solute. A second method involves adding small quantities of solvent until the traces of the crystalline material disappear, at which point more material is added until the solution becomes saturated such that crystal remain. It was this second method that was initially attempted in this work using a piece of equipment called Crystalline, a crystallisation platform that uses a camera with up to 0.63 microns per pixel resolution to identify the presence of solids retained in a solution. Using this technique traces of 0.5 mg of solid wax in 8 mL of TEHP were still seen after ~30 minutes of agitation. It was difficult to work on a lower mass of wax than this to build up to a saturation point in 8 mL of TEHP. As this small amount was deemed insoluble, this precluded this second method, and the first method was not probed also due to the small quantities already deemed insoluble.

Next, the two wax samples were both deemed mostly insoluble in TEHP at room temperature because 0.5 mg of material had not dissolved in up to 20 mL of TEHP. Figure 6.2 shows that there appeared to be a breakdown of the $C_{30}H_{61}OH$ particles, going from three larger particles (that may have been agglomerates) to several smaller particles suspended in the solution, whereas the $C_{31}H_{64}$ particle size and number appears to remain consistent to the eye.

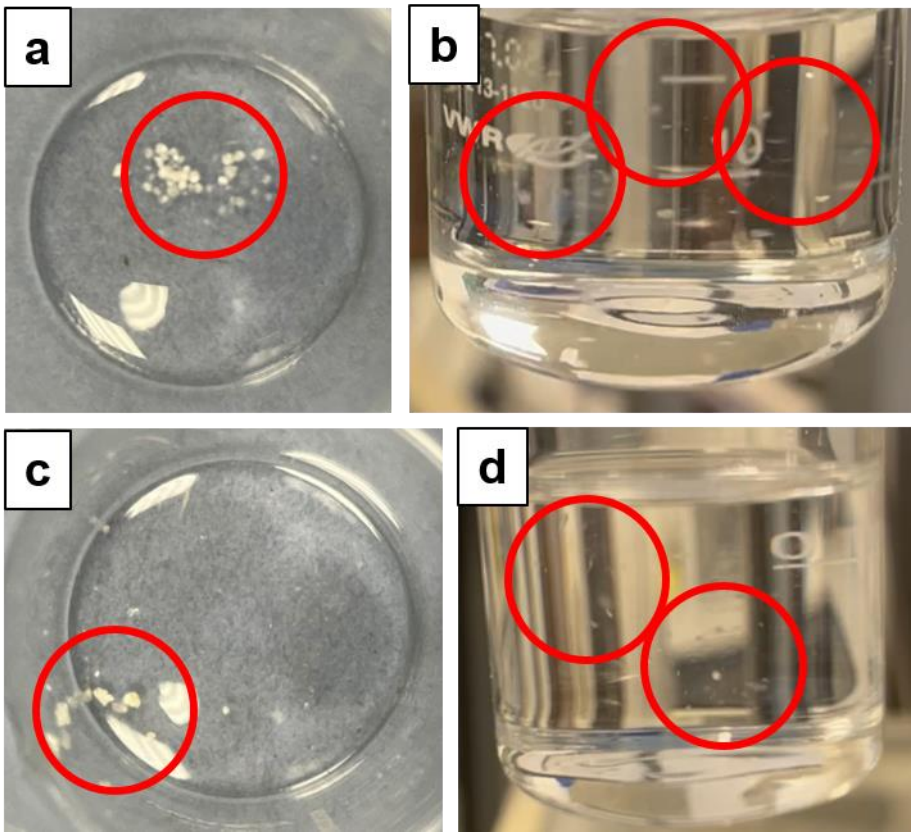

Figure 6.2: (a) 0.5 mg of $C_{31}H_{64}$ crystals in a glass beaker. (b) $C_{31}H_{64}$ crystals suspended in 20 mL of TEHP. (c) 0.5 mg of $C_{30}H_{61}OH$ crystals in a glass beaker. (d) $C_{30}H_{61}OH$ crystals suspended in 20 mL of TEHP. Red circles highlight the particles before and within the suspension.

6.3 Thermal Analysis

Thermal analytical techniques can offer insight into the phase transitions a material goes through upon heating, such as solid-solid transitions, solid-liquid transitions or decomposition of the material. Thermogravimetric analysis (TGA) analysis has previously been used when studying the effect of plasticisers on polymers, where the onset temperature of polymer degradation decreases in the presence of a plasticiser (Wong et al., 2017), (Maiza et al., 2015). TGA was performed on the two waxes, TEHP, a TEHP plus $C_{31}H_{64}$ mixture and a TEHP plus $C_{30}H_{61}OH$ mixture (Figure 6.3). In this mixture, 0.5 mg of $C_{30}H_{61}OH$ was suspended in 5 mL of TEHP (0.01% w/v). $C_{31}H_{64}$ has a single decomposition mass loss that is complete by 425 °C whereas $C_{30}H_{61}OH$ is complete by 442 °C and TEHP by 306 °C (Figures 6.3a, b and c respectively). The TEHP plus $C_{30}H_{61}OH$ mixture exhibits a two-step decomposition, two peaks are seen in the derivative (DTG), with peak 1 complete by 246 °C, and peak 2 complete by 307 °C. However, no $C_{30}H_{61}OH$ decomposition step ending at 442 °C was detected (Figure 6.3d). This second, high temperature peak falls at broadly the same temperature as the decomposition of the pure TEHP. This first, lower temperature peak aligns with a

smaller peak in the pure $C_{30}H_{61}OH$ sample, but it is not clear why the higher temperature peak does not appear in this sample. This suggests an interaction of the $C_{30}H_{61}OH$ with the TEHP. A similar test with TEHP plus $C_{31}H_{64}$ at the same mass concentration showed a very slight peak indicating a low temperature decomposition, but this peak at the lower temperature is more prominent in the $C_{30}H_{61}OH$ sample. The apparent TEHP interaction with the waxes may have altered the waxes in some way, for example plasticisation of the material, but this data alone offers no conclusive evidence.

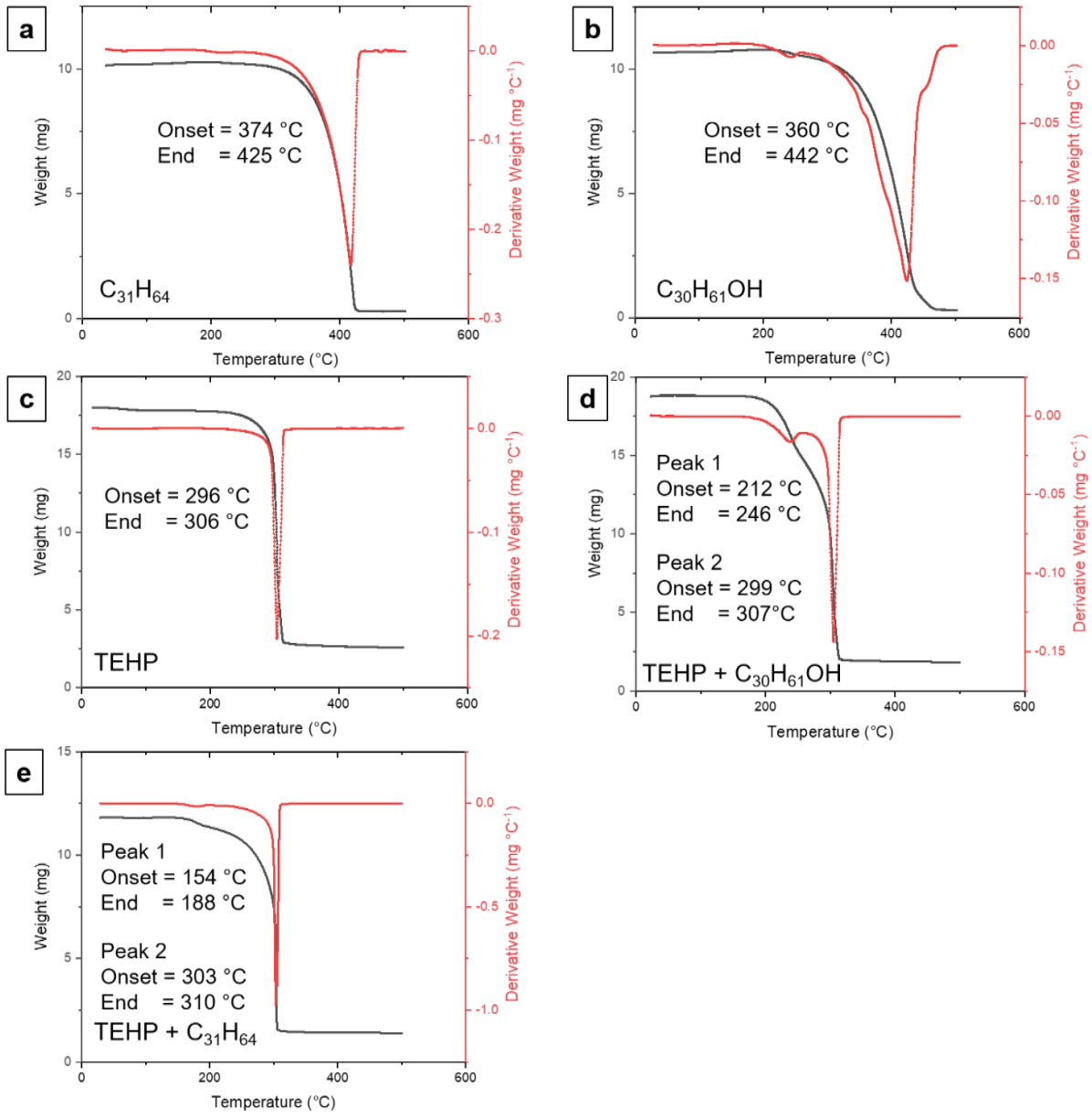

Figure 6.3: Thermogravimetric analysis curves of (a) $C_{31}H_{64}$, (b) $C_{30}H_{61}OH$, (c) TEHP, (d) $C_{30}H_{61}OH$ + TEHP, and (e) $C_{31}H_{64}$ + TEHP.

Differential scanning calorimetry (DSC) is a technique that can offer insight into phase transitions of a material. When a material is highly crystalline, a sharp endotherm peak

will be seen as latent heat is absorbed at the melting point of the material. When a material is amorphous no melting occurs and a lower temperature, glass transition endotherm is instead seen. DSC has been used extensively in the study of long-chain alkanes and has identified rotator phases (where the wax chains retain their positional order but rotate about their long chain axes) that the alkanes go through just below the melting point (Ungar, 1983), (Ungar and Mašić, 1985), (Sirota and Herhold, 2000), (Dirand et al., 2002).

DSC thermograms of each of the $C_{31}H_{64}$ and $C_{30}H_{61}OH$, taken at a heating rate of 5 °C per minute, show sharp melting point endotherms centred on 71 °C and 89 °C respectively (Figure 6.4a-b). Prior reports give the melt temperatures of $C_{31}H_{64}$ and $C_{30}H_{61}OH$ as 68 °C and 85 °C respectively (Boudouh et al., 2016), (Gil Archila and Cuca Suárez, 2018). The melt temperature is larger for the *n*-alkanol even though they are similar chain lengths, likely due to the hydrogen bonding network giving increased stability of the material. The narrow peaks observed (Figure 6.4) indicate a single crystalline phase melt (Gaisford et al., 2016). $C_{31}H_{64}$ or $C_{30}H_{61}OH$ mixtures with TEHP were also tested where the wax material is in excess (using a 2 mg wax: 1 µL TEHP ratio (200 % w/v) Figure 6.4c-d). This ratio reflects the ratio used in the XRD study found later in this chapter, where 4 mg of material fills the sample holder for powder XRD analysis and a 2 µL drop of TEHP was subsequently added to cover the sample (Section 6.4 on XRD). The addition of the TEHP has broadened the endotherms and lowered the temperature of the peaks by ~ 10 °C. The broadening effect is bigger in the mixture of $C_{30}H_{61}OH$ and TEHP with a longer low temperature tail. Broad, shallow endothermic peaks result from varied crystalline structure (Gaisford et al., 2016). Chapters 4 and 5 established that there is some disorder within both $C_{31}H_{64}$ and $C_{30}H_{61}OH$ crystals. However, it is apparent that this disorder does not broaden the melting endotherms of these wax crystals significantly whereas the addition of TEHP does. This broadening is seen to a greater extent in the $C_{30}H_{61}OH$ sample, suggesting a more pronounced effect of TEHP in the $C_{30}H_{61}OH$ thermal response. This suggests that TEHP interacts more strongly with *n*-alkanols and that it may affect crystal size or crystalline order in both waxes. It is important to note that the TEHP interaction may be activated above a specific temperature (a thermodynamic effect) or may be slower at lower temperatures (a kinetic effect).

Fagerström et al. studied the interaction between a 32 carbon long chain alkane and a 22 carbon long chain alcohol with water using a DSC study (Fagerström et al., 2013). They concluded that there was no interaction between the water and the alkane as there was little difference in the thermograms with increasing water content. However the addition of water to the long chain alcohol resulted in broad, shallow peak at a lower phase transition temperature, so they concluded the alcohol and water did

interact with a plasticising effect where the water interacted with the alcohol groups of the wax to weaken the secondary bonds between close packed chains to lower T_m. Applying similar logic to the results in Figure 6.4, the DSC results on $C_{31}H_{64}$ and $C_{30}H_{61}OH$ crystals suggest that both waxes interact with the TEHP, potentially with a plasticising effect, with an increased effect seen for the $C_{30}H_{61}OH$ crystals.

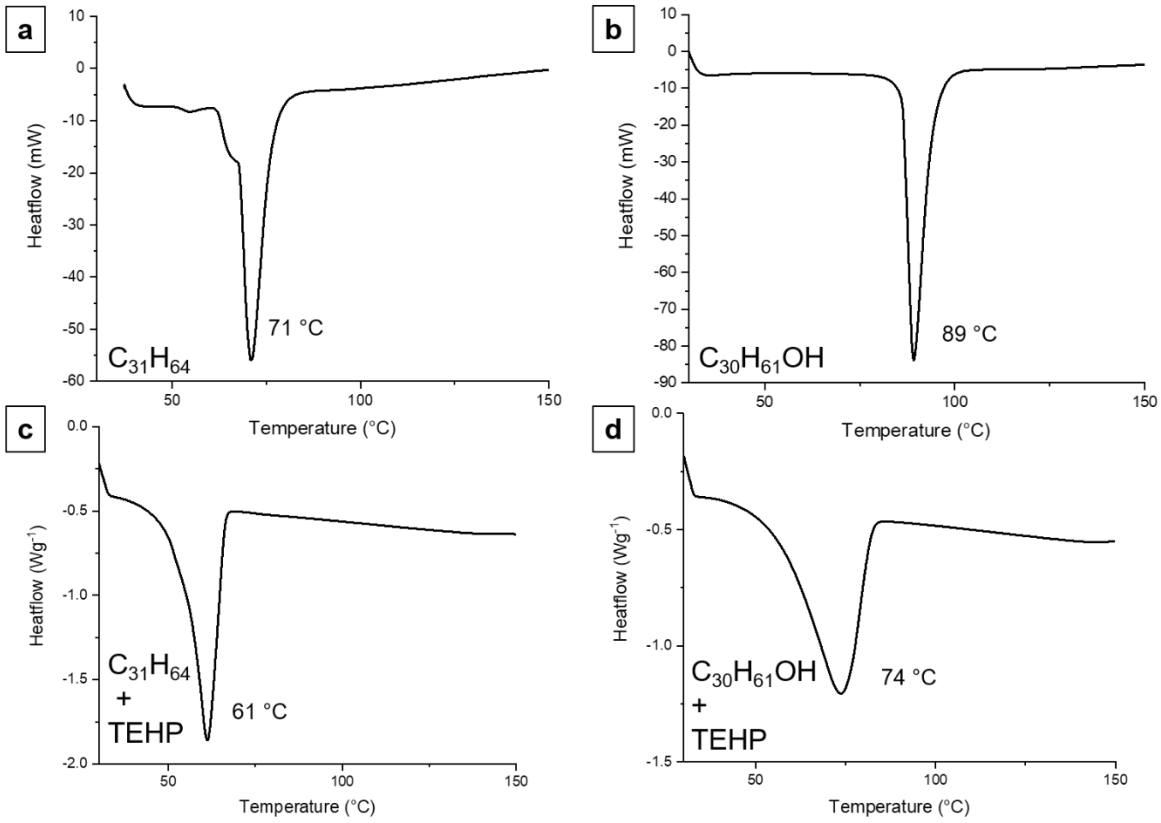

Figure 6.4: DSC thermograms for (a) pure $C_{31}H_{64}$ crystals (b) pure $C_{30}H_{61}OH$ crystals, (c) $C_{31}H_{64}$ crystals + TEHP mixture, and (d) $C_{30}H_{61}OH$ crystals + TEHP mixture.

6.4 Powder X-Ray Diffraction

Powder XRD (pXRD) is a common technique used for structural analysis of a material and offers insight into whether a material is crystalline, phase identification of the material, and can be compared against a known structure. The output of pXRD for a crystalline material is a trace containing a set of peaks at particular 2θ values where the arrangement of atoms has satisfied Bragg's law, whereas the output for an amorphous material is a trace with diffuse features with no defined 2θ peaks. pXRD also contains intensity information, which gives insight into the space group symmetry and structure factors. pXRD can show signs of disorder in the crystal structure, so XRD was examined to see whether the DSC peak broadening upon addition of TEHP

was caused by increased disorder of the crystalline wax. Figure 6.5 shows the XRD traces of $C_{31}H_{64}$ before and after TEHP exposure. This figure also explores how the XRD pattern varies for as received material, material re-crystallised from a melt, or material drop-cast from solution, and whether the method of preparation and therefore crystal orientation affects how an adjuvant interacts with the material. The drop cast materials will be oriented ‘chains-down’, the as received material will be randomly orientated, and the melted and recrystallised material may be oriented a particular way. The black line in the plots in Figures 6.5 a-c show the XRD trace of the crystal before exposure to the adjuvant, confirming detection of the crystalline phase of the material by the presence of the 2θ peaks. The relative intensities of the peaks in each plot differs. For example, where the material has been re-crystallised from the melt (Figure 6.5c), the 00ℓ peaks appear at much lower intensity. This change in 00ℓ peak intensity relative to the drop-cast sample (Figure 6.5a) is possibly due to the wax recrystallizing in a preferred orientation due to the sample preparation. The 00ℓ peaks correspond to long range lamellar ordering, so it is also possible re-crystallising from the melt reduces this fine lamellar ordering (Ensikat et al., 2006). Alkanes also go through several phases on heating and re-cooling, so it is possible going through those rotator phases causes recrystallization of the alkanes in a different symmetry (Ungar, 1983).

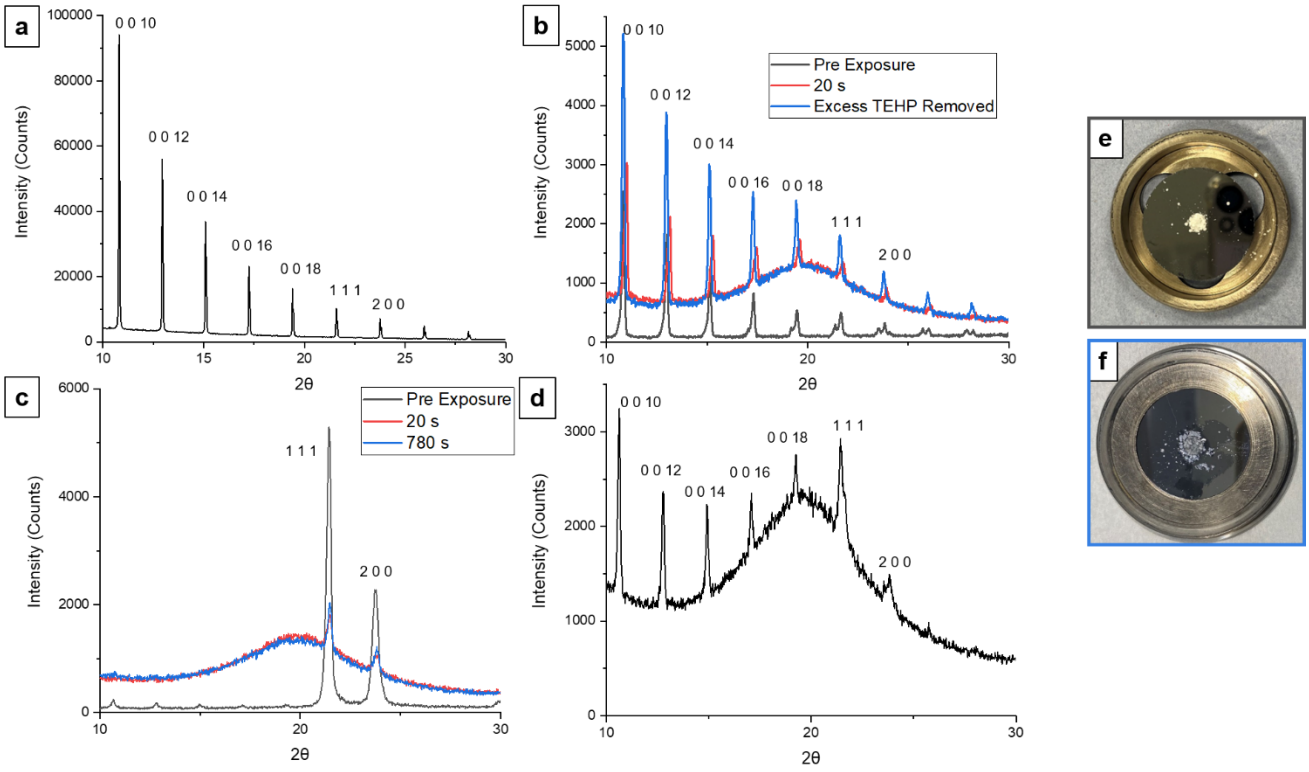

Figure 6.5: XRD trace of $C_{31}H_{64}$ crystals (a) drop cast onto the XRD holder, (b) $C_{31}H_{64}$ crystals as received, (c) recrystallised from the melt. The black lines show the initial scan, with the red line showing the immediate scan after TEHP addition, and the blue line showing the final scan. (d) XRD trace of $C_{31}H_{64}$ crystals where TEHP has been added and the mixture heated. (e,f) Picture of the holder before and after TEHP addition.

The red trace in Figure 6.5b and 6.5c shows the scan obtained after 4 mg of material was exposed to 2 µL of TEHP (200 % w/v). The TEHP droplet rapidly spread out across the top layer of wax. However, the final deposited liquid was not spread evenly as seen in Figure 6.5f. Due to the physical limitations of loading the holder in the diffractometer, the first scan was obtained 20 s after the TEHP was added. Immediately, a drop in intensity of the 2θ peaks was observed. The scans after TEHP addition were characterised by a diffuse feature in the middle of the plot, which is due to signal from TEHP. Figure 6.6 presents the XRD profile for TEHP as a control measurement, which shows a broad peak centred at 20°, with the diffuse features showing no difference to those in Figure 6.5b-d. This indicates the interaction with wax has not changed any features in this trace. The peak positions are not altered due to TEHP addition, which suggests there is no incorporation of the TEHP into the wax crystals. TEHP incorporation would alter the unit cell size and therefore the peak positions. This incorporation of the TEHP molecules within the chains can be ruled out as a mechanism of action for TEHP interaction. It was postulated that this liquid TEHP signal could be partially masking the signal from any crystalline wax material.

As seen in Figure 6.5f, liquid remained at the surface. Figure 6.5b shows in blue the XRD trace where excess TEHP was removed via pipette. In the resulting pattern, the intensity of the crystalline peaks increases, suggesting the intensities of the peaks in the pattern acquired after TEHP addition was due to the effect of liquid primarily at the surface.

To study the thermodynamic effects of this system interaction, the plot in Figure 6.5d shows an XRD trace of the as received $C_{31}H_{64}$ powder that has been exposed to TEHP, then heated at 100 °C (past the melting point) for 5 minutes to replicate the conditions seen in DSC, and finally allowed to cool. In this plot, there is a relative increase in the (111) and (200) peaks, the most intense peaks in Figure 6.5c, but the 00ℓ peaks remain. The peaks in the pattern have not changed position or shape, but some relative intensities have changed suggesting some effect of the interaction with TEHP at increased temperature. This suggests that in the DSC measurement, the peak broadening may not be due to complete disorder with the system, but the lowering of the melt temperature may be due to a plasticising effect.

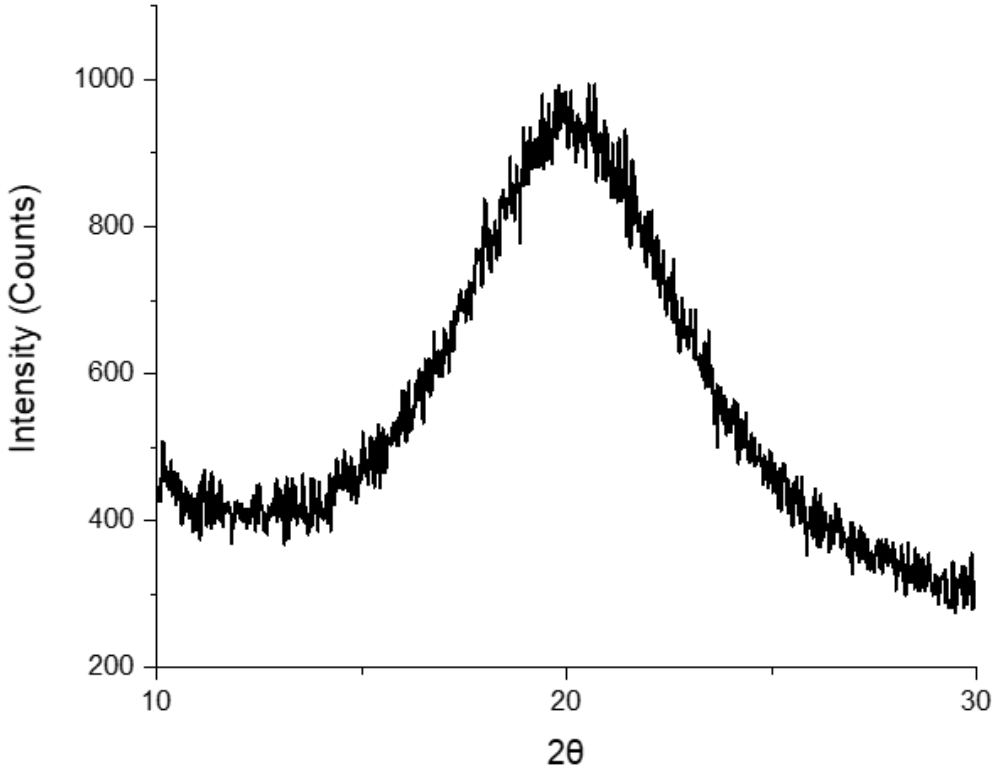

Figure 6.6: XRD pattern of TEHP.

In comparison, Figure 6.7 shows XRD traces of $C_{30}H_{61}OH$ crystals before and after exposure to TEHP.

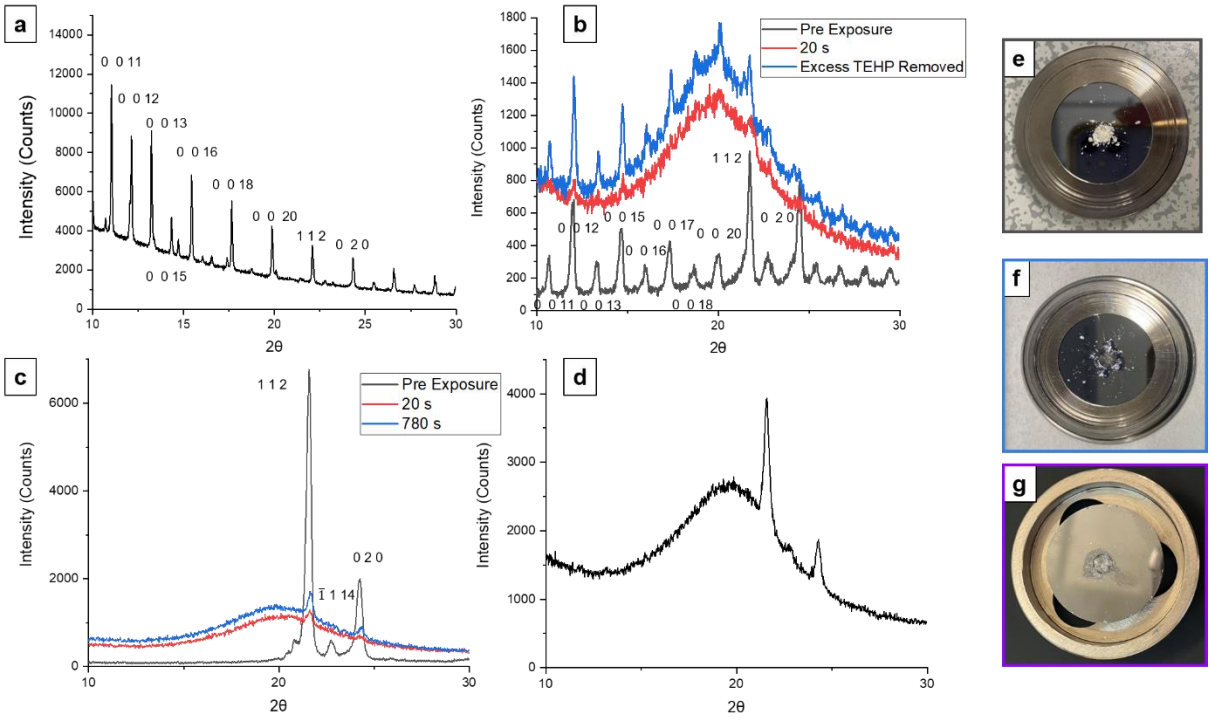

Figure 6.7: XRD trace of $C_{30}H_{61}OH$ crystals (a) drop cast onto the XRD holder, (b) $C_{30}H_{61}OH$ crystals as received, (c) recrystallised from the melt. The black lines show the initial scan, with the red line showing the immediate scan after TEHP addition, and the blue line showing the final scan. (d) XRD trace of $C_{30}H_{61}OH$ crystals where TEHP has been added and the mixture heated. (e-f) Picture of the holder before and after TEHP addition (g) Picture of the holder after removal of the excess TEHP by pipette.

As with the $C_{31}H_{64}$ sample, the different sample preparation methods were explored, with the melting and recrystallizing preparation leading to a sample where the 00ℓ peaks are not seen (Figure 6.7c). Again after addition of the TEHP, a non-uniformly spread droplet is left behind. However, after addition of 2 µL of TEHP to 4 mg of $C_{30}H_{61}OH$ crystals (200 % w/v), the intensity of the 2θ peaks immediately drops, with the remaining signal coming from the liquid TEHP. However, the intensities of the traces in Figure 7a are similar to the intensities of the XRD trace of pure TEHP (Figure 6.6).

As seen in Figure 6.7f, as with the $C_{31}H_{64}$ sample, liquid remained at the surface. Figure 6.7b shows in blue the XRD trace where excess TEHP was removed via pipette. Figure 6.7g shows an image of the holder after removal of this liquid. In the resulting pattern, crystalline peaks are once again visible, suggesting the pattern acquired after TEHP addition was purely due to the effect of liquid primarily at the surface.

As with the $C_{31}H_{64}$ sample, the as received $C_{30}H_{61}OH$ crystals that had been exposed to TEHP were also heated at 100 °C (past the melting point) for 5 minutes, and allowed

to cool, and an XRD measurement was taken (Figure 6.7d). The 00ℓ peaks are lost, with the symmetry and position of peaks the same as in the heated sample without TEHP addition (Figure 6.7c). From these results it can be concluded that the broadening of the peak in DSC is due to disorder in the crystal structure taking place at an elevated temperature.

Comparing the Figure 6.5d and Figure 6.7d indicates a difference in the response between $C_{31}H_{64}$ and $C_{30}H_{61}OH$ crystals upon exposure to TEHP and heated. Before this exposure and heating process, 00ℓ peaks are present in both samples (Figure 6.5a and Figure 6.7a). After this process, the 00ℓ peaks remain in the $C_{31}H_{64}$ sample, but not in the $C_{30}H_{61}OH$ sample. As proposed previously, it is also possible TEHP exposure and re-crystallising from the melt reduces this fine lamellar ordering.

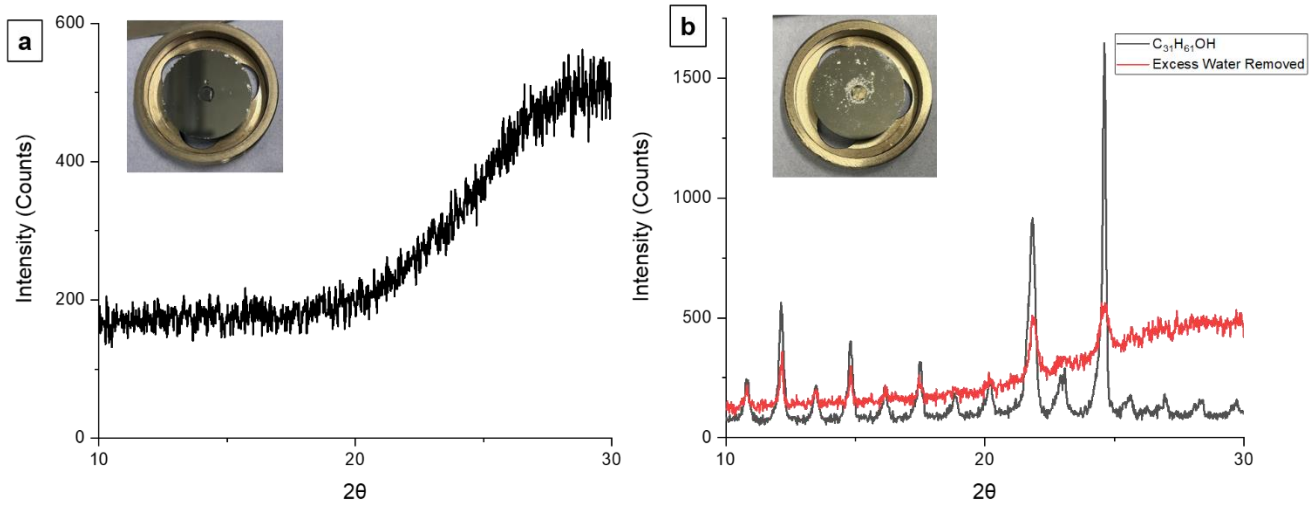

Figure 6.8: XRD traces of (a) water and (b) $C_{30}H_{61}OH$ after water addition and the subsequent removal of excess water.

As a further control experiment, the experiment was repeated using water instead of TEHP. Figure 6.8a shows the control XRD pattern of water, which further confirms the previous amorphous diffuse features in Figures 6.6 and 6.7 are due to TEHP as the amorphous diffuse features from water occurs at a higher 2θ value, with the peak occurring at 30° rather than centring around 20° as seen in the pure TEHP. Figure 6.8b shows XRD patterns of $C_{30}H_{61}OH$ before and after water addition and subsequent removal of the excess water. The initial scan straight after addition shows a complete loss in intensity of all peaks, with the trace resembling the pure water trace. However, again, once excess water was removed via a pipette, the resultant trace is found in Figure 6.8b. In this pattern, the crystalline peaks can still be seen. This does not involve complete removal of the liquid so the original pattern is not completely recovered, but instead shows consideration of the sensitivity of XRD to liquid at the surface potentially masking crystalline peaks where intensities are smaller. Due to

TEHP being a viscous liquid, complete removal was difficult without removing the wax material itself, hence why XRD traces were taken with some liquid still present.

The full width at half maximum (FWHM) was calculated for matching peaks across the set of samples to evaluate whether heating or TEHP addition resulted in observable changes in crystallite size (or coherent scattering volume). For the $C_{31}H_{64}$ samples, this value was taken from the $(1\ 1\ 1)$ peak at 21.6° (indexed to the *A2₁am* space group), and for the $C_{30}H_{61}OH$ samples, this value was taken from the $(1\ 1\ 2)$ peak at 21.7° (indexed to the *P2₁/c* space group). These planes are similar cuts across the unit cells. The difference in the (hkl) values is due to the c-axis being double in length in the *n*-alkanol due to the unit cell consisting of 4 chain lengths compared to 2 chain lengths in the *n*-alkane. These 2θ peaks were studied due to the disappearance of the lower angle 00ℓ peaks in the heated samples. Table 6.1 summarises the FWHM values for $C_{31}H_{64}$ and $C_{30}H_{61}OH$ crystals. These values were obtained from the fitted Gaussian function to the peaks in Origin. These values were taken from drop cast waxes, the waxes as received before and after TEHP addition, the as received waxes heated and allowed to cool and recrystallise, and the as received waxes heated in TEHP.

Table 6.1: FWHM values calculated by fitting the $(1\ 1\ 1)$ peak at 21.6° ($C_{31}H_{64}$) and $(1\ 1\ 2)$ peak at 21.7° ($C_{30}H_{61}OH$) peaks to a Gaussian function. Errors for each measurement are reported as calculated in Origin.

Sample	**FWHM**	
	$C_{31}H_{64}$	**$C_{30}H_{61}OH$**
Drop Cast	0.091 (± 0.002)	0.116 (± 0.003)
As Received	0.170 (± 0.005)	0.278 (± 0.018)
As Received + TEHP	0.218 (± 0.018)	0.314 (± 0.021)
As Received Heated	0.270 (± 0.004)	0.301 (± 0.002)
As Received Heated in TEHP	0.353 (± 0.051)	0.311 (± 0.006)

These values show the peaks are narrower in the drop cast samples than the other samples, with values of 0.091 and 0.116 in the drop cast sample versus 0.170 and 0.278 in the as received powder sample in $C_{31}H_{64}$ and $C_{30}H_{61}OH$ respectively. This suggests that the crystals are larger (or less interrupted structures) in the drop cast samples. The peaks are also mostly broader in the $C_{30}H_{61}OH$ samples (0.170 versus

0.278 for the as received powder for example), suggesting smaller crystallite size in the *n*-alkanol wax.

Peak broadening is a combination of instrumental broadening and sample broadening. Given the same instrumental parameters, then changes in broadening reflect changes in the coherent scattering volume. Peak broadening may also be due to increased disorder or strain in the crystals, essentially a decrease in the coherent scattering domain. Upon addition of TEHP to both waxes, there is a broadening of the peaks. For the $C_{30}H_{61}OH$ sample, the FWHM remains consistent whether this TEHP addition was done at room temperature or if the sample was heated and allowed to cool in the presence of TEHP. For the $C_{31}H_{64}$ sample, the FWHM is broader when the sample is heated in the presence of TEHP than at room temperature. This suggests there may be an element of TEHP breaking things down into smaller crystals or shorter regions of ordered chains, as the peaks would be broader if the crystals became smaller as a result of this addition. The broadening effect is more prominent in the $C_{31}H_{64}$ sample upon addition of TEHP than in the $C_{30}H_{61}OH$ sample, but this may be because *n*-alkanol crystals inherently exhibit a higher degree of disorder to begin with, so the effect of adding TEHP is not as prominent.

It must also be considered whether this peak broadening is due to slight adjustments to the unit cell if TEHP was incorporating in between the chains. Asymmetric peaks would then form from an overlap of peaks from a mixture of the pure wax crystals and these new unit cells with TEHP incorporated. However, the peaks remain symmetric with a good quality Gaussian fit, suggesting this is not the case and peak broadening is in fact due to the factors already proposed.

Combined, these results suggest retention of crystalline material after exposure to TEHP in both wax materials, and drops in intensity are seen due to the liquid masking signal from the sample. Due to this liquid background signal, it is difficult to quantify if the amount of crystalline material has stayed the same before and after TEHP exposure.

It was further explored whether a binary mixture would interact the same way with TEHP as with the $C_{31}H_{64}$ sample. A binary mixture with 30% $C_{30}H_{61}OH$ was chosen as this is the composition found in the *Schefflera elegantissima* plant. As discussed in Chapter 5 at this composition a solid solution with the structure of the *n*-alkane is likely to have formed, so it could be assumed the mixture would interact with the TEHP as the pure $C_{31}H_{64}$ sample did. To form the binary mixtures, the two endmembers are melted together and allowed to cool. Figure 6.9a shows the XRD traces of the mixture before and after TEHP exposure; the sample recrystallised as per the DSC equivalent heat treatment (Figures 6.5 and 6.7). Similar to the $C_{31}H_{64}$ sample, crystallinity is

retained upon exposure with TEHP with a decrease in intensity of the 2θ peaks after addition of the TEHP.

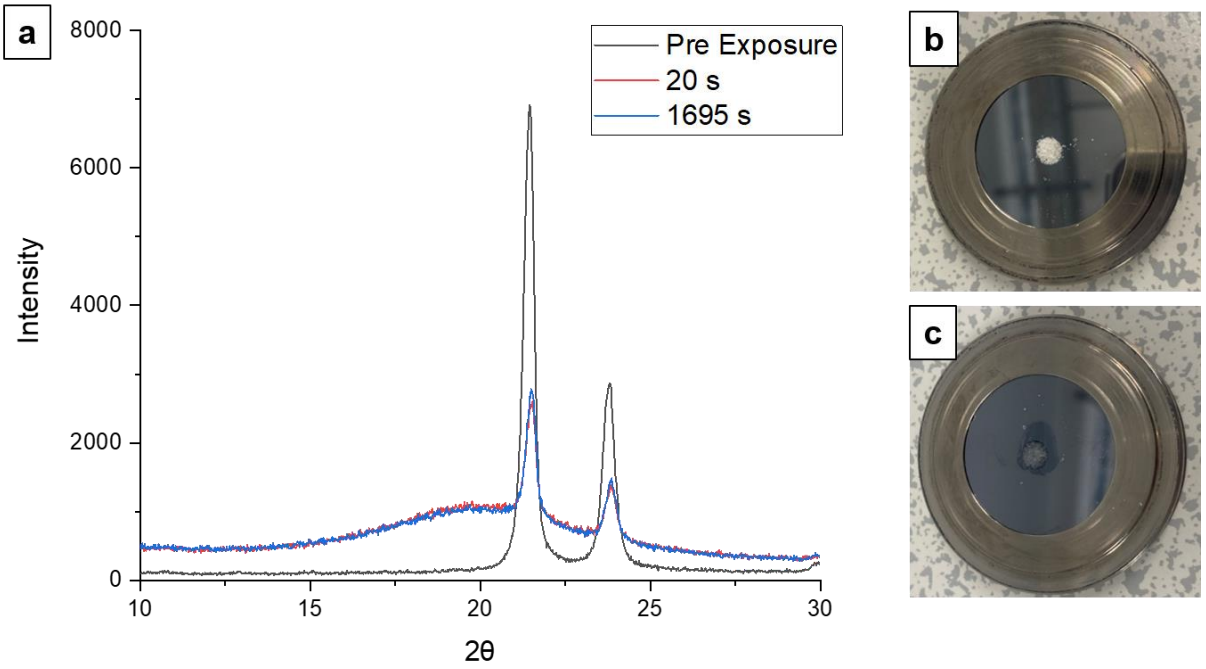

Figure 6.9: (a) XRD trace of a binary mixture containing 30 % $C_{30}H_{61}OH$ crystals The black line shows the initial scan, with the red line showing the immediate scan after TEHP addition, and the blue line showing the final scan. (b, c) Picture of the holder before and after TEHP.

In summary, these room temperature XRD results show that TEHP addition does not affect the crystal structure at the precision available (peak positions) of either wax material or a binary mixture, but peak broadening does suggest there is an element of TEHP introducing disorder within the materials as suggested by the endothermic peak in the DSC thermograms broadening. To prove this question further, first, further bulk techniques are used to determine any complex formation. This chapter will then use microscopic techniques in subsequent sections to explore any differences in the interaction of the two wax endmembers with TEHP to attempt to understand this mechanism of interaction to explain the difference observed in the DSC and XRD results.

6.5 NMR spectroscopy and ATR FT-IR spectroscopy

Previous work has suggested molecules with the P=O bond can form complexes through hydrogen bonding, which causes a shift of the P=O absorption in an IR spectrum towards lower frequency (Bellamy and Beecher, 1952). $C_{31}H_{64}$ and $C_{30}H_{61}OH$ molecules may interact differently with the TEHP because $C_{30}H_{61}OH$ may form hydrogen bonds with the P=O group in the TEHP, and the $C_{31}H_{64}$ being unable

to. This was explored through attenuated total reflectance FT-IR spectroscopy (ATR-IR) of TEHP and $C_{31}H_{64}$ or $C_{30}H_{61}OH$ exposed to TEHP (Figure 6.10). Firstly, measurements were taken on an added droplet (<1 mL) of the suspension of 0.5 mg of $C_{31}H_{64}$ or $C_{30}H_{61}OH$ in 5 mL of TEHP respectively (0.01% w/v). Figure 6.10 presents the spectra of these suspensions, with Table 6.2 presenting the wavenumber at which the P=O absorption peak occurs at in TEHP, and of $C_{31}H_{64}$ and $C_{30}H_{61}OH$ suspended in TEHP respectively.

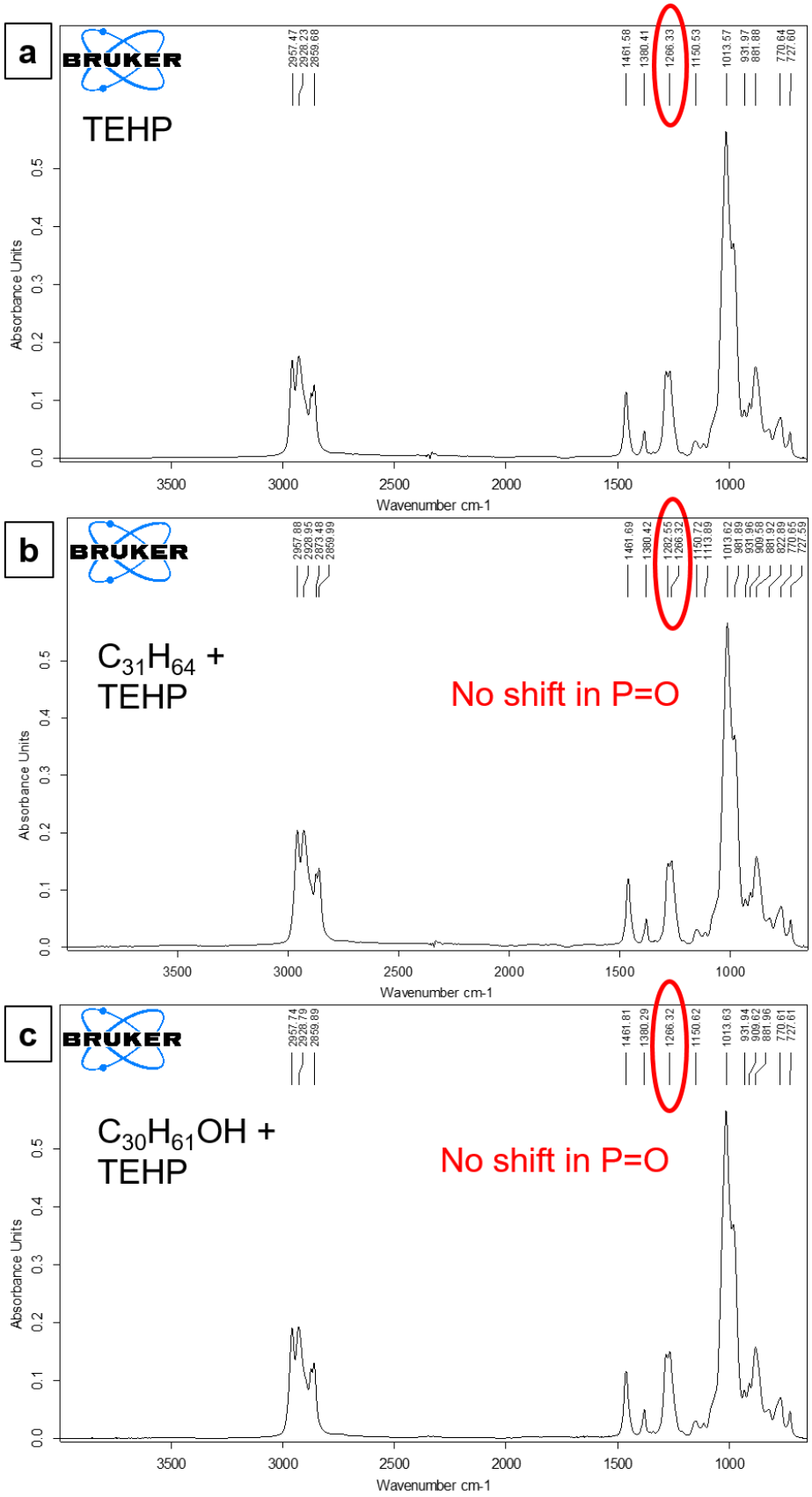

Figure 6.10: ATR-IR spectra of (a) TEHP, (b) $C_{31}H_{64}$ + TEHP, and (c) $C_{30}H_{61}OH$ + TEHP.

No shifts were seen in the P=O absorption peak as a result of adding TEHP to either of the wax samples. This suggests that ATR-IR cannot identify either of the wax samples forming a hydrogen bonding complex with TEHP at these concentrations studied. As ATR-IR is limited by penetration depth, typically 0.5 to 5 microns, it could be that these ATR-IR measurements are only sampling the bulk of the TEHP at the surface, and any complex formation is not being measured. Whilst the crystallites were on a micron scale, this technique may not have penetrated past an initial TEHP liquid layer to reach these crystallites at some distance from the ATR crystal. A peak around 3200 – 3550 would also be expected to be seen in the spectrum of the sample with $C_{30}H_{61}OH$ +TEHP because of the OH group in $C_{30}H_{61}OH$, but this is not seen in Figure 6.10c, which suggests these spectra are sampling the bulk TEHP only. A small drop (<1 µL) of TEHP was also added to a clamped sample of two separate samples of $C_{31}H_{64}$ and $C_{30}H_{61}OH$ (<1 mg) to acquire spectra when the wax was in excess (~100% w/v), but again no P=O peak shift was seen as summarised in Table 6.2.

Table 6.2: Summary of the wavenumber corresponding to the P=O absorption peak position for samples of TEHP, and of 0.5 mg of $C_{31}H_{64}$ and $C_{30}H_{61}OH$ suspended in 5 mL of TEHP respectively.

Sample	**P=O wavenumber (cm^{-1})**	
	TEHP in Excess	**Wax in Excess**
TEHP	1266	1266
$C_{31}H_{64}$ + TEHP	1266	1266
$C_{30}H_{61}OH$ + TEHP	1266	1266

Other work has used FT-IR to measure the diffusion kinetics of adjuvants across a wax spin-coated onto an ATR-crystal by determining the absorption of IR-radiation induced by the increased concentration of diffusant specific functional groups entering the wax region defined by the evanescent wave of the IR beam over time (Kunz et al., 2022). This suggests that it may be possible to detect a P=O peak shift using this specialised equipment as part of future experimental work.

Phosphorous NMR analysis was also performed on the suspensions, to determine if there was a more localised complex formation that could be measured by an NMR shift from the singular peak produced from the phosphorous atom. If the $C_{30}H_{61}OH$ formed hydrogen bonds with the P=O group, the phosphorous atom would be in a different environment and this peak would shift relative to that of the pure TEHP.

Phosphorous NMR shifts have been reported before when a P=O group forms hydrogen bonds with acids and bases (Giba et al., 2019). To be detectable by NMR, the complex formed would have to be an irreversible complex. If a reversible complex is formed, these components could dissociate and dissolve separately in the NMR solvent, so the phosphorous shift in TEHP would be unaffected. Table 6.3 summarises the δ shifts in the phosphorous NMR spectra of pure TEHP, and of the $C_{31}H_{64}$ and $C_{30}H_{61}OH$ in TEHP suspensions.

Table 6.3: Summary of the δ shifts in the phosphorous NMR spectra of pure TEHP, and of the $C_{31}H_{64}$ and $C_{30}H_{61}OH$ in TEHP suspensions. Shifts are referenced to the $CDCl_3$ deuterium signal.

Sample	**δ (ppm)**
TEHP	0.44
$C_{31}H_{64}$ + TEHP	0.42
$C_{30}H_{61}OH$ + TEHP	0.42

No significant shift of the phosphorous peak is seen. From the NMR results no possible permanent irreversible complexes that may form as a result of adjuvant interaction with either of the waxes can be detected.

The data so far in this chapter have studied the bulk properties of the interaction between the waxes and TEHP. DSC has indicated an increase in range and reduction of the melt temperature in both waxes, with a larger effect in the *n*-alkanol. This suggests there is plasticisation of the waxes upon addition of TEHP, but XRD studies show no change in crystal structure or size. However, none of the results thus far have been able to identify a mechanism of interaction explaining this difference. Focus is now placed on microscopic observations to see if this offers any insight into the interaction.

6.6 Optical Microscope Observations

Firstly, particles of the $C_{31}H_{64}$ and $C_{30}H_{61}OH$ were imaged using an optical microscope with a cross polarised lens attached before and after TEHP exposure (Figure 6.11). 4 mg of each respective wax material was weighed onto a glass slide, and a 2 µL drop of TEHP was added to the slide to replicate the XRD ratios (200% w/v). Polarised light can be used to determine whether a material is optically isotropic or not i.e., amorphous or crystalline in the case of polymeric materials.

If the material was amorphous, or isotropic, then the particles would ‘disappear’ against the background (Dombrowski, 2013). The wax particles imaged here are bright

(relative to the glass slide background) both before and after TEHP exposure, indicating crystallinity is retained (Figure 6.11).

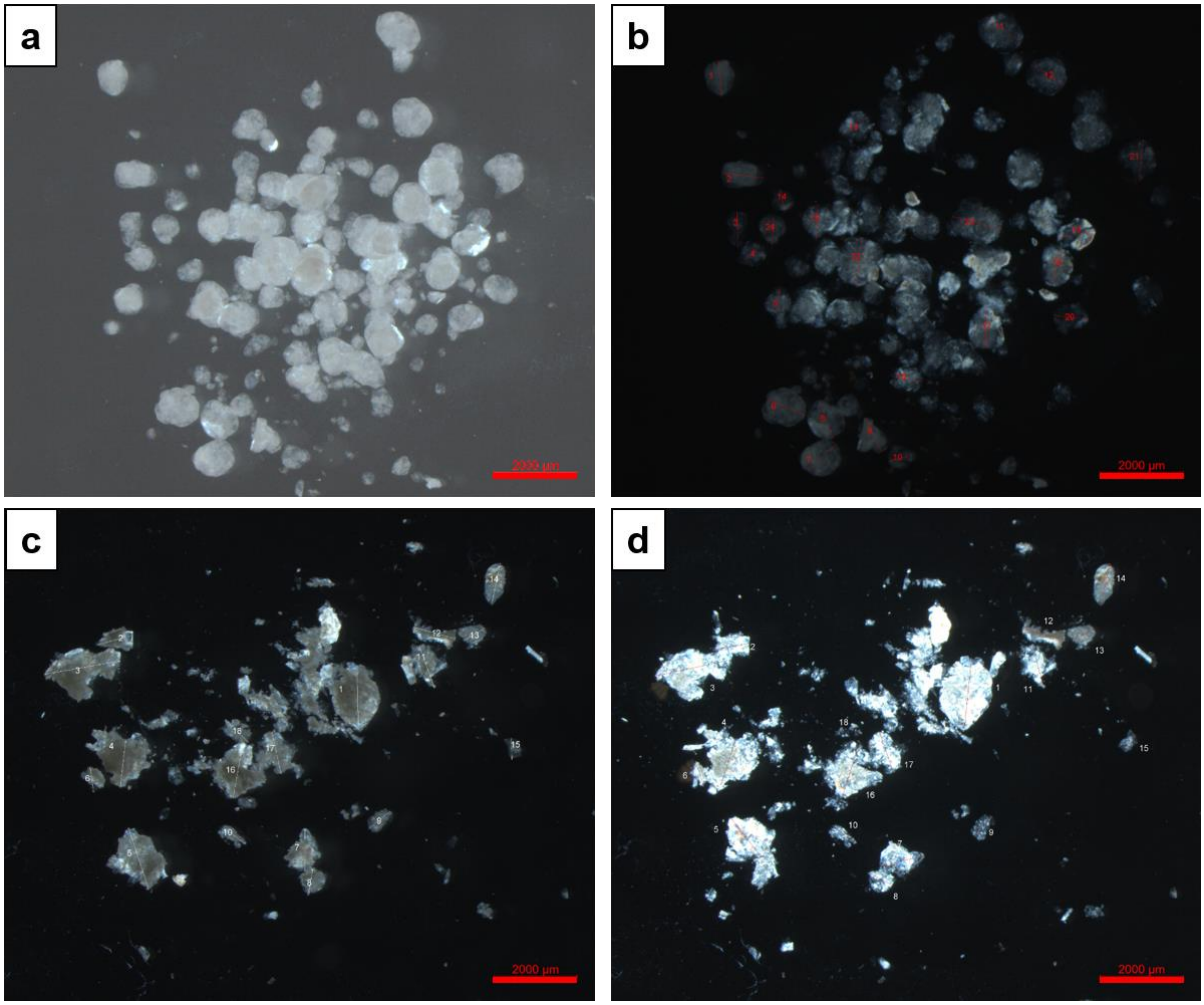

Figure 6.11: Polarized light optical microscope image of $C_{31}H_{64}$ (a) and $C_{30}H_{61}OH$ (c) before TEHP addition, and after TEHP addition for the respective samples (b, d). The scale bars indicate 2000 µm.

Particle size distribution from size measurement from the optical images indicate there is no significant change in size before and after addition of the TEHP for either $C_{31}H_{64}$ or $C_{30}H_{61}OH$ (Figure 6.12). The retained particle size is consistent with the attempts to dissolve the material being unsuccessful. However, this particle size is measured by measuring the longest distance across a particle (Feret diameter). This misses the subtleties of changes at the edges of the particles.

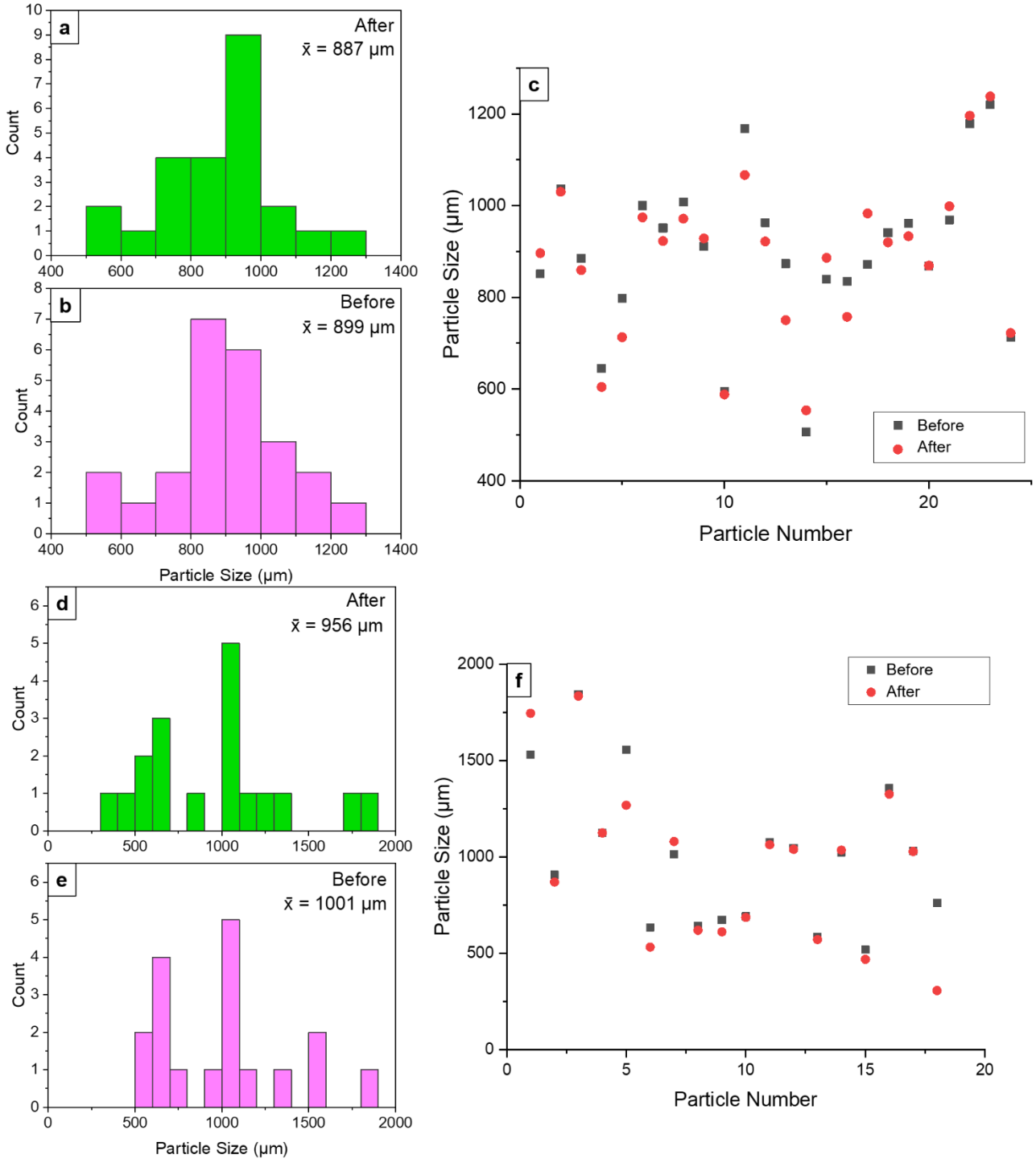

Figure 6.12: Histograms and comparisons of particle size (Feret diameter) before and after TEHP addition for $C_{31}H_{64}$ particles (a-c), and for $C_{30}H_{61}OH$ particles (d-f).

When the images are overlaid on one another, differences can be seen at the edges of the particles (Figures 6.13 and 6.14). Particles were isolated from the larger field to highlight these features at the particle edges. By overlaying pre- and post-exposure images of identical particles, changes in the edge structure arising from TEHP exposure are brought out in relief. In the overlay, the pre-exposure image has been

recoloured green and the post-exposure image has been recoloured blue to increase contrast between the two images. In the $C_{31}H_{64}$ sample, the edges remain smooth after TEHP addition with very little difference captured in the overlay image and particles remain the same size (Figure 6.13).

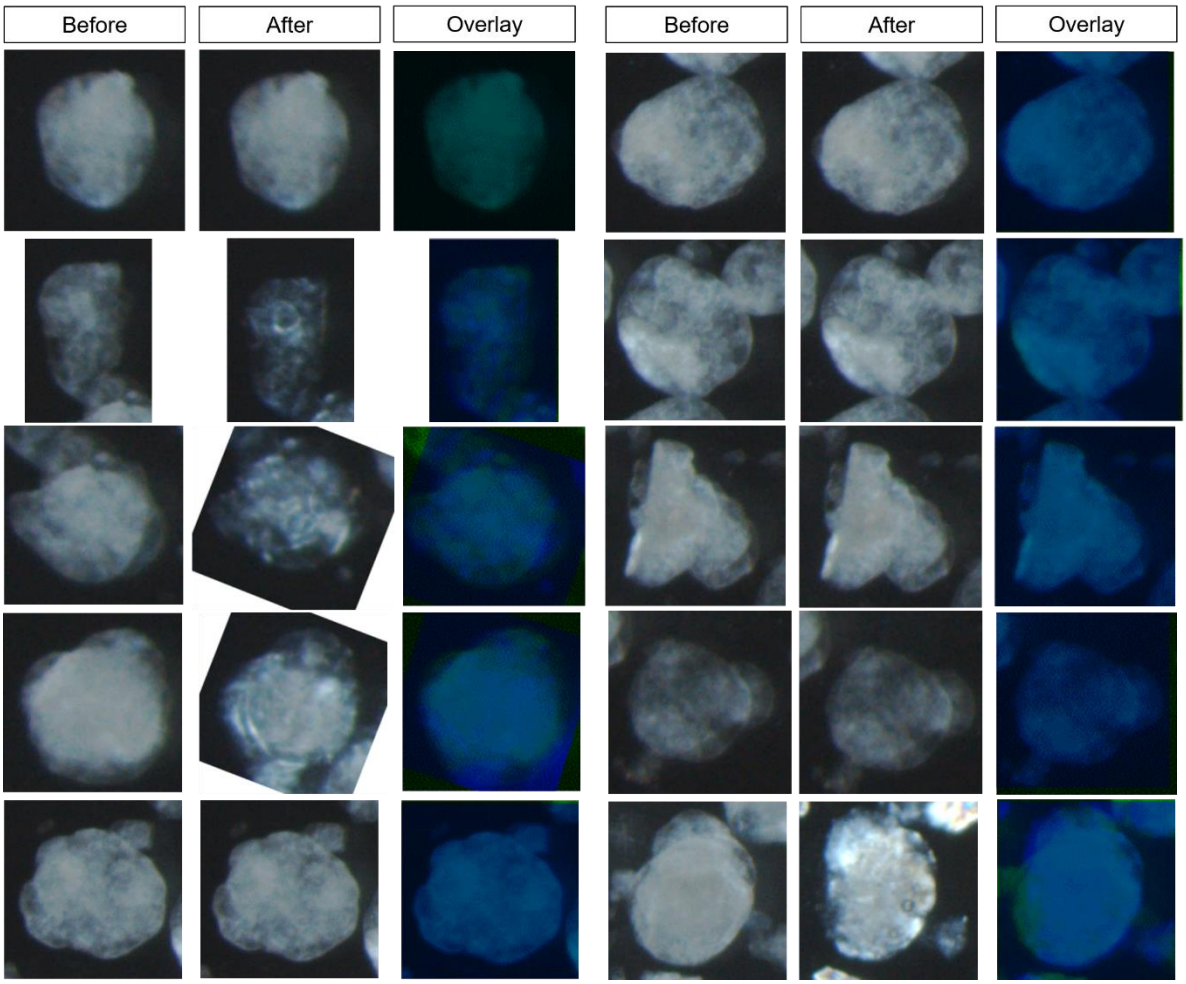

Figure 6.13: Images cropped to individual $C_{31}H_{64}$ particles from Figure 6.11. The left column shows the particles before TEHP addition, the middle column after TEHP addition, and the right column shows an overlay of the two particles. Where the particle has been rotated after the liquid addition, the after image has been rotated to match the initial orientation of the particle for direct comparison.

Repeats of the same type of overlay for isolated $C_{30}H_{61}OH$ particles reveals differences in the particles exposed to TEHP (Figure 6.14). In these, the removal of material at the edges of the particle can be observed. This is apparent where the green before image can be seen in areas not covered by the blue after image, leaving a concaved edge. These images capture the subtleties of the particle changing size and shape that is not captured by measuring the longest length of the particle.

A further difference between the two samples is that the initial $C_{30}H_{61}OH$ sample is made up of a wider variation in size of particles whereas the initial $C_{31}H_{64}$ sample is

comprised of more homogeneously sized particles. It is possible that this loss of sample at the edges of these particles is due to rearrangement of the particles instead of an interaction between the two components itself. However, this removal of material can be seen in particles that had not moved between the before and after image, such as the third example down in the left set of columns (also noted as particle 3 in Figure 6.11c). This suggests this effect is not purely due to movement of the material, and there is an element of breakdown of the material.

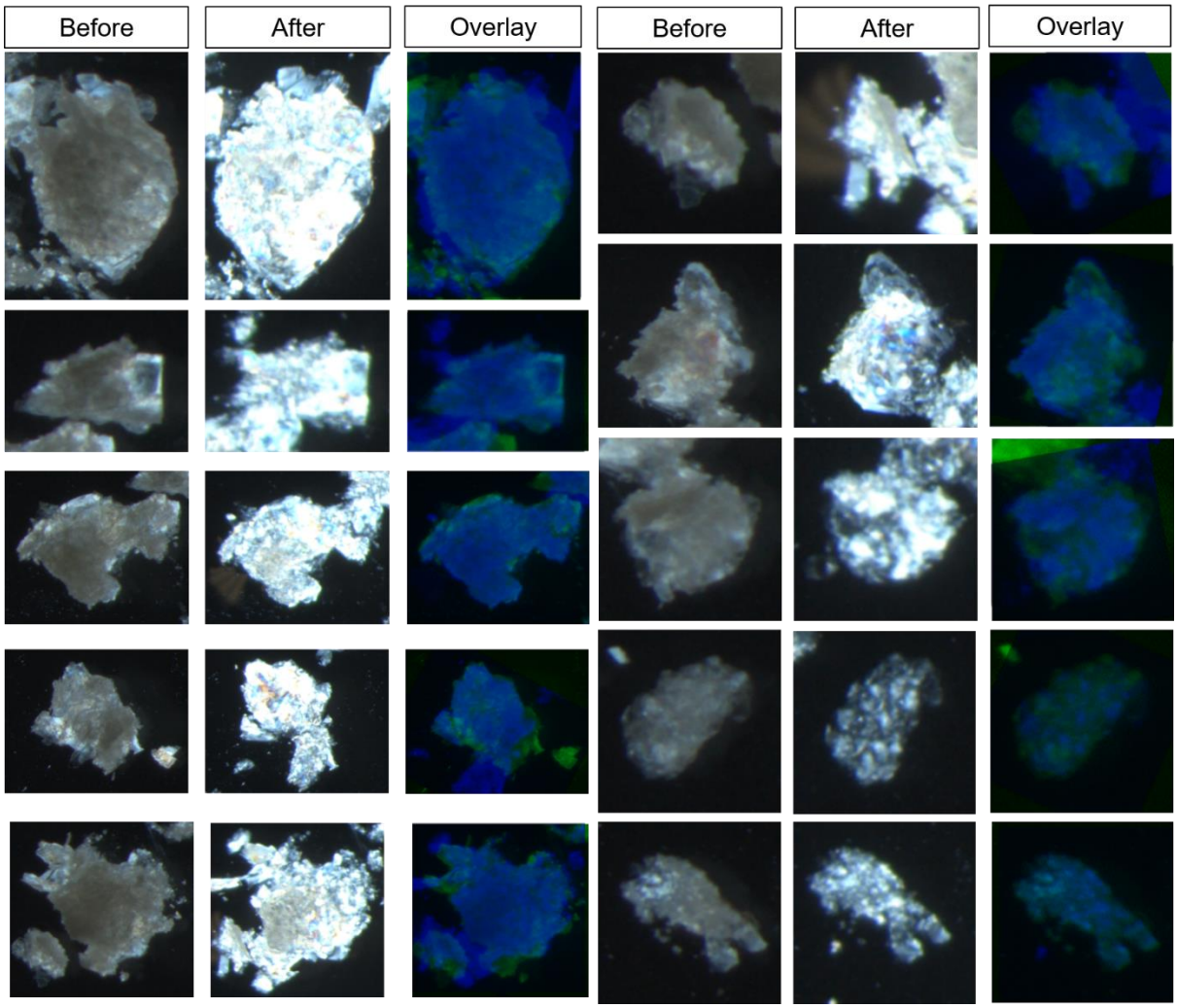

Figure 6.14: Images cropped to individual $C_{30}H_{61}OH$ particles from Figure 6.12. The left column shows the particles before TEHP addition, the middle column after TEHP addition, and the right column shows an overlay of the two particles. Where the particle has been rotated after the liquid addition, the after image has been rotated to match the initial orientation of the particle for direct comparison.

From these optical microscope images, it can be concluded that TEHP may interact differently with $C_{30}H_{61}OH$ crystals than the $C_{31}H_{64}$ crystals due to the difference in morphology of the remaining crystals after TEHP exposure. These structures are however not likely one crystal, but aggregates of larger crystals. The TEHP may therefore be breaking up these aggregates, showing as removal of material at the

edges. These images also suggest that the TEHP interaction of mechanism with the waxes has an element of dissolution.

Results now turn to electron microscopy techniques to attempt to further analyse these structural changes at a single crystal scale, to determine if the dissolution effect seen in optical microscopy was purely due to aggregate break up.

6.7 Transmission Electron Microscopy and Selected Area Electron Diffraction

Electron microscopy analysis was used to observe these changes at the single crystal scale. Both SAED and SED can also confirm whether the material is amorphous or crystalline.

As established in the prior chapters, $C_{31}H_{64}$ crystals are highly faceted diamond shaped crystals (Figure 4.7). Samples were prepared for EM analysis in the ‘down-chains’ orientation, where the wax crystals were dissolved in warm hexane and drop cast onto the grid. This orientation was chosen as preparation for the ‘chains-flat’ orientation resulted in only a small amount of material on the grid. Crystals in this orientation show bend contours with relatively few signs of disorder or grain boundaries within the crystals.

Initially, a 2 µL droplet of TEHP was drop cast on top of the prepared sample grid and the liquid removed by blotting, but this liquid removal removed wax material with it. To expose the grids to the TEHP without losing material, a prepared grid was partially dipped into a small volume of TEHP. This partial exposure resulted in a sample grid with a gradient of how exposed the samples had been, with the areas that were fully dipped nearly empty of material, and those at the exposure barrier partially exposed. Whilst the exact concentration of wax to TEHP liquid cannot be calculated with this method, it can be taken that TEHP is in excess.

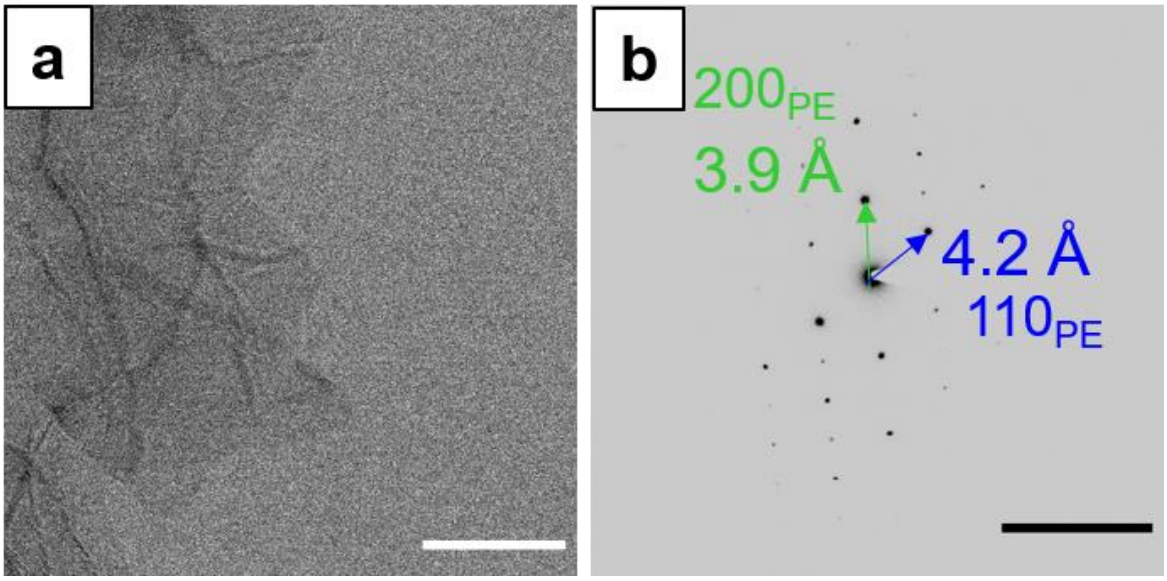

Figure 6.15: Bright field image of a faceted $C_{31}H_{64}$ crystal and the corresponding SAED pattern. Scale bar for the BF image indicates 2 µm, and the scale bar for the SAED pattern indicates 0.5 $Å^{-1}$.

Figure 6.15 shows a region on the side of the grid that was not dipped in TEHP, where crystals remain highly faceted, and the corresponding diffraction pattern confirms a crystalline ‘down-chains’ orientation.

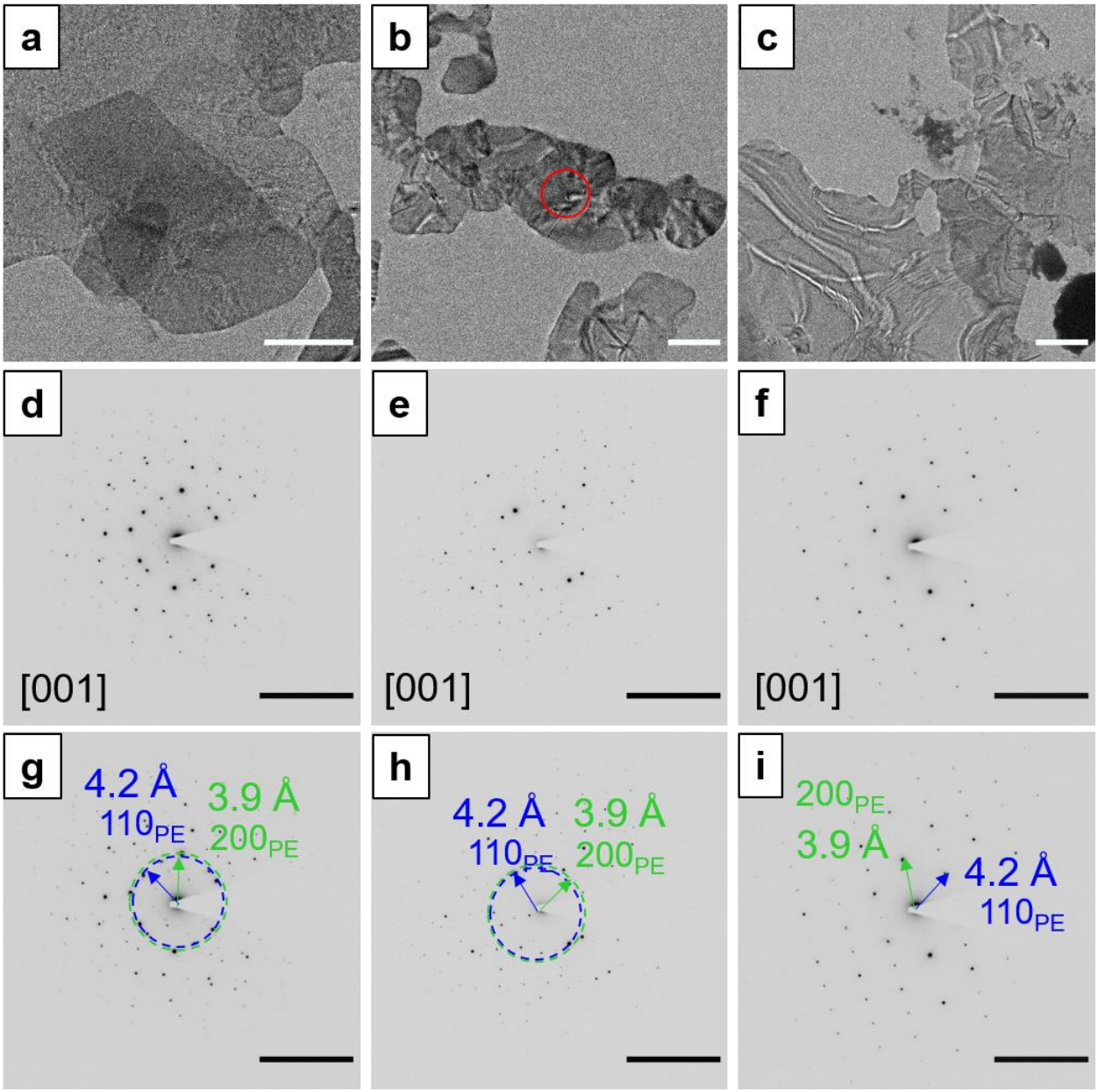

Figure 6.16: Bright field images of $C_{31}H_{64}$ crystals after TEHP exposure (a-c), the corresponding SAED pattern (d-f), and the indexed patterns (g-i). Where a polycrystalline pattern was seen, the circles represent a polycrystalline ring at the indexed d-spacing. Scale bar for the BF images indicate 2 µm, and the scale bars for the SAED patterns indicate 0.5 $Å^{-1}$.

Figure 6.16a-c shows examples of a field of view on the TEHP exposed area of the grid. In these areas, crystal separation is less defined, with more agglomerated overlapped round type structures formed versus the highly faceted separate crystal structures seen before TEHP exposure. In Figure 6.16a for example, the regions that appear darker are due to overlapping crystals lying on top of one another, with distinct edges as grain boundaries between these crystal structures. This is partnered with a loss of the well-defined facets, and the edges appearing more curved than the straight edges observed previously. However, the bend contours within crystals remain

smooth suggesting relatively few grains or defects within. The corresponding diffraction patterns confirm these structures are crystalline, and the patterns can be indexed to the [001] orientation confirming the chains are still in a ‘down-chain’ orientation with respect to the electron beam. These patterns are a combination of several crystal contributions with in-plane rotations, giving a more polycrystalline type diffraction pattern. In Figure 6.15b a red circle indicates the selected area where the diffraction pattern was taken from, in a region with overlapping crystals. Where a polycrystalline pattern was seen, a circle could be drawn to represent the polycrystalline ring that would be seen at these d-spacings that correspond to the major spots in the ‘down-chain’ orientation. These circles intersected with the spots in the pattern, again confirming the chains in a ‘down-chain’ orientation. In these patterns, some spots can be seen nearer to the central beam. These spots are likely due to reorientation of the crystals away from the ‘down-chain’ orientation as a result of the agglomeration seen in these crystals disrupting the crystal alignment, but this is not evidence for unit cell changes in the crystal. This corroborates earlier findings from the XRD results; that material that has been exposed to TEHP is still crystalline and there are no major lattice changes in the structure.

Following the same procedure, $C_{30}H_{61}OH$ crystals drop-cast on a grid were exposed to the adjuvant TEHP. In this sample, the edges of individual crystals have been partially removed, and the internal diffraction contrast is complex (compared to smooth bend contours in the pre and TEHP exposed alkane) and reflects what is seen in the larger particles in the optical microscopy results. This is different to the agglomerate structures formed in the $C_{31}H_{64}$ crystals. These edges now look rough as opposed to the smooth edges exhibited in unexposed $C_{30}H_{61}OH$ crystals (Figure 4.7, Chapter 4), where pits have been formed. This suggests an etching mechanism may have occurred at the edges of these crystals. An etching mechanism implies a dissolution mechanism, different from the previously proposed plasticisation mechanism in this chapter. Figure 6.17 shows three fields of view where the edges of individual crystals all exhibit these pit features (pointed out by red arrows) and therefore this etching effect.

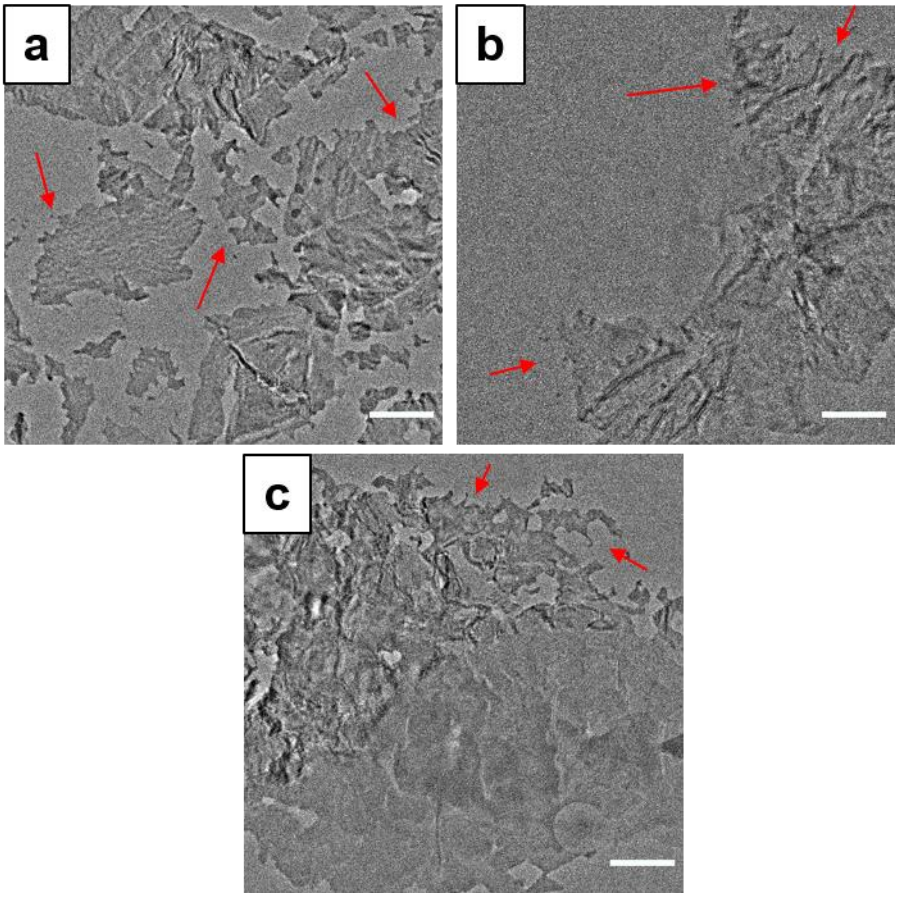

Figure 6.17: Bright field images of $C_{30}H_{61}OH$ crystals after TEHP exposure. Scale bars for the BF images indicate 2 µm. Red arrows point out edges where pits have formed.

Figure 6.18 shows two additional fields of view exhibiting the surface roughness pit formation, complex internal diffraction contrast and the corresponding selected area diffraction patterns. Again, these diffraction patterns confirm crystallinity after TEHP exposure, and can be indexed to the [001] direction indicating the 'down-chains' orientation is maintained after the adjuvant addition.

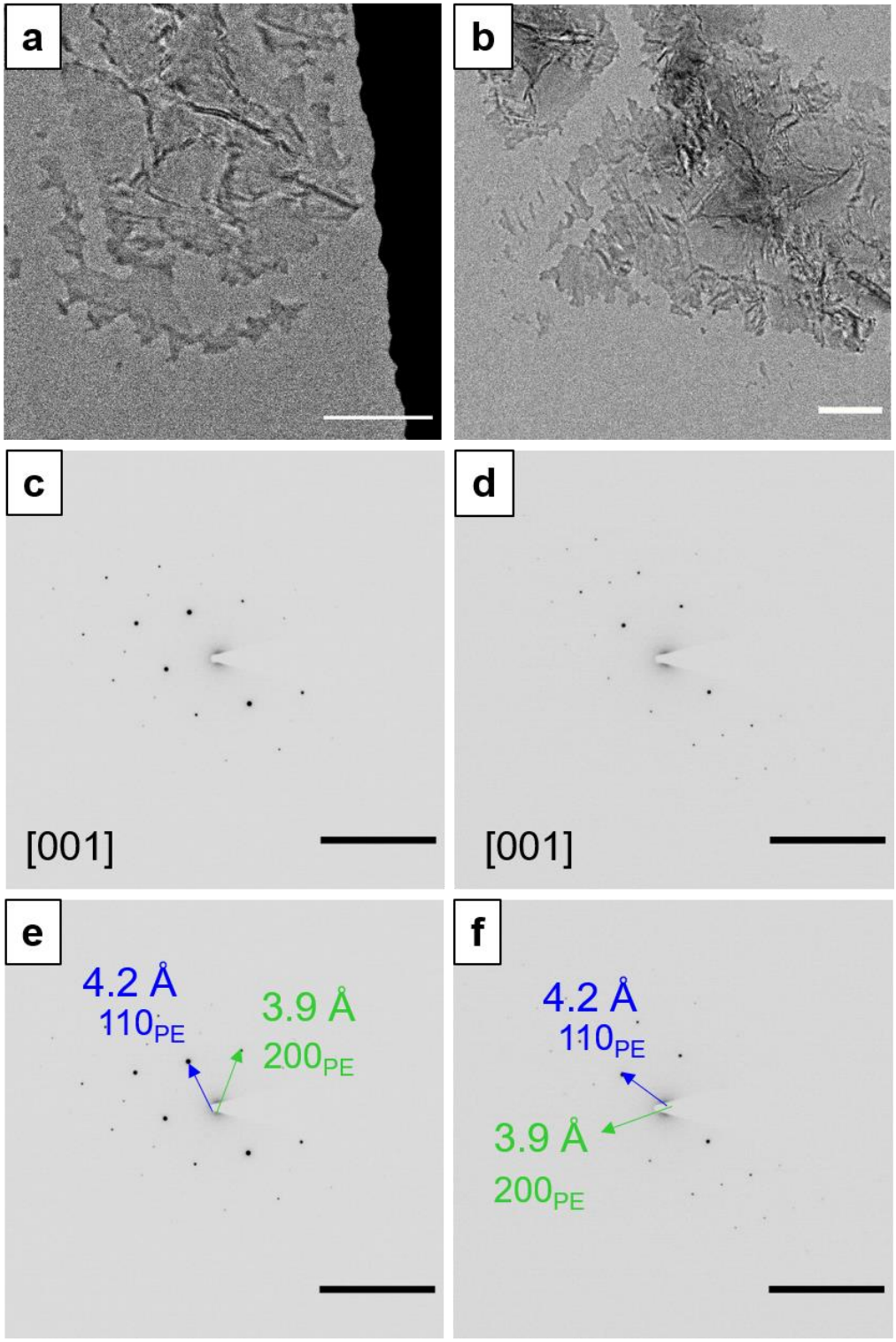

Figure 6.18: Bright field images of $C_{30}H_{61}OH$ crystals after TEHP exposure (a, b), the corresponding SAED patterns (c, d) and the indexed patterns (e, f). Scale bar for the BF images indicate 2 µm, and the scale bars for the SAED patterns indicate 0.5 $Å^{-1}$.

The same procedure was also repeated for a binary mixture sample with 50% $C_{30}H_{61}OH$ content. As Figure 6.19 presents, exposed crystals can again be indexed to the 'down-chains' orientation, the crystals have complex internal structure (as might

be expected from Chapter 5) and there is removal of material at the edges of some crystals (arrows inset in Figure 6.19), albeit with these features less pronounced than in the pure $C_{30}H_{61}OH$ sample. At this composition, phase separation is seen, and so TEHP may be interacting with the areas that are pure $C_{30}H_{61}OH$ regions.

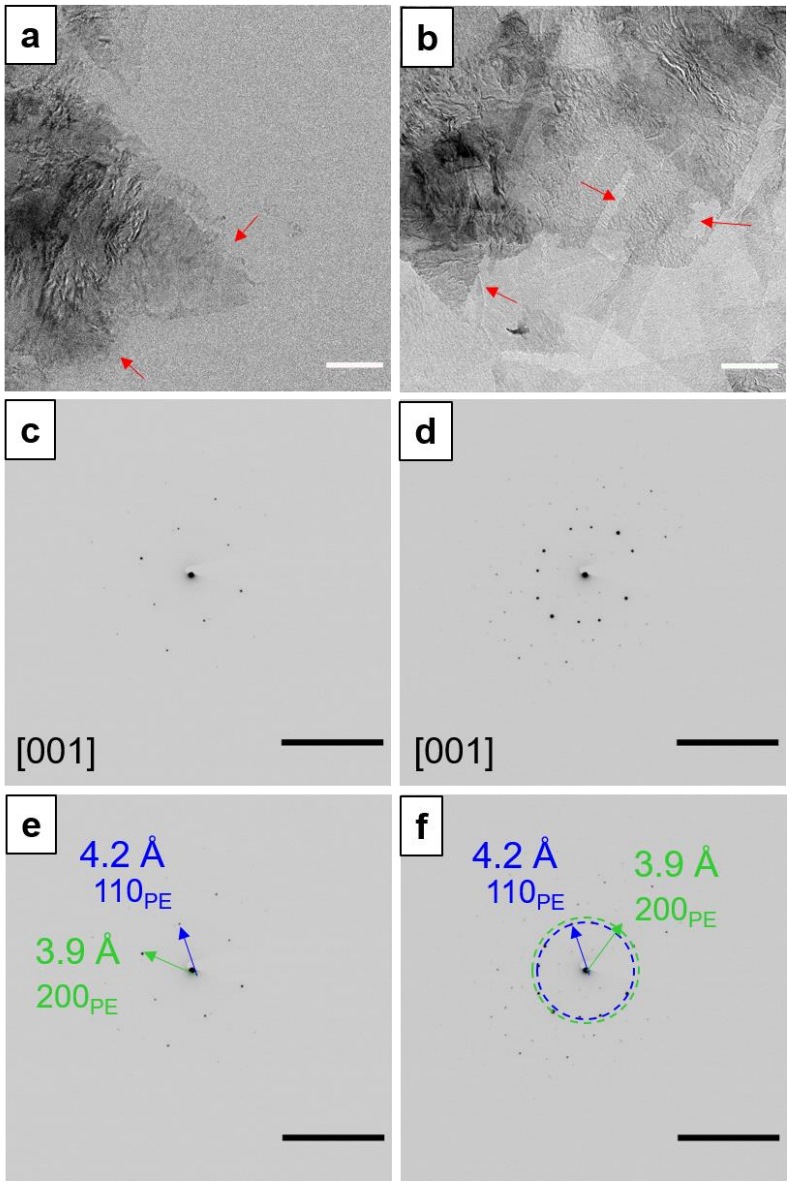

Figure 6.19: Bright field images of a binary mixture of $C_{31}H_{64}$ and $C_{30}H_{61}OH$ crystals with 50 % $C_{30}H_{61}OH$ content after TEHP exposure and the corresponding SAED pattern. Where a polycrystalline pattern was seen, the circles represent a polycrystalline ring at the indexed d-spacing. Scale bar for the BF images indicate 2 µm, and the scale bars for the SAED patterns indicate 0.5 $Å^{-1}$.

6.8 Energy-Dispersive X-ray Spectroscopy (EDX / EDS)

EDS spectra were taken on $C_{31}H_{64}$ and $C_{30}H_{61}OH$ crystals that had been exposed to TEHP (Figure 6.20). These spectra were obtained to examine the phosphorous signal that could only arise from the presence of TEHP.

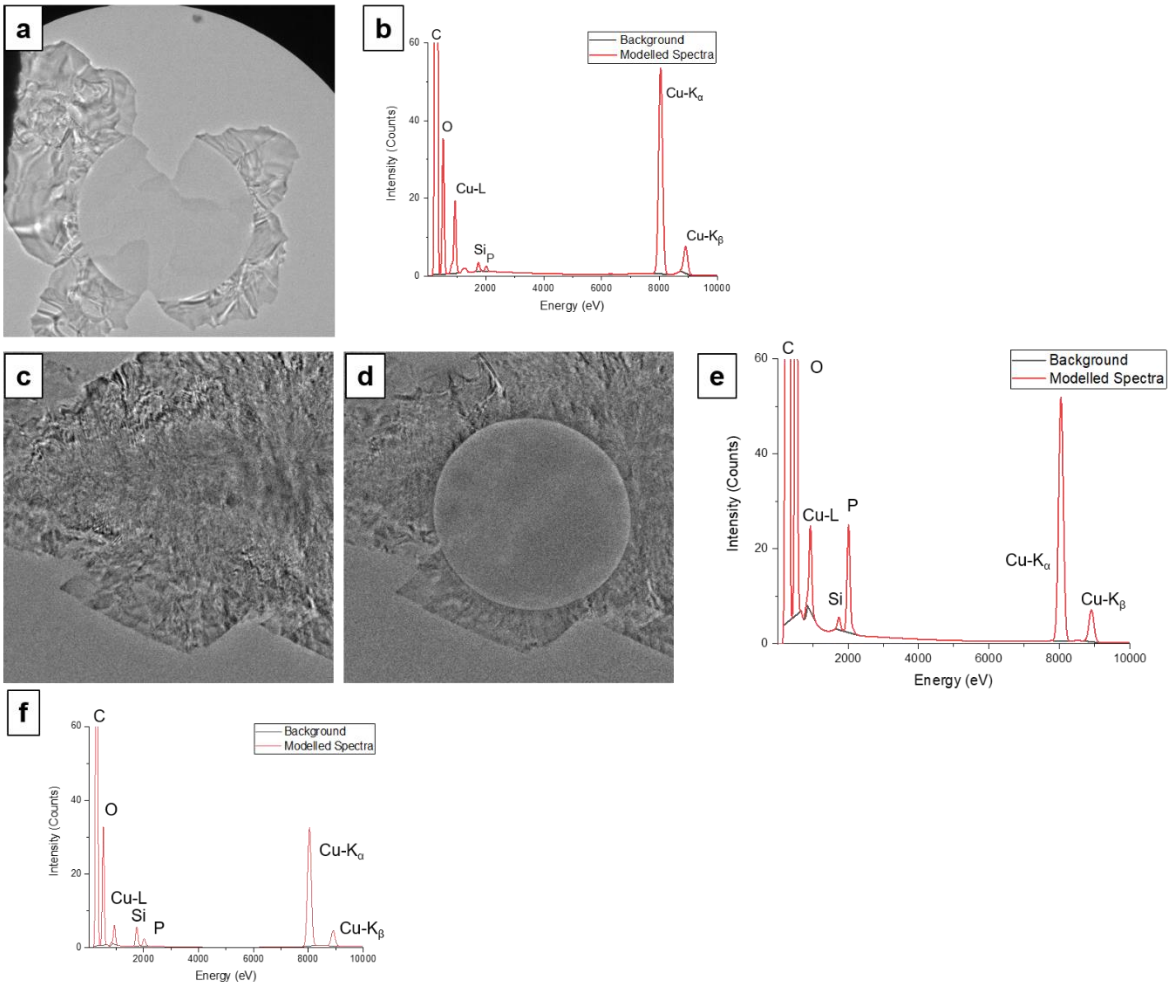

Figure 6.20: (a, b) $C_{31}H_{64}$ crystal exposed to TEHP and the corresponding EDS spectra. (c-e) $C_{30}H_{61}OH$ crystal exposed to TEHP before EDS measurement (c) and after EDS measurement (d) where the probe damage to the crystal is seen, and the corresponding EDS spectra (e). (f) EDS spectra taken on the amorphous carbon grid background.

From this data, a phosphorus peak can be seen in the $C_{30}H_{61}OH$ crystals that had been exposed to TEHP, but only a small peak, almost unresolvable from background, can be seen in the $C_{31}H_{64}$ exposed crystal spectrum. For a control measurement, a spectrum was taken of just the amorphous carbon film on the EM grid that held the $C_{30}H_{61}OH$ crystal sample (Figure 6.20f). This measurement was taken in the same grid square to ensure this was an environment that had been exposed to a similar volume / concentration of TEHP. In this spectrum, the intensity of the phosphorus peak is significantly reduced. These results together suggest that TEHP may associate

more with $C_{30}H_{61}OH$ crystals than $C_{31}H_{64}$ crystals, potentially associating at the surface through a complex with the alcohol groups and the phosphorous atoms. XRD ruled out the TEHP incorporating within the crystals so the sulphur signal is not likely arising from TEHP incorporation within the chains. Attempts were made to map this signal, to test whether this theory was correct, but the signal to noise was not sufficiently above background to obtain a conclusive map (and increasing the signal resulted in complete degradation of the wax crystals on the film).

6.9 Scanning Electron Diffraction

SAED of the crystals for all samples confirms that all samples contain crystalline material after TEHP addition and confirms orientation of the crystals relative to the electron beam, but SED can offer more detailed analysis on this system. Previous chapter results have shown the extra information SED can give on the order or disorder within these crystals, and the nanometre-resolved information that can be obtained on the structure (Chapters 4 and 5).

Also from the SED datasets, VDF images can be formed from specific (hkl) reflections showing how diffraction conditions vary across a field of view. Further, we have shown how SED can be used to analyse individual in-plane dislocations in molecular crystals using VDF images, where this analysis was applied to the wax crystals prepared for and studied in this thesis (Pham et al., 2025). A dislocation can be described as a planar cut through a section of a crystal followed by atomic displacements in a particular direction, the Burgers vector, **B** (Pham et al., 2025). Material is then added in or removed to fill the gap. This creates a linear defect, and the dislocation line vector, **u**, coincides with the dislocation core, i.e. the location of maximum lattice distortion. These dislocations can be edge, screw or mixed dislocations. Figure 6.21 is taken from Pham et al. (Pham et al., 2025) and gives a visual representation of these different types of dislocation. If a crystal is bent, then the Bragg condition will vary across the sample, and the bend contour is a map of where the Bragg condition is exactly satisfied. Where planes are distorted by the dislocation, a break in the otherwise continuous bend contour appears at this dislocation line, which corresponds to a displacement of the bend contour along **u**. In contrast, a feature such as a grain boundary would cause a consistent displacement in all $\mathbf{g}_{hkl}$ values or introduce additional $\mathbf{g}_{hkl}$ if this grain boundary was symmetry breaking. $\mathbf{g}_{hkl}$ is notation that refers to the scattering vectors i.e. the positions marked by spots in a diffraction pattern. The scattering vectors are perpendicular to the (hkl) planes. VDF images can be constructed from the different $\mathbf{g}_{hkl}$ spots from SED data, so these dislocations can be studied.

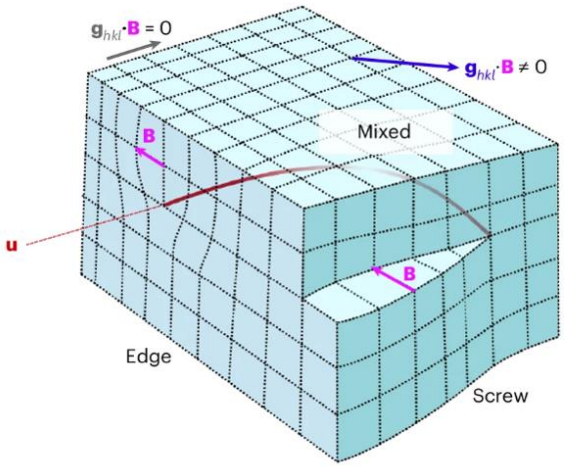

Figure 6.21: Illustration of the distortion of planes due to edge, mixed and screw dislocations, with no distortion for planes corresponding to diffraction vectors g_{hkl} at the invisibility criterion ($g_{hkl} \cdot B = 0$). Figure taken from Pham et al. (Pham et al., 2025).

In our study, we identified mixed dislocations in both $C_{31}H_{64}$ and $C_{30}H_{61}OH$ crystals, so results in this chapter use SED to look at the presence of dislocations before and after TEHP addition. The SED approach was therefore extended to the study of the wax crystals after TEHP addition.

6.9.1 $C_{31}H_{64}$ Before TEHP Addition

The conventional TEM images in Chapter 4 indicated that both $C_{31}H_{64}$ and $C_{30}H_{61}OH$ crystals are characterised by bend contours and diffraction contrast but this is relatively smooth in the *n*-alkanes and less so for the *n*-alkanols (Figure 4.7, Chapter 4). Figure 6.22 shows several ADF-STEM images of $C_{31}H_{64}$ crystals (without any TEHP exposure), where smooth bend contours are pointed out by red arrows, i.e. there is a relatively low density of defects in these crystals.

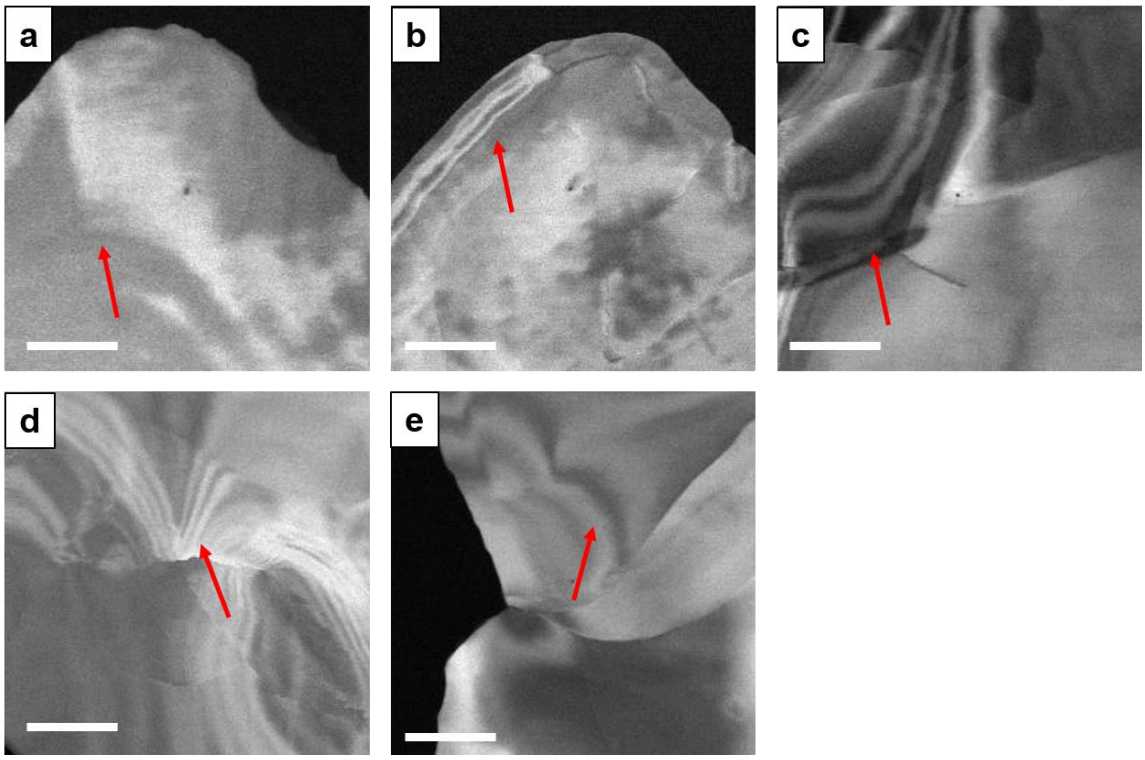

Figure 6.22: (a-e) ADF-STEM images of $C_{31}H_{64}$ crystals. Scale bars indicate 500 nm. Red arrows indicate examples of bend contours within the crystals.

Figure 6.23 shows a more detailed look at the crystal from Figure 6.22d, where VDF images were formed using the first order Bragg reflections. In this set of VDF images, the images formed from the {110} spots (green and blue) highlight the presence of a large bend contour in the top portion of the crystal. This contour is relatively smooth and unaltered across the top region suggesting there are relatively few flaws within this part of the crystal to disrupt it. This bend contour terminates at the highlighted pink line rather than being split (as would be expected if this was a dislocation) which indicates a grain boundary feature within the crystal.

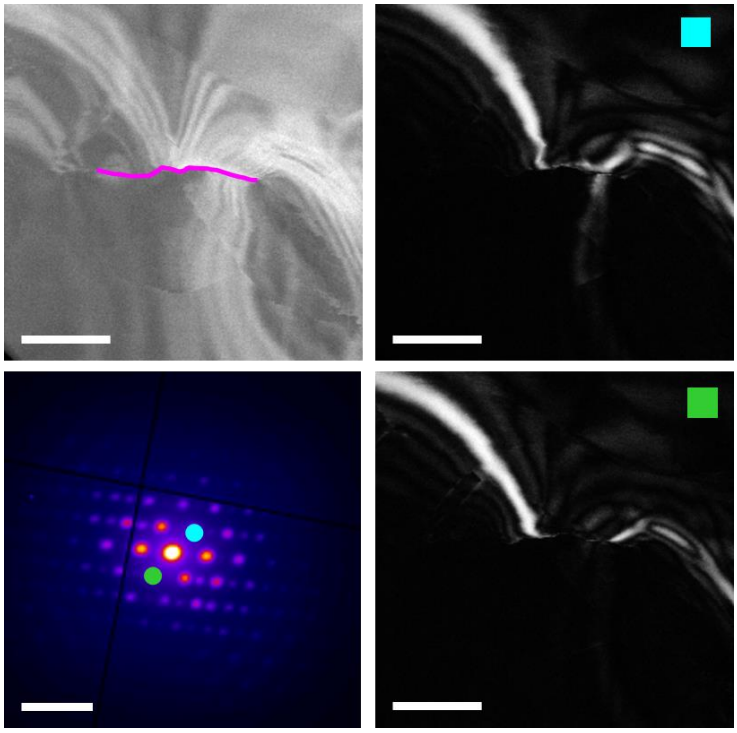

Figure 6.23: (a) ADF-STEM image repeated from Figure 6.22a, (c) VDF images produced from the Bragg spots in the average diffraction pattern (b) indicated by coloured spots matching to the coloured boxes of each image. ADF-STEM image scale bars indicate 500 nm, diffraction pattern scale bares indicate 0.5 $Å^{-1}$.

6.9.2 $C_{30}H_{61}OH$ Before TEHP Addition

Figure 6.24 shows examples of ADF-STEM images of $C_{30}H_{61}OH$ crystals. The $C_{30}H_{61}OH$ crystals are much more textured (having significantly more diffraction contrast within the crystals than in the $C_{31}H_{64}$ samples), with a high number of features that disrupt internal bend contours. These crystals appear to contain many grain boundaries or faults, similar to the grain contrast exhibited by $C_{31}H_{64}$ crystals in the 'chains-flat' orientation. This complex internal structure of the 'down-chain' $C_{30}H_{61}OH$ crystals was not the focus of the previous two chapter (or the associated publication). However, it appears as a regular feature of this wax as outlined here. It may occur as a result of more complex packing of the alcohol chain terminations where the *n*-alkanol chains have a higher level of disorder as previously discussed (Wynne et al., 2024).

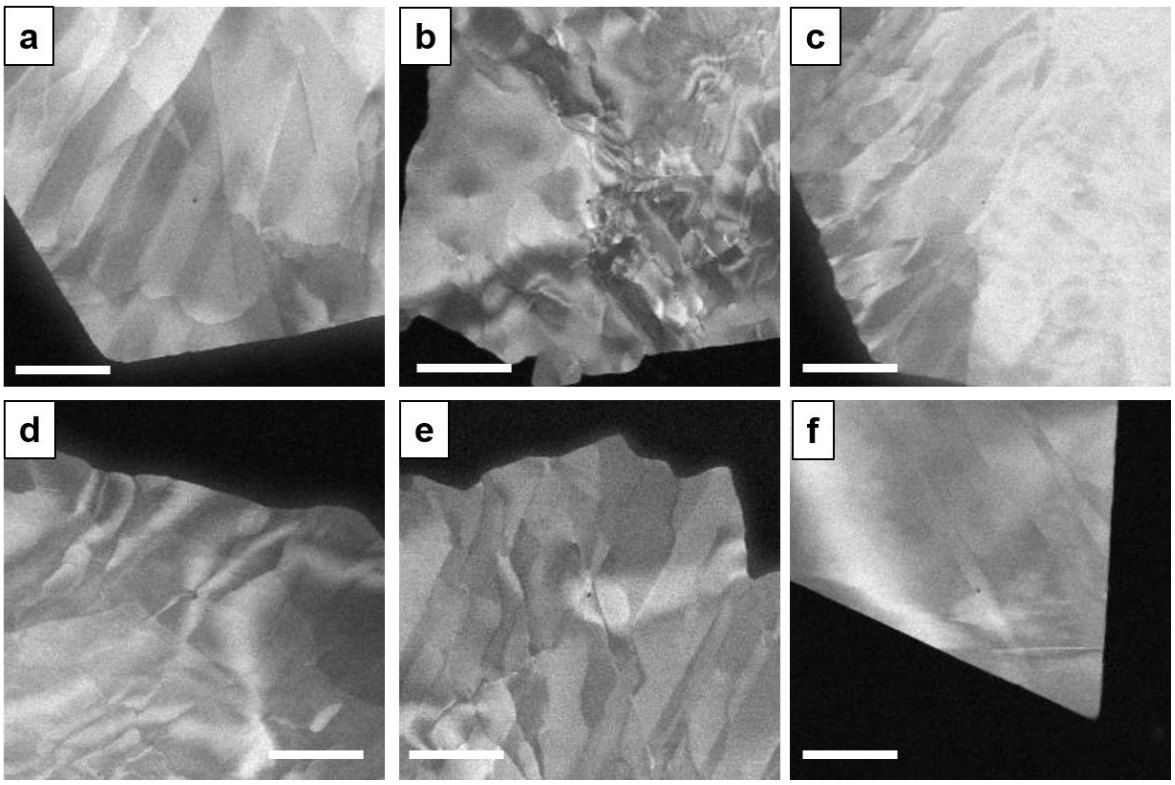

Figure 6.24: (a-f) ADF-STEM images of $C_{30}H_{61}OH$ crystals. Scale bars indicate 500 nm.

Figure 6.25 presents a breakdown of diffraction patterns taken from selected areas within these apparent grains in the $C_{30}H_{61}OH$ crystal in Figure 6.24e. There is some variation in the intensities of different diffraction spots across these internal features, implying there may be some crystal tilt and that these are indeed grains. The virtual ADF (vADF) images formed from increasing collection angles are also presented in this image (the collection angles were the same as the angles defined in Figure 5.3, Chapter 5). These grain boundaries are not visible at these higher collection angles, confirming the contrast arose from diffraction contrast effects.

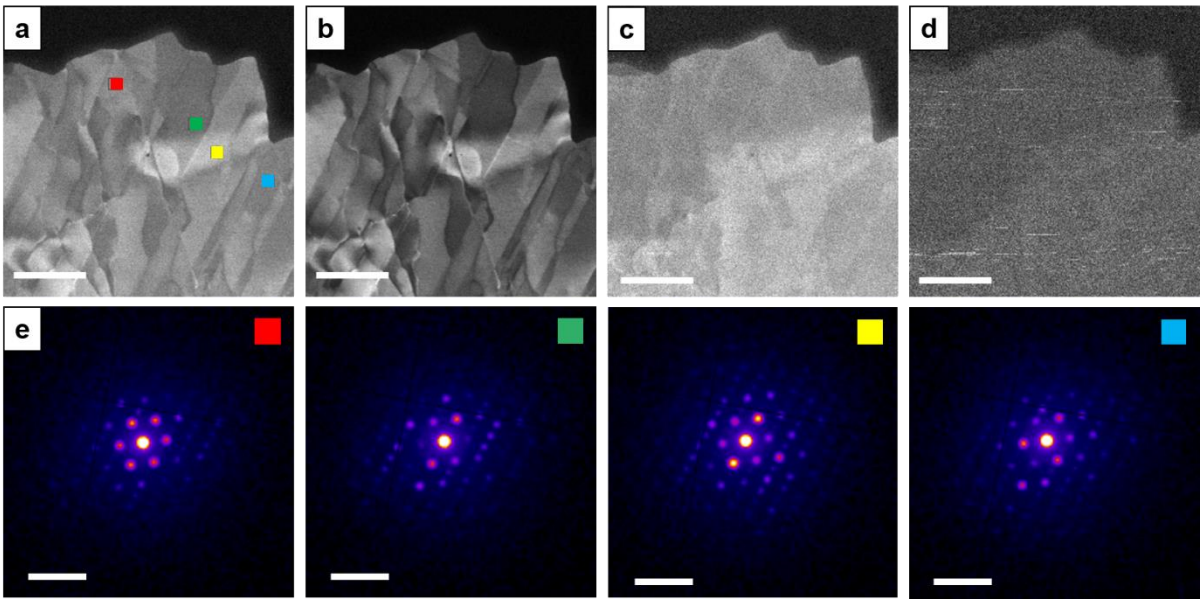

Figure 6.25: Images of a $C_{30}H_{61}OH$ crystal with increasing vADF angle, (b) low angle ADF (c) medium angle, ADF-1 (d) medium angle, ADF-2. (e) Summed diffraction patterns from an area of 10 x 10 pixels shown by the coloured boxes in the corresponding $C_{30}H_{61}OH$ crystal (a). All bright field image scale bars indicate 500 nm. All diffraction pattern scale bars indicate 0.5 $Å^{-1}$.

Figure 6.26 presents a detailed VDF analysis of another $C_{30}H_{61}OH$ crystal from Figure 6.24d. In this figure, VDF images formed from the {110} spots also reveal the presence of dislocations in this crystal. The green lines highlight an example of a dislocation running through the crystal disrupting several bend contours. In the VDF images, the bend contour is broken and shifted in a certain direction. This dislocation is further explored in Figure 6.26. Spot positions in the diffraction patterns either side of this line are the same, and the shift in the bend contour can be seen. The displacement magnitudes for non-collinear $\mathbf{g}_{hkl}$ values change, as can be seen in the shift in the red and orange images, which is characteristic of dislocations. These indicate this is likely a dislocation and not a bend contour.

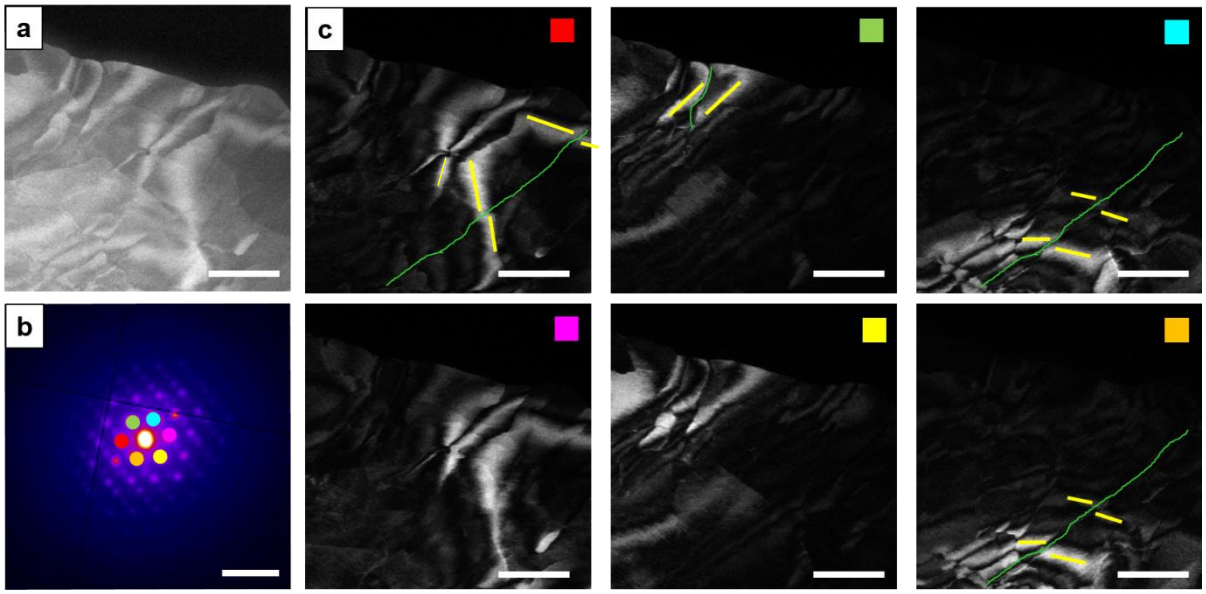

Figure 6.26: (a) ADF-STEM image repeated from Figure 6.24d, (c) VDF images produced from the Bragg spots in the average diffraction pattern (b) indicated by coloured spots matching to the coloured boxes of each image. ADF-STEM image scale bars indicate 500 nm, diffraction pattern scale bars indicate 0.5 Å^{-1}.

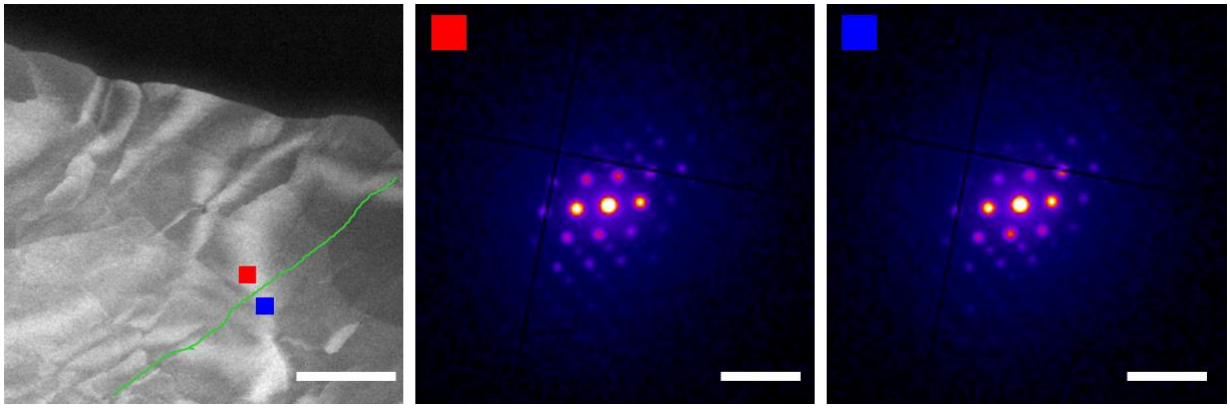

Figure 6.27: (a) ADF-STEM image repeated from Figure 6.24d with red and blue boxes corresponding the diffraction patterns in (c) and (d) respectively. (b) The green line indicates the dislocation line. ADF-STEM image scale bars indicate 500 nm, diffraction pattern scale bars indicate 0.5 Å^{-1}.

The work in Pham et al. provides further detailed analysis of the dislocations found in the $C_{30}H_{61}OH$ crystal in Figure 6.23f (Pham et al., 2025). In this study, the dislocation was identified with the Burgers vector direction along **B** = [010] illustrating a range of edge, screw, and mixed character. However, this thesis does not aim to do a full dislocation analysis, but looks at differences in the crystallisation behaviours of the *n*-alkane and *n*-alkanol, to consider whether these defects contribute to differences in response to TEHP.

This SED analysis has highlighted that even before TEHP addition there are already intrinsic differences between the two crystals, specifically the $C_{30}H_{61}OH$ crystals contain many grains and dislocations in comparison to the $C_{31}H_{64}$ crystals. This is however for a limited number of samples so may have some limited generalisability.

6.9.3 $C_{31}H_{64}$ After TEHP Addition

Figure 6.27 presents ADF-STEM images of $C_{31}H_{64}$ crystals after TEHP exposure. These images offer similar insights to the BF images from conventional TEM, where the $C_{31}H_{64}$ crystals form agglomerate structures. The materials on the TEM grid are crystalline as evidenced by the average diffraction patterns. These crystals remain characterised by the presence of large, smooth bend contours, similar to the crystals before TEHP addition. The edges of these crystals also remain smooth, in agreement with previous data in this chapter. However, there is evidence of some pit formation along primary crystal planes indicated by the green arrows in Figure 6.28, which may suggest an element of dissolution in the $C_{31}H_{64}$ crystals. In Figure 6.28h and Figure 6.28i, it can be seen that these green arrows correspond to the same set of crystallographic (110) planes.

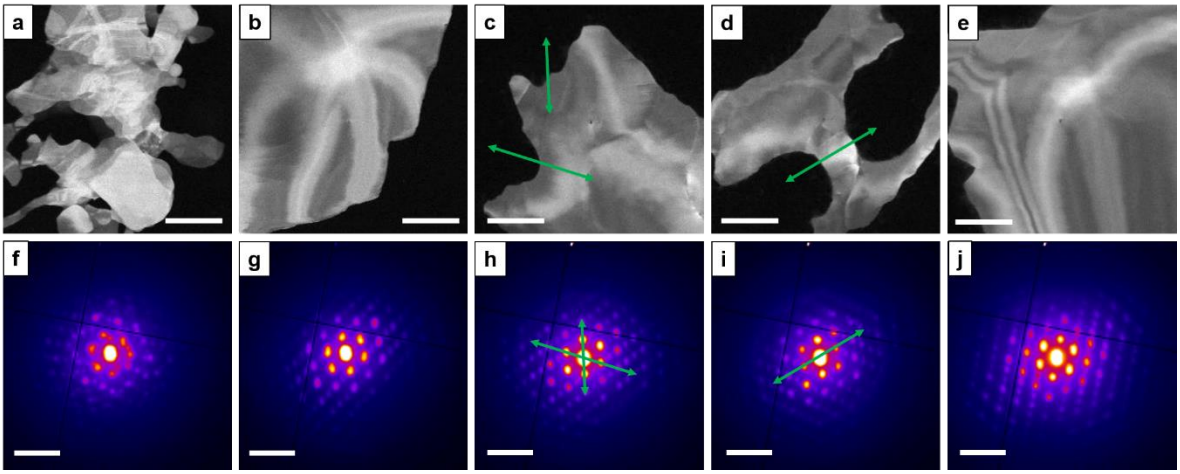

Figure 6.28: (a-e) ADF-STEM images $C_{31}H_{64}$ crystals after TEHP exposure, and the corresponding diffraction patterns (f-j). ADF-STEM image scale bars indicate 500 nm, diffraction pattern scale bars indicate 0.5 $Å^{-1}$.

Figure 6.29 shows a VDF breakdown of the $C_{31}H_{64}$ crystal in Figure 6.28c. In this example, what appears to be a dislocation (green line) can be seen disrupting the large bend contour, indicated by displacement in the yellow lines following the bend contour. There is not a large difference between the crystals before and after TEHP addition, which agrees with previous data proposing that TEHP addition has little effect on the structure of the $C_{31}H_{64}$ crystals.

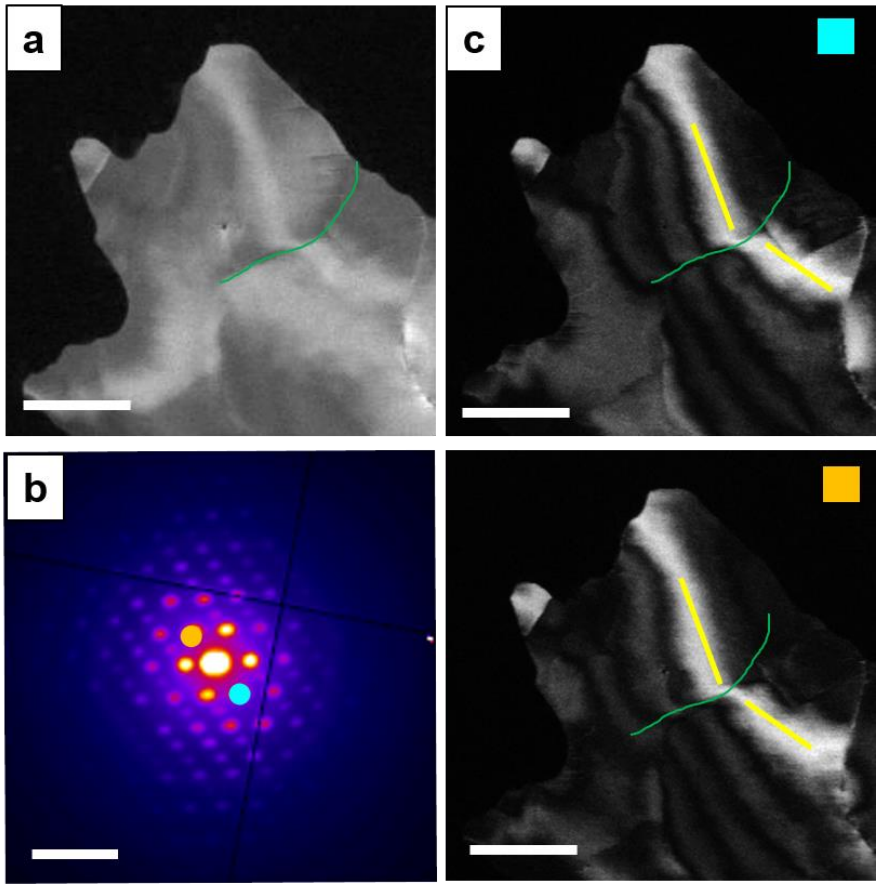

Figure 6.29: (a) ADF-STEM image repeated from Figure 6.28c, (c) VDF images produced from the Bragg spots in the average diffraction pattern (b) indicated by coloured spots matching to the coloured boxes of each image. ADF-STEM image scale bars indicate 500 nm, diffraction pattern scale bars indicate 0.5 $Å^{-1}$.

6.9.4 $C_{30}H_{61}OH$ After TEHP Addition

Figure 6.30 shows several $C_{30}H_{61}OH$ crystals after TEHP addition with average diffraction patterns confirming maintained crystallinity. These crystals are all characterised by the presence of clear pits at the projected surface facets as seen in the TEM data, providing further evidence for a proposed etching mechanism. These pits are sharper with flat edges than the rounded surfaces seen in $C_{31}H_{64}$. The internal diffraction contrast also remains a complex mixture of grains and dislocations.

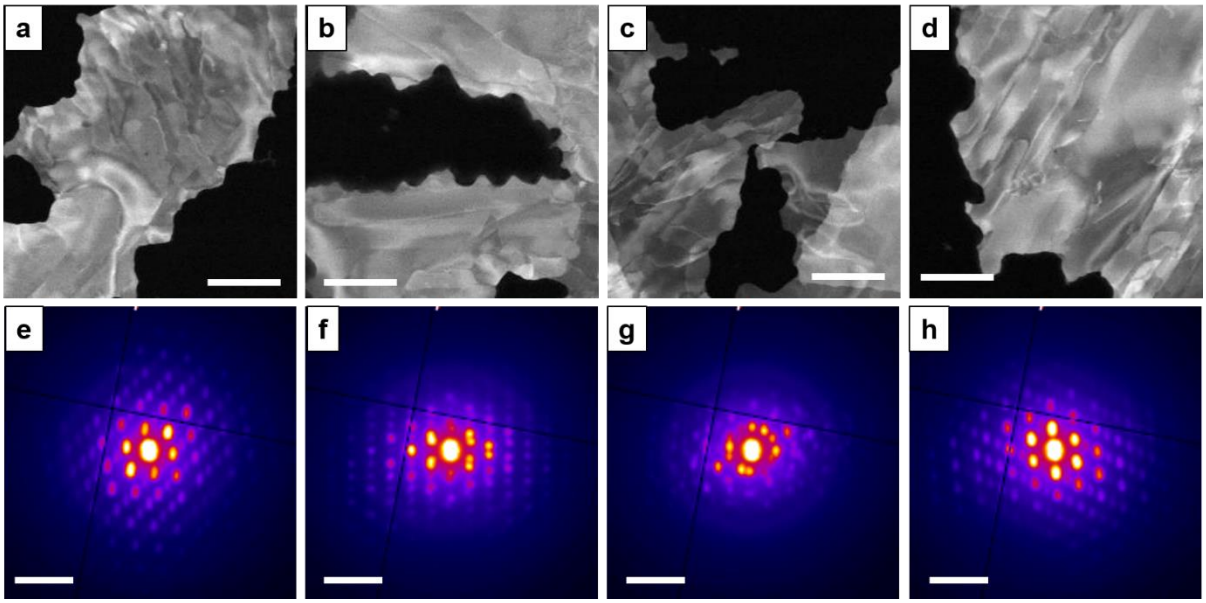

Figure 6.30: (a-d) ADF-STEM images $C_{30}H_{61}OH$ crystals after TEHP exposure, and the corresponding diffraction patterns (e-h). ADF-STEM image scale bars indicate 500 nm, diffraction pattern scale bars indicate 0.5 $Å^{-1}$.

The grain contrast is also maintained upon TEHP addition, and Figure 6.31 takes the $C_{30}H_{61}OH$ crystal from Figure 6.30d and presents vADF images with increasing collection angle. Figure 6.31e presents a set of diffraction patterns from selected areas which again show the variation in intensity across the linear features, implying a tilt in the crystal occurs and an internal grain structure prevails.

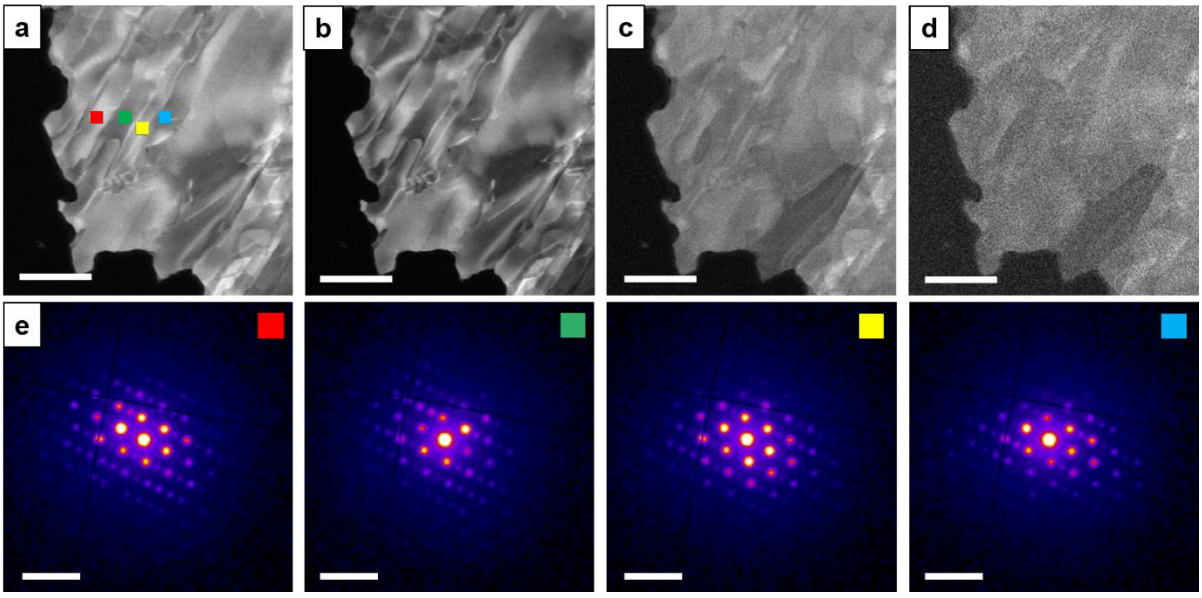

Figure 6.31: Images of a $C_{30}H_{61}OH$ crystal with increasing vADF angle, (b) low angle ADF (c) medium angle, ADF-1 (d) medium angle, ADF-2. (e) Summed diffraction patterns from an area of 10 x 10 pixels shown by the coloured boxes in the corresponding $C_{30}H_{61}OH$ crystal (a). All bright field image scale bars indicate 500 nm. All diffraction pattern scale bars indicate 0.5 $Å^{-1}$.

The VDF images in Figure 6.32 confirm the presence of a high number of bend contours and examples of dislocations are highlighted within inset the red boxes. Figure 6.33 explores an example of a dislocation further, with diffraction patterns on either side of a line that disrupts this bend contour being the same, showing this feature is likely in fact a dislocation and not a grain boundary, where an in-plane rotation may be expected to be seen, or multiple changing intensities in the Bragg spots. In this crystal, there are also some examples of bend contours terminating at the bottom of the pits formed.

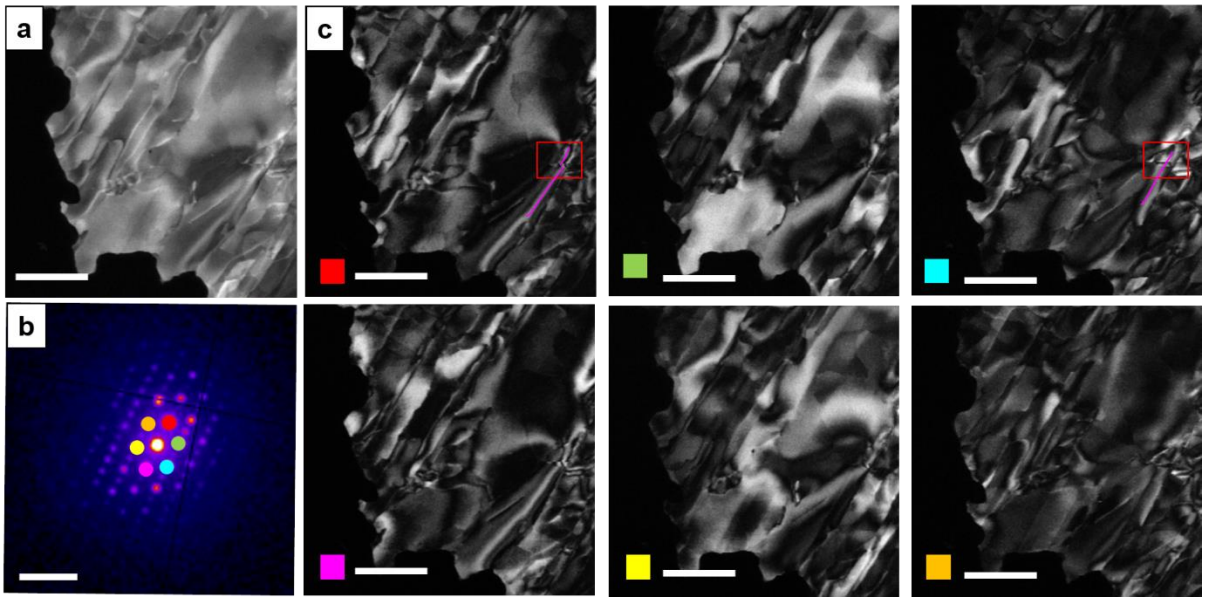

Figure 6.32: (a) ADF-STEM image repeated from Figure 29d, (c) VDF images produced from the Bragg spots in the average diffraction pattern (b) indicated by coloured spots matching to the coloured boxes of each image. ADF-STEM image scale bars indicate 500 nm, diffraction pattern scale bares indicate 0.5 Å^{-1}.

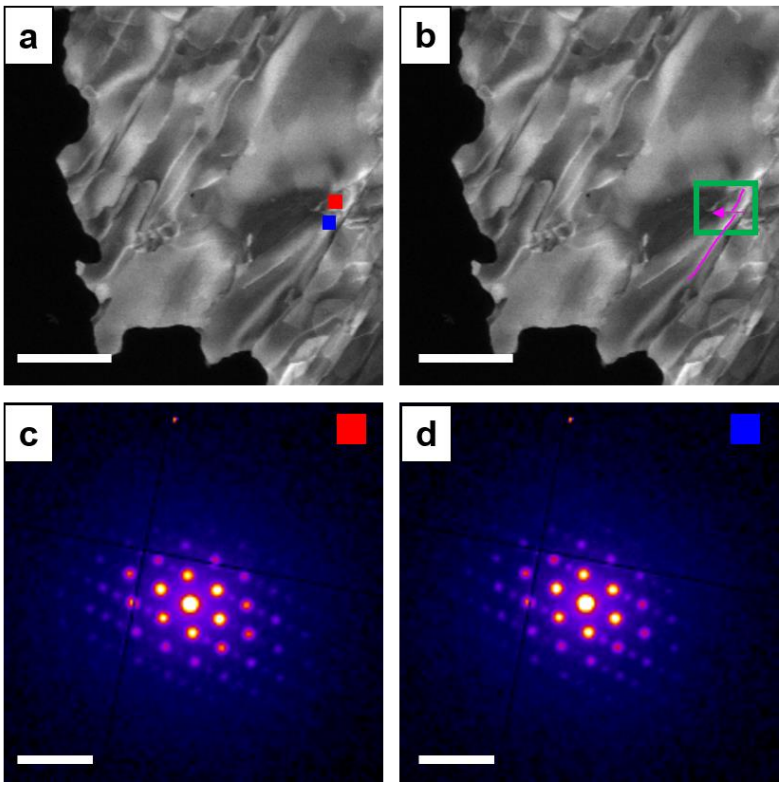

Figure 6.33: (a) ADF-STEM image repeated from Figure 29d with red and blue boxes corresponding the diffraction patterns in (c) and (d) respectively. (b) Green box highlights the bend contour that is disrupted in different VDF images in Figure 32. The pink arrow indicates the movement of this shift. ADF-STEM image scale bars indicate 500 nm, diffraction pattern scale bares indicate 0.5 $Å^{-1}$.

6.9.4.1 Facet Analysis

For these TEHP exposed $C_{30}H_{61}OH$ crystals, the 'sawtooth' edge characteristics prompted further investigation of the particular crystallographic planes involved. The main chemical difference between the $C_{31}H_{64}$ and $C_{30}H_{61}OH$ is the alcohol group; given that TEHP is soluble in alcohol, the presence of alcohol groups at a surface may lead to preferential interactions with TEHP and enhancing material removal. A paper looking at etch pit formations in calcite looked at different acids as etchants (Keith and Gilman, 1960). They looked at lactic acid and acetic acid, which differ by a chemically inactive -OH group on the carbon next to the carboxyl group in the lactic acid instead of hydrogen in the acetic acid. This lactic acid etching, above a 1 H_2O: 5 acid concentration, produced pits of a different shape. They concluded that the interaction between the ions in the etchants and the geometric arrangement of ions on the crystal surfaces was significant to the rate of etch pit formation. This may suggest that the OH groups in the $C_{30}H_{61}OH$ crystals do in fact play a significant part in the interaction with TEHP compared to the alkyl groups, and potentially surfaces with a higher percentage of alcohol groups would etch faster.

Figure 6.34 presents a facet analysis of three $C_{30}H_{61}OH$ crystals. These surfaces were analysed by drawing a straight line parallel to the inferred pre-exposure, defined by aligning the line along the top of the remaining protruding features. The normal of the real space planes corresponds to the direction of the reciprocal lattice vector, so the crystal plane this facet corresponds to can be determined from the corresponding diffraction pattern. The facets of $C_{30}H_{61}OH$ crystals before TEHP addition primarily follow the (110) crystal planes, with a smaller sample following the (010) and (100) planes.

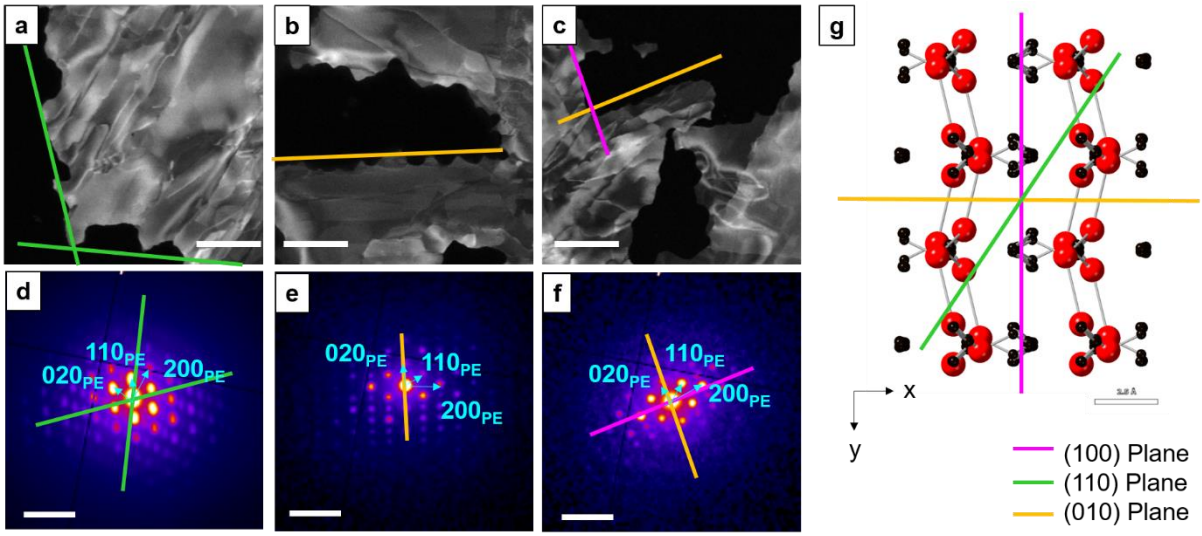

Figure 6.34: (a-f) Analysis of the edges where the etched pits form from, with a representation of the crystal planes these straight lines (edges) correspond to (g). The black spheres correspond to carbon atoms, and the red spheres correspond to oxygen atoms. This representation is viewed down the [001] zone axis.

Figure 6.34 shows the pre-exposed facets in the TEHP exposed crystals mainly follow the (100), (110), and (010) crystal planes. In the structural model presented in Figure 6.34g, the red atoms correspond to the oxygen atoms and the black atoms correspond to the carbon atoms. In the *P2₁/c* $C_{30}H_{61}OH$ structure, the alcohol groups are aligned with *trans* and *gauche* conformations at the chain ends.

Figure 6.35 takes one of the $C_{30}H_{61}OH$ crystals from Figure 6.34 and measures the angles between these straight lines and the bottom of the 'dips'. These angles were measured to be between 30-50° away from the (010) plane. In the simulated crystal structure, the *gauche* alcohol groups lie roughly at these angles away from the (120) and (230) planes. It could therefore be assumed that these planes etched at a slower rate than the previous surface plane. It was evaluated whether more alcohol groups or alkyl groups are presented at the surface of these planes, and whether this information could provide information as to why these remaining surface planes etched at a slower rate.

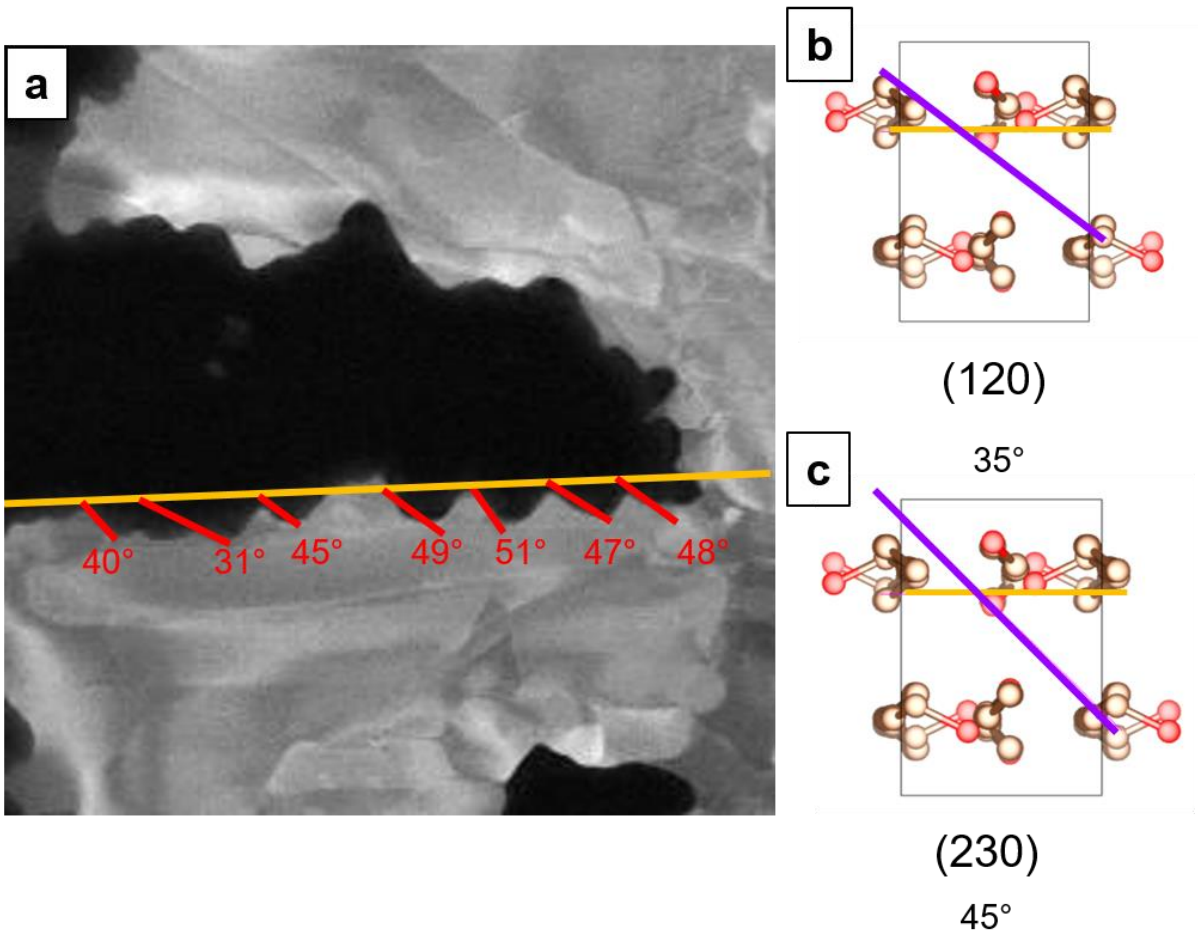

Figure 6.35: (a) A $C_{30}H_{61}OH$ crystal where the angle of the facet compared to the (010) plane has been measured. The red lines are drawn from the orange line to the bottom of the respective pit. (b, c) A representation of the (120) and (230) crystal planes (purple lines) and the angle these planes lie away from the (010) plane (orange lines). In these representations, the brown circles represent carbon atoms and the red circles represent oxygen atoms.

Table 6.4 presents a breakdown of the number of chains that contain an alcohol group presented at the surface, as a percentage of the total number of chain terminations presented at each projected surface, for the common planes studied in these results. These percentages have been broken down into whether the alcohol group is a *trans* or a *gauche* oriented group. This difference is important to note in cases where the alcohol groups presenting at the surface is 50%, as a potential explanation for increased etching at certain surfaces. With the *trans* or *gauche* groups taking up different physical space, etching may occur at different rates. It is noted that the crystal planes identified are a set of equivalent planes in the crystal structure, so where the plane has been set in Vesta is an arbitrary position. However, when assessing groups at the surface, it was ensured the plane was adjusted to ensure the position of the plane left all molecules intact, so only whole molecule projections were assessed. Molecules were also counted as being at the surface if there was empty space

between that molecule and the drawn surface, meaning TEHP interaction could be possible. The positive and negative columns refer to the positive and negative Miller indices orientation of the same plane. For example, when looking ‘down-chains’, where the (100) crystal plane line is drawn affects whether a *trans* or *gauche* group presents at this surface. Figure 6.36 presents a set of representations of where these planes have cut the crystal structure, and where these surfaces present for the (010) and (230) planes. However as can be seen from the percentages presented in Table 6.4, the other planes have an element of symmetry where the *gauche* or *trans* groups presents at the surface equally from either direction, due to the alternate nature of the *trans* / *gauche* and alcohol group packing.

Table 6.4: A table presenting the number of alcohol groups presenting at the surface of a crystallographic plane as a percentage of the total number of chain terminations presenting at each surface, and broken down to the positive and negative integers of each plane, and whether these alcohol groups are *trans* or *gauche*.

Plane	**Total**	**+**	**-**
100	50%	50% gauche	50% trans
110	50%	30% trans 20% gauche	30% trans 20% gauche
010	50%	25% trans 25% gauche	25% trans 25% gauche
120	50%	17% trans 33% gauche	17% trans 33% gauche
230	30%	10% trans 20% gauche	10% trans 20% gauche
210	38%	21% trans 17% gauche	21% trans 17% gauche

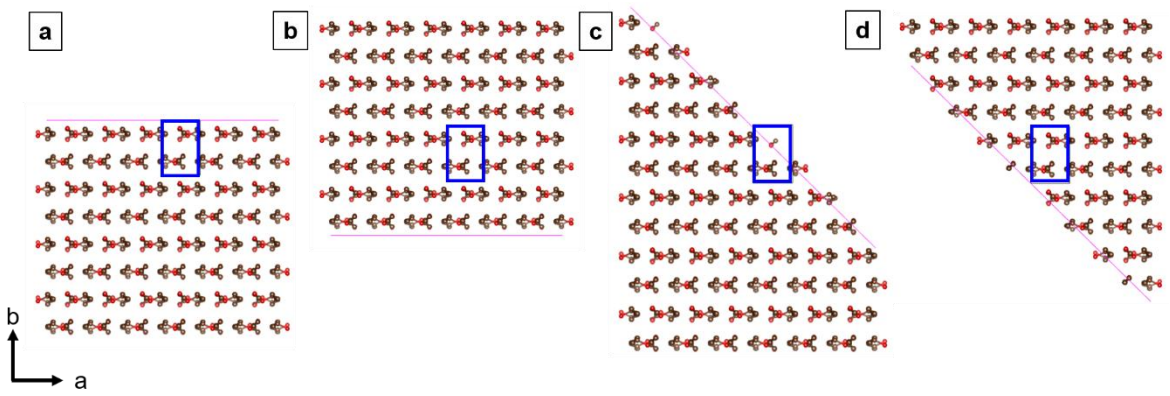

Figure 6.36: Representation of (a) the (010) plane, (b) the $(0\bar{1}0)$ plane, (c), the (230) plane, and the (d) $(\bar{2}\bar{3}0)$ plane. The unit cell was expanded to 6 unit cells up and across, and cut at the lattice plane.

The number of alcohol groups at the surface of the planes before and after etching can then be compared. Taking the planes from Figure 6.35, (010) before, and (230) after, it can be observed that the (230) plane has fewer alcohol groups at the surface than (010). If the TEHP interacts with the alcohol groups, it would make sense why a plane with fewer alcohol groups at the surface would etch more slowly. When comparing the (010) plane to the (120) plane, the number of alcohol groups is the same at each surface. However, in this case the difference between the percentage of either the *trans* or *gauche* groups differs, with a higher percentage of *trans* alcohol groups at the surface of (010), the surface that has etched quicker, than the (120) plane. The *trans* groups are in plane with the rest of the carbon chain, whereas the *gauche* groups stick out at an angle from the C-C backbone. This means the *gauche* alcohol groups are less sterically hindered, so perhaps TEHP can interact with this group without a closer interaction with the rest of the chain. This would be less disruptive to the extended crystal structure so the material is not as easily removed.

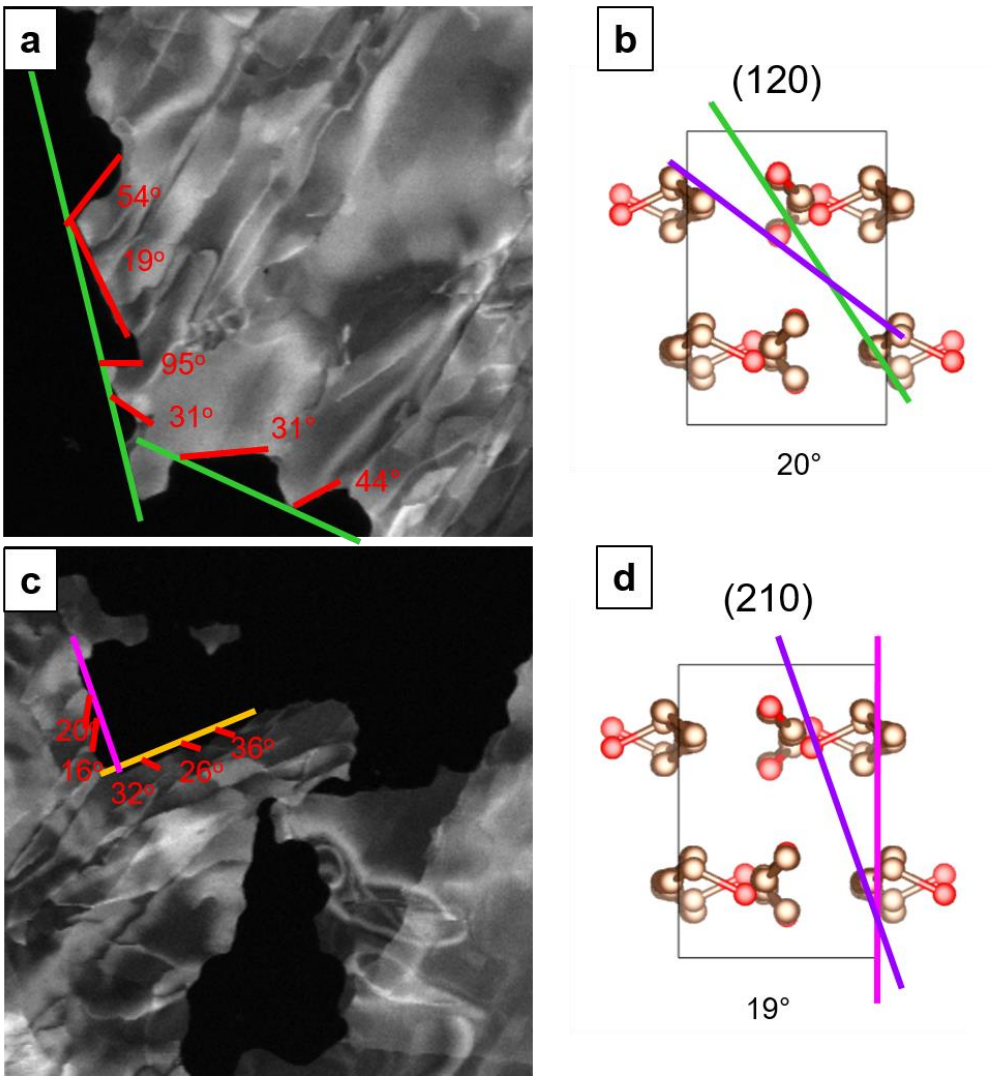

Figure 6.37: (a, c) $C_{30}H_{61}OH$ crystals where the angle of the facets compared to the (010) plane (orange line), the (100) plane (pink line) and the (110) plane (green line) has been measured. (c, d) A representation of the (120) and (210) crystal planes (purple lines) and the angle these planes lie away from (100) plane (pink line) and the (110) plane (green line).

Similar pit phenomenon can be seen in further $C_{30}H_{61}OH$ examples when observing the angle of the dips in comparison to further crystal planes. Figure 6.37a shows a $C_{30}H_{61}OH$ crystal with two facets following the (110) and $(\bar{1}\bar{1}0)$ plane, noted with green lines. Figure 6.36b shows a matched angle of one of the facets between the (110) and (120) plane, with the measured angle of one pit being 19°. Comparing the alcohol groups at the surface, whilst the total number is again the same, there are again more *trans* groups at the surface that has been apparently etched away more quickly.

The (110) plane lies 55° away from the (010) plane, and 35° away from the (100) plane which matches some of the larger angle dips away from these (110) planes. In both of these cases, the *trans* groups at the surface are of a higher percentage in the plane that has etched away.

Figure 6.37c shows another $C_{30}H_{61}OH$ crystal with a pink line facet aligned to the (100) plane, and Figure 35c shows a (210) plane which lies 19° away from the (100) plane, roughly matching the two measured angles of the pits. The (210) plane has fewer alcohol groups at the surface than the (100) plane, so one might expect this plane to interact less with the TEHP, and therefore etch away slower.

The other orange line facet aligns with the (010) plane, and the (120) plane lies 35° away from this plane explaining the angle of the dips from this line. This however is a case where the remaining plane has more *gauche* oriented alcohol groups.

The limitations of this approach are that the crystals have been shown to not be perfectly ordered, so the number of alcohol groups at different surfaces may differ. However, previous analysis in Chapter 5 has shown that diffuse scattering can be seen as a result of very small chain displacements. This suggests that, despite the disorder in these crystals, the number of alcohol groups at the surface may still match that in the unit cell representation. The SED data has also identified a consistent etching character across several crystals, which suggests there is an underlying motivation for formation of these etch pits.

6.9.5 Comparison of $C_{31}H_{64}$ and $C_{30}H_{61}OH$ Crystals Before and After TEHP Addition

To summarise the SED results thus far, it is apparent that even before TEHP addition, $C_{30}H_{61}OH$ crystals contain a higher density of internal disorder characterised by many linear grains and some dislocations relative to the $C_{31}H_{64}$ crystals. On TEHP addition, there are examples of dislocations in both $C_{31}H_{64}$ and $C_{30}H_{61}OH$ crystals. While the size, morphology and internal structure of $C_{31}H_{64}$ crystals is maintained, the morphology of $C_{30}H_{61}OH$ crystals changes with pits forming from the original crystal facets (without significant change in crystal size or internal structure although optical microscopy might suggest the $C_{30}H_{61}OH$ crystals do break apart more than the $C_{30}H_{61}OH$ crystals). The morphological differences can be seen as presented in Figure 6.38, where the differences between the two crystals, and differences in both of them after TEHP addition, are apparent.

There are a few possible reasons why there is more disorder seen in the $C_{30}H_{61}OH$ crystals in this orientation. As established in Chapter 4, the $C_{30}H_{61}OH$ chains pack with an alternate stacking unit cell, where either the alcohol group presents at the surface or the alkyl group. AFM results also showed the presence of patches of differing adhesion within these crystals, which was attributed to the different groups presenting at the surface. In some cases, these neighbouring regions occurred at the same height, but in this unit cell an alcohol group or an alkyl group cannot present at the

same height. So any neighbouring areas with differing adhesion at the same height would form a grain boundary as their crystal packing will differ. The grains seen in SED are smaller than the differing adhesion patches seen in AFM, but indicates that stacking faults and grains are more likely in the *n*-alkanol sample.

For the $C_{30}H_{61}OH$ crystals, 4 chains end-to-end form a unit cell, in comparison to the $C_{31}H_{64}$ unit cell which consists of only 2 chains end-to-end. The greater number of chains and atoms in a given $C_{30}H_{61}OH$ unit cell gives a greater number of opportunities for faulting or disorder that leads to the formation of grain boundaries and/ or the nucleation of dislocations.

In Chapter 4 the possible unit cells for $C_{31}H_{64}$ and $C_{30}H_{61}OH$ were investigated. The possible unit cells for $C_{31}H_{64}$ were simple and similar, both containing end-to-end chain packing with distinct lamellae. Out of the possible unit cells for $C_{30}H_{61}OH$, two of them exhibit end-to-end packing with distinct lamellae, but the *C2/c* unit cell does not. If the $C_{30}H_{61}OH$ usually preferentially crystallises with the *C2/c* symmetry but cannot in this orientation because of crystallization onto a flat surface, this may cause a lot of disorder within the system, leading to the high density of grain boundaries and dislocations seen. Future work could look to quantify the differences in boundaries, faults and dislocations between these two crystal waxes in this orientation, using techniques such as AFM and scanning tunnelling microscopy (STM) to also observe the groups presenting at the surface, and seeing if different groups are found at each side of a grain boundary.

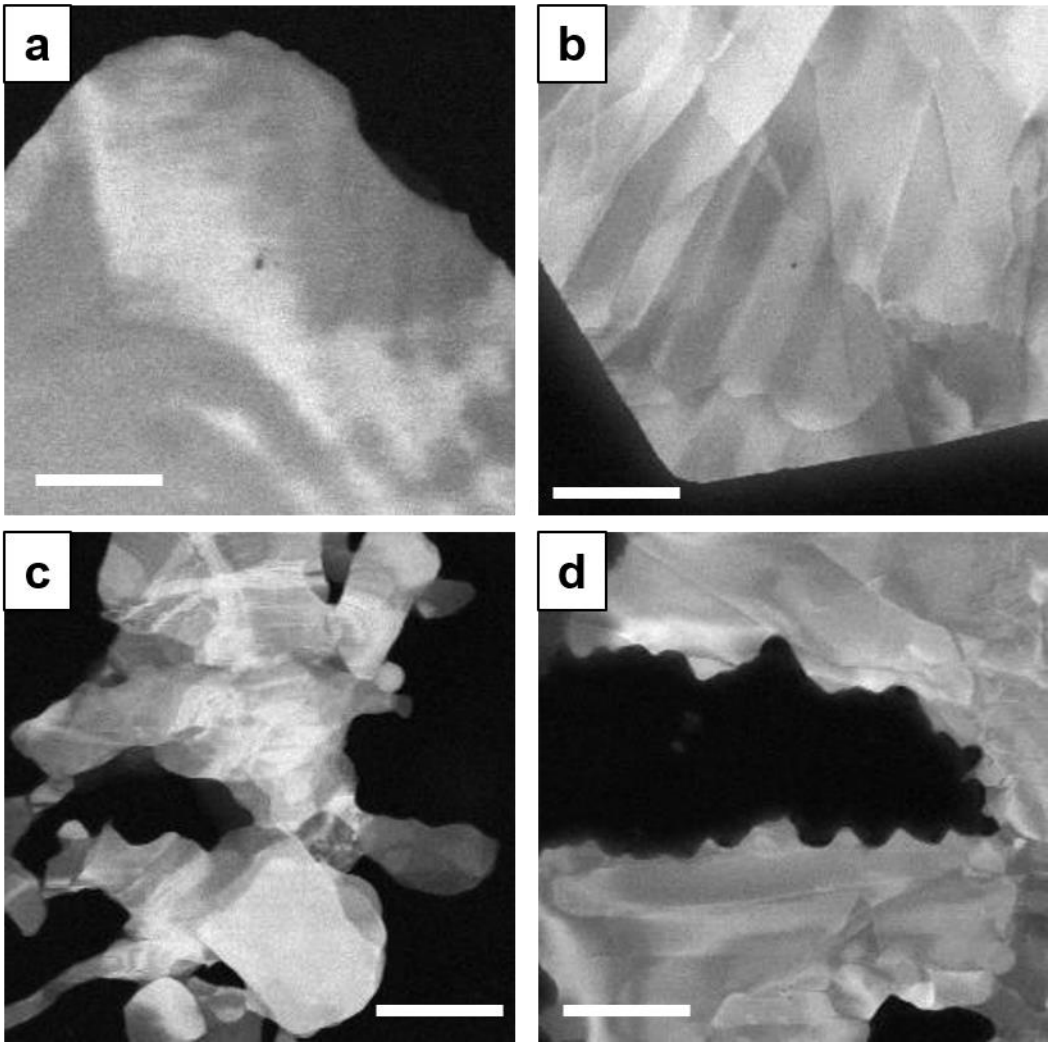

Figure 6.38: ADF-STEM images of (a) $C_{31}H_{64}$ crystal, (b) $C_{30}H_{61}OH$ crystal, (c) $C_{31}H_{64}$ crystal exposed to TEHP, (d) $C_{30}H_{61}OH$ crystal exposed to TEHP. Scale bars indicate 500 nm.

Crystal facet analysis has found that in certain $C_{30}H_{61}OH$ crystal cases, preferential TEHP-induced etching appears to occur at surfaces where there is a higher proportion of alcohol groups at the surface. In a majority of other cases, it is where there are more *trans* oriented alcohol groups at the surface that etching is enhanced.

Formation of etch pits at dislocation sites in metals (Gilman et al., 1958) and calcites (Teng, 2004) have been reported previously. There are examples of dislocations terminating at these etched ‘dips’ in the $C_{30}H_{61}OH$ crystals (Figure 6.37), although this is not always the case. The $C_{30}H_{61}OH$ crystals notably have a higher grain boundary and dislocation network within. Again, this could explain the formation of these ‘dips’ in these crystals.

6.9.6 Binary Mixture After TEHP Addition

A binary mixture was also studied, using a composition with 50% $C_{30}H_{61}OH$ content. Figure 6.39 shows the crystals before TEHP addition, where the crystals draw similarities with the pure $C_{30}H_{61}OH$ crystals showing grain boundaries, and a high density of distorted bend contours.

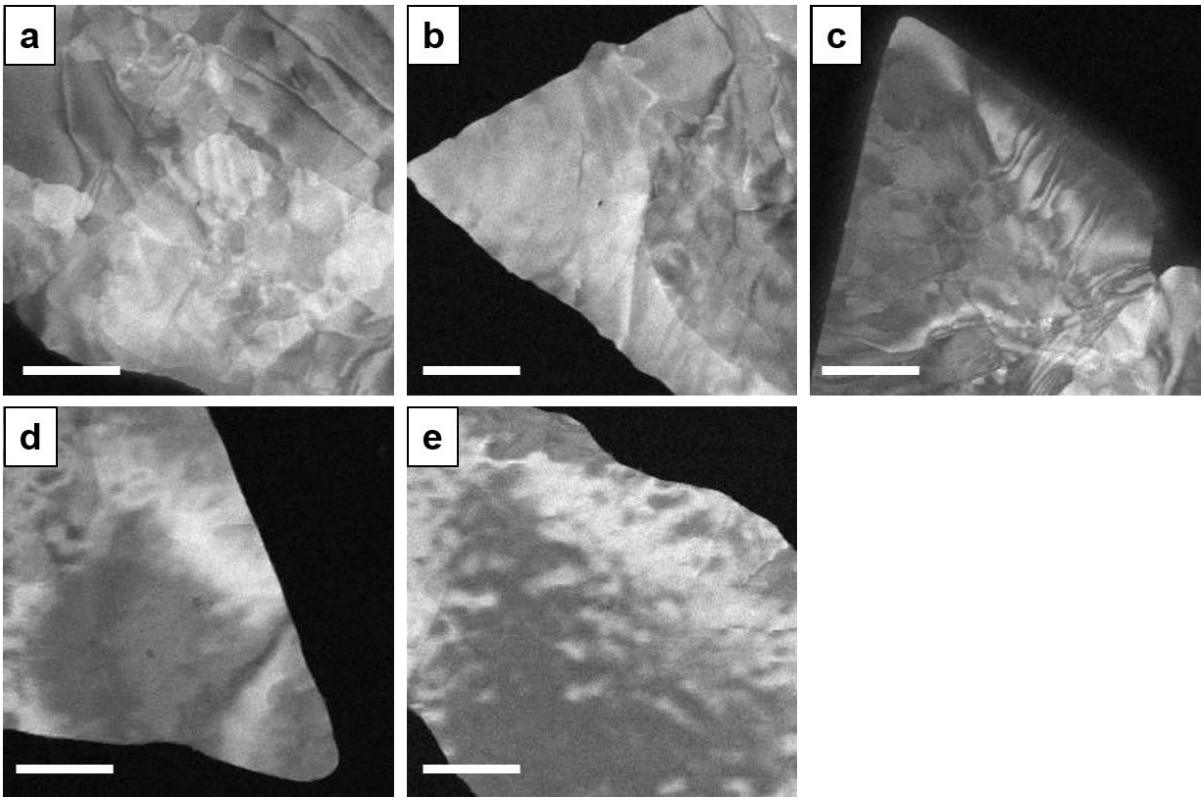

Figure 6.39: (a-e) ADF-STEM images of binary mixture crystals with 50% $C_{30}H_{61}OH$ content. Scale bars indicate 500 nm.

Figure 6.40 then shows the 50% $C_{30}H_{61}OH$ binary mixture crystals after TEHP addition. These crystals are still characterised by a high density of grains and distorted bend contours within the crystals. There is also what looks to be the removal of material at some of the edges of the crystals (inset red arrows). These dips are not as deep as the pure $C_{30}H_{61}OH$ sample but can be seen in Figure 6.40a and 6.40b. This is a similar observation to what was seen in the TEM data for this same binary mixture. This binary mixture is where phase separation between the alkane and alkanol is meant to occur, which would explain why this pit formation is seen, as it would be expected to behave similarly to the pure $C_{30}H_{61}OH$ crystals. This would also explain why the effect is less prominent, as there should be regions of $C_{31}H_{64}$ structure and alkyl group termination, where the edges maintain a smooth morphology.

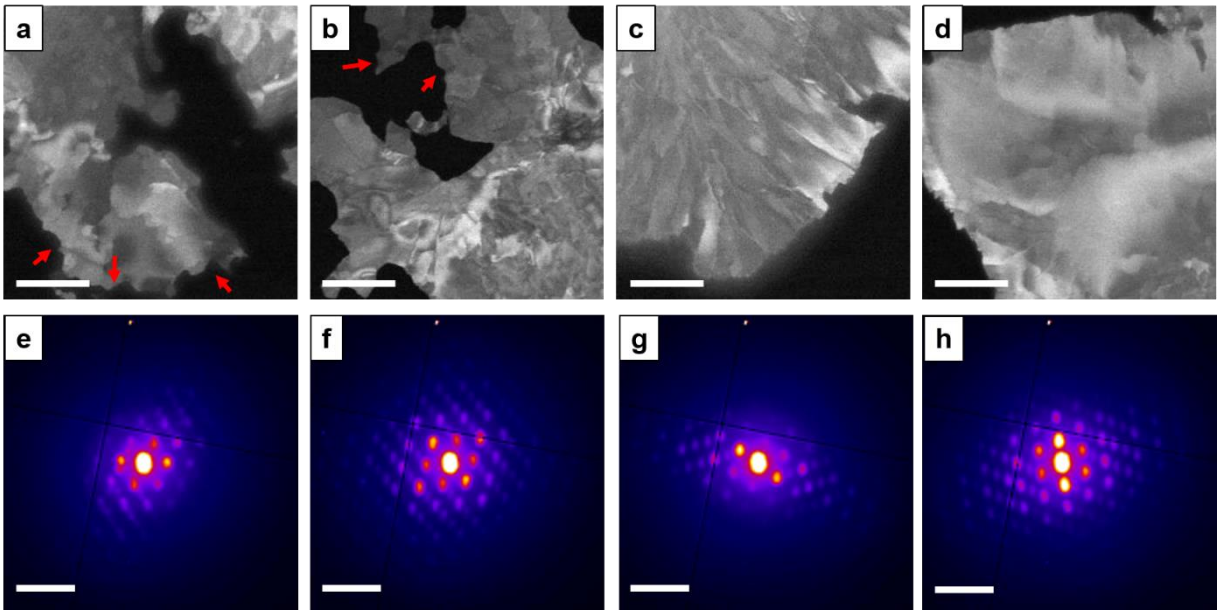

Figure 6.40: (a-d) ADF-STEM images of binary mixture crystals with 50% $C_{30}H_{61}OH$ content after TEHP exposure, and the corresponding diffraction patterns (e-h). ADF-STEM image scale bars indicate 500 nm, diffraction pattern scale bars indicate 0.5 $Å^{-1}$. Red arrows indicate removal of material (pits) at the crystal edges.

6.10 Conclusions

In this chapter, a multi-technique approach was used examine the mechanism of action of an adjuvant, TEHP, found in crop protection products on a replica IW leaf wax layer. From bulk, thermal techniques TEHP associated changes were observed, such as the melting point (and decomposition temperature) decreasing. These suggested that TEHP did interact with the material due to the changes in these properties. The thermal analysis suggests the TEHP plasticizes both $C_{31}H_{64}$ and $C_{30}H_{61}OH$ waxes to some extent and the $C_{30}H_{61}OH$ to a greater extent. NMR and ATR-IR spectroscopies could not offer any insights into a potential mechanism such as a hydrogen bond interaction of the alkyl or alcohol groups with the P=O bonds of TEHP. XRD analysis confirmed the crystal structure of the waxes was maintained after TEHP addition at room temperature and over the 30 minute time span studied. This technique could therefore rule out entire amorphisation of the material as a mechanism of adjuvant interaction. Broadening of the peaks after TEHP addition suggested increased disorder (or reduced coherent scattering domain sizes) within the crystals, in agreement with DSC data. However, this XRD study only focused on thermodynamic effects where the samples were heated in TEHP. Future work could include a kinetic study, studying the effects of exposing the waxes to TEHP over a several day period instead of the short timescales studied in this thesis. The combination of these bulk techniques suggested there may be a difference in the

mechanism of interaction based around increased plasticisation of the $C_{30}H_{61}OH$ on exposure to TEHP but did not provide strong evidence for an interaction mechanism.

Results then turned to microscopic techniques to look at the localised scale of the material, where results suggested a potential dissolution mechanism instead of a plasticisation mechanism. Chapters 4 and 5 highlighted the necessity to view the structure at a high resolution to gather a complete perspective. Optical microscopy provided insight into the structural changes that happened as a result of TEHP interaction, as the loss of material at the edges of TEHP exposed $C_{30}H_{61}OH$ crystals is evident, but not for $C_{31}H_{64}$ crystals. Conventional TEM data contextualised this further, showing the formation of pits at the edges of TEHP exposed $C_{30}H_{61}OH$ crystals, so it could be proposed that these crystals undergo an etching mechanism as a result of TEHP interaction. It was also noted the pristine $C_{30}H_{61}OH$ crystals had a far density of grain boundaries and dislocations within the chains-down orientated crystals than the pristine $C_{31}H_{64}$ suggesting flaws in the crystallisation process of the $C_{30}H_{61}OH$ due to difficult packing to the alcohol groups. This carried through to the TEHP exposed crystals.

Facet analysis has offered evidence that particular planes of the $C_{30}H_{61}OH$ crystals where a higher percentage of alcohol groups present themselves at the surface etch faster on exposure to TEHP. SED analysis therefore points towards a possible mechanism of adjuvant interaction, where TEHP preferentially interacts with the OH groups. This would be significant when assessing the alcohol chain content in leaf wax materials, for example an IW layer with higher alcohol content may be disrupted more by TEHP, potentially increasing the molecular diffusivity through the layer.

The mechanism of interaction may be concentration dependent. Where the wax is in excess such as in XRD, results indicate plasticisation or increased disorder, but where TEHP is in large excess, such as in TEM and SED, results indicate partial dissolution or removal of material. However DSC, where TEHP is in excess, suggests a plasticisation mechanism too. Therefore, the mechanism of action of TEHP may have contributions from dissolution and plasticisation effects.

Future work could look to quantify this etching mechanism further. The current work is limited by the lack of concentration control of TEHP for addition in the electron microscopy studies. Ideally, the concentration of the TEHP could have been reduced by diluting in water, but TEHP is not miscible in water. TEHP is soluble in ethanol, but this would not be a suitable diluent if looking to study the interaction with OH groups in $C_{30}H_{61}OH$ crystals. Varying concentration of the TEHP may also have been able to provide evidence for the theory that TEHP etches alcohol groups faster. If the TEHP could be diluted to a lower concentration, it could be studied whether this etching effect

was reduced, and to try and capture the advancement of this process in-situ of a liquid cell. Samples for the bulk techniques used in this chapter looked at the wax in excess, so future work could look to make these exposed crystals suitable for electron microscopy analysis – i.e. sufficiently thin enough for the electron beam to pass through.

Another way of expanding this work could be achieved by looking at more binary mixture compositions to quantify the changes in this pit formation on increasing alcohol content, and how this can be extended to the real leaf wax system at around only 15% alcohol content but with other complexities such as different terminations and varying chain lengths. Both of these results together would offer insight into the progress of TEHP interaction with alcohol groups, by varying either the concentration of OH groups in the crystal, or the concentration of applied TEHP. Molecular dynamics or other simulation modelling approaches could also be useful for consideration of TEHP and wax surface interactions, such as in the study by Ray et al. (Ray et al., 2022).

Chapter 7
A Barbituric Acid / Thiobarbituric Acid Solid Solution

7.1 Introduction

In the opening literature review, the implications of solid solution formations, both in the presence of impurities and not, was established as important for crystal engineering. There is opportunity for the exploration of the nanoscale of these systems and their phases, and the presence or not of a true solid solution, with scanning electron diffraction (SED). Bulk techniques fail to give information about the local composition of these products, for example XRD gives the phase of the bulk powder or a single crystal, but if there are a mixture of isostructural but different composition phases it does not tell us how well mixed these phases are.

In the previous chapters, a solid solution system between a long chain alkane and long chain alcohol was investigated. However, it was not possible to distinguish between the two chains in that system by spectroscopic techniques, or diffraction probes due to the small composition difference (presence of the –OH group or not at the end of the wax chains) plus similar d-spacings and diffraction pattern symmetry between the two waxes. This chapter explores a solid solution system of barbituric and thiobarbituric acids with a more significant identifying chemical group (containing sulphur) in the latter component, allowing spectroscopic differentiation. The crystal structure of the solid solution is likely structurally similar to the components of the solid solution, as the two components have very similar molecular structures so are expected to mix in a similar manner to form a solid solution.

Barbituric acid (BA) is an organic compound that is the parent compound of many barbiturate drugs, a class of central nervous system depressant drugs. Thousands of related barbiturate compounds have been synthesised in the century or so since its first introduction, of which 50 are or have been used clinically (López-Muñoz et al., 2005). Thiobarbituric acid (TBA) is an isostructural organic compound, where one of three oxygen atoms that bind to the pyrimidine heterocyclic skeleton has been replaced by a sulphur atom. BA and TBA derivatives have been used in herbicides, fungicides, and as antiviral agents (Kidwai et al., 2005). These compounds are therefore of interest to both the pharmaceutical and agricultural sectors. The structures of each compound can be found in Figure 7.1 below, showing the six-membered rings that forms the main molecule structure in each compound, and the substitution of the oxygen atom for a sulphur atom in one of the C=O bonds.

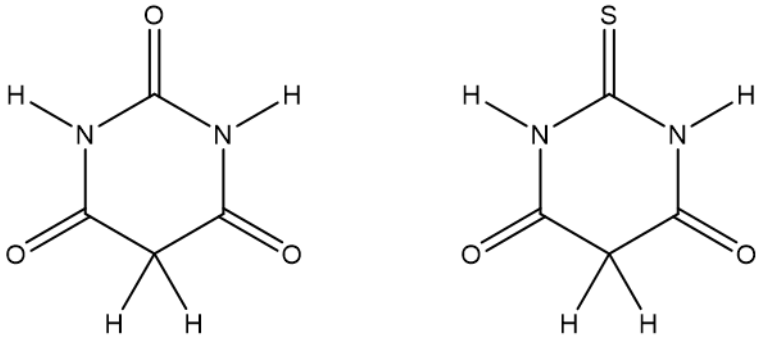

BA **TBA**

Figure 7.1: Barbituric acid and thiobarbituric acid molecular structures.

These compounds both exhibit polymorphism and also tautomeric polymorphism. It is the C=O bonds that allow these molecules to exhibit keto-enol tautomerism. For TBA, there is one form and a hydrated form present in the enol molecular structure, three in the keto molecular structure, and one form with a 50:50 ordered mixture of enol and keto molecules (Chierotti et al., 2010). These forms vary in stability due to the number of hydrogen bonds they can make. For example, molecules in form III and V (keto) contain only two N-H--O interaction sites, and readily convert to the more stable form IV (keto/enol), which has five hydrogen bonds with the alcohol group, the nitrogen and the sulphur group (Chierotti et al., 2010).

For BA, two polymorphs and one hydrated form are found in the keto molecular structure, and the stable thermodynamic form IV is the enol structure (Schmidt et al., 2011), (Braga et al., 2022). Again, this enol form is the most stable due to the formation of a strong hydrogen bonding network within the crystal, leading to a more favourable lattice energy. The commercially available forms (BA form II, and TBA form I) are reported to both be their keto forms, and are isomorphous crystallising with the $P2_1/c$ space group symmetry (Lewis et al., 2004).

Work by Shemchuk et al. looks at the solid solution and co-crystal system that forms between BA and TBA in differing compositions. The 50:50 co-crystal is found to be highly stable, and is isomorphous with the keto based forms of both components. Figure 7.2 shows representations of BA form II, the 50:50 co-crystal system, and TBA form I. The similarities between the unit cells of the two forms of BA and TBA, and the co-crystal between these two forms are visualised in Figure 7.2.

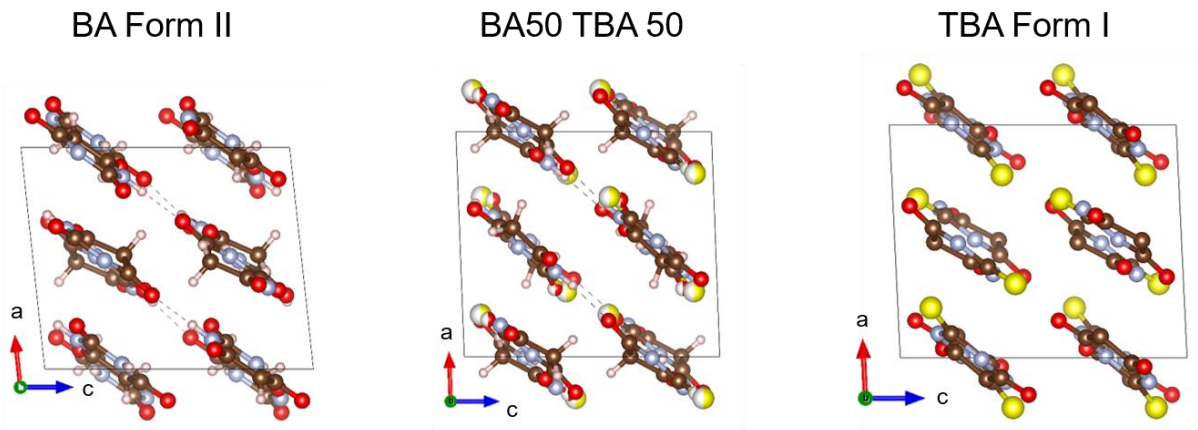

Figure 7.2: Structural representations of the commercially available forms of BA and TBA, and the 50: 50 co-crystal structure.

Shemchuk et al. propose that BA and TBA also form solid solutions in the range of 20 – 80 % TBA content. The unit cell changes size dependent on sulphur content, with Table 7.1 giving the reported single crystal data for TBA form I and BA form II at room temperature.

Table 7.1: Reported single crystal data for TBA form I and BA form II at room temperature, taken from Shemchuk et al. (Shemchuk et al., 2016)

	TBA form I	BA form II
Space group	*$P2_1/c$*	*$P2_1/c$*
a (Å)	8.450	8.199
b (Å)	13.140	12.613
c (Å)	10.420	9.823
α (°)	90	90
β (°)	92.70	95.7
γ (°)	90	90

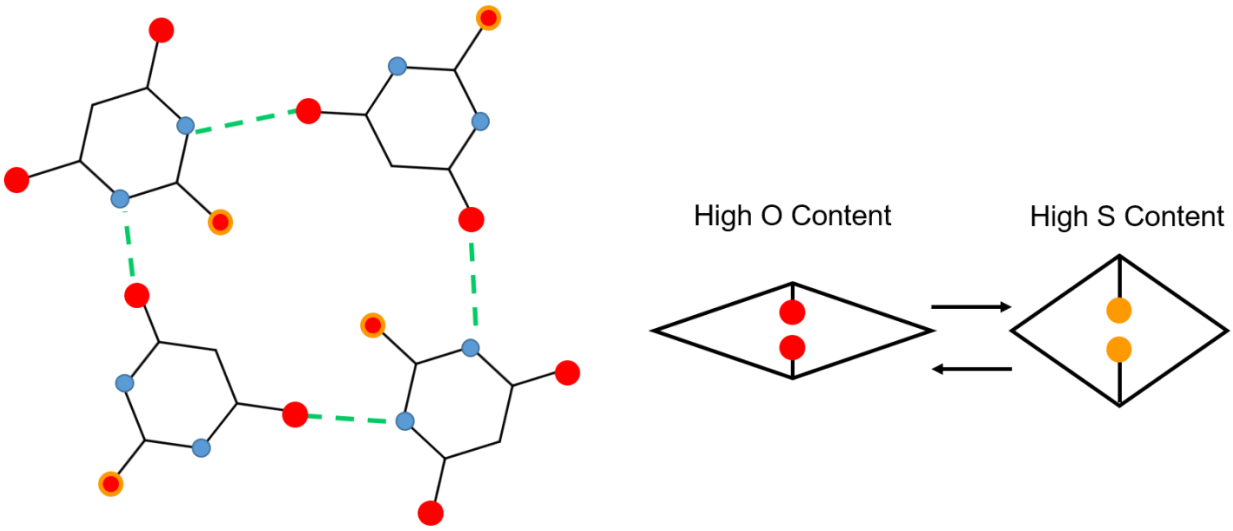

Figure 7.3: Simplified representation of intermolecular packing in the solid solutions formed between BA and TBA. The blue circles represent the nitrogen atoms, the red circles represent oxygen atoms, and the red/ orange circles represent the location where either a sulphur or oxygen atom will reside based on solid solution composition. Green dashed lines represent the hydrogen bonds that arise between molecules. Diagrams are recreated from Shemchuk et al. (Shemchuk et al., 2016).

Figure 7.3 includes a representative structure of the intermolecular packing that forms between BA and TBA in solid solution. The orange and red circles represent the atom that could be either sulphur or oxygen, dependent on composition. This centre section becomes more symmetric based on sulphur content, to allow sulphur-sulphur interactions and optimal hydrogen bonds between the N-H group and the C=O. When these sulphur atoms are replaced by oxygen atoms, the number of O-O interactions increases, which causes the cell volume to decrease. This change in unit cell volume has implications for the shifts of peaks in diffraction patterns and XRD traces obtained from cell packing, so can be used to track the sulphur content in the composition (Shemchuk et al).

Shemchuk et al. use the (202) reflection of BA form II as a means of tracking compositional change across the mixtures. Figure 7.4 includes structural representations of BA form II and TBA form I, with the (202) planes indicated in pink. It can be seen how the unit cell changes that are a result of sulphur incorporation lead to a change in angle the (202) plane lies along relative to the unit cell, leading to this shift. This leads to different d-spacings of these planes, with d-spacing values of 2.94 Å and 3.205 Å for the (202) plane in BA Form II and TBA form I respectively.

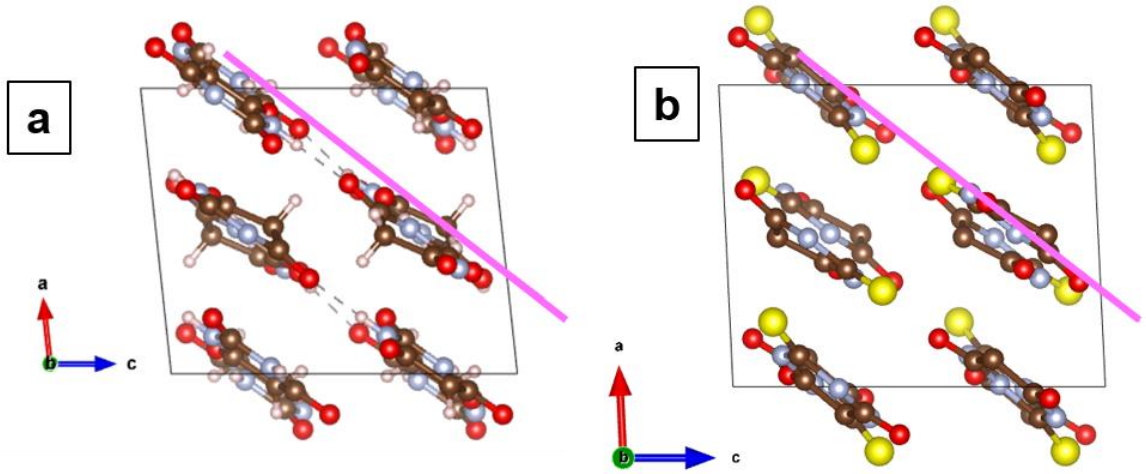

Figure 7.4: Structural representations of BA form II (a) and TBA form I (b). The (202) plane is indicated with a pink line.

7.2 Results and Discussion

Solid solutions of BA and TBA were formed by measuring out molar fractions of the two solid components in a desired ratio and dissolving in ethanol. The resulting solution was heated to boiling for 5 minutes, cooled and the ethanol left to evaporate overnight to leave a powder. After collection of the powder, the samples were ground to a consistent texture in a pestle and mortar. XRD analysis before and after this grinding confirmed that the grinding did not affect crystallinity of the sample as peak position, width and symmetry remained the same before and after (Figure 7.5).

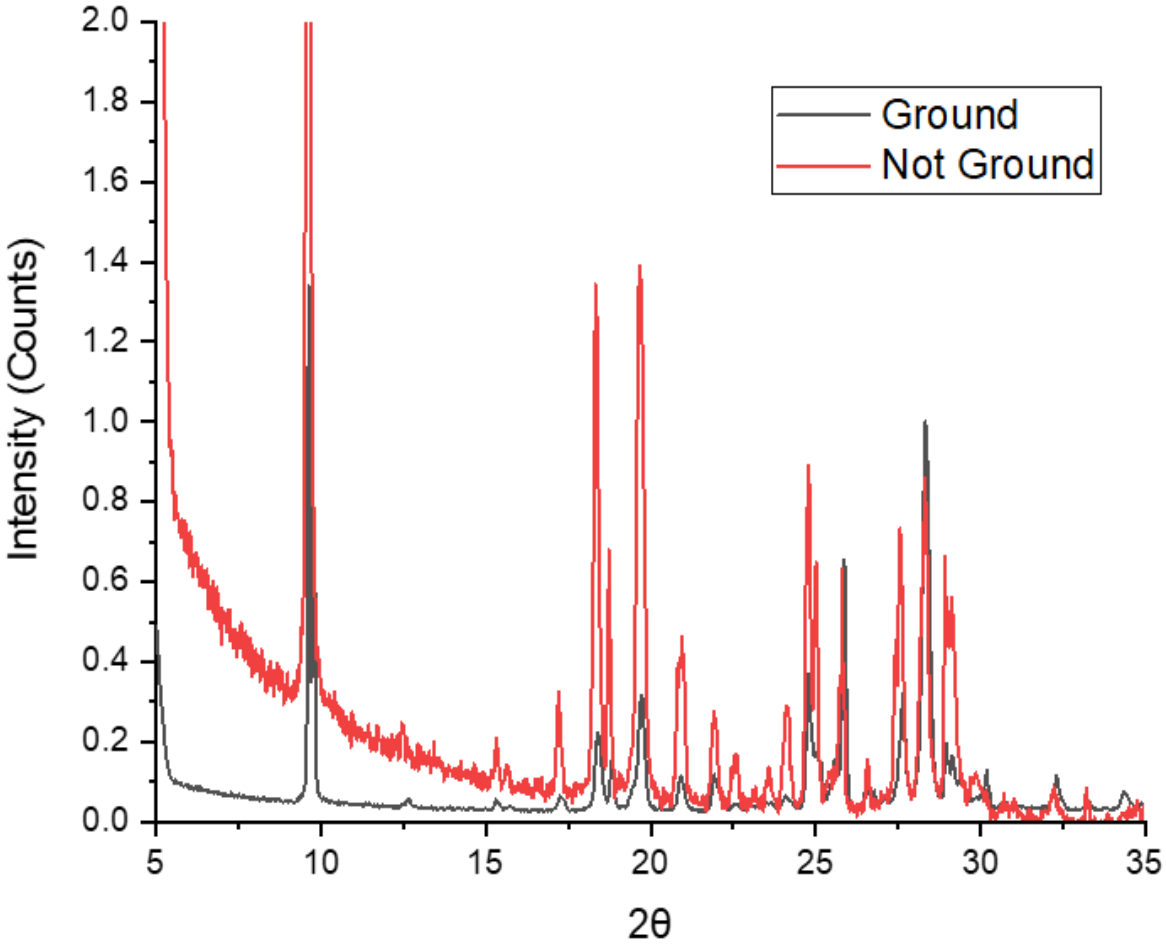

Figure 7.5: XRD trace of a composition containing 70% TBA in BA as obtained from solvent evaporation (red) and after subsequent grinding to a consistent texture (black).

7.3 NMR (Nuclear Magnetic Resonance) spectroscopy

NMR spectroscopy was used to confirm the compositions of the mixed powders. The powders were dissolved in DMSO-d6. Figure 7.6 shows the proton NMR spectra of (a) BA and (b) TBA. The two protons in the N-H bond in the environments nearest the C=O or C=S groups, labelled 1 and 2 in Figure 7.6, shifted to different ppm on going from BA to TBA, so could be used as indicative peaks for the respective components within any solid solution. This assignment was made in agreement with previous reports (Lukin et al., 2018), (Xiao et al., 2020).

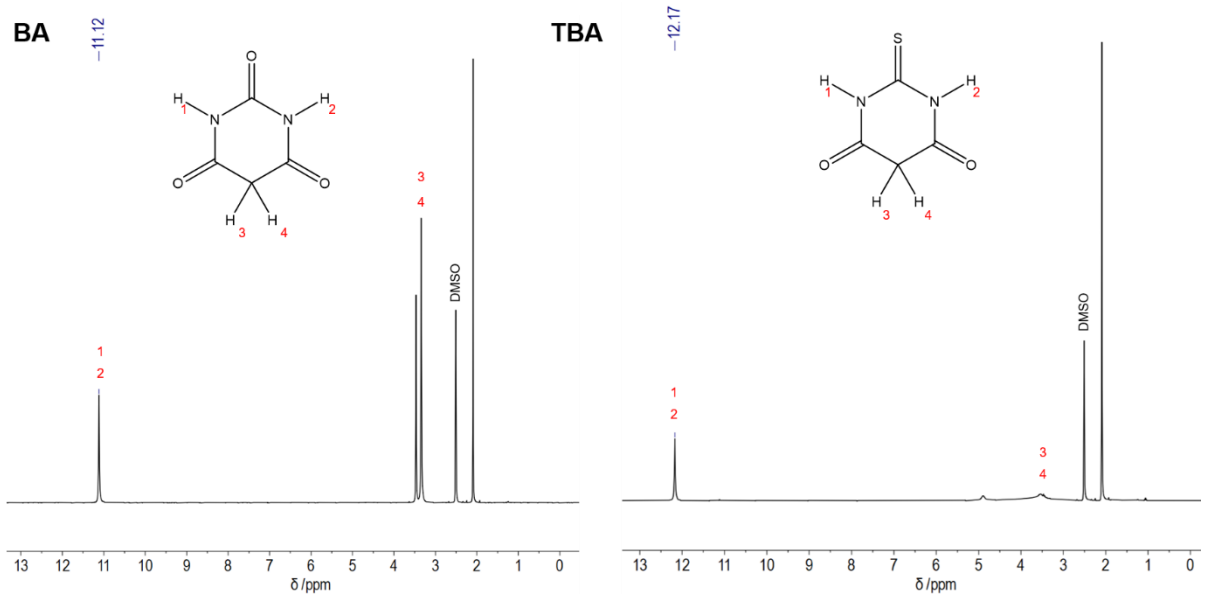

Figure 7.6: NMR spectra of BA and TBA. Hydrogens in the molecules, and the peaks, are labelled. These shifts were referenced relative to the DMSO-d6 solvent.

The NMR spectra of the solid solutions contain both peaks that correspond to these different environments in the BA and TBA. The ratio of the integral of the two peaks can be taken as the ratio of the two respective molecular components within the mixture. Figure 7.7a shows the NMR spectra obtained from the 50: 50 binary mixture. The integral of the peak at 11.1 ppm was set to 1 (the peak indicative of BA), and the integral of the peak at 12.17 ppm (indicative of TBA) was calculated relative to this. The integral of this peak is higher than 1, so the measured TBA value is calculated and reported as 51% rather than 50%. Figure 7.7b shows the calculated ratios versus expected ratio of the two components across the potential solid solution series produced here, and shows good agreement between the two values. This graph was fitted to a linear gradient of 1.01 versus the expected value of 1.

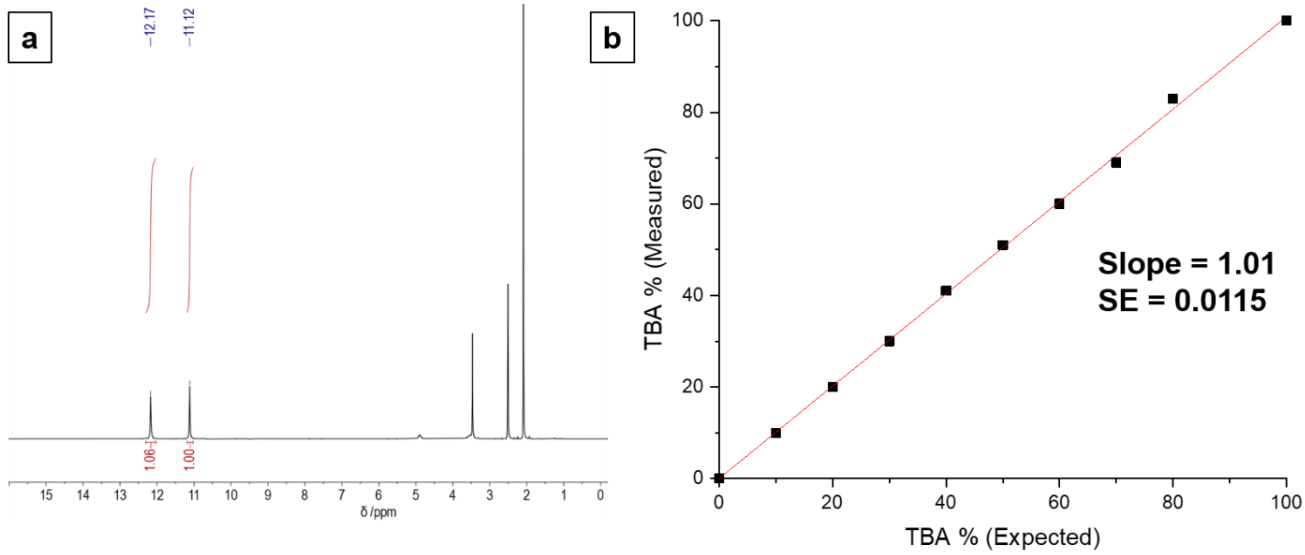

Figure 7.7: (a) NMR spectra of a 50:50 BA: TBA mixture. (b) Graph comparing the measured TBA percentage from NMR spectral peak analysis versus the expected TBA percentage from the relative starting ratios of compounds added.

7.4 Differential Thermal Calorimetry (DSC)

DSC can be used to characterise solid solutions through the change of heatflow profiles upon solid solution formation compared to the pure components. Solid solutions have a singular melting point, typically between or lower than that of the two separate components (West, 1984). This is because incorporation of a different component when forming a solid solution disrupts the regular structure of the pure component. This can mean a lower stability of the crystal structure, so requires less energy to break up the crystalline structure. Figure 7.8 exhibits the DSC curves of the binary mixtures produced here. The changes in temperature of the heatflow endotherm minima are attributed to melting of the components, rather than another process such as phase transition or decomposition; the melting point for pure BA is found at 254.8 °C, with the melting point of pure TBA found at 246.3 °C, as previously reported by (Shemchuk et al., 2016) and (Masoud et al., 2012). The melting point of the solid solution compounds is actually higher than the melting point of either component, falling between 263 – 265 °C (agreeing with previous (Shemchuk et al., 2016)). This is likely due to the solid solution having stronger intermolecular interactions, possibly due to more optimum hydrogen bonding networks formed in the solid solution structure. Shemchuk et al. present the DSC spectra for each composition they produced and find the compositions with excess TBA (above 50:50) are unstable with respect to “demixing”, where the BA and TBA melts followed by recrystallization to the 50:50 co-crystal, and suggest there may even be a mixture of phases in the powder above 80% TBA. In their data, endotherms in these excess TBA compositions are seen at the melting point for pure BA, pure TBA, and the higher co-crystal melting

point. The data in Figure 7.8 shows a similar phenomenon at >70% TBA compositions produced here, which suggests not every composition forms a solid solution. For example for the composition containing 80% TBA content, a melting point is seen at 245.7 °C, matching the melting point of the pure TBA, and a smaller peak is observed at the higher solid solution melting point. However, no peak is seen for pure BA. The trace for the 70% TBA content compound does not exhibit this peak at the TBA or BA melting point, and exhibits a peak at the solid solution melting point. From these results it may be possible that a solid solution is only formed up to 70% and not 80% TBA content as previously reported, or that the excess TBA is pushed out with the remaining BA and TBA molecules forming a solid solution.

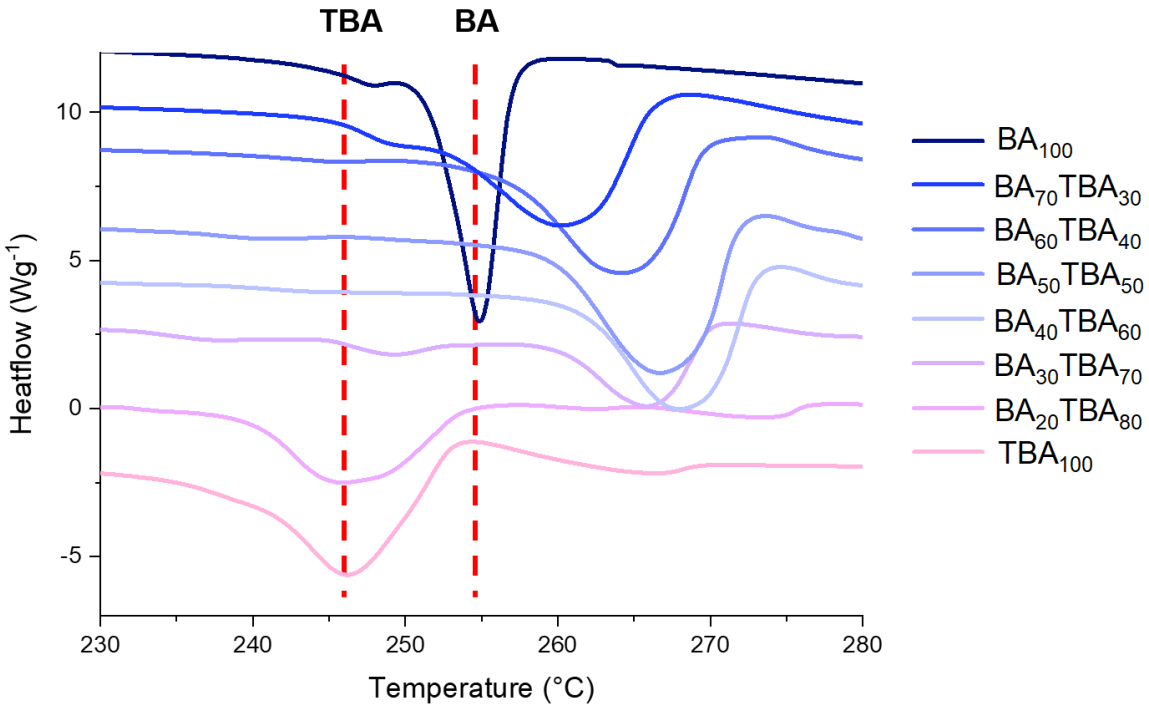

Figure 7.8: DSC traces of differing compositions of BA: TBA mixtures. The melt point of BA and TBA have been indicated with the red dashed lines for comparison.

7.5 Powder X-Ray Diffraction (pXRD)

It has been established that the BA and TBA components crystallise in different polymorphs. XRD can be used as a diagnostic tool to determine the polymorph a particular compound is crystallising in by comparing against simulated patterns and evaluating a best match, and to identify mixtures of phases. This section looks to determine what polymorphs and phases are present in the pure components and the BA and TBA mixtures.

7.5.1 BA and TBA Assignments

Figure 7.9 shows the XRD traces of the BA compound as received, and after being dissolved in boiling EtOH and allowing to cool and recrystallise. This was done to test the effect of the solvent used in solid solution formation. The two experimental BA patterns exhibit different crystallinity. The traces of the experimental data are plotted alongside simulated XRD patterns of BA form II and BA dihydrate. In Figure 7.9a, the as received BA can be matched to the form II simulated pattern with slight unit cell adjustments. The BA that has been recrystallised is more complicated and cannot be indexed to a single form. This ethanol recrystallised BA was first compared to the as received BA. Figure 7.9b shows several of the peaks in the black and red patterns match, symmetry wise, albeit with a lower intensity than pure as received BA. The remaining peaks can be attributed to the BA dihydrate (green pattern). This must have occurred due to traces of water present in the ethanol used. Shemchuk et al. do not report any hydrate formation when using ethanol as a solvent, only methanol. However, the current results shown here already indicate the importance of considering hydrates in any solid solution system.

TBA was also assessed for hydrate presence. The as received TBA can be matched to form I (Figure 7.10a), as expected from reports of the commercially available form (Shemchuk et al., 2016). The TBA recrystallised in ethanol can be matched to the TBA hydrate simulated pattern (Figure 7.10b). This pattern is characterised by a significant peak at ~9.6°, which can be indexed to the (002) peak. This peak is also significantly not present in simulated patterns for other TBA forms, so this peak can be diagnostic of TBA hydrate present in any compounds containing TBA. This is important when considering the solid solutions formed here. Notably, the TBA hydrate (202) peak falls at a much lower value than in form I TBA, arising at 18.3° in the hydrated version versus 27.9° in form I.

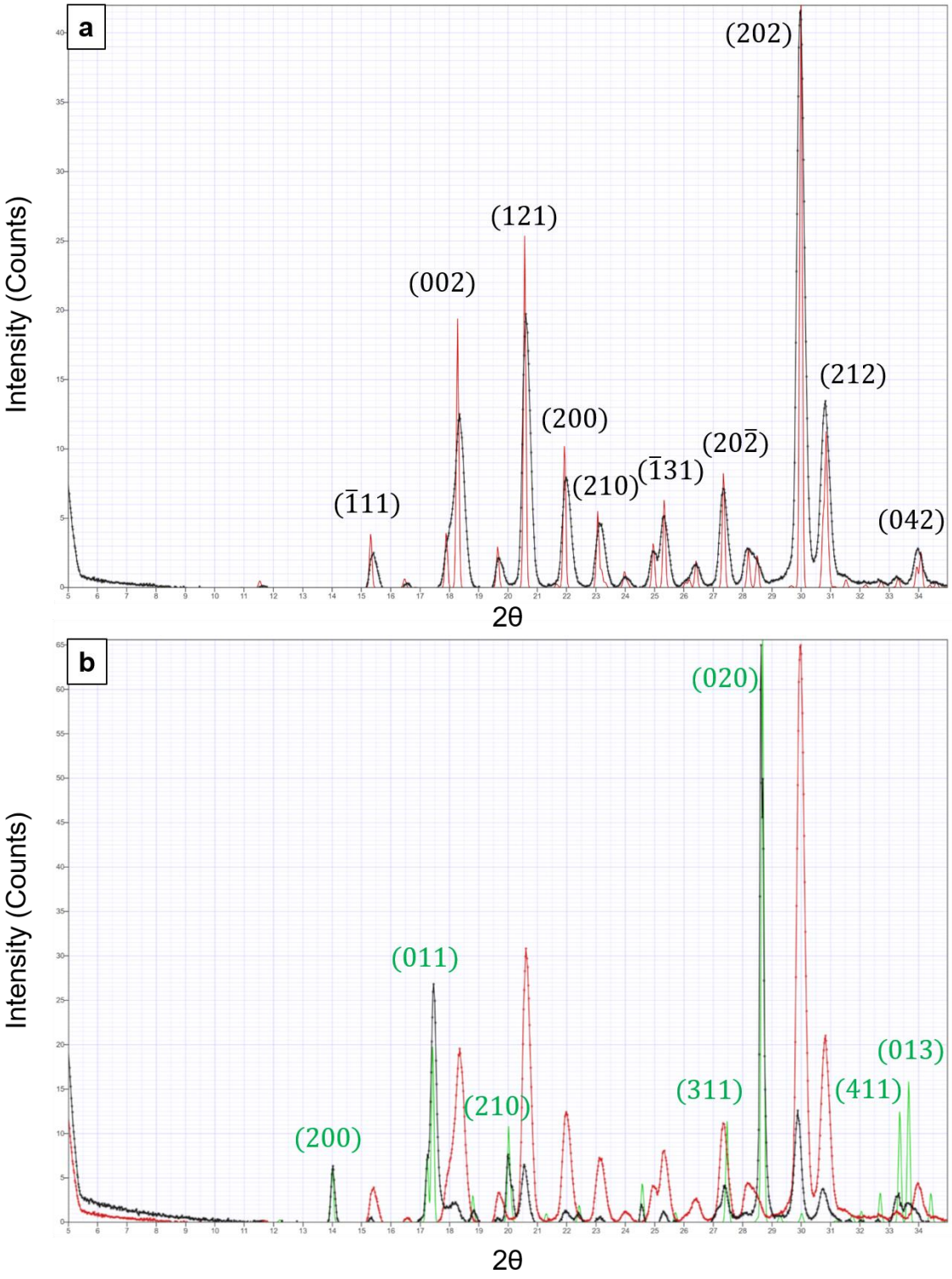

Figure 7.9: Comparison of experimentally obtained powder XRD patterns versus simulated patterns. (a) BA as received experimental pattern (black) vs. BA form II simulated pattern (red). (b) BA recrystallised in ethanol experimental pattern (black) vs. BA as received experimental pattern (red), and BA dihydrate simulated pattern (green).

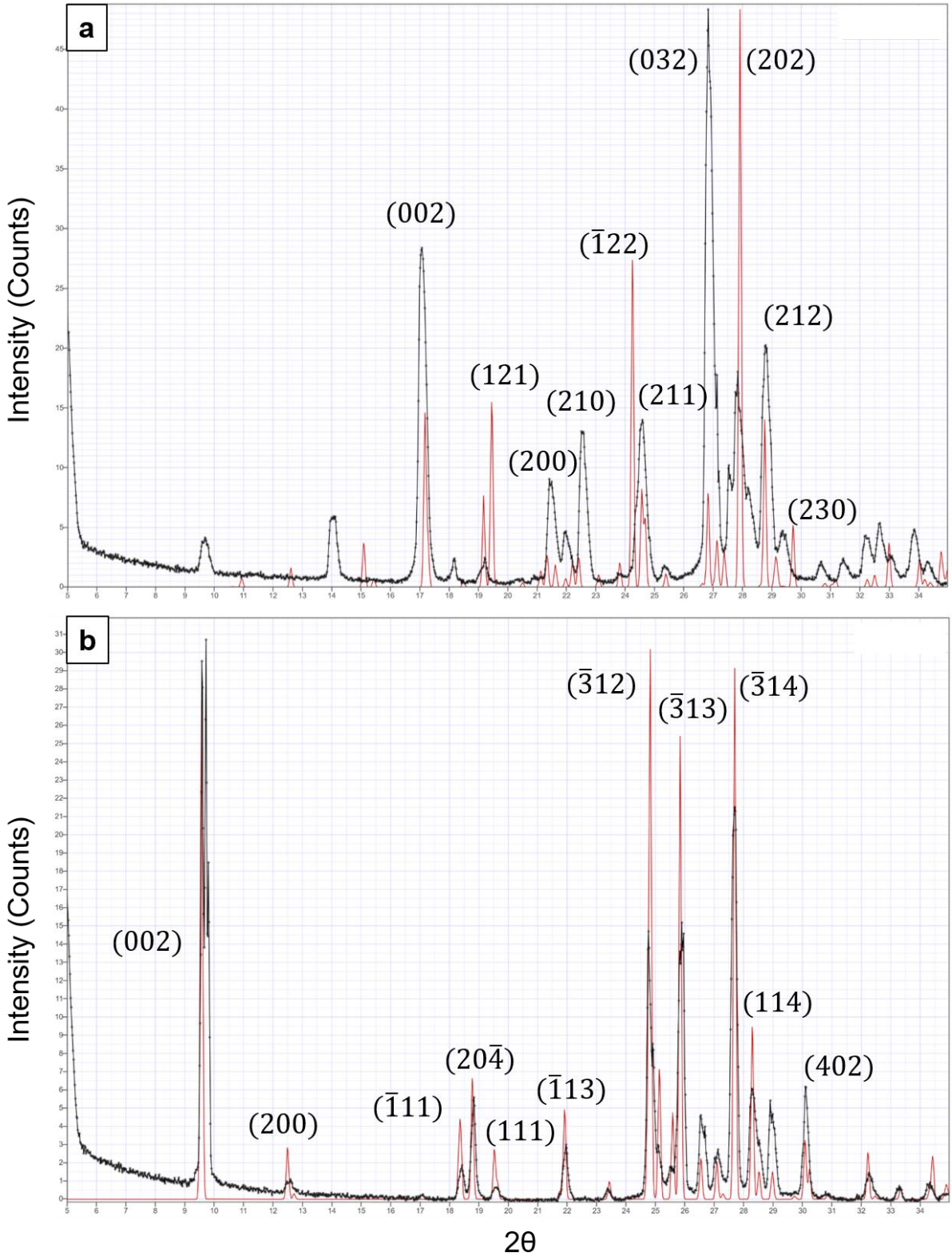

Figure 7.10: Comparison of experimentally obtained powder XRD patterns versus simulated patterns. (a) TBA as received experimental pattern (black) vs. TBA form I simulated pattern (red). (b) TBA recrystallised in ethanol experimental pattern (black) TBA hydrate simulated pattern (red).

7.5.2 Binary Mixtures and (202) Peak Shift

Shemchuk et al. report the shifting of the (202) diffraction peak towards higher angles with increasing BA content. This occurs due to the change in the unit cell shape to accommodate the difference in the radii of the oxygen versus the sulphur. However, first the XRD patterns of the mixtures were examined against simulated patterns of the co-crystal and against the BA and TBA hydrates to account for any extra peaks.

Figure 7.11 shows the XRD pattern of the mixture with 10% TBA content. This composition is not expected to form a solid solution. As expected, the XRD pattern is dominated by BA signal, and Figure 7.11 also shows how this pattern can be matched to the as received pattern. Interestingly in this case, recrystallizing in ethanol has not directed crystallisation to the hydrate form (contained in the recrystallised in ethanol BA). This suggests the presence of TBA has directed crystallisation to a different polymorph than seen in pure BA recrystallisation in ethanol.

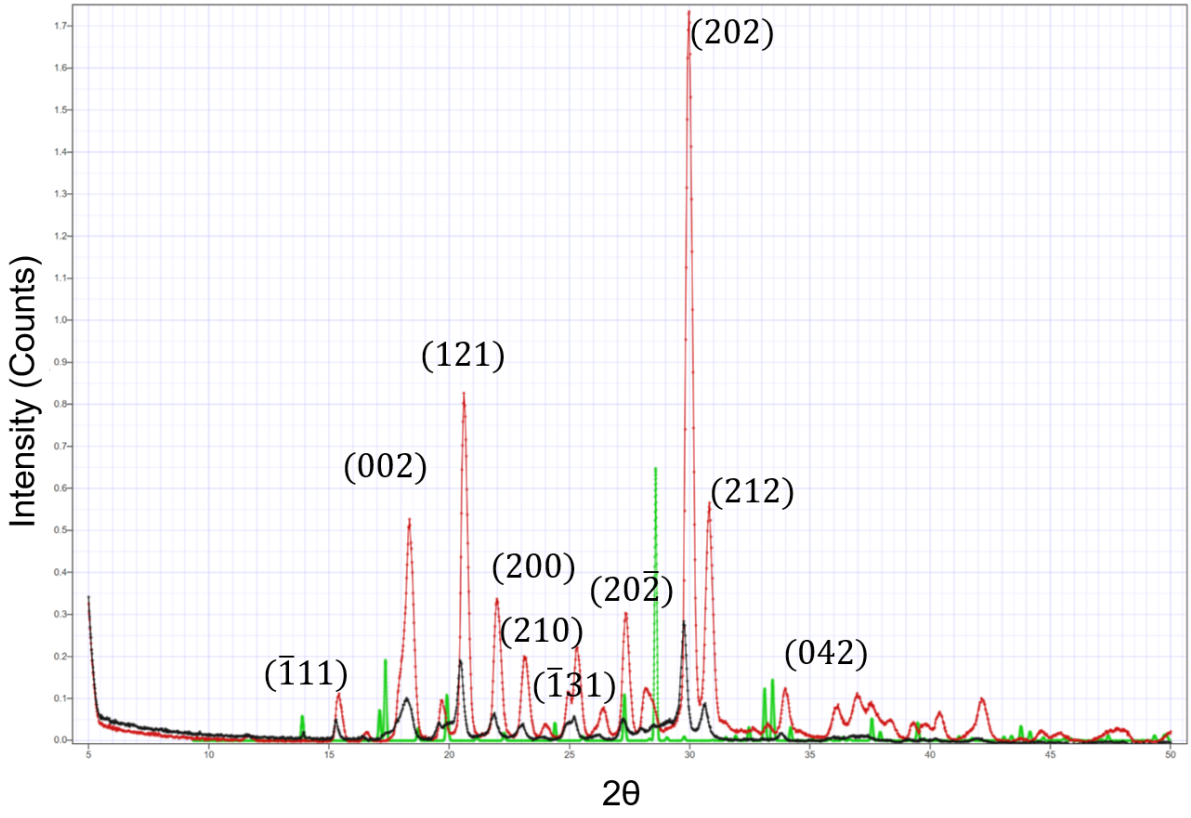

Figure 7.11: Comparison of experimentally obtained powder XRD pattern for the composition containing 10% TBA versus the experimental pattern for the as received BA (red), and the recrystallised in ethanol BA (green).

Figure 7.12 examines the 50: 50 mixture. Shemchuk et al. suggest this composition forms a co-crystal, and Figure 7.12 plots the simulated co-crystal pattern in green against the experimental pattern in black. With some slight unit cell adjustments, this

simulated pattern can be matched to most peaks in the experimental data. The remaining peaks, notably the peaks at 9.6° and 18.7° can be explained by the presence of TBA hydrate. Shemchuk et al. do not report a (002) TBA hydrate peak in the co-crystal structure, and do not present a full pattern for comparison. It is clear this paper has not considered the effect of hydrated forms in this system.

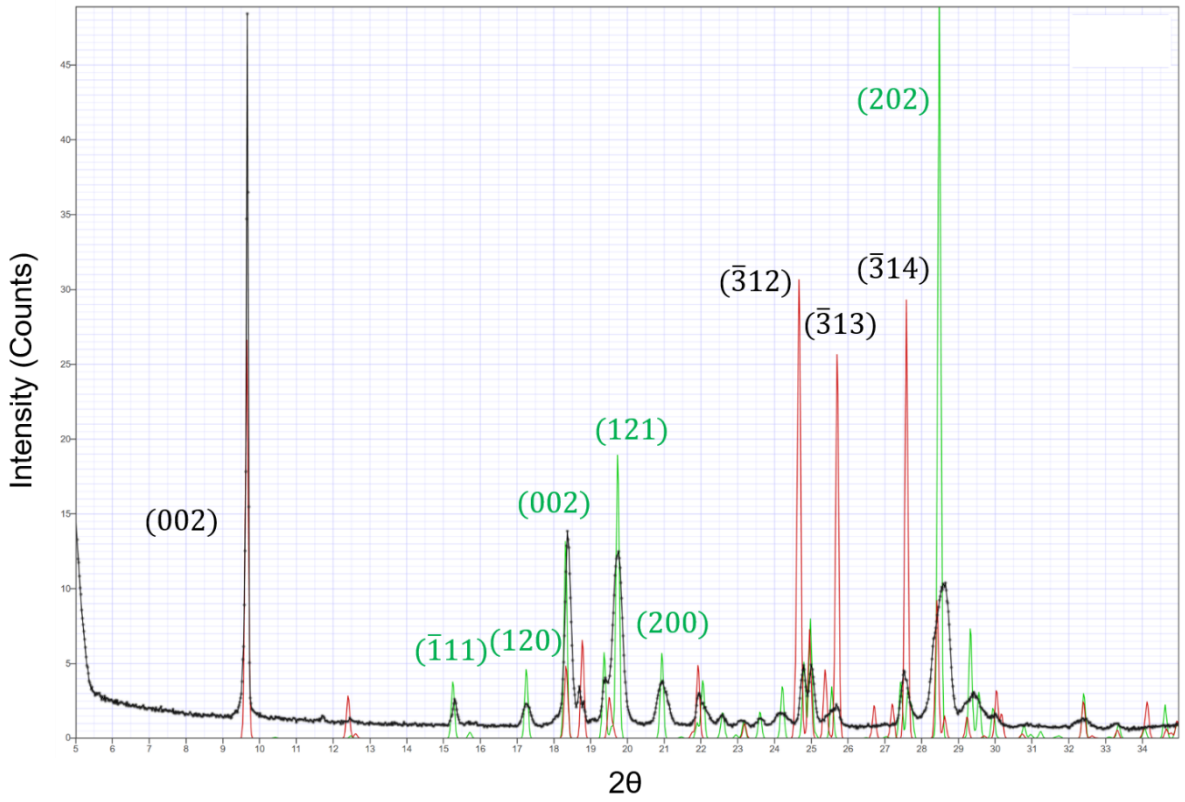

Figure 7.12: Comparison of experimentally obtained powder XRD pattern for the composition containing 50% TBA versus the simulated pattern for the 50: 50 co-crystal (green), and the simulated pattern for TBA hydrate (red).

7.5.2.1 Excess BA

Figure 7.13 presents two comparisons where there is excess BA within the reported solid solution range. Figure 7.13a presents a composition with 20% TBA, and Figure 7.13b presents a composition with 30% TBA. In this case, the structures were compared to simulated patterns of the solid solution formed with 30% TBA compositions, with the reported structure taken from the CCDC. The unit cell values were adjusted for a best match. Additional peaks unaccounted for by the solid solution simulated pattern can be accounted for by the presence of BA dihydrate. In these patterns, the (202) peaks lie close to the (020) peak that arises from the BA hydrate. This was important to consider when assigning the (202) peak shift in these compositions.

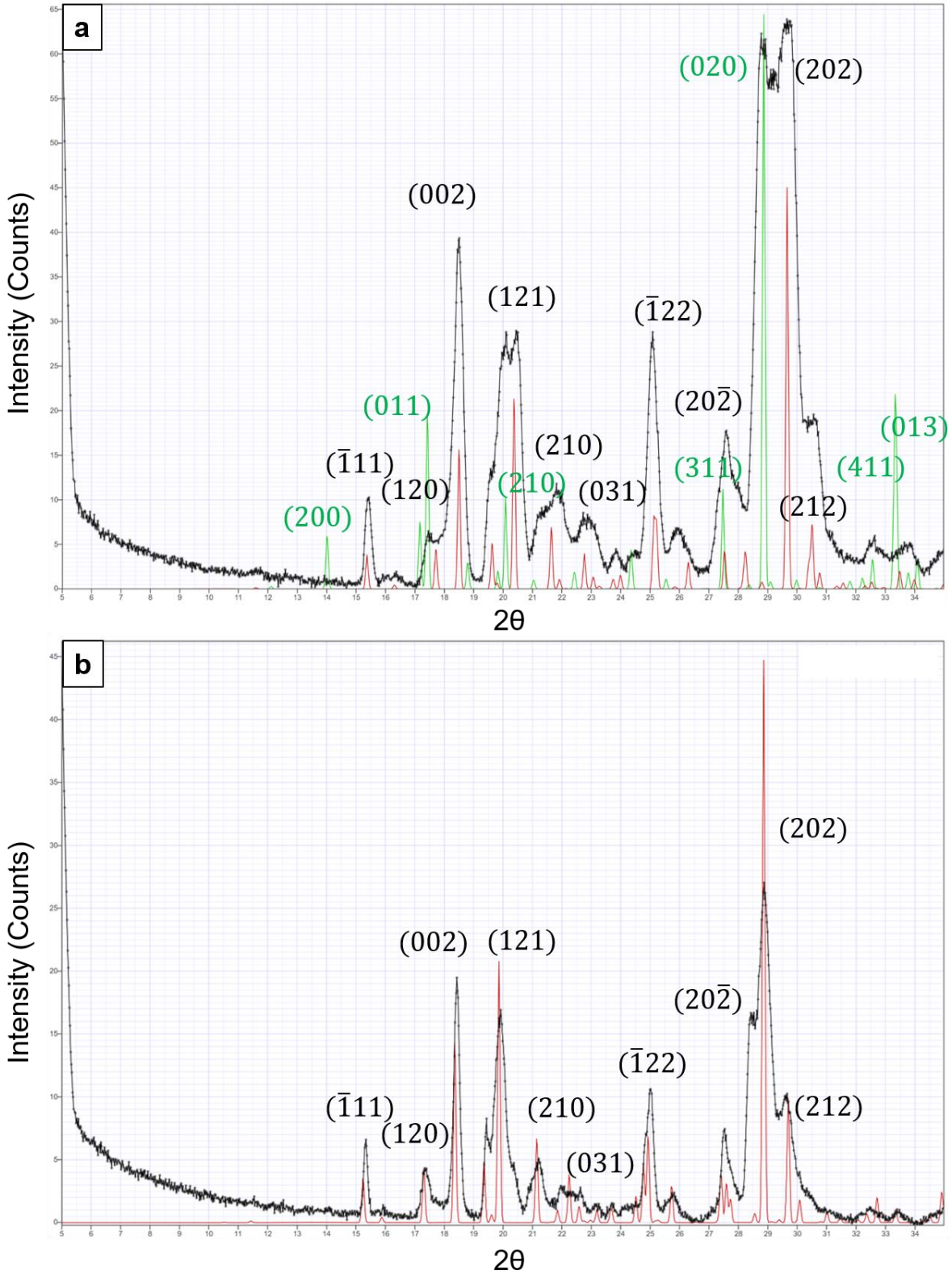

Figure 7.13: Comparison of experimentally obtained powder XRD patterns for the compositions containing 20% TBA (a) and 30% TBA (b) versus the simulated pattern for the 30% TBA solid solution (red), and the simulated pattern for BA hydrate (green).

The solid solution patterns are characterised by a trio of peaks from 27 – 31°, the $(20\bar{2})$, the (202) and (212) peaks, with (202) being the largest, central peak. Another phenomenon that can be seen is the broadening of these peaks with increasing BA content in the solid solution.

7.5.2.2 Excess TBA

Figure 7.14 looks at two of the solid solution compounds formed with excess TBA, with Figure 7.14a showing the composition with 80% TBA, and Figure 7.14b showing the composition with 70% TBA. Shemchuk et al. propose solid solutions formed in this range are unstable, and after a period convert into a 50: 50 co-crystal with excess TBA. Again, the (002) TBA hydrate peak is present in both of these samples (the red trace showing the TBA hydrate simulated pattern). These patterns were compared against the 50: 50 co-crystal simulated pattern. The unit cell parameters were initially changed to match the updated parameters that match the experimental 50:50 experimental peaks. For the 80% TBA composition, the green simulated pattern then aligned with the peaks that could not be explained by the TBA hydrate pattern, for example the (200) peak just below 21°. This indicates a mixture of 50: 50 co-crystal and TBA hydrate are formed. As can be seen, the largest green peak (the (202) peak in the co-crystal) does not align with the experimental data, so there is no (202) spot to compare for this composition. The signal in this XRD pattern is dominated by the TBA hydrate signal.

For the 70% TBA composition, adjusting to the 50% co-crystal parameters meant the (202) peak for the simulated pattern was at too high a 2θ value in the simulated pattern. Further adjusting the unit cell parameters yielded a match for this (202) peak at a lower shifted value of 28.32°. This shift of the (202) peak to lower values with increased TBA content is expected, and was explored by Shemchuk et al. However, these results suggest that the 80% TBA composition does in fact not form a solid solution, and instead forms a 50:50 co-crystal with excess hydrate TBA, but the 70% TBA composition does form a solid solution, indicated by the (202) peak shift.

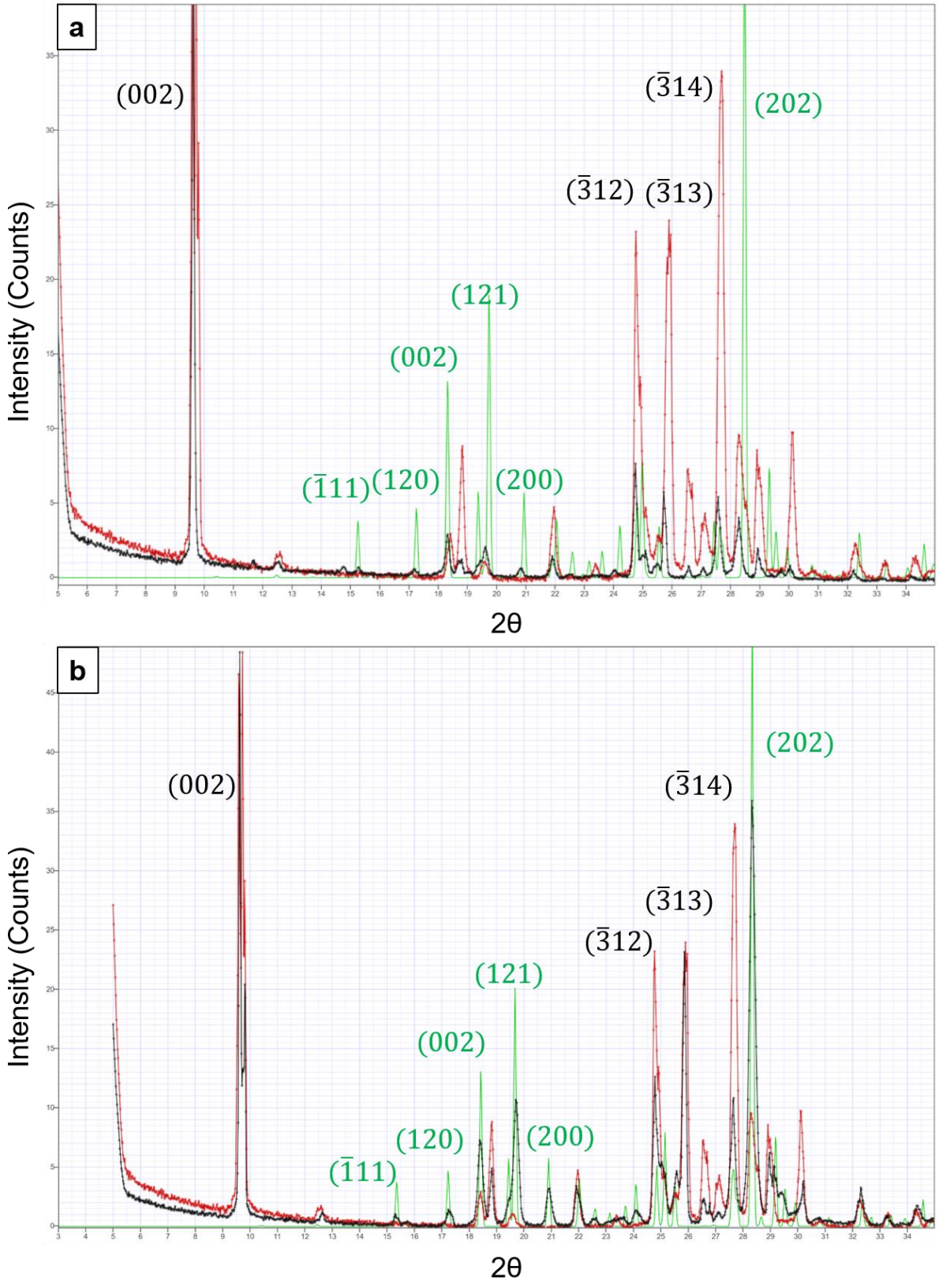

Figure 7.14: Comparison of experimentally obtained powder XRD pattern for the compositions containing 80% TBA (a) and 70% TBA (b) versus the simulated pattern for the 50: 50 co-crystal (green), and the simulated pattern for TBA hydrate (red).

The 2θ value of the (202) peak can be measured, and the value versus TBA percentage in the composition is plotted in Figure 7.15. For the TBA hydrate, the (202) peak lies at a much lower 2θ value, so there is no reported value for the 80% TBA composition as since it has been concluded the TBA present in this system is in the hydrated form. The 2θ value for the pure TBA was taken from the as received TBA sample. This graph confirms the trend where increasing TBA content leads to a shift towards lower 2θ angles in a linear relationship. This graph was fit to a linear equation, with a slope of -0.023 with standard error of 0.0029 calculated.

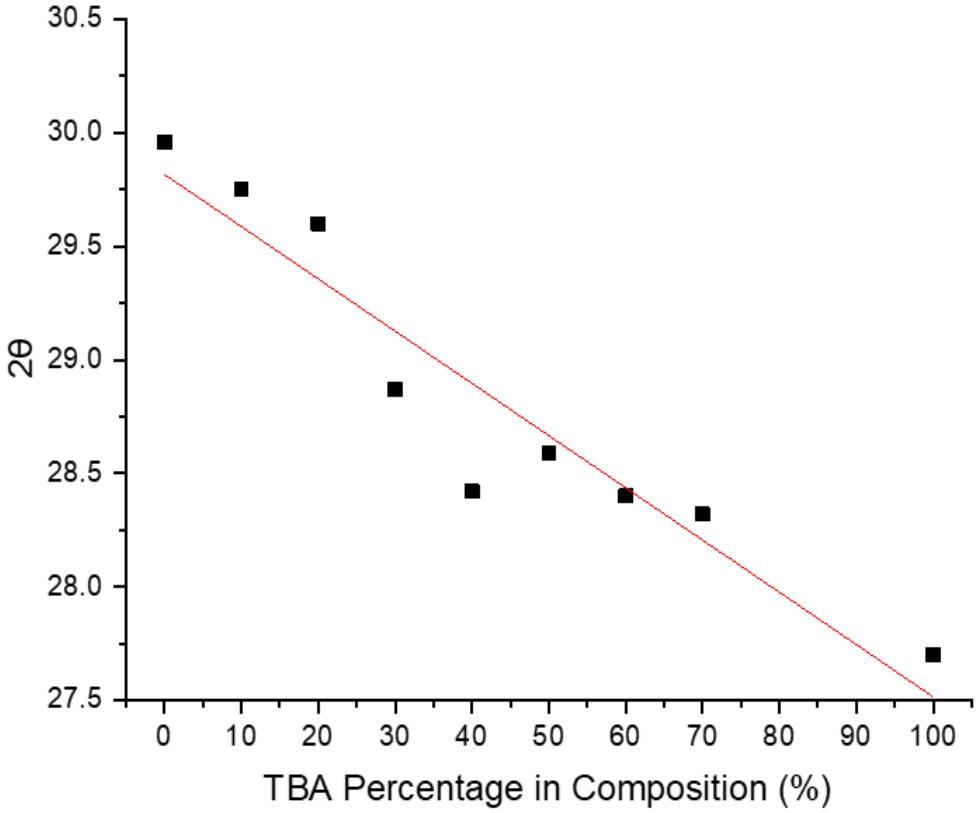

Figure 7.15: Measured 2θ value of the (202) peak across the range of compositions from pure BA to pure TBA.

7.5.3 Solid Solution Stability

Shemchuk et al. also report the instability of the solid solutions with excess TBA over the space of three months. This paper reports that whilst the solid solutions between 20 – 40% TBA content remain a solid solution as confirmed by XRD measurements after one month and then three months, solid solutions with 60 – 80% TBA content convert to the 50: 50 co-crystal structure with TBA after one month. These samples were kept under ambient conditions.

This work repeated the same measurements, taking the samples that had been stored under ambient conditions for three months and repeating XRD measurements. Figure

7.16 presents the XRD patterns taken directly after compound formation versus after 3 months storage for compositions with TBA content below 50%. These plots are shown between 25 and 35° as Figure 7.11 established the peak at roughly 29° is attributed to excess dihydrate BA, and the peak at 25° could be attributed to the solid solution, so it can be easy to track any change in these peaks as a result of ageing. In these plots, there are no differences in the symmetry or shifts of the peaks in the patterns after 3 months, confirming the stability of the solid solution formation, or physical mixture in the 10% TBA case. There is a slight shift in the 2θ values for the 40% TBA composition, but these shifts are seen across the range of peaks, suggesting these differences are due to differing sample height between the two measurements instead of due to co-crystal formation causing shifting of the peaks.

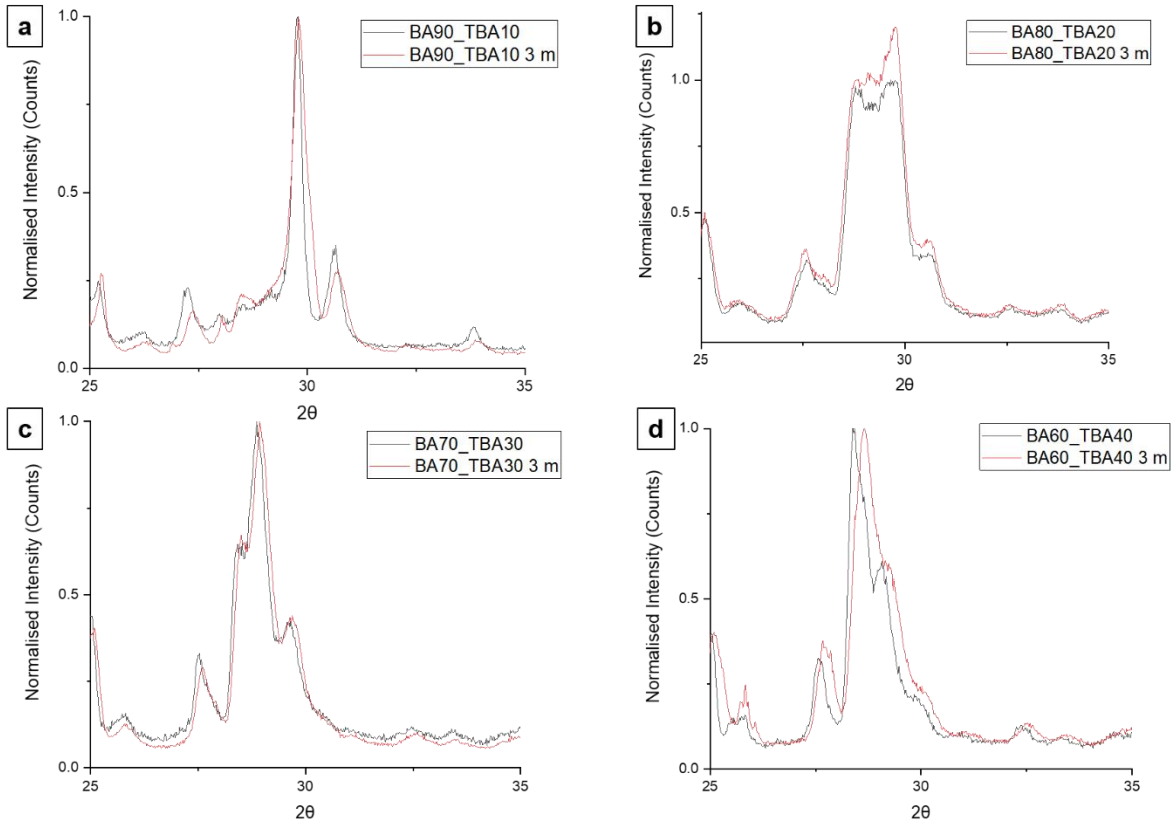

Figure 7.16: XRD patterns between the range of 25 – 35° for compounds containing excess BA immediately after formation (black traces), and after being stored for 3 months under ambient conditions (red traces).

Conversely, Figure 7.17 presents the XRD patterns taken directly after compound formation versus after 3 months storage for the compounds with TBA content above 50%. In the 60% TBA composition (Figure 7.17a), the same symmetry and intensity of the peaks before and after the three months storage is seen, suggesting there is no conversion to the co-crystal. There is a slight shift in the 2θ peaks, but again this is seen across all the peaks, suggesting these differences are due to changes in sample

height. For the 70% TBA composition (Figure 7.17b), there is an increase in intensity of the peak at 27.5°. This peak is indicative of TBA hydrate, as shown by Figure 7.10b. There is also a shift in the (202) peak to a higher value, which could suggest a 50: 50 co-crystal is formed as the (202) peak does shift to a higher value with lower TBA content. In this composition, this is also the only peak that shifts, so not likely due to changes in sample height. These pieces of evidence combined suggest there is a conversion to the co-crystal, presumably with excess TBA pushed out therefore increasing the TBA hydrate signal. In the 80% composition, it has already been established it is likely this composition already forms a co-crystal with excess TBA hydrate. In Figure 7.17c, there are however differences in the pattern taken after three months. The peaks at ~26° and the two peaks at ~ 30° are no longer present in the pattern after ageing. These peaks were indicative of the co-crystal being present. It is possible the TBA signal has become dominant after this ageing process, but this is not clear why. Other studies have proposed ageing the 80% TBA composition at elevated temperature in a humid environment causes the "pushing out" of the TBA to the surface of crystals (Elliott, 2024), so perhaps if this same phenomenon has occurred here this excess TBA at the surface may therefore be dominating the signal.

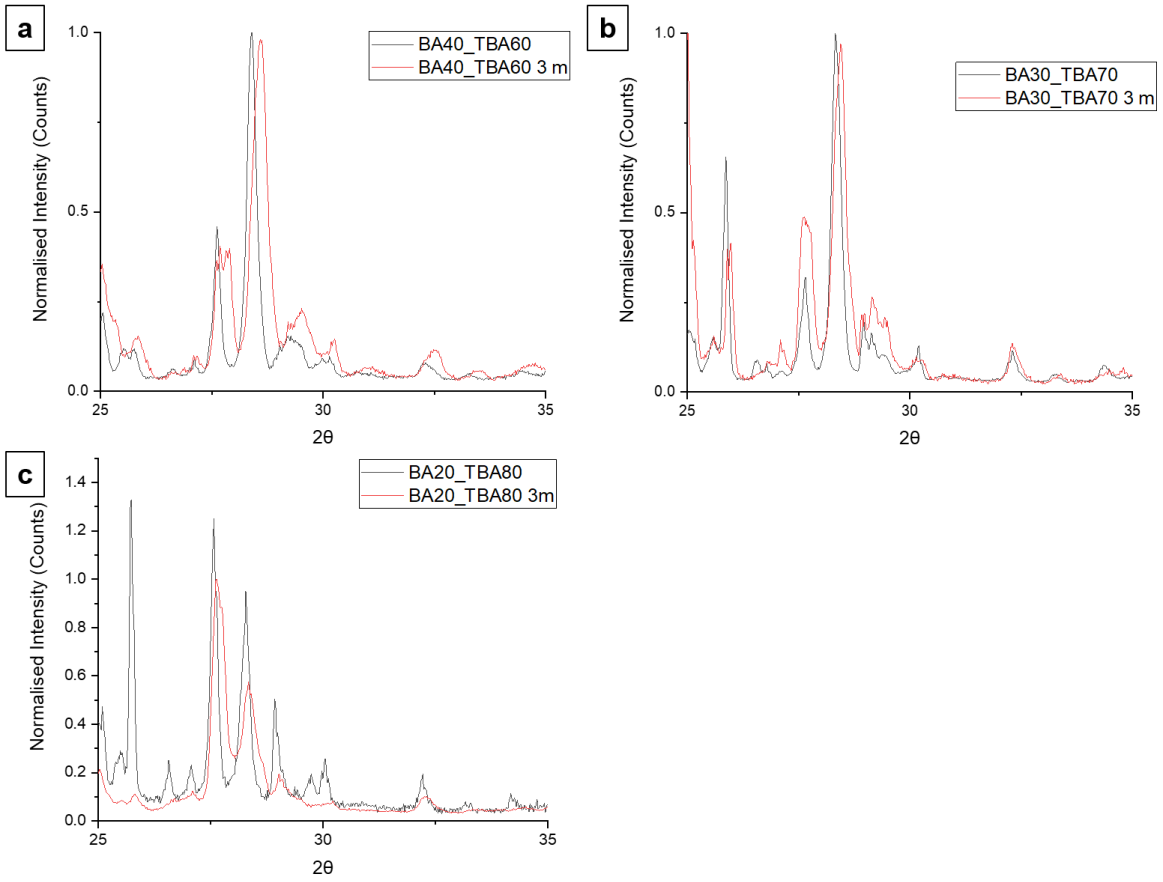

Figure 7.17: XRD patterns for compounds containing excess TBA immediately after formation (black traces), and after being stored for 3 months under ambient conditions (red traces).

Overall, the XRD results mostly agree with previous literature, where solid solution formation can be confirmed from 20 – 70 % TBA in BA. These results differ from Shemchuk et al by perhaps showing that phase separation is seen at 80% TBA, with the XRD patterns from this composition actually showing a mixture of both components. However, the presence of a peak at ~ 10° in the solid solutions with excess TBA is indicative of hydrated TBA being present and suggests that there is some phase separation at these compositions. Analysis now therefore turns to microscopic techniques, to see if localised compositional changes can be seen where bulk techniques do not offer a complete picture.

7.6 TEM Based Energy Dispersive Spectroscopy (EDS)

This solid solution system was analysed to determine if nanoscale mapping could be used to evaluate localisation of TBA vs BA, furthering previous analysis of solid solution formation and unmixing at TBA contents above 70%. Determining whether EM techniques could be sensitive enough to identify the solid solution or any phase separation in this system may be useful for other molecular compound solid solutions too. EDS identifies which elements are in a material by measuring the characteristic X-rays that are generated by the interaction of the electron beam with the material. In this solid solution system, the sulphur atom was unique to TBA so is representative of the relative proportion of TBA in the composition. EDS-STEM mapping has been used in prior work to determine the differing composition of elements across a particle (Batista et al., 2017), so it is possible this information could be resolved from this system too.

It was first looked at whether it was possible to identify whether the composition from the bulk powder could be tracked reliably. This system was studied by EDS mapping to see if sulphur atoms were concentrated in one part of the solid solution particles. However, EDS maps of sulphur across differing compositions, presented in Figure 7.18, show no localisation of sulphur in these particles.

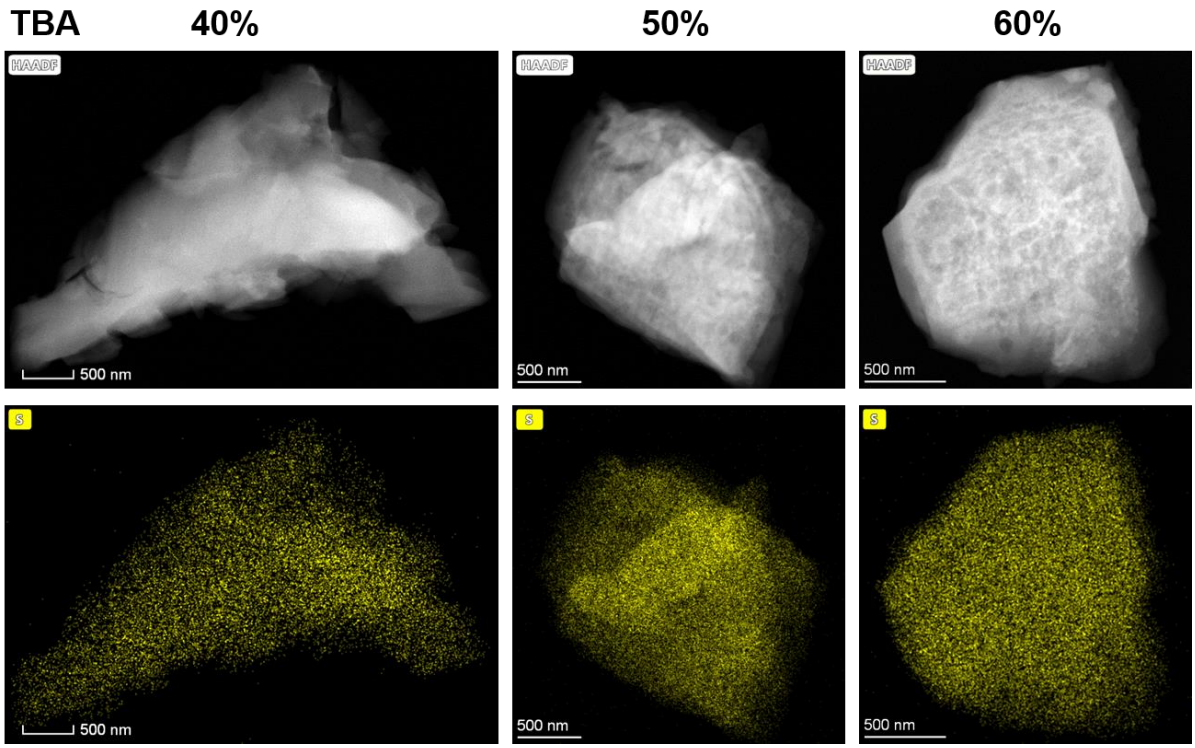

Figure 7.18: HAADF images and sulphur elemental X-ray maps of particles containing 40, 50, and 60% TBA.

Figure 7.19a shows an example of the spectra obtained from a pure TBA particle, with the main peaks of C, N, O and S labelled.

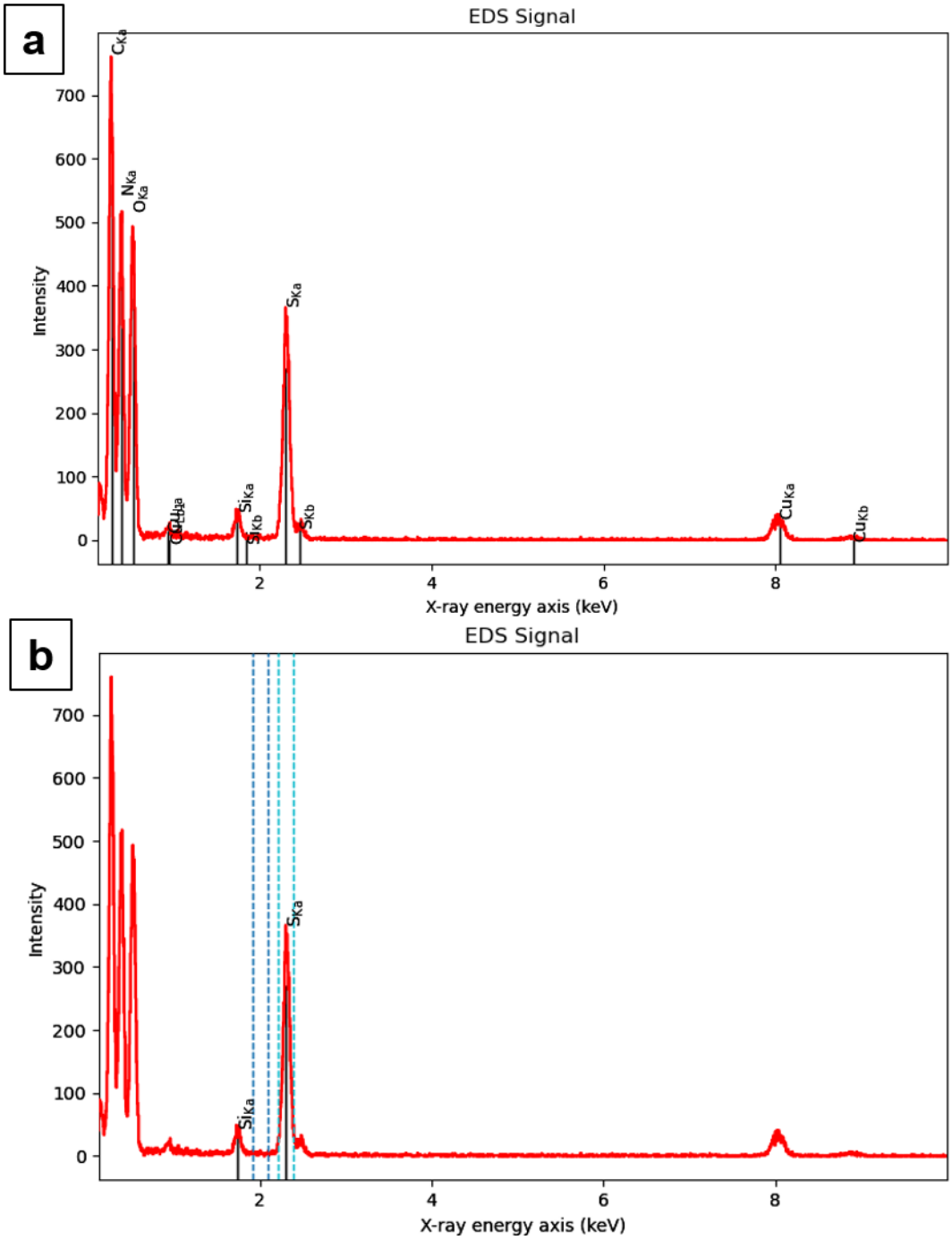

Figure 7.19: (a) EDS spectra for pure TBA with labelled peaks. (b) EDS spectra repeated from (a) with the integration windows for the background and the sulphur signal window marked.

Initially, it was thought the ratio of the intensity of the sulphur to nitrogen peaks may be an appropriate measure of the amount of TBA in the system as the number of nitrogen atoms are consistent in both compounds. As the EM grid is made from amorphous carbon, it is difficult to separate a quantitative carbon signal from the compounds. Low energy X-rays also suffer from absorption effects, meaning these peaks are not as accurate for quantitative analysis. The measured sulphur to nitrogen

intensity ratios showed a slight increase in this ratio with increasing sulphur content in the compositions (Figure 7.20a), but this is not a definitive trend as it decreases again after 80% TBA. Figure 7.20b shows the relationship between the calculated S to N peak ratio versus particle size across all compositions to determine if absorption is contributing significantly (if absorption effects are significant, the larger the particle the larger the background contribution so the larger the ratio). Particle size was measured by measuring the longest diameter of a particle (Feret diameter). This may explain the loose positive correlation, as long narrower particles may be misrepresented as a larger particle contributing a larger signal, than a smaller thicker particle. This positive correlation is evidence supporting the idea that there is an increased background signal leading to increased intensity from these peaks in bigger (hence thicker) particles i.e. suppression of the true S:N Peak ratio.

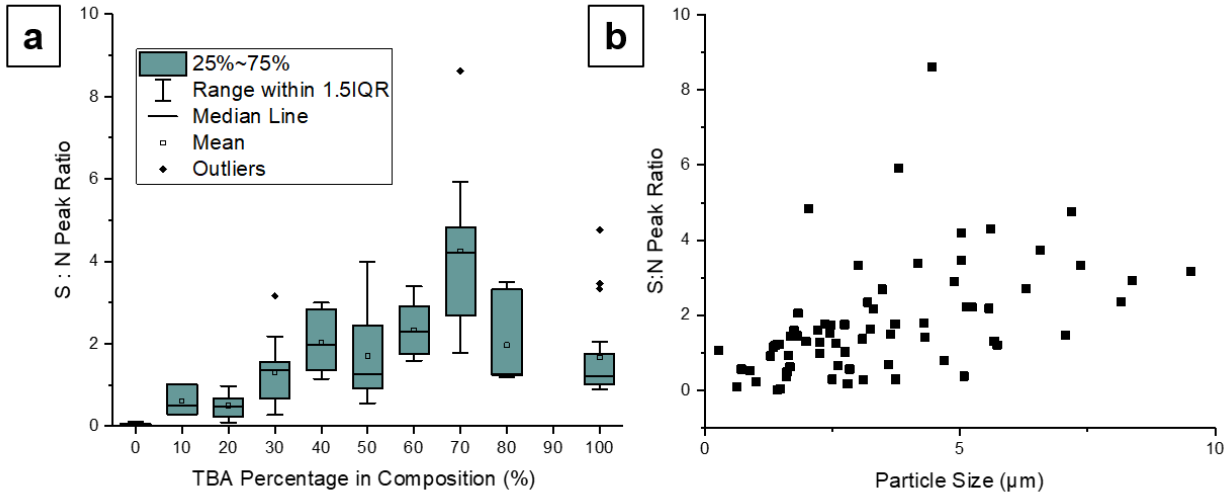

Figure 7.20: (a) Box plot showing the measured ratio of the sulphur to nitrogen peak from individual EDS spectra across the range of compositions. (b) Measured ratio of the sulphur to nitrogen peak from individual EDS spectra across the range of compositions versus particle size.

The ratio between the sulphur peak and the background was instead calculated, an approach used in microanalysis for biological systems as an example (Warley, 1997). This was calculated by integrating the signal under the *K*α sulphur peak, found at 2.3 keV, and dividing it by the integrated signal of a same sized window immediately before the sulphur peak of pure background signal (Figure 7.19b). EDS measurements were taken on individual particles so is a single particle measurement not a bulk measurement. Several repeat measurements were taken for each composition from different particles on the same grid. Box plots for each composition were formed, with the results presented in Figure 7.21 by %TBA content in the nominal composition.

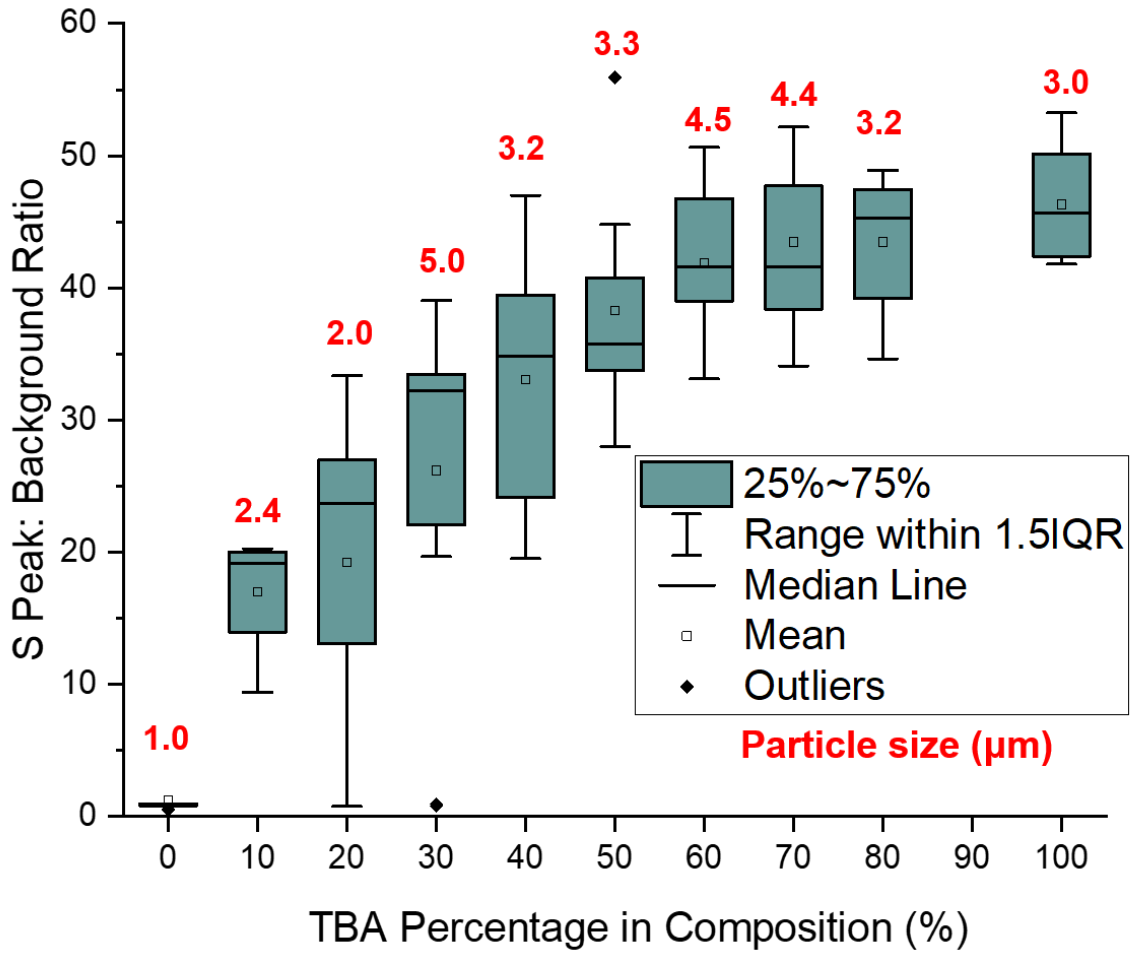

Figure 7.21: Box plots of the measured sulphur to background peak ratio across compositions from pure BA to pure TBA. Average particle size is noted in red atop each formed box plot, measured along the longest diameter of the particle (Feret diameter).

For up to 60% TBA content, the average sulphur: background ratio measured in the particles increases systematically. This regular increase was fitted to a linear function, and the slope calculated to be 0.64 with a standard error of 0.06. Measurements were repeated over several particles (10 – 20 for each composition) so that outliers where plots that have suffered from a poor signal to noise ratio could be identified and removed.

For mixtures 60% TBA content and above, the curve plateaus and the average value increases only slightly. The median peak to background ratio for the pure TBA value is 45.7, compared to median values of 41.6, 41.6 and 45.2 for 60, 70, and 80% TBA respectively. The IQR for 60, 80 and 100% TBA are all calculated to be 7 (1 s.f.), with 70% TBA having an IQR of 9. These values above 60% TBA are not significantly different, suggesting this is the maximum TBA content that can be measured.

It would also be expected that the pure TBA value should be larger than any of the compositions if the ratio increased in a purely linear manner. Due to Bremsstrahlung background contributions from the change in composition with increasing TBA content, it was tested whether the ratio would be expected to increase in a linear manner with increasing TBA content. The average value of the sulphur: background ratio for each composition was plotted against the percentage of TBA.

The y value of the graph is defined as the ratio between the intensity of the sulphur peak to the background, or:

$$y = \frac{I_s}{I_{BK}} \tag{7.1}$$

The intensity of the sulphur signal, I_s, is proportional to the number of sulphur atoms multiplied by a constant, A and thickness, t, over the volume of the particle.

$$I_s \propto (At)\frac{N_s}{V} \tag{7.2}$$

X-ray intensities are explicitly related to the number densities of atoms by the partial cross section for a single atom of any given element, *x*, as given by:

$$I_x = \sigma_x D n_x t A \tag{7.3}$$

where $n_x t$ is the atom density per unit area *A* defined in atoms/m^2 and *A* is the illuminated area, *D* is the fluence, and σ_x is the partial cross section of the atom.

The intensity of the background, I_{BK}, is proportional to Z^2, multiplied by thickness (Seltzer and Berger, 1985).

$$I_{BK} \propto Z^2 t \tag{7.4}$$

This Z^2 term can be broken down into the atomic number multiplied by the number of each atom for every atom in the system, divided by the total number of atoms, N_{total}, for a weighted average.

$$Z^2 = \frac{(N_H Z_H + N_C Z_C + N_N Z_N + N_O Z_O + N_S Z_S)^2}{N_{total}} \tag{7.5}$$

which can be simplified to a constant, *B* (which incorporates all non-oxygen and sulphur terms and the division factor), + a constant multiplied by however many sulphur atoms remain in the composition after oxygen substitution.

$$Z^2 = (B + N_S Z_S + (6 - N_S) Z_O)^2 \tag{7.6}$$

Substituting this term back into the original ratio gives the following expression,

$$y = \frac{K N_S t}{(B + N_S Z_S + (6 - N_S) Z_O)^2 t} \tag{7.7}$$

In this Equation 7.7, *K* is a scaling factor assuming proportionality i.e. that *σZ* remains constant for all compositions (Equation 7.3). This mathematical form can be approximated to the following Equation 7.8 for the percentage of TBA, *x*, since $x = 100*[N_S/(N_S + N_O)]$, to give the ratio of sulphur signal: background signal, and fitted to the acquired EDS data (Figure 7.22). In this expression, *K'*, *B'* and *C'* are fitting constants when using *x*, i.e. will be different to Equation 7.7.

$$y = \frac{K'x}{(B' + C'x)^2} \tag{7.8}$$

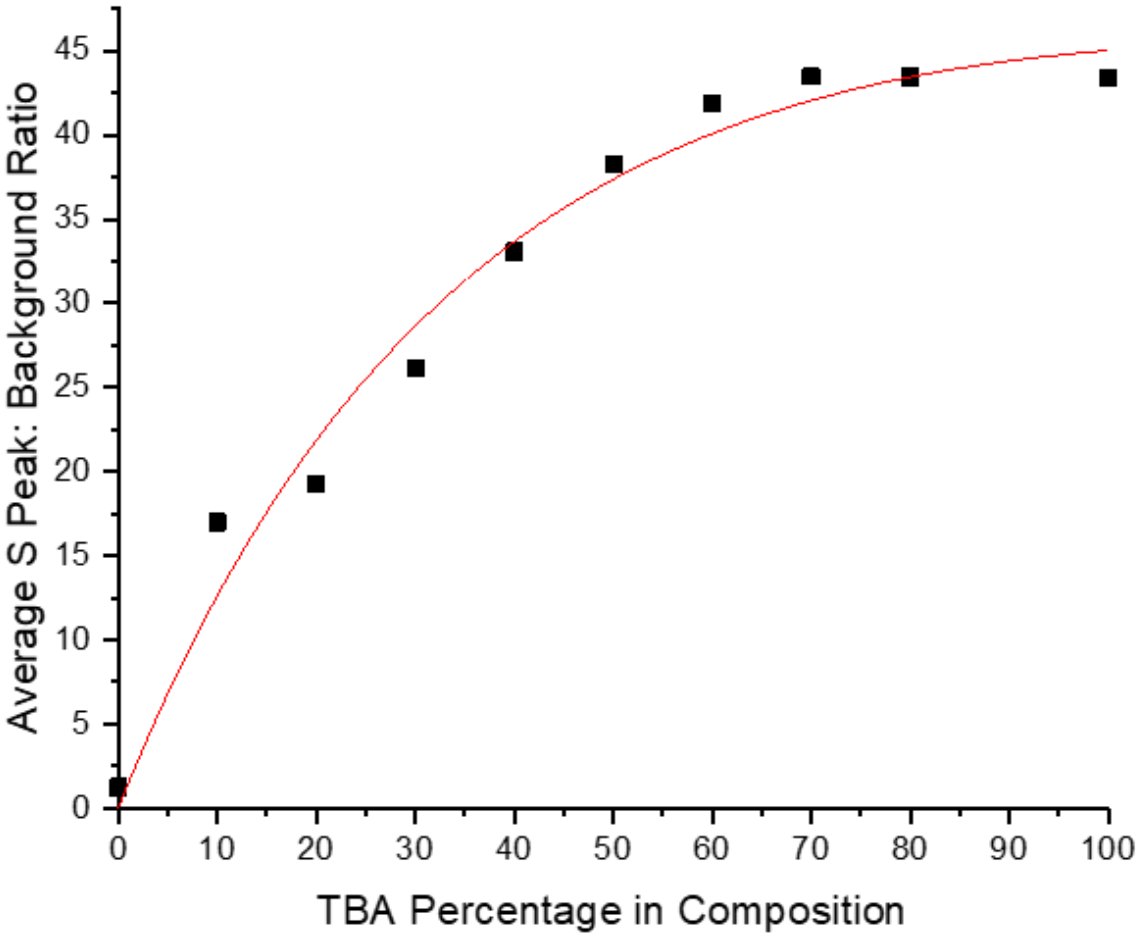

Figure 7.22: Average sulphur peak to background ratios plotted versus composition and fit to Equation 7.8

Table 7.2 presents the parameters derived from the fitting in Figure 7.22.

Table 7.2: Parameters derived from fitting the graph in Figure 7.22 to the Equation 7.8.

Parameter	Value
K'	65 ± 10000
B'	7 ± 500

C’	0.05 ± 4
Reduced Chi-Sq	6.057
R-Square	0.98
Adj. R-Square	0.97

The general form of the sulphur: background ratio plateauing may be expected because the sulphur atom has a higher atomic number than oxygen, however the exact value at which the plateauing occurs will be dependent on additional contributions from the carbon support film. Nonetheless, for every oxygen atom replaced by a sulphur atom, the overall atomic number will increase, meaning the Bremsstrahlung radiation background signal will increase with increasing TBA content alongside the sulphur signal. These results suggest that peak to background ratio can only differentiate increasing sulphur versus background content up to a ‘saturation’ point which to a first approximation for this system is about 60% TBA.

It was suggested by Shemchuk et al that the compounds formed above 50 % TBA contained particles of 50: 50 solid solution and excess TBA was pushed out. But the results above suggest EDS would not be capable of detecting this. There is also an element of user bias in EDS when choosing particles to take a measurement from. To ensure it was not user bias picking only larger particles, and perhaps missing smaller particles, the particle size was measured, which is noted in red above the box plot for each composition. It can be seen that there is no systematic variation in size across the range of compositions, with the pure BA particles having the smallest average size by at least a factor of two.

To further test the theory that co-crystal and separate TBA particles were being measured, a histogram was formed for compositions with excess TBA and a histogram of the pure TBA values (Figure 7.23). If the compounds formed above 50 % TBA contained particles of 50: 50 solid solution with excess TBA pushed out then the histograms would appear bimodal with the values falling into two groups. One of these groups would be the value of the sulphur: background ratio for the pure TBA, and the other being the value of the sulphur: background ratio for the 50:50 co-crystal. Figure 7.23 presents the histograms for the binary mixtures (Figure 7.23a) and pure TBA (Figure 7.23b). Whilst the histogram for the pure TBA is skewed to the higher values, there is no clear element of bimodality in the compositions where there is a possible mixture of phases, so it is likely this plateau is due to the background noise limiting the value that sulphur can be calculated to as per Figure 7.22.

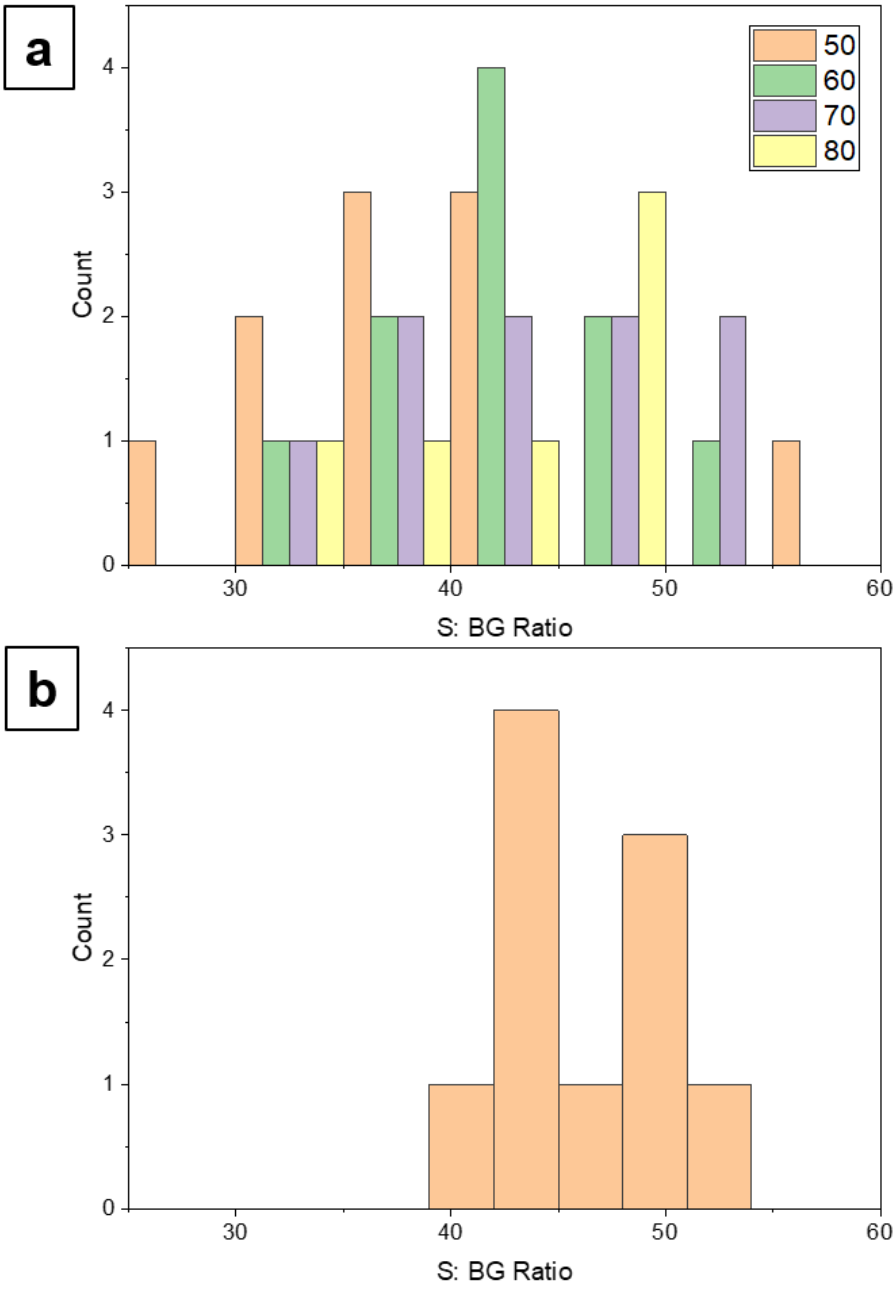

Figure 7.23: (a) Histogram showing the sulphur to background peak ratio measured in individual particles across compositions with equal and excess TBA, the legend indicated the percentage of TBA within the composition. (b) Histogram showing the sulphur to background peak ratio measured in individual particles in pure TBA.

7.7 Scanning Electron Diffraction (SED)

7.7.1 (202) Spot Shift Across Solid Solution Range

As microscopy is a local technique, it can be utilised to track localised changes in samples that bulk techniques may not capture. As used in previous chapters, SED

offers highly spatially resolved structural information. It was tested here whether SED would be sensitive enough to determine the shift in the centre of the Bragg diffraction spot corresponding to (202), i.e. the shift detected by XRD (Figure 7.15). Potentially SED could be used to determine any change in unit cell structure and therefore the local composition of this solid solution instead of the overall composition of the powder. SED has been used previously to determine phases in nanocrystals within metallic alloy layers (Bergh et al., 2021). Due to the resolution of the microscope and the difference in measured d-spacings between the end-members here it should be possible to differentiate between at least the end-members. Table 7.3 presents the expected d-spacing values as measured by XRD.

Table 7.3: d-spacings of the (202) spot as measured by XRD.

BA %	**0**	**30**	**50**	**70**	**100**
d-spacing (nm; as measured by XRD)	0.32	0.32	0.31	0.31	0.3

The microscope setup uses a convergence angle of 0.8 mrad using a 10 µm condenser aperture. At 300 kV, this produces a 3 nm diffraction-limited probe diameter $d_{diff} = 1.22\lambda/\alpha$, where λ is the electron de Broglie wavelength and α is the convergence semiangle. Calibrated to a gold cross-grating pattern, the diffraction pattern resolution was calculated to be 0.01 nm^{-1}.

Samples of pure BA and TBA were prepared with the as received powder, to be able to track this (202) spot spacing. This also means for these samples, hydrate contribution did not have to be considered. The measured d-spacing of the interim compositions are very similar to the end-members, for example the d-spacing for pure TBA was measured from XRD as 0.32 nm which is the same as the measured d-spacing for the composition containing 30% TBA when rounded. Whilst the d-spacing changes to 0.31 nm at 50% TBA, this is the same as 70% TBA when rounded. So whilst it is possible to resolve the two end-members from one another, in between is more difficult.

SED datasets were collected on pure BA, pure TBA, and compositions across this range containing 30, 50, and 70% TBA. These samples were prepared for EM analysis via a dry powder transfer. This involved taking the powder as already prepared without any further preparation and placing a small amount of powder on top of a TEM grid (with continuous carbon support film) within two pieces of lens paper. The pieces of paper were shaken, with the powder and grid within, to disperse the powder onto the

EM grid. This preparation method, however, meant there was no orientation control of the sample in relation to the electron beam, so there was no guarantee the (202) spot would be seen in the crystals imaged. As a lot of SED data analysis takes place as a post-processing stage, an immediate feedback loop to direct data acquisition is also difficult. These combined factors meant collection of a large number of datasets with (202) spots was hard to achieve.

To sift the acquired data, a set of VDF images was used using an aperture set to the diameter of the (202) distance for each given composition. The output was a set of images where the bright regions had Bragg spots within this aperture. Average diffraction patterns were taken from within these areas to resolve the highest possible (202) intensity for spot measurement.

The whole diffraction patterns were then indexed using CrystBox software to determine if the spots at the target d-spacing could in fact be assigned to a (202) spot and not another spot with a similar d-spacing. The .cif file that was input into this software contained the adjusted unit cell parameters of the solid solution as determined from XRD data. This software was able to index the patterns to varying success. This was due to the patterns not always being fully on zone axis. The software works by measuring d-spacings and interplanar angles, with the output being a set of directions that are the best fits to these values. Where the patterns do not include a full set of Bragg spots, the number of measured values is therefore reduced, so fits are less definite. There is also a high density of Bragg spots within the spacing range the (202) spot falls within, so it is possible to wrongly assign a Bragg spot. Due to XRD establishing there is a contribution from the TBA hydrate form in certain compositions, these compositions were also indexed to the TBA hydrate to see if this could find a better fit, or explain any extra spots that could not be explained by the solid solution simulated pattern alone. Figure 7.24 shows an example of a diffraction pattern with a simulated pattern from the 50: 50 co-crystal pattern overlaid in orange where this software has found a good match. The best fit the software found for the hydrate structure can also be viewed in the green overlay in Figure 7.24. As can be seen, this pattern does not align with the diffraction pattern as well as the structure with the orange overlay with any of the most intense spots, suggesting signal in this diffraction pattern is primarily not from hydrate contributions but from the co-crystal.

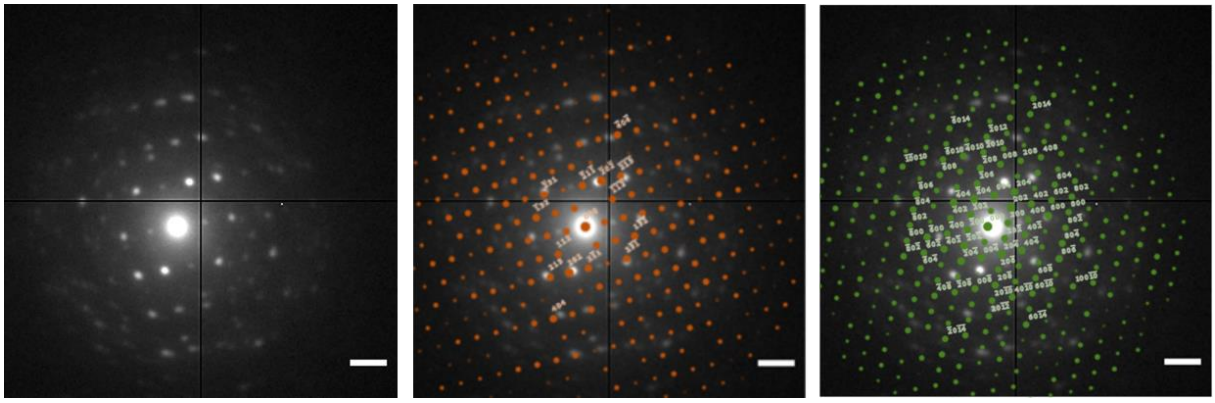

Figure 7.24: An example of a diffraction pattern where CrystBox was able to find a successful match for the zone axis of the crystal (orange overlay) for a composition containing 50% TBA. CrystBox best match to the TBA hydrate structure (green overlay).

Figure 7.25 however shows an example where the software was unable to find a good match from the top three best matches for the 50:50 co-crystal to a different diffraction pattern from a different crystal containing 50% TBA.

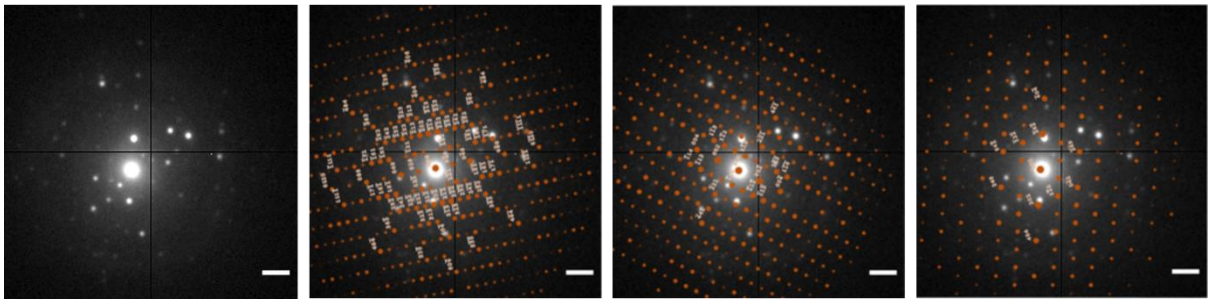

Figure 7.25: An example of a diffraction pattern where CrystBox was not able to find a successful match for the zone axis of the crystal from the top three best matches of the 50: 50 co-crystal structure relative to the electron beam.

Figure 7.26 also shows an example of where the diffraction pattern from Figure 7.25 has been evaluated against the top three best matches from the TBA hydrate structure in this software. This also does not give a clear perfect match versus the experimental data, but there is good alignment with some of the most intense spots. It is possible this diffraction pattern contains contributions from both structures, which may mean the software is not finding a good fit as it cannot distinguish between the two phases. In any case, for any of these best found fits, no (202) spots were indexable for this particular crystal with 50% TBA.

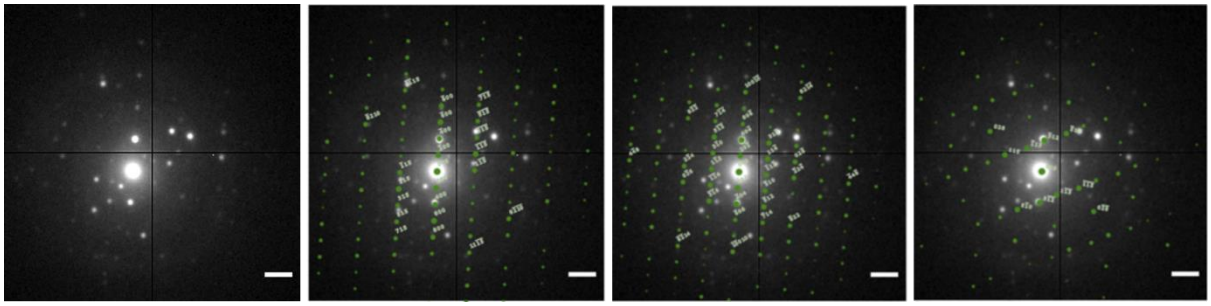

Figure 7.26: The dataset repeated from Figure 7.25, evaluated instead against the best fits from the TBA hydrate structure.

For the measurement of (202) spot d-spacings, datasets were evaluated against the best matches and discarded if there was no suitable match, or if the best match did not include a (202) spot. There were 5 datasets over the range of compositions that included a $(20\bar{2})$ spot, which had a similar d-spacing to the (202) spot, but this is not equivalent to the (202) spot as they indicate different crystal planes, so these datasets were also discarded. Table 7.4 presents the d-spacing values measured from the datasets with confirmed (202) spots for pure BA, and solid solution compositions of 30 and 50 % BA. Unfortunately, no (202) spots were able to be attributed to the patterns found for pure TBA, or for the solid solution containing 70% BA.

Table 7.4: Measured (202) spot shift from pure TBA to pure BA across a range of compositions where indexation was possible.

BA %	**0**	**30**	**50**	**70**	**100**
d-spacings (Å)	-	3.48	3.21	-	2.51
	-	-		-	2.78
Average (Å)	-	3.48	3.21	-	2.65
Average (nm)	-	0.35	0.32	-	0.25
d-spacing (nm; as measured by XRD)	0.32	0.32	0.31	0.31	0.3

As the table shows, there are maximum two datasets for each composition that remained after the spot analysis, from ~ 15 datasets taken for each composition. For pure BA, the only composition with more than one dataset, there is also a large variation between measurements, when it would be expected that within compositions values should be consistent.

These values are also not consistent with the XRD measurements of the (202) peak shift. Whilst there is a 6 – 8 % increase in reported d-spacing values for the 30 and 50% BA compositions, the pure BA value actually decreases by double this amount, exhibiting a 15 % decrease. Observing these SED values alone, there is a general trend of decrease of the d-spacing with increasing BA content as would be expected.

Whilst some conclusions from this analysis can be drawn, with a limited set of data it is difficult to judge whether SED could reliably measure a (202) spot shift across a range of compositions to be able to measure phase separation.

7.8 Conclusions and Future Work

Results in this chapter have analysed a solid solution system formed between two organic molecules, BA and TBA, that exhibit polymorphism. XRD has shown how a small amount of one component can direct crystallisation to a different polymorph than otherwise seen in the same solvent (Figure 7.11). XRD also highlighted the presence of hydrates in this system, indicating the sensitivity of this system to water content (Figures 7.9 and 7.10). This is important when considering the applications of these molecules. Water and humidity are important for medicines, agrochemicals and fine chemicals crystallisation and hydrate formation changes dissolution rates and or bioavailability. Future work could involve further unpacking the contribution of these hydrates to the system, to observe how the stability and subsequent molecular availability would change in a real environment. Solid solution formation was confirmed between 20 and 70 % TBA, with DSC analysis suggesting phase separation of the TBA seen above this composition.

EDS analysis has shown that solid solution can be confirmed for compositions below 60 % TBA content. Above this value, the expected sulphur: background ratio plateaus due to the change in composition itself (signal plus Bremsstrahlung), so it is not possible to differentiate these TBA-rich compositions from pure TBA. But these results do suggest it may be possible to use EDS as a way to study composition within a solid solution system of small compositional variation at the microscale.

SED was also employed to determine if local diffraction spot shifts could be seen across a sample. There were suggestions that this could be possible, but the lack of reproducible data means the conclusions that can be drawn are limited to a decrease in spacing with increasing BA content as is already expected/ reported.

Future work on this system could involve attempting to control orientation of the sample for EM analysis. This could be achieved by drop-casting methods using different solvents, but solvent choice would have to ensure that the molecules were not dissolved and recrystallised as separate components if trying to study the solid

solution or co-crystals formed. An additional experiment to consider is performing EELS on this system as this would not suffer the same absorption effects as EDS. EELS could be directly quantitative for the ratio between the sulphur and nitrogen peaks. However, EELS also has experimental challenges, for example samples need to be much thinner for reliable quantification.

To further probe the intrinsic stability of solid solution in the BA: TBA system anhydrous solvents should be used to remove hydrate contribution to the solid solution. This would offer information on the pure solid solution system between the two components, and could potentially make SED analysis simpler.

This chapter has shown that with further refinement EM techniques can be used to study solid solution systems, and start to uncover local composition versus bulk composition. The system used here was for compositions where the “impurity” was at relatively large amounts compared to those seen in the pharmaceutical industry e.g. where impurities at only 0.15% have to be qualified (Jacobson-Kram and McGovern, 2007). Future work could involve testing the minimum amount of an impurity that a technique such as EDS, SED or EELS could quantify, or using SED to track the structural or polymorphic changes that may arise due to this impurity incorporation.

Chapter 8
Conclusions and Future Work

8.1 Conclusions

The aim of this thesis was to understand structural heterogeneity at the nanoscale of organic molecular systems using low-dose electron microscopy techniques. Scanning electron diffraction (SED) implemented with a low convergence angle probe (<1 mrad) of ~5 nm diameter is shown to enable low dose electron microscopy of nanoscale features in two molecular solid solution systems, unveiling structural features not resolvable using other techniques. The identification of crystal form, grain and order domain packing within measured solid solution limits of these molecular systems has important implications for the understanding of structure-property relationships in the agrochemical and pharmaceutical sectors and beyond.

Chapter 4 evaluated the crystalline packing of two wax components of a simplified replica leaf wax system, $C_{31}H_{64}$ and $C_{30}H_{61}OH$, by SAED and AFM. First, critical fluence measurements established that the primary damage mechanism of these waxes was radiolysis and provided a 300 kV 'dose' budget of 10 $e^{-}/Å^{2}$ to work within. SAED pattern analysis indicates that the $C_{31}H_{64}$ alkane crystallised with $A2_1am$ symmetry, and the $C_{30}H_{61}OH$ alkanol crystallised with $P2_1/c$ symmetry when prepared in thin film form by drop-casting/ benzoic acid templating. AFM revealed terracing on drop-cast crystals consistent with the *n*-alkane packing end-to-end in a chains down form, whilst the *n*-alkanol crystals appear to pack with alternate stacking of the alcohol chain termination. Understanding the underlying unit cell picture was important to understand the effect of the single site substitution of the $C_{30}H_{61}OH$ alkanol in the pure form on the packing to understand how introduction of this $C_{30}H_{61}OH$ alkanol to the $C_{31}H_{64}$ alkane would impact the structures formed in the solid solution system studied in the next chapter.

Chapter 5 then used SED to assess the nanoscale packing of each wax type, and binary mixtures between the two. A combination of diffraction pattern analysis and virtual dark field imaging unveiled the presence of highly ordered lamellae domains within larger, anisotropic grains of the $C_{31}H_{64}$ crystals. Nematic phases of disordered chain packing was also found surrounding these highly ordered domains, where chain displacement leads to a diffuse scatter signal in the corresponding diffraction patterns. This model is shown in Figure 8.1 and was likened to the proposed 'brick and mortar model' of the IW layer in a leaf, in the *Schefflera elegantissima* plant, where the disordered regions could offer the high diffusivity pathways. It differs from this model as no amorphous zones were identified, instead being a model of order vs disorder. A

full composition in an IW layer may be more complicated due to the increased number of different components, but this binary mixture model can be taken as a simplified representative.

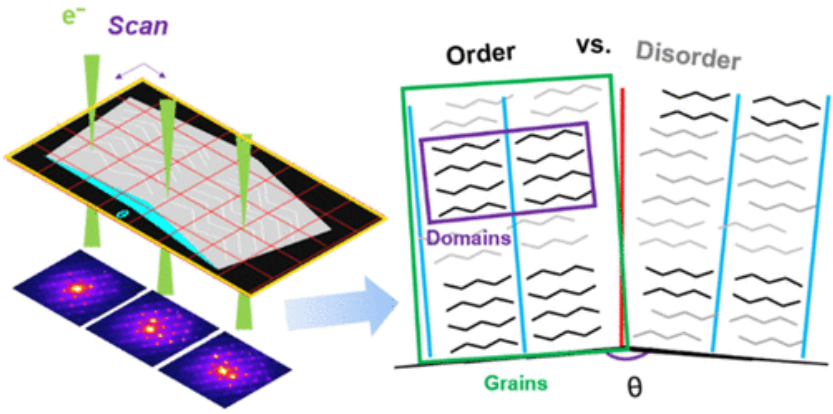

Figure 8.1: Proposed structural model for order and disorder at the nanoscale in $C_{31}H_{64}$ crystals using SED analysis.

In this model highly ordered domains (with lamellar chain packing) are surrounded by nematic phase regions and the model may suggest that these more disordered regions could offer high diffusivity pathways through a wax crystal such as might form in the intracuticular wax layer of a leaf. The $C_{30}H_{61}OH$ alkanol crystals showed no such domain ordering although subsequent work (Chapter 6) did reveal these crystals to contain more grains and defects than the $C_{31}H_{64}$ crystals. This lack of domain ordering in the $C_{30}H_{61}OH$ alkanol crystals may be due to the alcohol chain termination promoting staircase packing and mixing with alternating stacking as seen by AFM.

Binary mixtures of increasing $C_{30}H_{61}OH$ alkanol content produced more disordered crystals than the pure $C_{31}H_{64}$ crystals, with AFM suggesting solid solution formation up to 30 % *n*-alkanol content, and the loss of lamellar domains and the reduction in grain microstructure by 30-50% *n*-alkanol content. IW layers in the *Schefflera elegantissima* plant are thought to have ~ 15% *n*-alkanol content within an *n*-alkane matrix, indicating domains of lamellar ordering may be expected in the plant. These results can be taken as a simple structural model for this plant, but it must be considered that the real IW layer in the plant has extra components outside of this wax mixture, and IW layer composition varies from plant to plant.

Chapter 6 investigated the impact of exposure to a solvent molecule, TEHP (typically used as an adjuvant in agrochemical spray formulations), to each wax type, and binary mixtures between the two. TEHP is added to crop protection products to increase the take-up of active ingredients across the leaf wax barrier. A difference in interaction with TEHP exposure for the *n*-alkane and *n*-alkanol was demonstrated. It is expected that the wax components in the *Schefflera elegantissima* plant would form a solid

solution at the composition of ~15% *n*-alkanol content in this plant. This may therefore have implications for how TEHP interacts with the IW layer, as it is *n*-alkane dominated and therefore more likely to interact as TEHP does with the pure *n*-alkane. Bulk thermal analysis techniques suggested plasticisation of the wax components on exposure of wax to an excess of TEHP, with an increased effect on the *n*-alkanol. XRD measurements where the wax was in excess, showed an increase in disorder (or reduced coherent scattering domain sizes) upon exposure to TEHP, also suggesting a possible element of plasticisation but that crystallinity was maintained. Microscopic techniques following exposure to an excess of TEHP however suggested a potential dissolution mode of action instead of plasticisation. TEM and SED contextualised this dissolution further, by showing the formation of small pits at the edges of $C_{30}H_{61}OH$ crystals, which suggested a possible etching mechanism. Differences in the crystal packing between the $C_{31}H_{64}$ and $C_{30}H_{61}OH$ crystals was also examined further, and a higher density of grains, grain boundaries and dislocations within the $C_{30}H_{61}OH$ crystals was identified, which may cause inherent differences in the interaction between these crystals and TEHP. Facet analysis found that edges with a higher percentage of alcohol groups at the surface of a $C_{30}H_{61}OH$ crystal plane etched faster than ones with a lower percentage, suggesting an interaction between TEHP and the alcohol group in the *n*-alkanol chains. These results suggest that the mechanism of action of TEHP may be concentration dependent, with dissolution seen where the TEHP was in excess, and increased disorder seen where the wax was in excess; it is likely that both of these mechanisms of action operate together with concentration of TEHP dictating which dominates. Spectroscopic methods were shown not to have sufficient signal to noise to distinguish each individual wax component within the binary mixtures, so a different system was then analysed.

In Chapter 7, analysis focused on a different solid solution of the structurally similar thiobarbituric acid (TBA) in barbituric acid (BA), where molecular mixing might be tracked by the presence of sulphur, which was present in TBA and not BA. This single substitution of one oxygen for a sulphur atom consisted of a greater wt% in the solid solution than the substitution of one methyl group for an OH group in the wax system, making it easier to obtain a higher signal to noise ratio to distinguish between the two components. A solid solution was confirmed between 20 – 70% TBA using DSC and XRD measurements although hydrates were also detected due to the solvents used for crystallisation which may have implications for the shelf-life of compounds in solid solution forms. EDS analysis was first used to determine detectability of the sulphur signal in the BA and TBA mixtures. EDS analysis was therefore used to track sulphur content changes across the solid solution range, and was able to do so up until ~60% TBA, beyond which the signal to background ratio remained constant due to the

increasing contribution of the S atoms to the Bremsstrahlung background. This is within the solid solution range, with a solid solution forming up to 70% TBA. EDS analysis could therefore not be used to study any possible phase separation above this composition. Below this solid solution range at 10% TBA, EDS mapping did not offer any information on phase separation. SED analysis suggested that tracking of local unit cell changes as a result of solid solution formation may be possible by measurement of the spacing of the (202) planes of the form I BA crystal structure.

As outlined in the literature review of this thesis, solid solution characterisation of molecular systems was a topic overlooked for many years (Lusi, 2018a), (Lusi, 2018c). There is now opportunity to understand more about these systems, and how structural heterogeneity at the nanoscale affects the properties of multicomponent molecular solids, the stability of these solid solutions, and how these systems interact with external molecules. Work in this thesis has shown it is possible to use low-dose EM techniques such as SED for nanoscale structural characterisation of molecular solid solutions with a single substitution site and has highlighted the opportunities for development of this technique further.

8.2 Future Work

To further develop the research reported in this thesis, there are several possibilities for future work.

Tertiary and Quaternary Wax Systems

The results presented in this thesis on wax solid solutions are of a simple mixture of two hydrocarbon chains with similar lengths. This system was based on the *Schefflera elegantissima* plant, a leaf with a relatively simple leaf wax composition. Results in this thesis could be taken as representative of a simple model, and findings applied to the more complicated compositions of other plants. Future work could start to look at tertiary and quaternary solid solution systems, incorporating hydrocarbons of different chain lengths. These will become relatively complicated systems, so studying the range of solid solution solubility of the components will be key. Dorset has used electron diffraction to study a three-component solid solution and found similar behaviour to binary mixtures, but with the sequence of phase separation being more complicated than the binary mixture (Dorset and Snyder, 1999). SED showed how in the case of the *n*-alkane and *n*-alkanol system that *n*-alkanol incorporation increased disorder through the loss of lamellar ordering within the system, so SED could be used to understand lamellar order or disorder at the nanoscale within a multicomponent solid solution.

SED analysis could be explored on the IW layer of the actual *Schefflera elegantissima* plant to evaluate against the model from the replica IW layer system. In this work, leaves could be prepared by cryo-microtome, cryo-transferred into the TEM and analysed by SED in the same manner. Cryo-microtome is a method that has been used for the preparation of thin leaf samples for EM analysis previously (Maekawa and Kawamoto, 2002). Orientation control of the chains would be difficult with this sample preparation, but conversely may offer information on chain orientation within a real leaf system, something not fully considered in this work.

Adjuvant Exposure

In Chapter 6, the microstructural changes of the two waxes upon exposure to an adjuvant, TEHP, was studied. Two different concentrations were studied; where the wax was in excess and where the adjuvant was in excess. Where TEHP was in excess, such as in the TEM analysis, a potential etching mechanism was seen. Where the wax was in excess, such as in the XRD measurements, an increase in disorder (or reduced coherent scattering domain sizes) was seen, suggesting a possible element of plasticisation. Future work could investigate the effect of a range of TEHP concentration to offer further insight into these two mechanisms. As TEHP is not miscible with water, it would have to be explored how concentration could be controlled without incorporation of any other components that may themselves have an effect on wax structure if trying to define adjuvant effect only e.g. ethanol (in which TEHP is miscible). Walker (2017) suggests a mixture can be formed between TEHP and water when the mixture was stirred and heated at 50 °C overnight (Walker, 2017), but efforts to replicate this have not been successful. It could be possible to try and form larger single crystal wax films, and control exposure to TEHP using microdroplets of TEHP. Microdroplets can be formed as oil-in-water emulsions, and are 5 – 500 μm in diameter so the concentration of TEHP to wax film could be controlled this way (van Tatenhove-Pel et al., 2020).

Adjuvant Effect on Wax Film Properties

This thesis has looked at microstructural changes to wax crystals as a result of adjuvant exposure. Future work could try to link these microstructural changes to changes in the wax properties, for example thermal analysis already shows the melt temperatures broaden. One way of doing this could be through the use of quartz crystal microbalance with dissipation monitoring (QCM-D). This technique has already been used to study the interaction of a different type of adjuvant, two surfactants $C_{10}EO_7$ and $C_8G_{1.6}$, with a wax layer, a mixture of $C_{22}H_{45}OH$ and $C_{32}H_{66}$, deposited on the QCM-D sensor (Fagerström et al., 2014). This technique measures the weight of a thin film on a sensor via changes in frequency, and rigidity of the film with dissipation

measurements. It is therefore used to study systems where one material is added to another to determine the effect of the added material on the properties of the thin film. This could be used to study the effects of adding TEHP to thin wax films. TEHP is a structurally different molecule to the surfactants, so may not interact in the same way as those reported by (Fagerström et al., 2014). There are potential challenges associated with using this technique. The Fagerström paper suggested that thin film formation by spin coating formed a continuous film, but provided no characterisation of this film. Due to this, it was also unknown which orientation the waxes crystallise in using spin coating to prepare the films. For this technique to be used, there should be investigation into both whether this method forms a continuous film (and if not, how this impacts QCM-D measurements), and in which orientation the wax chains lie so that the property measurements can be linked to the known crystalline structure.

Orientation and Solvent Control in BA: TBA Solid Solution System

Chapter 7 highlighted the complexities in solid solution characterisation where the BA and TBA compounds formed hydrate polymorphs as well as the expected form I solid solution polymorph. To more easily assess whether SED can be used to track microstructural change across this BA-TBA solid solution, there could be further efforts to evaluate the effect of water content and humidity in the formation of solid solutions and hydrates. This would also involve the use of anhydrous solvents to determine solid solution formation with no water present as a comparison.

Another way to increase reliability in the analysis of the (202) spacing across different compositions would be to control orientation of the resulting crystals on thin films for TEM. Potentially, the ethanol solution containing the BA and TBA mixture could be drop cast straight onto the EM grid but this may impact how the solid solution forms when crystallising from this drop casting method or the layer may be too thick. Efforts could be made to control layer thickness by methods such as spin coating.

It may also be possible to use EELS to track compositional change across these solid solution particles. However, samples for EELS must be much thinner than used here so far for reliable quantification so sample preparation would again need to be considered. Work by Koniuch et al. has shown how local composition could be determined in polymeric nanoparticles using EELS in cryo-STEM suggesting this may be feasible for the BA and TBA solid solution particles (Koniuch et al., 2023).

Solid Solution Compositional Change Tracking by EDS

The EDS results in Chapter 7 in this thesis looked promising for tracking compositional change across a solid solution range up to a solute concentration of 60% TBA in BA. At this point, the contribution of the solute to the background Bremsstrahlung radiation

as well as the signal makes it difficult to quantify any additional sulphur content (TBA) in the solid solution. Where heavier elements differ between compounds used in solid solution, the difference in atomic number would change the constant for the fitting parameters established in Equation 7.8 in Chapter 7. This is because the intensity of the background signal is proportional to Z^2 (Seltzer and Berger, 1985). This may lead to a different saturation concentration of the signal to background ratio. If applied to other systems at concentrations below the signal to background ratio saturation, this mode of EDS could be a useful tool for tracking compositional change across individual solid solution particles, which may be useful when looking at systems that potentially phase separate above a certain solubility range. These techniques may also be useful to track impurities in solid solution systems, as any impurity concentration is likely to be below this saturation point. Other methods such as absorption correction for EDS analysis could be employed to resolve the carbon, nitrogen or oxygen peaks (Eibl, 1993), (Newbury and Ritchie, 2013). Then, the ratio between sulphur and one of these elements could instead be analysed to see if this ratio changed with differing composition. Future work could look at using EDS to quantify small impurity amounts in individual particles by establishing a lower limit of detection, which could be linked to changes in properties such as dissolution and bioavailability or the formation of different polymorphs (Kras et al., 2021), (Paolello et al., 2024).

General Wider Applications in Solid Solution Studies

Knowledge of solid solution structure is relevant across agrochemical and pharmaceutical sectors for the design of pharmaceutical products, or crop protection products that interact with the solid solution system. This thesis has made the first step delving into solid solution microstructure in organics, and there is possibility for general wider applications in solid solution studies. This thesis has focused on two systems with single site substitutions between the two molecules, but many solid solutions will form between molecular crystals with multiple different sites. This work has also focused on solid solutions between structurally similar and volumetrically similar compounds as per Kitaigorodskii rules, but as other studies have identified some solid solutions form outside of these rules. Future work could look to build upon the knowledge gained in this thesis, and use 4D-STEM techniques to gain more insight into these more complex systems.

Chapter 9

References

Alexander, J.A., Scheltens, F.J., Drummy, L.F., Durstock, M.F., Gilchrist, J.B., Heutz, S. and McComb, D.W. 2016. Measurement of optical properties in organic photovoltaic materials using monochromated electron energy-loss spectroscopy. *Journal of Materials Chemistry A*. **4**(35), pp.13636–13645.

Altoe, V., Martin, F., Katan, A., Salmeron, M. and Aloni, S. 2012. Electron microscopy reveals structure and morphology of one molecule thin organic films. *Nano Letters*. **12**(3), pp.1295–1299.

Arand, K., Asmus, E., Popp, C., Schneider, D. and Riederer, M. 2018. The Mode of Action of Adjuvants - Relevance of Physicochemical Properties for Effects on the Foliar Application, Cuticular Permeability, and Greenhouse Performance of Pinoxaden. *Journal of Agricultural and Food Chemistry*. **66**(23), pp.5770–5777.

Ariga, Katsuhiko, Hill, Jonathan P, Ji, Qingmin, Ariga, K, Hill, J P and Ji, Q 2008. Biomaterials and Biofunctionality in Layered Macromolecular Assemblies. *Macromolecular Bioscience*. **8**(11), pp.981–990.

Asbach, G.I., Geiger, K. and Wilke, W. 1979. X-ray investigations of binary solid solutions of n-alkanes as modelsystems for extended chain crystals of polyethylene. *Colloid and Polymer Science Kolloid-Zeitschrift & Zeitschrift für Polymere*. **257**(10), pp.1049–1059.

Atkinson, C.M.L. and Richardson, M.J. 1969. Phase behaviour of n-alkanes and polyethylene. A thermodynamic study. *Transactions of the Faraday Society*. **65**(0), pp.1749–1763.

Baker, L.A. and Rubinstein, J.L. 2010. Radiation Damage in Electron Cryomicroscopy. *Methods in Enzymology*. **481**(C), pp.371–388.

Basson, I. and Reynhardt, E.C. 1992. The structure and melting of paraffinic Fischer-Tropsch waxes. *Chemical Physics Letters*. **198**(3–4), pp.367–372.

Batista, A.H., Melo, V.F. and Gilkes, R. 2017. Scanning and transmission analytical electron microscopy (STEM-EDX) identifies minor minerals and the location of minor elements in the clay fraction of soils. *Applied Clay Science*. **135**, pp.447–456.

Bauer, J., Spanton, S., Henry, R., Quick, J., Dziki, W., Porter, W. and Morris, J. 2001. Ritonavir: An extraordinary example of conformational polymorphism. *Pharmaceutical Research*. **18**(6), pp.859–866.

Bellamy, L.J. and Beecher, L. 1952. 315. The infra-red spectra of organo-phosphorus compounds. Part II. Esters, acids, and amines. *Journal of the Chemical Society (Resumed)*. (0), pp.1701–1706.

Bergh, T., Sandnes, L., Johnstone, D.N., Grong, Ø., Berto, F., Holmestad, R., Midgley, P.A. and Vullum, P.E. 2021. Microstructural and mechanical characterisation of a second generation hybrid metal extrusion & bonding aluminium-steel butt joint. *Materials Characterization*. **173**, p.110761.

Boese, R., Weiss, H.-C. and Bläser, D. 1999. The Melting Point Alternation in the

Short-Chain n-Alkanes: Single-Crystal X-Ray Analyses of Propane at 30 K and of n-Butane to n-Nonane at 90 K**. *Angew. Chem. Int. Ed*. **38**(7).

Boudouh, I., Djemai, I., González, J.A. and Barkat, D. 2016. Solid–liquid equilibria of biphenyl binary systems. *Journal of Molecular Liquids*. **216**, pp.764–770.

Braga, D., Casali, L. and Grepioni, F. 2022. The Relevance of Crystal Forms in the Pharmaceutical Field: Sword of Damocles or Innovation Tools? *International Journal of Molecular Sciences 2022, Vol. 23, Page 9013*. **23**(16), p.9013.

Bragg, W.H., Bragg Apr, W.L., H Bragg, B.W. and Professor of Physics, C. 1913. The reflection of X-rays by crystals. *Proceedings of the Royal Society of London. Series A, Containing Papers of a Mathematical and Physical Character*. **88**(605), pp.428–438.

Bronzato, M., Burriss, A., King, N., Donaldson, C., Sayer, D. and Baker, C.M. 2023. Measuring the photostability of agrochemicals on leaves: understanding the balance between loss processes and foliar uptake. *Pest Management Science*. **79**(9), pp.3114–3121.

Burghardt, M., Schreiber, L. and Riederer, M. 1998. Enhancement of the Diffusion of Active Ingredients in Barley Leaf Cuticular Wax by Monodisperse Alcohol Ethoxylates. *Journal of Agricultural and Food Chemistry*. **46**(4), pp.1593–1602.

Burnham, N.A., Dominguez, D.D., Mowery, R.L. and Colton, R.J. 1990. Probing the surface forces of monolayer films with an atomic-force microscope. *Physical Review Letters*. **64**(16), pp.1931–1934.

Burzlaff, H. and Zimmermann, H. 2016. Space-group symbols and their use *In*: *International Tables for Crystallography* [Online]. International Union of Crystallography, pp.777–791. [Accessed 7 September 2025]. Available from: http://xrpp.iucr.org/cgi-bin/itr?url_ver=Z39.88-2003&rft_dat=what%3Dchapter%26volid%3DAc%26chnumo%3D3o3%26chvers%3Dv0001.

Buschhaus, C. and Jetter, R. 2012. Composition and Physiological Function of the Wax Layers Coating Arabidopsis Leaves: β-Amyrin Negatively Affects the Intracuticular Water Barrier. *Plant Physiology*. **160**(2), pp.1120–1129.

Buschhaus, C. and Jetter, R. 2011. Composition differences between epicuticular and intracuticular wax substructures: How do plants seal their epidermal surfaces? *Journal of Experimental Botany*. **62**(3), pp.841–853.

Bustillo, K.C., Zeltmann, S.E., Chen, M., Donohue, J., Ciston, J., Ophus, C. and Minor, A.M. 2021. 4D-STEM of Beam-Sensitive Materials. *Accounts of Chemical Research*. **54**(11), pp.2543–2551.

Calderón Ortiz, G.A., Zhu, M., Wadsworth, A., Dou, L., McCulloch, I. and Hwang, J. 2024. Unveiling Nanoscale Ordering in Amorphous Semiconducting Polymers Using Four-Dimensional Scanning Transmission Electron Microscopy. *ACS Applied Materials and Interfaces*. **16**, p.55863.

Cappuccino, C., Spoletti, E., Renni, F., Muntoni, E., Keiser, J., Voinovich, D., Perissutti, B. and Lusi, M. 2023. Co-Crystalline Solid Solution Affords a High-Soluble and Fast-Absorbing Form of Praziquantel. *Molecular Pharmaceutics*. **20**(4), pp.2009–2016.

Chen, M., Bustillo, K.C., Patel, V., Savitzky, B.H., Sternlicht, H., Maslyn, J.A., Loo, W.S., Ciston, J., Ophus, C., Jiang, X., Balsara, N.P. and Minor, A.M. 2024. Direct Imaging of the Crystalline Domains and Their Orientation in the PS-b-PEO Block Copolymer with 4D-STEM. *Macromolecules*. **57**(12), pp.5629–5638.

Chen, Q., Dwyer, C., Sheng, G., Zhu, C., Li, X., Zheng, C. and Zhu, Y. 2020. Imaging Beam-Sensitive Materials by Electron Microscopy. *Advanced Materials*. **32**(16), p.1907619.

Chen, Z., Jiang, Y., Shao, Y.T., Holtz, M.E., Odstrčil, M., Guizar-Sicairos, M., Hanke, I., Ganschow, S., Schlom, D.G. and Muller, D.A. 2021. Electron ptychography achieves atomic-resolution limits set by lattice vibrations. *Science*. **372**(6544), pp.826–831.

Cheng, Y.Q. and Ma, E. 2011. Atomic-level structure and structure–property relationship in metallic glasses. *Progress in Materials Science*. **56**(4), pp.379–473.

Cherukuvada, S. and Nangia, A. 2013. Eutectics as improved pharmaceutical materials: design, properties and characterization. *Chemical Communications*. **50**(8), pp.906–923.

Chierotti, M.R., Ferrero, L., Garino, N., Gobetto, R., Pellegrino, L., Braga, D., Grepioni, F. and Maini, L. 2010. The Richest Collection of Tautomeric Polymorphs: The Case of 2-Thiobarbituric Acid. *Chemistry – A European Journal*. **16**(14), pp.4347–4358.

Choe, H., Ponomarev, I., Montgomery, E., Lau, J., Zhu, Y., Zhao, Y., Liu, A., Kanareykin, A. and Jing, C. 2020. Mitigation of radiation damage in biological macromolecules via tunable picosecond pulsed transmission electron microscopy. *bioRxiv*., 2020.05.15.099036.

Colby, R., Williams, R.E.A., Carpenter, D.L., Bagués, N., Ford, B.R. and McComb, D.W. 2023. Identifying and imaging polymer functionality at high spatial resolution with core-loss EELS. *Ultramicroscopy*. **246**, p.113688.

Colliex, C. 2022. From early to present and future achievements of EELS in the TEM. *The European Physical Journal Applied Physics*. **97**, p.38.

Cox, C. and Zeiss, M. 2022. Health, Pesticide Adjuvants, and Inert Ingredients: California Case Study Illustrates Need for Data Access. *Environmental Health Perspectives*. **130**(8), p.085001.

Craig, S.R., Hastie, G.P., Roberts, K.J. and Sherwood, J.N. 1994. Investigation into the structures of some normal alkanes within the homologous series C13H28 to C60H122 using high-resolution synchrotron X-ray powder diffraction. *Journal of Materials Chemistry*. **4**(6), pp.977–981.

Cruz-Cabeza, A.J., Lestari, M. and Lusi, M. 2018. Cocrystals Help Break the ‘rules’ of Isostructurality: Solid Solutions and Polymorphism in the Malic/Tartaric Acid System. *Crystal Growth and Design*. **18**(2), pp.855–863.

Cuevas-Diarte, M.A. and Oonk, H.A.J. (eds.). 2021. *Molecular Mixed Crystals* [Online]. Cham: Springer. [Accessed 28 July 2022]. Available from: https://link.springer.com/10.1007/978-3-030-68727-4.

Curie, P. 1885. Sur la formation des cristaux et sur les constantes capillaires de leurs

différentes faces. *Bulletin de Minéralogie*. **8**(6), pp.145–150.

Denny, M.S., Parent, L.R., Patterson, J.P., Meena, S.K., Pham, H., Abellan, P., Ramasse, Q.M., Paesani, F., Gianneschi, N.C. and Cohen, S.M. 2018. Transmission Electron Microscopy Reveals Deposition of Metal Oxide Coatings onto Metal-Organic Frameworks. *Journal of the American Chemical Society*. **140**(4), pp.1348–1357.

Dirand, M., Bouroukba, M., Chevallier, V., Petitjean, D., Behar, E. and Ruffier-Meray, V. 2002. Normal alkanes, multialkane synthetic model mixtures, and real petroleum waxes: Crystallographic structures, thermodynamic properties, and crystallization. *Journal of Chemical and Engineering Data*. **47**(2), pp.115–143.

Doherty, T.A.S., Winchester, A.J., Macpherson, S., Johnstone, D.N., Pareek, V., Tennyson, E.M., Kosar, S., Kosasih, F.U., Anaya, M., Abdi-Jalebi, M., Andaji-Garmaroudi, Z., Wong, E.L., Madéo, J., Chiang, Y.H., Park, J.S., Jung, Y.K., Petoukhoff, C.E., Divitini, G., Man, M.K.L., Ducati, C., Walsh, A., Midgley, P.A., Dani, K.M. and Stranks, S.D. 2020. Performance-limiting nanoscale trap clusters at grain junctions in halide perovskites. *Nature 2020 580:7803*. **580**(7803), pp.360–366.

Dombrowski, R.T. 2013. Microscopy techniques for analyzing the phase nature and morphology of biomaterials. *Characterization of Biomaterials*., pp.1–33.

Dorset, D.L. 2000a. Chain Length Distribution and the Lamellar Crystal Structure of a Paraffin Wax. *Journal of Physical Chemistry B*. **104**(35), pp.8346–8350.

Dorset, Douglas L. 1997a. Crystal structure of an n-paraffin binary eutectic solid. An electron diffraction determination. *Journal of Physical Chemistry B*. **101**(25), pp.4870–4874.

Dorset, D.L. 1985a. Crystal Structure of n-Paraffin Solid Solutions: An Electron Diffraction Study. *Macromolecules*. **18**, pp.2158–2163.

Dorset, D.L. 1985b. Crystal Structure of n-Paraffin Solid Solutions: An Electron Diffraction Study. *Macromolecules*. **18**, pp.2158–2163.

Dorset, Douglas L 1997. Crystallography of waxes - an electron diffraction study of refined and natural products. *Journal of Physics D: Applied Physics*. **30**(3), p.451.

Dorset, Douglas L. 1997b. Crystallography of waxes - An electron diffraction study of refined and natural products. *Journal of Physics D: Applied Physics*. **30**(3), pp.451–457.

Dorset, D.L. 1999. Development of lamellar structures in natural waxes - an electron diffraction investigation. *Journal of Physics D: Applied Physics*. **32**(11), pp.1276–1280.

Dorset, D.L. 1990. Direct structure analysis of a paraffin solid solution. *Proceedings of the National Academy of Sciences of the United States of America*. **87**(21), pp.8541–8544.

Dorset, D.L. 1986. Electron diffraction structure analysis of epitaxially crystallized n-paraffins. *Journal of Polymer Science Part B: Polymer Physics*. **24**(1), pp.79–87.

Dorset, D.L. 2002. From waxes to polymers - Crystallography of polydisperse chain assemblies. *Structural Chemistry*. **13**(3–4), pp.329–337.

Dorset, D.L. 2000b. 'Nematocrystalline' chain packing: Three-dimensional structure of

low molecular weight linear polyethylene. *Journal of Physical Chemistry B*. **104**(45), pp.10543–10548.

Dorset, D.L. 1979. Orthorhombic n-octadecanol: An electron diffraction study. *Chemistry and Physics of Lipids*. **23**(4), pp.337–347.

Dorset, D.L. 1987. Role of Symmetry in the Formation of n-Paraffin Solid Solutions. *Macromolecules*. **20**(11), pp.2782–2788.

Dorset, D.L. 1995a. The crystal structure of waxes. *Acta Crystallographica Section B*. **51**(6), pp.1021–1028.

Dorset, D.L. 1995b. The crystal structure of waxes. *Acta Crystallographica Section B*. **51**(6), pp.1021–1028.

Dorset, D.L. and Annis, B.K. 1996. Lamellar order and the crystallization of linear chain solid solutions. *Macromolecules*. **29**(8), pp.2969–2973.

Dorset, D.L. and Hauptman, H.A. 1976. Direct phase determination for quasi-kinematical electron diffraction intensity data from organic microcrystals. *Ultramicroscopy*. **1**(3–4), pp.195–201.

Dorset, D.L. and Moss, B. 1983. Crystal structure analysis of polyethylene with electron diffraction intensity data: Deconvolution of multiple scattering effects. *Polymer*. **24**(3), pp.291–294.

Dorset, D.L., Moss, B., Wittmann, J.C. and Lotz, B. 1984. The pre-melt phase of n-alkanes: Crystallographic evidence for a kinked chain structure. *Proceedings of the National Academy of Sciences of the United States of America*. **81**(6), p.1913.

Dorset, D.L. and Snyder, R.G. 1999. Phase separation of a metastable three-component n-paraffin solid solution. *Journal of Physical Chemistry B*. **103**(16), pp.3282–3286.

Eddleston, M.D., Bithell, E.G. and Jones, W. 2010. Transmission Electron Microscopy of Pharmaceutical Materials. *Journal of Pharmaceutical Sciences*. **99**(9), pp.4072–4083.

Egerton, R.F. 2011. An Introduction to EELS. *Electron Energy-Loss Spectroscopy in the Electron Microscope*., pp.1–28.

Egerton, R.F. 1980. Chemical measurements of radiation damage in organic samples at and below room temperature. *Ultramicroscopy*. **5**(4), pp.521–523.

Egerton, R.F. 2014. Choice of operating voltage for a transmission electron microscope. *Ultramicroscopy*. **145**, pp.85–93.

Egerton, R.F. 2013. Control of radiation damage in the TEM. *Ultramicroscopy*. **127**, pp.100–108.

Egerton, R.F. 2012. Mechanisms of radiation damage in beam-sensitive specimens, for TEM accelerating voltages between 10 and 300 kV. *Microscopy Research and Technique*. **75**(11), pp.1550–1556.

Egerton, R.F. 2019. Radiation damage to organic and inorganic specimens in the TEM. *Micron*. **119**, pp.72–87.

Egerton, R.F., Li, P. and Malac, M. 2004. Radiation damage in the TEM and SEM. *Micron*. **35**(6), pp.399–409.

Egerton, R.F. and Rauf, I. 1999. Dose-rate dependence of electron-induced mass loss from organic specimens. *Ultramicroscopy*. **80**(4), pp.247–254.

Egerton, R.F. and Watanabe, M. 2022. Spatial resolution in transmission electron microscopy. *Micron*. **160**.

Eggeman, A.S., Illig, S., Troisi, A., Sirringhaus, H. and Midgley, P.A. 2013. Measurement of molecular motion in organic semiconductors by thermal diffuse electron scattering. *Nature Materials*. **12**(11), pp.1045–1049.

Eibl, O. 1993. New method for absorption correction in high-accuracy, quantitative EDX microanalysis in the TEM including low-energy x-ray lines. *Ultramicroscopy*. **50**(2), pp.179–188.

Elliott, R. 2024. *Impact of Particle Surface Properties and Molecular Dynamics on Powder Caking, Flow and Formulation Performance*. University of Leeds.

Ensikat, H.J., Boese, M., Mader, W., Barthlott, W. and Koch, K. 2006. Crystallinity of plant epicuticular waxes: electron and X-ray diffraction studies. *Chemistry and Physics of Lipids*. **144**(1), pp.45–59.

Eskelsen, J.R., Qi, Y., Schneider-Pollack, S., Schmitt, S., Hipps, K.W. and Mazur, U. 2013. Correlating elastic properties and molecular organization of an ionic organic nanostructure. *Nanoscale*. **6**(1), pp.316–327.

Esparza, R., García-Ruiz, A.F., Velázquez Salazar, J.J., Pérez, R. and José-Yacamán, M. 2013. Structural characterization of Pt-Pd core-shell nanoparticles by Cs-corrected STEM. *Journal of Nanoparticle Research*. **15**(1), pp.1–9.

Ewald, P.P. 1969. Introduction to the dynamical theory of X-ray diffraction. *Acta Crystallographica Section A*. **25**(1), pp.103–108.

Fagerström, A., Kocherbitov, V., Westbye, P., Bergström, K., Arnebrant, T. and Engblom, J. 2014. Surfactant softening of plant leaf cuticle model wax – A Differential Scanning Calorimetry (DSC) and Quartz Crystal Microbalance with Dissipation (QCM-D) study. *Journal of Colloid and Interface Science*. **426**, pp.22–30.

Fagerström, A., Kocherbitov, V., Westbye, P., Bergström, K., Mamontova, V. and Engblom, J. 2013. Characterization of a plant leaf cuticle model wax, phase behaviour of model wax–water systems. *Thermochimica Acta*. **571**, pp.42–52.

Forwood, C.T. and Clarebrough, L.M. 2021. *Electron Microscopy of Interfaces in Metals and Alloys* [Online]. CRC Press. [Accessed 2 April 2025]. Available from: https://www.taylorfrancis.com/books/mono/10.1201/9780203758656/electron-microscopy-interfaces-metals-alloys-clarebrough.

Freund, M. and Mózes, G. 1982. Applications of paraffin waxes and liquid paraffins. *Developments in Petroleum Science*. **14**(C), pp.240–329.

Fryer, J.R., Mcconnell, C.H., Dorset, D.L., Zemlin, F. and Zeitler, E. 1997. High resolution electron microscopy of molecular crystals. IV. Paraffins and their solid solutions. *Proceedings of the Royal Society A: Mathematical, Physical and Engineering Sciences*. **453**(1964), pp.1929–1946.

Gaisford, S., Kett, V. and Haines, P. (eds.). 2016. *Principles of Thermal Analysis and Calorimetry* 2nd ed. Royal Society of Chemistry.

Giba, I.S., Mulloyarova, V. V., Denisov, G.S. and Tolstoy, P.M. 2019. Influence of

Hydrogen Bonds in 1:1 Complexes of Phosphinic Acids with Substituted Pyridines on 1 H and 31 P NMR Chemical Shifts. *Journal of Physical Chemistry A*. **123**(11), pp.2252–2260.

Gil Archila, E. and Cuca Suárez, L.E. 2018. Phytochemical study of leaves of Ocotea caudata from Colombia. *Natural Product Research*. **32**(2), pp.195–201.

Gill, P., Moghadam, T.T. and Ranjbar, B. 2010. Differential Scanning Calorimetry Techniques: Applications in Biology and Nanoscience. *Journal of Biomolecular Techniques : JBT*. **21**(4), p.167.

Gilman, J.J., Johnston, W.G. and Sears, G.W. 1958. Dislocation Etch Pit Formation in Lithium Fluoride. *Journal of Applied Physics*. **29**(5), pp.747–754.

Glaeser, R.M. 1971. Limitations to significant information in biological electron microscopy as a result of radiation damage. *Journal of Ultrasructure Research*. **36**(3–4), pp.466–482.

Grubb, D.T. 1974. Radiation damage and electron microscopy of organic polymers. *Journal of Materials Science*. **9**(10), pp.1715–1736.

Guo, W., Xing, Y., Wen, W., Su, W., Hou, C., Li, G. and Ye, L. 2024. Thermodynamic Analysis of n-Nonadecane (C19H40)/1-Octadecanol (C18H37OH) Blends. *Molecules*. **29**(12), p.2722.

Haneef, H.F., Zeidell, A.M. and Jurchescu, O.D. 2020. Charge carrier traps in organic semiconductors: a review on the underlying physics and impact on electronic devices. *Journal of Materials Chemistry C*. **8**(3), pp.759–787.

Hazen, J. 2000. Adjuvants — Terminology, Classification, and Chemistry. *Weed Technology*. **14**(4), pp.773–784.

He, X., Kostin, R., Knight, E., Han, M.G., Mun, J., Bozovic, I., Jing, C. and Zhu, Y. 2024. Development of a liquid-helium free cryogenic sample holder with mK temperature control for autonomous electron microscopy. *Ultramicroscopy*. **267**, p.114037.

Helmholtz and Fripp, H. 1876. On the Limits of the Optical Capacity of the Microscope. *The Monthly Microscopical Journal*. **16**(1), pp.15–39.

Henderson, R. and Glaeser, R.M. 1985. Quantitative analysis of image contrast in electron micrographs of beam-sensitive crystals. *Ultramicroscopy*. **16**(2), pp.139–150.

Hetherington, C. 2004. Aberration correction for TEM. *Materials Today*. **7**(12), pp.50–55.

Hill, A., Kras, W., Theodosiou, F., Wanat, M., Lee, D. and Cruz-Cabeza, A.J. 2023. Polymorphic Solid Solutions in Molecular Crystals: Tips, Tricks, and Switches. *Journal of the American Chemical Society*. **145**(37), pp.20562–20577.

Hodoroaba, V.D. 2019. Energy-dispersive X-ray spectroscopy (EDS) *In*: *Characterization of Nanoparticles: Measurement Processes for Nanoparticles*. Elsevier, pp.397–417.

Holder, C.F. and Schaak, R.E. 2019. Tutorial on Powder X-ray Diffraction for Characterizing Nanoscale Materials. *ACS Nano*. **13**(7), pp.7359–7365.

Hooley, R.W.M., Brown, A.P., Kulak, A.N., Meldrum, F.C. and Brydson, R.M.D. 2017.

A Quantitative Evaluation of Electron Beam Sensitivity in Calcite Nanoparticles *In*: *Journal of Physics: Conference Series* [Online]. Institute of Physics Publishing, p.012005. [Accessed 5 July 2021]. Available from: https://iopscience.iop.org/article/10.1088/1742-6596/902/1/012005.

Hu, X., Gong, H., Li, Z., Ruane, S., Liu, H., Hollowell, P., Pambou, E., Bawn, C., King, S., Rogers, S., Ma, K., Li, P., Padia, F., Bell, G. and Ren Lu, J. 2019. How does solubilisation of plant waxes into nonionic surfactant micelles affect pesticide release? *Journal of Colloid and Interface Science*. **556**, pp.650–657.

Isaacson, M. 1979. Electron beam induced damage of organic solids: Implications for analytical electron microscopy. *Ultramicroscopy*. **4**(2), pp.193–199.

Jacobson-Kram, D. and McGovern, T. 2007. Toxicological overview of impurities in pharmaceutical products. *Advanced Drug Delivery Reviews*. **59**(1), pp.38–42.

Janku, J.. C.Z.U.. P.. K.A. a B., Bartovska, L.. V.S.C.P.. U.F.C., Soukup, J.. C.Z.U.. P.. K.A. a B., Jursik, M.. C.Z.U.. P.. K.A. a B. and Hamouzova, K.. C.Z.U.. P.. K.A. a B. 2012. Density and surface tension of aqueous solutions of adjuvants used for tank-mixes with pesticides. *Plant, Soil and Environment (Czech Republic)*. **58**(12).

Jenks, M.A., Hasegawa, P.M. and Jain, S.M. 2007. *Advances in molecular breeding toward drought and salt tolerant crops* (M. A. Jenks, P. M. Hasegawa, & S. M. Jain, eds.). Heidelbergy, Germany: Springer Netherlands.

Jesson, D.E. and Pennycook, S.J. 1995. Incoherent imaging of crystals using thermally scattered electrons. *Proceedings of the Royal Society of London. Series A: Mathematical and Physical Sciences*. **449**(1936), pp.273–293.

Jetter, R. and Riederer, M. 2016. Localization of the Transpiration Barrier in the Epi- and Intracuticular Waxes of Eight Plant Species: Water Transport Resistances Are Associated with Fatty Acyl Rather Than Alicyclic Components. *Plant Physiology*. **170**(2), pp.921–934.

Jiang, N. 2015. Electron beam damage in oxides: A review. *Reports on Progress in Physics*. **79**(1), p.016501.

Jiang, N. and Spence, J.C.H. 2012. On the dose-rate threshold of beam damage in TEM. *Ultramicroscopy*. **113**, pp.77–82.

Johnstone, D.N., Allen, C.S., Danaie, M., Copley, R.C.B., Brum, J., Kirkland, A.I. and Midgley, P.A. 2019. Low-Dose Scanning Electron Diffraction Microscopy of Mechanochemically Nanostructured Pharmaceuticals. *Microscopy and Microanalysis*. **25**(S2), pp.1746–1747.

Johnstone, Duncan N., Crout, P., Laulainen, J., Høgås, S., Martineau, B., Bergh, T., Smeets, S., Francis, C., Opheim, E., Prestat, E., Collins, S., Danaie, M., Furnival, T., Ånes, H.W., Morzy, J., Iqbal, A., Doherty, T., Lany, M. von, Ostasevicius, T., Tovey, R., Jacobsen, E. and Poon, T. 2020. pyxem/pyxem: pyxem 0.11.0.

Johnstone, Duncan N, Firth, F.C.N., Grey, C.P., Midgley, P.A., Cliffe, M.J., Collins, S.M. and Johnstone, D.N. 2020. Direct Imaging of Correlated Defect Nanodomains in a Metal-Organic Framework. *Journal of the American Chemical Society*. **142**(30), pp.13081–13089.

Johnstone, D.N. and Midgley, P.A. 2017. The Microstructure of Pharmaceutical

Materials Revealed by Scanning Electron Diffraction. *Microscopy and Microanalysis*. **23**(S1), pp.1192–1193.

Jones, W., Thomas, J.M. and Williams, J.O. 1975. Electron and optical microscopic studies of a stress-induced phase transition in l,8-dichloro-10-methylanthracene. *Philosophical Magazine*. **32**(1), pp.1–11.

Kanomi, S., Marubayashi, H., Miyata, T. and Jinnai, H. 2023. Reassessing chain tilt in the lamellar crystals of polyethylene. *Nature Communications*. **14**(1), pp.1–9.

Kanomi, S., Marubayashi, H., Miyata, T., Tsuda, K. and Jinnai, H. 2021. Nanodiffraction Imaging of Polymer Crystals. *Macromolecules*. **54**(13), pp.6028–6037.

Keith, R.E. and Gilman, J.J. 1960. Dislocation etch pits and plastic deformation in calcite. *Acta Metallurgica*. **8**(1), pp.1–10.

Keller, A. 1957. A note on single crystals in polymers: Evidence for a folded chain configuration. *Philosophical Magazine*. **2**(21), pp.1171–1175.

Kidwai, M., Thakur, R. and Mohan, R. 2005. Ecofriendly synthesis of novel antifungal (thio) barbituric acid derivatives. *Acta Chimica Slovenica*. **52**(1), pp.88–92.

Kim, H.K., Ha, H.Y., Bae, J.H., Cho, M.K., Kim, J., Han, J., Suh, J.Y., Kim, G.H., Lee, T.H., Jang, J.H. and Chun, D. 2020. Nanoscale light element identification using machine learning aided STEM-EDS. *Scientific Reports 2020 10:1*. **10**(1), pp.1–12.

Kinoshita, M., Yamaguchi, S. and Matsumori, N. 2020. Low-flux scanning electron diffraction reveals substructures inside the ordered membrane domain. *Scientific Reports*. **10**(1), pp.1–11.

Kirkwood, R.C. 1993. Use and mode of action of adjuvants for herbicides: A review of some current work. *Pesticide Science*. **38**(2–3), pp.93–102.

Kitaigorodskii, A.I. 1961. *Organic chemical crystallography.* New York: Consultants Bureau.

Kitaigorodsky, A.I. 1984. Mixed Crystals.

Klang, V., Valenta, C. and Matsko, N.B. 2013. Electron microscopy of pharmaceutical systems. *Micron*. **44**(1), pp.45–74.

Kolb, U., Gorelik, T.E., Mugnaioli, E. and Stewart, A. 2010. Structural Characterization of Organics Using Manual and Automated Electron Diffraction. *Polymer Reviews*. **50**(3), pp.385–409.

Koniuch, N., Ilett, M., Collins, S.M., Hondow, N., Brown, A., Hughes, L. and Blade, H. 2023. Structure of polymeric nanoparticles encapsulating a drug – pamoic acid ion pair by scanning transmission electron microscopy. *Heliyon*. **9**(6).

Kras, W., Carletta, A., Montis, R., Sullivan, R.A. and Cruz-Cabeza, A.J. 2021. Switching polymorph stabilities with impurities provides a thermodynamic route to benzamide form III. *Communications Chemistry 2021 4:1*. **4**(1), pp.1–7.

Kunz, M. 2023. *Diffusion kinetics of organic compounds and water in plant cuticular model wax under the influence of diffusing barrier-modifying adjuvants*.[Online] Universität Würzburg. [Accessed 14 March 2025]. Available from: https://opus.bibliothek.uni-wuerzburg.de/frontdoor/index/index/docId/27487.

Kunz, M., Staiger, S., Burghardt, M., Popp, C., George, N., Roberts, K. and Riederer, M. 2022. Diffusion Kinetics of Active Ingredients and Adjuvants in Wax Films: An Attenuated Total Reflection-Infrared Spectroscopy Study of a Leaf Surface Model. *ACS Agricultural Science and Technology*. **2**(3), pp.625–638.

Leung, Helen W., Copley, R.C.B., Lampronti, G.I., Day, S.J., Saunders, L.K., Johnstone, D.N. and Midgley, P.A. 2025. Revealing the Crystal Structure of the Purine Base Xanthine with Three-Dimensional (3D) Electron Diffraction. *Crystal Growth and Design*. **25**, pp.1293–1298.

Leung, Helen W, Copley, R.C.B., Lampronti, Giulio I, Day, Sarah J, Saunders, Lucy K, Johnstone, D.N., Midgley, Paul A, Leung, M.H.W., Lampronti, G I, Midgley, P A, Day, S J and Saunders, L K 2025. Polytypes and Planar Defects Revealed in the Purine Base Xanthine using Multi-Dimensional Electron Diffraction.

Lewis, T.C., Tocher, D.A. and Price, S.L. 2004. An experimental and theoretical search for polymorphs of barbituric acid: The challenges of even limited conformational flexibility. *Crystal Growth and Design*. **4**(5), pp.979–981.

Leyva-Gutierrez, F.M.A. and Wang, T. 2021. Crystallinity and Water Vapor Permeability of n-Alkane, Alcohol, Aldehyde, and Fatty Acid Constituents of Natural Waxes. *Industrial and Engineering Chemistry Research*. **60**(41), pp.14651–14663.

Li, J. and Sun, J. 2017. Application of X-ray Diffraction and Electron Crystallography for Solving Complex Structure Problems. *Accounts of Chemical Research*. **50**(11), pp.2737–2745.

Li, P. and Egerton, R.F. 2004. Radiation damage in coronene, rubrene and p-terphenyl, measured for incident electrons of kinetic energy between 100 and 200 kev. *Ultramicroscopy*. **101**(2–4), pp.161–172.

Li, R., Zhang, X., Dong, H., Li, Q., Shuai, Z. and Hu, W. 2016. Gibbs–Curie–Wulff Theorem in Organic Materials: A Case Study on the Relationship between Surface Energy and Crystal Growth. *Advanced Materials*. **28**(8), pp.1697–1702.

Li, X., Huang, W., Krajnc, A., Yang, Y., Shukla, A., Lee, J., Ghasemi, M., Martens, I., Chan, B., Appadoo, D., Chen, P., Wen, X., Steele, J.A., Hackbarth, H.G., Sun, Q., Mali, G., Lin, R., Bedford, N.M., Chen, V., Cheetham, A.K., Tizei, L.H.G., Collins, S.M., Wang, L. and Hou, J. 2023. Interfacial alloying between lead halide perovskite crystals and hybrid glasses. *Nature Communications 2023 14:1*. **14**(1), pp.1–12.

Li, Z.G., Harlow, R.L., Foris, C.M., Li, H., Ma, P., Vickery, R.D. and Maurin, M.B. 1999. New Applications of Electron Diffraction in Pharmaceutical Industry: Polymorph Determination of GP Ilb/IIIa Antagonist, Roxifiban, Using a Combination of Electron Diffraction and Synchrotron X-ray Powder Diffraction Techniques. *Microscopy and Microanalysis*. **5**(S2), pp.214–215.

Liu, C., Zheng, Z., Xi, C. and Liu, Y. 2021. Exploration of the natural waxes-tuned crystallization behavior, droplet shape and rheology properties of O/W emulsions. *Journal of Colloid and Interface Science*. **587**, pp.417–428.

Liu, H., Xu, J., Li, Yongjun and Li, Yuliang 2010. Aggregate nanostructures of organic molecular materials. *Accounts of Chemical Research*. **43**(12), pp.1496–1508.

Liu, Y., Yang, Z., Du, J., Yao, X., Zheng, X., Lei, R., Liu, J., Hu, H. and Li, H. 2008.

Interaction of Taxol with intravenous immunoglobulin: An inhibition of Taxol from crystallizing in aqueous solution. *International Immunopharmacology*. **8**(3), pp.390–400.

López-Muñoz, F., Ucha-Udabe, R. and Alamo, C. 2005. The history of barbiturates a century after their clinical introduction. *Neuropsychiatric Disease and Treatment*. **1**(4), p.329.

Lueth, H., Nyburg, S.C., Robinson, P.M. and Scott, H.G. 1974. CRYSTALLOGRAPHIC AND CALORIMETRIC PHASE STUDIES OF THE n-EICOSANE, C20H42: n-DOCOSANE, C22H46 SYSTEM. *Mol Cryst Liq Cryst*. **27**(3–4), pp.337–357.

Lukin, S., Tireli, M., Lončarić, I., Barišić, D., Šket, P., Vrsaljko, D., Di Michiel, M., Plavec, J., Užarević, K. and Halasz, I. 2018. Mechanochemical carbon–carbon bond formation that proceeds via a cocrystal intermediate. *Chemical Communications*. **54**(94), pp.13216–13219.

Lusi, M. 2018a. A rough guide to molecular solid solutions: design, synthesis and characterization of mixed crystals. *CrystEngComm*. **20**(44), pp.7042–7052.

Lusi, M. 2018b. A rough guide to molecular solid solutions: design, synthesis and characterization of mixed crystals. *CrystEngComm*. **20**(44), pp.7042–7052.

Lusi, M. 2018c. Engineering Crystal Properties through Solid Solutions. *Crystal Growth and Design*. **18**(6), pp.3704–3712.

Lusi, M., Vitorica-Yrezabal, I.J. and Zaworotko, M.J. 2015. Expanding the Scope of Molecular Mixed Crystals Enabled by Three Component Solid Solutions. *Crystal Growth and Design*. **15**(8), pp.4098–4103.

MacArthur, K.E., Slater, T.J.A., Haigh, S.J., Ozkaya, D., Nellist, P.D. and Lozano-Perez, S. 2016. Quantitative Energy-Dispersive X-Ray Analysis of Catalyst Nanoparticles Using a Partial Cross Section Approach. *Microscopy and Microanalysis*. **22**(1), pp.71–81.

Maekawa, M. and Kawamoto, T. 2002. Intact Sectioning of Plant Tissues with a Cryomicrotome. *Breeding Science*. **52**(1), pp.57–60.

Maiza, M., Benaniba, M.T., Quintard, G. and Massardier-Nageotte, V. 2015. Biobased additive plasticizing Polylactic acid (PLA). *Polímeros*. **25**(6), pp.581–590.

Malkin, T. 1952. The molecular structure and polymorphism of fatty acids and their derivatives. *Progress in the Chemistry of Fats and Other Lipids*. **1**(C), pp.1–17.

Marklund, A., Andersson, B. and Haglund, P. 2005. Organophosphorus flame retardants and plasticizers in Swedish sewage treatment plants. *Environmental Science and Technology*. **39**(19), pp.7423–7429.

Masoud, M.S., Abd El-Kaway, M.Y., Hindawy, A.M. and Soayed, A.A. 2012. Chemical speciation and equilibria of some nucleic acid compounds and their iron(III) complexes. *Spectrochimica Acta Part A: Molecular and Biomolecular Spectroscopy*. **92**, pp.256–282.

Mayoral, A., Anderson, P.A. and Diaz, I. 2015. Zeolites are no longer a challenge: Atomic resolution data by Aberration-corrected STEM. *Micron*. **68**, pp.146–151.

Meyer, J.C., Eder, F., Kurasch, S., Skakalova, V., Kotakoski, J., Park, H.J., Roth, S., Chuvilin, A., Eyhusen, S., Benner, G., Krasheninnikov, A. V. and Kaiser, U. 2012.

Accurate measurement of electron beam induced displacement cross sections for single-layer graphene. *Physical Review Letters*. **108**(19), p.196102.

Meyer, J.C., Girit, C.O., Crommie, M.F. and Zettl, A. 2008. Imaging and dynamics of light atoms and molecules on graphene. *Nature*. **454**(7202), pp.319–322.

Michaud, F., Ventolà, L., Calvet, M.T., Cuevas-Diarte, M.A., Solans, X. and Font-Bardéa, M. 2000. The γ-form of n-eicosanol. *Acta Crystallographica Section C: Crystal Structure Communications*. **56**(2), pp.219–221.

Mnyukh, Y. V. 1960. The structure of normal paraffins and of their solid solutions. *Journal of Structural Chemistry*. **1**(3), pp.346–365.

Mohan, R., Lorenz, H. and Myerson, A.S. 2002. Solubility measurement using differential scanning calorimetry. *Industrial and Engineering Chemistry Research*. **41**(19), pp.4854–4862.

Monnerie, L. 1999. Polymer materials *In*: M. Daoud and C. E. Williams, eds. *Polymer Materials* [Online]. Berlin, Heidelberg: Springer, Berlin, Heidelberg, pp.219–260. [Accessed 15 April 2025]. Available from: https://link.springer.com/chapter/10.1007/978-3-662-03845-1_7.

Nairn, J.J. and Forster, W.A. 2024. Importance of leaf surface and formulation properties in predicting wetting outcomes. *Pest Management Science*. **80**(2), pp.202–211.

Natusch, M.K.H., Humphreys, C.J., Menon, N. and Krivanek, O.L. 1999. Experimental and theoretical study of the detection limits in electron energy-loss spectroscopy. *Micron*. **30**(2), pp.173–183.

Nellist, P.D. and Pennycook, S.J. 1996. Direct Imaging of the Atomic Configuration of Ultradispersed Catalysts. *Science*. **274**(5286), pp.413–415.

Newbury, D.E. and Ritchie, N.W.M. 2013. Is Scanning Electron Microscopy/Energy Dispersive X-ray Spectrometry (SEM/EDS) Quantitative? *Scanning*. **35**(3), pp.141–168.

Nong, A., Schleper, C., Martin, A., Paolello, M., Nordstrom, F.L. and Capellades, G. 2024. Impurity retention and pharmaceutical solid solutions: visualizing the effect of impurities on dissolution and growth using dyed crystals. *CrystEngComm*. **26**(38), pp.5337–5350.

Nyburg, S.C. and Potworowski, J.A. 1973. Prediction of unit cells and atomic coordinates for the n -alkanes. *Acta Crystallographica Section B Structural Crystallography and Crystal Chemistry*. **29**(2), pp.347–352.

Olson, I.A., Shtukenberg, A.G., Kahr, B. and Ward, M.D. 2018. Dislocations in molecular crystals. *Reports on Progress in Physics*. **81**(9), p.096501.

Ophus, C. 2019. Four-Dimensional Scanning Transmission Electron Microscopy (4D-STEM): From Scanning Nanodiffraction to Ptychography and Beyond. *Microscopy and Microanalysis*. **25**(3), pp.563–582.

Van Oss, C.J., Good, R.J. and Chaudhury, M.K. 1986. The role of van der Waals forces and hydrogen bonds in “hydrophobic interactions” between biopolymers and low energy surfaces. *Journal of Colloid and Interface Science*. **111**(2), pp.378–390.

Pal, R., Bourgeois, L., Weyland, M., Sikder, A.K., Saito, K., Funston, A.M. and Bellare,

J.R. 2021. Chemical Fingerprinting of Polymers Using Electron Energy-Loss Spectroscopy. *ACS Omega*. **6**(37), pp.23934–23942.

Pan, Y.H., Sader, K., Powell, J.J., Bleloch, A., Gass, M., Trinick, J., Warley, A., Li, A., Brydson, R. and Brown, A. 2009. 3D morphology of the human hepatic ferritin mineral core: New evidence for a subunit structure revealed by single particle analysis of HAADF-STEM images. *Journal of Structural Biology*. **166**(1), pp.22–31.

Panova, O., Ophus, C., Takacs, C.J., Bustillo, K.C., Balhorn, L., Salleo, A., Balsara, N. and Minor, A.M. 2019. Diffraction imaging of nanocrystalline structures in organic semiconductor molecular thin films. *Nature Materials*. **18**(8), pp.860–865.

Paolello, M., Mohajerani, S.S., Linehan, B., Ricci, F., Capellades, G. and Nordstrom, F.L. 2024. Polymorphic Stability Shifts, Co-Crystals, and Crystalline Solid Solutions: The T-X Phase Diagram of Salicylic Acid-Salicylamide. *Crystal Growth and Design*. **24**(5), pp.2188–2201.

Papworth, A.J., Kiely, C.J., Burden, A.P., Silva, S.R.P. and Amaratunga, G.A.J. 2000. Electron-energy-loss spectroscopy characterization of the sp2 bonding fraction within carbon thin films. *Physical Review B - Condensed Matter and Materials Physics*. **62**(19), pp.12628–12631.

Peng, L.M. 1999. Electron atomic scattering factors and scattering potentials of crystals. *Micron*. **30**(6), pp.625–648.

Pennycook, S.J. and Jesson, D.E. 1991. High-resolution Z-contrast imaging of crystals. *Ultramicroscopy*. **37**(1–4), pp.14–38.

Pham, S.T., Koniuch, N., Wynne, E., Brown, A. and Collins, S.M. 2025. Microscopic crystallographic analysis of dislocations in molecular crystals. *Nature Materials 2025*., pp.1–6.

Qiao, N., Li, M., Schlindwein, W., Malek, N., Davies, A. and Trappitt, G. 2011. Pharmaceutical cocrystals: An overview. *International Journal of Pharmaceutics*. **419**(1–2), pp.1–11.

Qu, H., Louhi-Kultanen, M. and Kallas, J. 2006. Solubility and stability of anhydrate/hydrate in solvent mixtures. *International Journal of Pharmaceutics*. **321**(1–2), pp.101–107.

Rades, T. and Müller-Goymann, C.C. 1997. Electron and light microscopical investigation of defect structures in mesophases of pharmaceutical substances. *Colloid and Polymer Science*. **275**(12), pp.1169–1178.

Ray, S., Savoie, B.M., Dudareva, N. and Morgan, J.A. 2022. Diffusion of volatile organics and water in the epicuticular waxes of petunia petal epidermal cells. *The Plant Journal*. **110**(3), pp.658–672.

Ricarte, R.G., Lodge, T.P. and Hillmyer, M.A. 2015. Detection of pharmaceutical drug crystallites in solid dispersions by transmission electron microscopy. *Molecular Pharmaceutics*. **12**(3), pp.983–990.

Ricarte, R.G., Lodge, T.P. and Hillmyer, M.A. 2016. Nanoscale Concentration Quantification of Pharmaceutical Actives in Amorphous Polymer Matrices by Electron Energy-Loss Spectroscopy. *Langmuir*. **32**(29), pp.7411–7419.

Ricarte, R.G., Van Zee, N.J., Li, Z., Johnson, L.M., Lodge, T.P. and Hillmyer, M.A.

2019. Recent Advances in Understanding the Micro- and Nanoscale Phenomena of Amorphous Solid Dispersions. *Molecular Pharmaceutics*. **16**(10), pp.4089–4103.

Riederer, M. 2007. *Annual Plant Reviews, Volume 23, Biology of the Plant Cuticle | Wiley* [Online] (C. Muller, ed.). [Accessed 15 March 2021]. Available from: https://www.wiley.com/en-us/Annual+Plant+Reviews%2C+Volume+23%2C+Biology+of+the+Plant+Cuticle-p-9780470988718.

Riederer, M. and Müller, C. 2007. *Annual Plant Reviews*. Wiley Blackwell.

Riederer, M. and Schreiber, L. 2001. Protecting against water loss: Analysis of the barrier properties of plant cuticles *In*: *Journal of Experimental Botany* [Online]. Oxford University Press, pp.2023–2032. [Accessed 15 March 2021]. Available from: https://pubmed.ncbi.nlm.nih.gov/11559738/.

Riederer, M. and Schreiber, L. 1995. Waxes: The transport barriers of plant cuticles *In*: *Waxes: Chemistry, molecular biology and functions* [Online]. Oily Press, pp.131–156. [Accessed 9 August 2023]. Available from: https://cir.nii.ac.jp/crid/1571980075659137152.bib?lang=en.

Roux, J.H. le 1969. Fischer-tropsch waxes. II. Crystallinity and physical properties. *Journal of Applied Chemistry*. **19**(3), pp.86–88.

S'Ari, M., Blade, H., Brydson, R., Cosgrove, S.D., Hondow, N., Hughes, L.P. and Brown, A. 2018. Toward Developing a Predictive Approach to Assess Electron Beam Instability during Transmission Electron Microscopy of Drug Molecules. *Molecular Pharmaceutics*. **15**(11), pp.5114–5123.

S'Ari, M., Blade, H., Cosgrove, S., Drummond-Brydson, R., Hondow, N., Hughes, L.P. and Brown, A. 2021. Characterization of Amorphous Solid Dispersions and Identification of Low Levels of Crystallinity by Transmission Electron Microscopy. *Molecular Pharmaceutics*. **18**(5), pp.1905–1919.

S'ari, M., Cattle, J., Hondow, N., Brydson, R. and Brown, A. 2019. Low dose scanning transmission electron microscopy of organic crystals by scanning moiré fringes. *Micron*. **120**, pp.1–9.

Saleki-Gerhardt, A., Ahlneck, C. and Zografi, G. 1994. Assessment of disorder in crystalline solids. *International Journal of Pharmaceutics*. **101**(3), pp.237–247.

Schmidt, M.U., Brüning, J., Glinnemann, J., Hützler, M.W., Mörschel, P., Ivashevskaya, S.N., Van De Streek, J., Braga, D., Maini, L., Chierotti, M.R. and Gobetto, R. 2011. The Thermodynamically Stable Form of Solid Barbituric Acid: The Enol Tautomer. *Angewandte Chemie International Edition*. **50**(34), pp.7924–7926.

Schönherr, J. 1976. Water permeability of isolated cuticular membranes: The effect of cuticular waxes on diffusion of water. *Planta*. **131**(2), pp.159–164.

Schonherr, J. and Riederer, M. 1989. Foliar Penetration and Accumulation of Organic Chemicals in Plant Cuticles. *Reviews of Environmental Contamination and Toxicology*. **108**, pp.1–70.

Schreiber, L., Riederep, M., Schord, K., Riederer, M. and Schorn, K. 1996. Mobilities of Organic Compounds in Reconstituted Cuticular Wax of Barley Leaves : Effects

of Monodisperse Alcohol Ethoxylates on Diffusion of Pentachlorophenol and Tetracosanoic Acid. *Pestic. Sci*. **48**, pp.117–124.

Schur, E., Nauha, E., Lusi, M. and Bernstein, J. 2015. Kitaigorodsky Revisited: Polymorphism and Mixed Crystals of Acridine/Phenazine. *Chemistry – A European Journal*. **21**(4), pp.1735–1742.

Seltzer, S.M. and Berger, M.J. 1985. Bremsstrahlung spectra from electron interactions with screened atomic nuclei and orbital electrons. *Nuclear Instruments and Methods in Physics Research Section B: Beam Interactions with Materials and Atoms*. **12**(1), pp.95–134.

Seto, T. 1962. Crystal Structures of n-Higher Alcohols. *Memoirs of the College of Science, University of Kyoto. Series A*. **30**(1), pp.89–107.

Shemchuk, O., Braga, D. and Grepioni, F. 2016. Alloying barbituric and thiobarbituric acids: from solid solutions to a highly stable keto co-crystal form. *Chemical Communications*. **52**(79), pp.11815–11818.

Sirota, E.B. and Herhold, A.B. 2000. Transient rotator phase induced nucleation in n-alkane melts. *Polymer*. **41**(25), pp.8781–8789.

Smith, A.E. 1953. The Crystal Structure of the Normal Paraffin Hydrocarbons. *The Journal of Chemical Physics*. **21**(12), pp.2229–2231.

Smith, D.J. 2008. Development of Aberration-Corrected Electron Microscopy. *Microscopy and Microanalysis*. **14**(1), pp.2–15.

Spoletti, E., Verma, V., Cappuccino, C. and Lusi, M. 2023. Solid solution polymorphs afford two highly soluble co-drug forms of tolbutamide and chlorpropamide. *Chemical Communications*. **59**(96), pp.14321–14324.

Spurgeon, S.R., Du, Y. and Chambers, S.A. 2017. Measurement Error in Atomic-Scale Scanning Transmission Electron Microscopy—Energy-Dispersive X-Ray Spectroscopy (STEM-EDS) Mapping of a Model Oxide Interface. *Microscopy and Microanalysis*. **23**(3), pp.513–517.

Stan, G. and King, S.W. 2020. Atomic force microscopy for nanoscale mechanical property characterization. *Journal of Vacuum Science & Technology B, Nanotechnology and Microelectronics: Materials, Processing, Measurement, and Phenomena*. **38**(6).

Steed, J.W. 2013. The role of co-crystals in pharmaceutical design. *Trends in Pharmacological Sciences*. **34**(3), pp.185–193.

Stenn, K. and Bahr, G.F. 1970. Specimen damage caused by the beam of the transmission electron microscope, a correlative reconsideration. *Journal of Ultrastructure Research*. **31**(5–6), pp.526–550.

Stock, D. and Briggs, G. 2000. Physicochemical Properties of Adjuvants: Values and Applications 1. *Weed Technology*. **14**(4), pp.798–806.

Talmon, Y. 1982. Thermal and radiation damage to frozen hydrated specimens. *Journal of Microscopy*. **125**(2), pp.227–237.

van Tatenhove-Pel, R.J., Hernandez-Valdes, J.A., Teusink, B., Kuipers, O.P., Fischlechner, M. and Bachmann, H. 2020. Microdroplet screening and selection for improved microbial production of extracellular compounds. *Current Opinion in Biotechnology*. **61**, pp.72–81.

Teerakapibal, R., Li, H., Linehan, B. and Nordstrom, F.L. 2020. Material Impurity Distribution of Lattice-Incorporated Impurities in Salicylic Acid. *Crystal Growth and Design*. **20**(3), pp.1716–1728.

Teng, H.H. 2004. Controls by saturation state on etch pit formation during calcite dissolution. *Geochimica et Cosmochimica Acta*. **68**(2), pp.253–262.

Tiernan, H., Byrne, B. and Kazarian, S.G. 2020. ATR-FTIR spectroscopy and spectroscopic imaging for the analysis of biopharmaceuticals. *Spectrochimica Acta. Part A, Molecular and Biomolecular Spectroscopy*. **241**, p.118636.

Tu, M. and Randall, J.M. 2003. *Adjuvants 8.1 Weed Control Methods Handbook, The Nature Conservancy, Tu et al. Chapter 8-ADJUVANTS* [Online]. [Accessed 3 October 2022]. Available from: http://www.herbicide-adjuvants.com/index.html.

Ungar, G. 1983. Structure of rotator phases in n-alkanes. *Journal of Physical Chemistry*. **87**(4), pp.689–695.

Ungar, G. and Mašić, N. 1985. Order in the rotator phase of n-alkanes. *Journal of Physical Chemistry*. **89**(6), pp.1036–1042.

Veeman, W.S. 1997. Nuclear magnetic resonance, a simple introduction to the principles and applications. *Geoderma*. **80**(3–4), pp.225–242.

Ventolá, L., Ramírez, M., Calvet, T., Solans, X., Cuevas-Diarte, M.A., Negrier, P., Mondieig, D., van Miltenburg, J.C. and Oonk, H.A.J. 2002. Polymorphism of N-alkanols: 1-heptadecanol, 1-octadecanol, 1-nonadecanol, and 1-eicosanol. *Chemistry of Materials*. **14**(2), pp.508–517.

Walker, S.C. 2017. *Micro and Nanoscale Imaging of Leaf Surfaces*. University of Nottingham.

Wang, Y., Li, H., Raikes, M., Linehan, B., Robson, J. and Nordstrom, F.L. 2021. Formation of Macrotubular Crystals of Salicylic Acid through Ripening of Solid Solution Crystals Containing Impurity Gradients. *Crystal Growth and Design*. **21**(7), pp.4100–4110.

Wang, Y., Song, R., Li, Y. and Shen, J. 2003. Understanding tapping-mode atomic force microscopy data on the surface of soft block copolymers. *Surface Science*. **530**(3), pp.136–148.

Warley, A. 1997. *X-ray Microanalysis for Biologists* (A. Warley, ed.). Cambridge: Portland Press.

West, A. 1984. *SOLID STATE CHEMISTRY AND ITS APPLICATIONS.* [Online]. [Accessed 3 February 2025]. Available from: https://www.wiley.com/en-es/Solid+State+Chemistry+and+its+Applications%2C+2nd+Edition%2C+Student+Edition-p-9781119942948.

Williams, D.B. and Carter, C.B. 2009. The Transmission Electron Microscope *In*: *Transmission Electron Microscopy* [Online]. Boston, MA: Springer US, pp.3–22. [Accessed 16 March 2021]. Available from: http://link.springer.com/10.1007/978-0-387-76501-3_1.

Winokur, M.J. and Chunwachirasiri, W. 2003. Nanoscale structure–property relationships in conjugated polymers: Implications for present and future device applications. *Journal of Polymer Science Part B: Polymer Physics*. **41**(21), pp.2630–2648.

Wittmann, J.C., Hodge, A.M. and Lotz, B. 1983. Epitaxial crystallization of polymers onto benzoic acid: Polyethylene and paraffins, aliphatic polyesters, and polyamides. *Journal of Polymer Science: Polymer Physics Edition*. **21**(12), pp.2495–2509.

Wittmann, J.C. and Lotz, B. 1990. Epitaxial crystallization of polymers on organic and polymeric substrates. *Progress in Polymer Science*. **15**(6), pp.909–948.

Wolman, M. 1975. Polarized light microscopy as a tool of diagnostic pathology. A review. *Journal of Histochemistry and Cytochemistry*. **23**(1), pp.21–50.

Wong, C.Y., Wong, W.Y., Loh, K.S. and Mohamad, A.B. 2017. Study of the plasticising effect on polymer and its development in fuel cell application. *Renewable and Sustainable Energy Reviews*. **79**, pp.794–805.

Wynne, E., Connell, S.D., Shinebaum, R., Blade, H., George, N., Brown, A. and Collins, S.M. 2024. Grain and Domain Microstructure in Long Chain N-Alkane and N-Alkanol Wax Crystals. *Crystal Growth and Design*. **15**, p.22.

Xiao, L., Kolaczkowski, M.A., Min, Y. and Liu, Y. 2020. Substitution Effect on Thiobarbituric Acid End Groups for High Open-Circuit Voltage Non-Fullerene Organic Solar Cells. *ACS Applied Materials and Interfaces*. **12**(37), pp.41852–41860.

Yao, W. and Zhao, Y.S. 2014. Tailoring the self-assembled structures and photonic properties of organic nanomaterials. *Nanoscale*. **6**(7), pp.3467–3473.

Zainal, N.F.A., Saiter, J.M., Halim, S.I.A., Lucas, R. and Chan, C.H. 2021. Thermal analysis: Basic concept of differential scanning calorimetry and thermogravimetry for beginners. *Chemistry Teacher International*. **3**(2), pp.59–75.

Zeisler-Diehl, V.V., Barthlott, W. and Schreiber, L. 2018. Plant Cuticular Waxes: Composition, Function, and Interactions with Microorganisms *In*: *Hydrocarbons, Oils and Lipids: Diversity, Origin, Chemistry and Fate* [Online]. Springer International Publishing, pp.1–16. [Accessed 15 March 2021]. Available from: https://link.springer.com/referenceworkentry/10.1007/978-3-319-54529-5_7-1.

Zemlin, F., Reuber, E., Beckmann, E., Zeitler, E. and Dorset, D.L. 1985. Molecular Resolution Electron Micrographs of Monolamellar Paraffin Crystals. *Science*. **229**(4712), pp.461–462.

Zhang, J., Cheng, N. and Ge, B. 2022. Characterization of metal-organic frameworks by transmission electron microscopy. *Advances in Physics: X*. **7**(1), p.2046157.

Zhao, L., Tang, P., Luo, D., Dar, M.I., Eickemeyer, F.T., Arora, N., Hu, Q., Luo, J., Liu, Y., Zakeeruddin, S.M., Hagfeldt, A., Arbiol, J., Huang, W., Gong, Q., Russell, T.P., Friend, R.H., Grätzel, M. and Zhu, R. 2022. Enabling full-scale grain boundary mitigation in polycrystalline perovskite solids. *Science Advances*. **8**(35), p.3733.

Zhong, X., Shtukenberg, A.G., Hueckel, T., Kahr, B. and Ward, M.D. 2018. Screw Dislocation Generation by Inclusions in Molecular Crystals. *Crystal Growth and Design*. **18**(1), pp.318–323.

Zhu, H., Yuen, C. and Grant, D.J.W. 1996. Influence of water activity in organic solvent + water mixtures on the nature of the crystallizing drug phase. 1. Theophylline. *International Journal of Pharmaceutics*. **135**(1–2), pp.151–160.